Alignment of Diatomic Molecules Induced by Intense Laser Fields

VRIJE UNIVERSITEIT

Alignment of Diatomic Molecules Induced by Intense Laser Fields

ACADEMISCH PROEFSCHRIFT

ter verkrijging van de graad van doctor aan
de Vrije Universiteit Amsterdam,
op gezag van de rector magnificus
prof.dr. T. Sminia,
in het openbaar te verdedigen
ten overstaan van de promotiecommissie
van de faculteit der Exacte Wetenschappen
op dinsdag 18 december 2001 om 15:45 uur
in het hoofdgebouw van de universiteit,
De Boelelaan 1105

door

Florentina Roşca-Prună

geboren te Beijing, China

Promotor: prof.dr. H.G. Muller
Copromotor: dr. M.J.J.Vrakking

pentru Nicu

Promotiecommissie:

Prof.dr. H.J. Bakker
Prof.dr. B.Girard
Prof.dr. D.J. Parker
Prof.dr. S. Stolte
Prof.dr. W.v.d. Zande

Cover: Two-dimensional image resulting from the Coulomb explosion of I_2 molecules excited using a 100 femtosecond laser pulse. The image shows the projection of the three-dimensional velocity distribution of I^+ fragments and was measured using a velocity map ion imaging detector.

ISBN-90-9015452-3

The work described in this thesis was performed at the FOM Institute for Atomic and Molecular Physics (AMOLF), Kruislaan 407, 1098 SJ, Amsterdam, the Netherlands (www.amolf.nl).

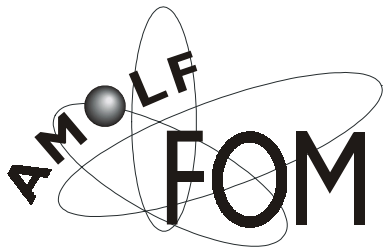

This work is part of the research program of the Stichting voor Fundamenteel Onderzoek der Materie (Foundation for Fundamental Research on Matter) and was made possible by financial support from the Nederlandse Organisatie voor Wetenschappelijk Onderzoek (Netherlands Organization for the Advancement of Research).

This thesis is based on the following publications:

Chapter 4 *Spatial alignment of diatomic molecules in intense laser fields (I): experimental results.*
F. Rosca-Pruna, E. Springate, H. L. Offerhaus, M. Krishnamurthy, N. Farid, C. Nicole and M.J.J. Vrakking,
Journal of Physics B, accepted for publication (2001).

Chapter 5 *Spatial alignment of diatomic molecules in intense laser fields (II): numerical modeling.*
E. Springate, F. Rosca-Pruna, H. L. Offerhaus, M. Krishnamurty and M. J. J. Vrakking,
Journal of Physics B, accepted for publication (2001).

Chapter 6 *Experimental Observation of Revival Structures in Picosecond Laser-Induced Alignment of I_2*
F. Rosca-Pruna and M.J.J. Vrakking,
Physical Review Letters **87** (15), 153902 (2001).

Revival structures in Femtosecond Laser-Induced Alignment of I_2 molecules (I): Experimental Results
F. Rosca-Pruna and M.J.J. Vrakking,
Journal of Chemical Physics, submitted for publication (2001).

Revival structures in Femtosecond Laser-Induced Alignment of I_2 molecules (II): Numerical Modelling
F. Rosca-Pruna and M.J.J. Vrakking,
Journal of Chemical Physics, submitted for publication (2001).

In addition, the author participated in the following publications:

Slow photoelectron imaging.
C. Nicole, I. Sluimer, F. Rosca-Pruna, M. Warntjes, M. Vrakking, Ch. Bordas, F. Texier and F. Robicheaux, Physical Review Letters **85** (19), 4024 (2000).

Two-channel competition of autoionizing Rydberg electrons in an electric field.
J.B.M. Warntjes, C. Nicole, F. Rosca-Pruna, I. Sluimer, M.J.J. Vrakking and L.D. Noordam, Physical Review A **63**, 053403 (2001).

Atomic streak camera operating in the XUV.
J.B.M. Warntjes, A. Gürtler, A. Osterwalder, F. Rosca-Pruna, M.J.J. Vrakking and L.D. Noordam, Review of Scientific Instruments **72** (8), 3205 (2001).

Atomic spectral detection of tunable XUV pulses.
J.B.M. Warntjes, A. Gürtler, A. Osterwalder, F. Rosca-Pruna, M.J.J. Vrakking and L.D. Noordam, Optics Letters, **26** (19), 143 (2001).

A magnifying lens for velocity map imaging for electrons and ions.
H.L. Offerhaus, C. Nicole, F. Lepine, Ch. Bordas, F. Rosca-Pruna and M.J.J. Vrakking, Review of Scientific Instruments **72** (8), 3245 (2001).

Contents

Chapter 1

Introduction

It is a fascinating and challenging task to observe and to control processes in nature on a time scale of several femtoseconds. One femtosecond ($1fs$) is the 1:10^{15}th part of a second and corresponds to half an optical period of red light. The ratio of one femtosecond to one second is about the same as the ratio of five minutes to the age of the earth. During one femtosecond, visible light travels over a distance of a 300 nanometers, which is hardly of any concern to us in our daily routine. However, this distance corresponds to several thousands of unit cells in a solid. This suggests the importance that the femtosecond time scale might have in the microcosm. Indeed, various essential processes in atoms and molecules as well as interactions among them, proceed faster than what can be resolved on a picosecond time scale ($1ps = 10^{-12}sec$). These events include primary steps for many processes in physics, chemistry and biology.

The pulsed nature of many laser sources makes it possible to observe very fast events. Thus, in the same way that a flash lamp can stop the motion of a runner in a photograph, or even a bullet piercing an apple, a laser too can act as a flash lamp, capturing objects in fast motion. The femtosecond lasers are therefore of extreme interest since femtosecond is the fundamental time scale of atomic motion. Short-pulse femtosecond lasers have become our 'flash lamp' to illuminate the atomic world. In typical experiments using femtosecond lasers, a 'pump' pulse initiates an event like a chemical reaction, and a 'probe' pulse observes the event at a later instant in time. In this way, the pump-probe experiment provides us with a movie of the chemical reaction. In 1999 the inventor of this technique, Prof. Ahmed Zewail from Caltech University in the United States, received the Nobel Prize in Chemistry for his pioneering work in this area [1].

An important aspect of femtosecond laser pulses is that the pulses are not only very short, but typically also very intense [2]. In recent years, femtosecond lasers have provided many new opportunities in studies of molecular dynamics [3–7]. Rapid advances are seen in the way femtosecond lasers are used to generate ultrashort pulses in the soft and hard x-ray regime [8]. These pulses show considerable promise for applications in research in physics, chemistry and biology [9]. At the same time, there are many new and exciting developments in studies of the direct interaction of intense

femtosecond lasers with individual molecules. Recent years have seen experiments where the progress of a molecular dissociation could be followed in real time [10]. Intense femtosecond lasers are increasingly finding applications in mass spectroscopy, due to the lack of parent fragmentation in multi-photon ionization with femtosecond versus nanosecond lasers [11]. One aspect of the interaction of intense femtosecond lasers with molecules, which is attracting considerable interest, is the aspect of control. At the focus of an intense laser, oscillating electric fields are present that are comparable to or may even exceed the electrostatic fields experienced by electrons in an atom or a molecule. As a result molecules are strongly polarized in an intense laser field, and experience driving forces that have the tendency to both trap and align the molecules [12–15]. Several groups in the world are considering the application of intense laser fields in what has sometimes been called 'molecular optics' [16]. In the future, it may even be possible to use short pulses to manipulate molecules and molecular reactions in very precise ways, i.e. to make new chemicals.

In this thesis, experiments concentrated on two characteristics of high intensity femtosecond lasers which are present. Firstly, the generation of ultrashort, high-intensity near-infrared laser pulses and their application to the production of ultrashort XUV pulses and to the control of molecules is reported. In Part 1 of the thesis the home-built Amolf Table-Top Terawatt (T^3) laser system is presented. This laser system is based on the Chirp Pulse Amplification (CPA) technique [17]. In this technique the laser pulse is amplified and optical damage is avoided by stretching the pulse in time prior to the amplification and then compressing it back to its original duration after the amplification is completed. In this way high-peak-power pulses in the Terawatt ($1TW = 10^{12}W$) range can be produced, which can be focussed to intensities in the range of 10^{19} to 10^{20} W/cm^2 [18]. The theoretical design and practical implementation of the Amolf laser system are presented in Chapter 2 of this thesis. Part 1 of this thesis also gives a description of the experimental apparatus (in Chapter 3), which was used in all the experiments presented here, and which includes a velocity map imaging detector.

Secondly, in Part 2 of the thesis experiments are presented that are aimed at studying alignment of molecules in intense laser fields. In an experimental investigation which is presented in Chapter 4, we have studied kinetic energy and angular distributions in multi-electron dissociative ionization (MEDI) of iodine and bromine molecules as a function of the duration and energy of the intense near-infrared femtosecond/picosecond laser pulse used. Multiply charged atomic fragments were recorded using the velocity map-imaging detector described in Chapter 3. A significant narrowing in the angular distribution was observed when the pulse durations were increased from 100 femtoseconds to about 2 picoseconds. In these experiments, the angular distribution is due to a combination of three effects, namely (i) laser-induced ground state alignment, (ii) the angular dependence of the molecular ionization and (iii) the angular dependence of the subsequent Coulomb explosion. Using a theoretical investigation which is presented in Chapter 5, we concluded that the significant narrowing of the angular distribution for longer pulses is a manifestation of the fact that under these

conditions the molecules have a longer time to adapt to the potential well generated by the laser, i.e. the narrower angular distributions are a manifestation of alignment of the molecule in the ground state prior to the loss of the first electron. After ionization the singly charged molecular ions dissociate until they reach a critical distance (which typically is about 5Å) where the laser intensity needed for further ionization (i.e. Coulomb explosion) is minimal. Due to the existence of this critical distance, a widening of the angular distribution is predicted in the absence of ground state alignment, quite contrary to what is observed experimentally. Hence the conclusion is drawn that ground state alignment prior to ionization is an important factor.

Building on the understanding gained in the experiments presented above, we have also carried out a two-laser pump-probe experiment which is presented in Part 3 of this thesis (Chapter 6). In this experiment the alignment induced by a relatively long near-infrared pump pulse ($1 - 10ps$) was probed using multi-electron dissociative ionization with a short probe pulse ($80fs$). These experiments showed the onset of the alignment during the pump pulse, and importantly, revealed the formation of a rotational wavepacket by the pump pulse, leading to periodic recurrences of the alignment at characteristic time delays following the pump pulse. The observation of these recurrences is particularly significant, since it allows us to prepare aligned molecules under field-free conditions, paving the way to studies of angular-resolved molecular photoionization and photodissociation in the molecular frame.

When an atom is subjected to a strong laser field, the electron response is highly nonlinear. One consequence of this is the generation of harmonics of the driving field. This means that light from an intense femtosecond laser in the near-infrared part of the spectrum can be converted into ultrashort pulses in the extreme ultra-violet (XUV) or even soft x-ray range [19]. In Chapter 7 high-harmonic generation in noble gas atoms irradiated with an intense short-pulse laser is used with the aim of studying photoionization and photodissociation of molecules. A few preliminary results are presented. In high-harmonic generation using short pulses it is known that the pulse duration of the radiation which is generated is generally much shorter than the pulse duration of the driving laser [20–22]. A beautiful experiment was performed recently by one of our colleagues at Amolf [23], who demonstrated that intense $40fs$ laser pulses can be used to create a train of attosecond laser pulses ($1as = 10^{-18}s$), in what was the first experimental demonstration of the formation of sub-femtosecond pulses. In our setup, a grating can be used to select the harmonic needed in the experiments. Due to frequency chirp induced by the grating (see Chapter 2) the harmonic that reaches the interaction region in the experimental chamber does not have a bandwidth-limited pulse duration and is longer than the driving field. An attempt to measure the pulse duration of a few harmonics after the diffraction off the grating is presented in Chapter 7. The method used is based on a cross-correlation measurement that monitors the appearance of side-bands in the photoelectron spectra, which are obtained when high harmonics are sent into the interaction region together with the fundamental radiation in order to ionize atoms (i.e. argon). The side-bands are produced when atoms absorb one high-harmonic photon and absorb or emit one or more fundamental photons. Therefore,

the appearance of side-bands requires the spatial and temporal overlap of the high harmonics and the fundamental radiation, and hence it can be monitored in a cross-correlation measurement.

An application for harmonic generation which is intended in our group, is to use harmonics as a source for time-resolved spectroscopy. Here, the short duration of high harmonics allows high temporal resolution. Experiments are planned where high harmonics will be used to probe the molecular alignment (reported in Chapter 6) and where velocity map imaging detection will give the photoelectron angular distributions in the molecular frame. High harmonics will also be used in studies of time-resolved photoionization and photodissociation. When the difference in wavelength between neighboring harmonics becomes sufficiently small so that their bandwidth overlaps, then the high-harmonic generation becomes a continuously tunable radiation source. Another application for high harmonic radiation is soft x-ray microscopy of biological samples. High spatial resolution is possible with x-rays given their short wavelength. The ability to penetrate water is an important advantage of x-rays over the electrons used in an electron microscope, and allow living organisms to be studied in an aqueous environment [24]. Short-pulse harmonics would furthermore permit ultrashort exposures thereby overcoming image blurring from hydrodynamic motion of the laser-heated sample. The high spatial coherence of the harmonics should allow holography, opening up a powerful technique for high-resolution three-dimensional spectroscopy.

Part 1

The experimental setup.

Chapter 2

Table Top Terawatt laser system

In all the experiments that will be presented in this thesis the AMOLF Terawatt laser was used. This laser system is presented in this chapter. A brief history of modern laser development and various aspects of ultrashort pulse generation and amplification are given. Theoretical design considerations for the laser system are presented. The practical design of the laser system is discussed in the third section. In the last part the performance of the laser is presented.

2.1 Introduction

2.1.1 Ultrashort laser pulse generation

The first laser to be operated successfully, in June 1960 [25], was a solid state ruby laser. A solid-state laser has as gain medium a crystal or a glass that has a fluorescent spectrum and is transparent and heat resistant. Typically it contains transition metals or rare earth elements as active ions. Ruby crystals contain 0.01-0.1% of Cr^{3+} in Al_2O_3 (sapphire) and are used for generating and amplifying laser light of $694nm$ wavelength.

In this thesis we will only deal with solid-state lasers. However, the laser gain medium can also be gaseous or a liquid. The first gas laser that generated continuous waves (CW) output, in December 1960, was the $1.15\mu m$ He-Ne laser, based on a discharge in a mixture of helium and neon gas. Since then a large variety of gas lasers have been developed in a wide range of wavelengths, from the vacuum ultraviolet to the far infrared or even millimeter waves. In most cases the gas is either excited by an electrical discharge or optically pumped [26, 27].

Laser action can also be attained in an optically pumped solution of an organic dye. This is called a dye laser [28] and since the fluorescence spectrum of a dye can be as wide as $100 - 200cm^{-1}$, the laser wavelength can be easily tuned by using a diffraction grating or a prism. The efficiency of a dye laser can be relatively high and the pulse duration can be as short as $0.1ps$. Dye lasers are used extensively in spectroscopic

research, being the most convenient tunable lasers in the visible. Since the successful development of a pulsed dye laser in 1966, lasers have been operated with over 500 different dyes, but relatively few of these dyes allow CW operation.

Semiconductor lasers were proposed in 1957 and were first demonstrated in 1962 in pulsed operation at low temperature. After CW operation was successfully achieved at room temperature in 1970, rapid progress has been made to develop this light source for optical fiber communication [29].

The first generation of lasers producing pulses with durations less than $100ps$ was based on the development of mode-locking (1970). The term "mode-locking" originates from a description of the laser in the frequency domain, where the emission is considered to be made up of a sum of the radiation of the longitudinal modes of the cavity. In a free-running laser, the relative phase of a comb of equally spaced modes (frequency spacing Δ) can be a set of random numbers. The time domain transformation of such a frequency spectrum is an infinite series of identical bursts of incoherent light, spaced in time by $2\pi/\Delta$, which is the time needed to complete a cavity round-trip. Constant phase difference between modes (mode-locking) implies in the time domain that all waves of different frequency add constructively at one point in the cavity, resulting in a very intense and short burst of light. It is possible to lock the modes in phase using a nonlinear optical element inserted into the laser resonator, or by modulating the cavity losses at the round-trip frequency of the cavity. When modes are locked by externally applying a voltage to a modulator, this is called *active mode-locking*. When modes are locked as a result of the insertion of a nonlinear optical component like a saturable absorber [30], one speaks of *passive mode-locking*. Since the laser medium is nonlinear, mode-locking can sometimes also be obtained without any additional nonlinear optical element, if the pump conditions and the resonator are appropriately adjusted. This is called *self mode-locking*.

Actively mode-locked Nd:YAG (Neodymium: Yttrium Aluminium Garnet) lasers and passively mode-locked flashlamp-pumped Nd:glass lasers were the standard sources of picosecond optical pulses for several years. More recently, other host material like Nd:YLF (Yttrium Lithium Fluoride), Ti:Sa (Titanium:Sapphire), Alexandrite [18,31], etc. were developed. The wavelength of these lasers is in the near infrared region, around $1.0\mu m$.

The pulse duration of mode-locked lasers is limited by two parameters: the spectral bandwidth and the dispersion. The spectral bandwidth ($\Delta\lambda$) is related to the minimum pulse duration (τ) as:

$$\tau = \frac{a \times \lambda_1 \times \lambda_2}{c \times \Delta\lambda}, \tag{2.1}$$

where τ is the FWHM of the pulse duration, a is a constant that depends on pulse shape ($a = 0.441$ for gaussian shape and $a = 0.315$ for $sech^2$ shape), c is the speed of light and $\Delta\lambda = \lambda_1 - \lambda_2$ (where λ_1 and λ_2 are the values corresponding to the FWHM in the pulse spectrum). Therefore, an active medium with a large fluorescence bandwidth can support the generation of short pulses. Another important parameter, that has

to be compensated in order to achieve short pulses is the dispersion that is introduced by the active medium and/or the other optical components present in the laser cavity. Individual wavelength components have different round-trip times through the cavity. The output bandwidth of a laser oscillator is determined by the dispersion in the laser cavity.

By the early 1980's, a novel passive mode-locking technique, namely colliding pulse mode-locking (CPM) was invented [32]. It was shown that the dispersion inside a laser could be continuously adjusted and optimized by inserting a prism sequence into the laser cavity. As a result of this development, sub-picosecond, synchronously pumped dye lasers and 100-femtosecond passively mode-locked dye lasers became standard equipment.

Due to the low pump threshold and broader fluorescence linewidths, solid-state lasers allow for the generation of shorter pulses and a wider tuning range than dye lasers. A technique which dramatically improved the performances of solid-state lasers is Kerr-lens mode-locking (KLM). The nonlinear response of a material to laser radiation leads to a change in the refractive index:

$$n = n_0 + n_2 I \tag{2.2}$$

where n_0 is the normal refractive index, n_2 is the nonlinear refractive index and I is the intensity of the laser field. This effect is referred to as the '*optical Kerr effect*' and can produce several nonlinear phenomena. One of these is the self-focusing of an optical beam. For a positive value of n_2, the more intense part of the beam experiences a higher refractive index. Therefore it propagates slower and the phase front is altered in such a way that the optical medium acts as a weak positive lens. Kerr-lens mode-locking is based on achieving minimal losses for self-focusing beams and thus concentrating the energy in a short pulse. If the self-focusing effect exceeds the diffraction spreading of the optical beam while propagating through a given length of the medium, the optical beam may even collapse into self-focused filaments. This not only distorts the transverse beam profile but can also cause optical damage.

Kerr-lens mode-locked lasers initially generated pulses as short as $60fs$ [33], but the pulse duration has been shortened very rapidly [34–37]. The original self-mode-locked Ti:sapphire laser demonstrated by *Sibbett* used a $2cm$ long crystal and prisms made from highly dispersive SF14 glass for dispersion compensation. The dispersion compensation has been improved by using different glass types for the prisms or by using chirped mirrors to control the dispersion [38,39]. Most femtosecond lasers today can generate very stable pulses shorter than $15fs$ with an energy of $1-5nJ$ per pulse at $\sim 80MHz$.

The optical Kerr effect can also produce '*self-phase-modulation*' (SPM) when the variation in intensity along the pulse is in time rather than in space. The refractive index change follows the pulse intensity and therefore different parts of the pulse feel a different refractive index, leading to a phase change across the pulse. This SPM produces new frequency components and broadens the pulse spectrum. This extra

time varying phase modulation can be simply evaluated as:

$$\phi_{SPM}(t) = -\frac{2\pi}{\lambda} n_2 I(l,t) l, \tag{2.3}$$

where l is the length of the optical medium. In high power laser systems there exists a limit on the total amount of self-phase modulation that can be tolerated before the beam properties degrade. This can be characterized by the so-called B-integral:

$$B = \frac{2\pi}{\lambda} \int_0^l n_2 I(l,t) dl \tag{2.4}$$

A generally accepted criterion for high power systems is that the B-integral must be kept below 3 to 5. The fact that SPM produces new frequency components and broadens the pulse spectrum is used successfully for pulse compression. In this way pulses as short as $4-5fs$ have been obtained [40].

2.1.2 Ultrashort laser pulse amplification

Once ultrashort laser pulses are generated they often have to be amplified to meet the requirements of experiments. Before 1985 the traditional approach was amplification in organic dye or excimer amplifiers. These systems have rather low saturation fluences, on the order of a millijoule per square centimeter, which limits the energy extraction and therefore the gain. The saturation fluence of a gain medium can by approximated by:

$$J_{sat}(\lambda) \approx \frac{h\upsilon}{\sigma_e(\lambda)}, \tag{2.5}$$

where $h\upsilon$ is the energy of the pump photon and σ_e the emission cross-section.

For an organic dye the emission cross-section is relatively large, in the range of σ_e = 1 to 5 x $10^{-16} cm^2$. Solid-state media have smaller emission cross-sections (σ_e = 10^{-18} to $10^{-20} cm^2$) and therefore larger saturation fluences, on the order of $1 J/cm^2$, and very broad bandwidths. Solid-state media have also large upper-state life-times, thus good energy storage capabilities. This is an important parameter when these materials are used for amplification. However the peak intensity produced can quickly exceed the damage threshold of the material. This is why the so-called "chirped pulse amplification" (CPA) technique is used (Fig.2.1). This technique is based on the fact that pulse distortions and the likelihood of damage to optical components can be strongly reduced by lowering the average intensity of the pulse. One way to achieve this is to stretch the pulse in time. The stretching factor needs to be 10^3 or higher, so that the peak intensity of the pulse and thus the value of the B-integral, are reduced significantly. The stretching must be done in a reproducible manner, in order to be able to recompress the pulse to its original duration after amplification. The compression step compensates for the accumulated phase for each frequency component. The

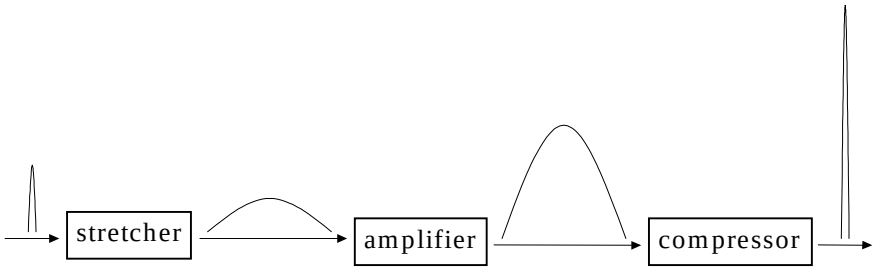

Figure 2.1: *The amplification of ultrashort pulses is done using a technique called "Chirped Pulse Amplification". As the name suggests, in this technique the short pulse is first chirped (stretched in time), then amplified and in the end of the laser system compressed back to its original duration.*

stretching and compression can be done by sending the pulse through a dispersive optical setup where different wavelength components of the short pulse are delayed with respect to each other. The resulting pulse has a frequency that changes in time and is therefore called a '*chirped*' pulse. *Chirped pulse amplification* was used for the first time by Maine *et al.* in a Nd:glass amplification chain [41]. Nowadays, based on this technique pulses as short as $10fs$ can be amplified to Terawatt power levels [42–48].

In CPA systems, uncompensated phase errors in the stretching and compression process and distortions due to the dispersive optics can cause broadening of the final pulse duration that is significant compared to the bandwidth limited value. Therefore compensation of higher order dispersion and the elimination of aberrations becomes indispensable (see section 2.2).

2.1.3 Ti:sapphire as active medium

Ti:sapphire is a three-level system. The energy level diagram of the lasing process in Ti:sapphire is shown in Fig.2.2 (taken from [49]). Titanium atoms in level A ($^2T_{2g}$) are excited to level B(^2E_g) by absorption of pump photons. The suitable wavelength for this transition is around $500nm$. There is a range of pump lasers available for this wavelength region (CW argon lasers - $514nm$, Nd:YLF laser - $527nm$, Nd:YAG lasers - $532nm$). The excited atoms will quickly relax to the state C. This relaxation is accompanied by the emission of phonons and prevents stimulated emission back to the ground state by the pump photons. After relaxation, the ion is in a long-lived excited state ($3.2\mu s$ at room temperature). The laser transition is from this state to an excited portion of the ground state (D). The relaxation process that takes place in the ground state (from D to A) prevents reabsorption in the crystal. Since there is a large geometry change between states C and D, a non-zero Franck-Condon overlap is found for a large range of wavelengths and this leads to a large emission spectrum ($\Delta\lambda \sim 75nm$).

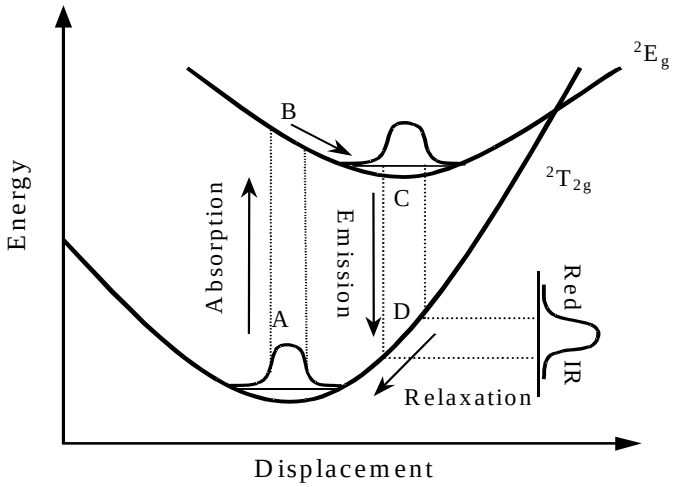

Figure 2.2: *Energy level diagram of the lasing process in Ti:sapphire* [49].

Ti:sapphire has a few important parameters that make it one of the best candidates for short pulse laser generation and amplification. The cross-section for stimulated emission is small which means that the saturation fluence, which is inversely proportional to the emission cross-section, is relatively large and this enables efficient energy extraction. The stimulated emission cross-section peaks around $800nm$ and is $4.1 \times 10^{-19} cm^2$. Both cross-sections favor the same polarization for the pump (absorption) and the laser (emission). The absorption cross-section peaks at $500nm$ and is on the order of $6 \times 10^{-20} cm^2$ ($5.6 \times 10^{-20} cm^2$ at $532nm$). Though the absorption cross-section is small, the absorption is efficient in highly doped crystals. Another important parameter is the large spectral bandwidth. For Ti:sapphire the fluorescence bandwidth full-width at half maximum (FWHM) is $\sim 75nm$, which makes this crystal suitable for generation and amplification of ultrashort pulses. The nonlinear refractive index at the peak of the emission spectrum is $n_2 = 3.2 \times 10^{-16} cm^2/W$.

The low stimulated emission cross-section does, however, also imply that the gain is relatively low so the interaction length has to be increased to obtain high gain. A common solution to achieve high overall gain is to make several passes through the amplifier. Such an amplifier is called a multi-pass amplifier. A relevant parameter for the amplification is the lifetime of the excited state, which should be long enough to allow for several passes. For very low gain, a common amplifying scheme is regenerative amplification, which allows for a considerable number of passes (20 or higher). A regenerative amplifier consists of a cavity containing the active medium, where the pulse is coupled in, amplified and then coupled out after a number of round-trips when the amplification reaches a maximum (see section 2.3.3). When choosing one of these schemes, one has to take into account the mode of the laser beam (spatial profile), the stability and the dispersion during the amplification. The regenerative amplifier gives a better beam profile and has a higher stability, while the dispersion is lower in

the multi-pass amplifier due the reduced number of round-trips and - therefore - the reduced amount of material the laser has to pass through. Using a long active medium also has another advantage: the amplified spontaneous emission (ASE) is weaker, due to the fact that the spontaneous emission takes place in all directions. Only the ASE emitted within a small solid angle can be transmitted through the crystal and can further be amplified.

Taking all the above listed arguments into account, Ti:sapphire seems to be an ideal material to be used as an amplifier: the low emission cross-section favors efficient energy extraction ($J_{sat} = 0.9J/cm^2$), the bandwidth is large enough to amplify femtosecond pulses and furthermore, the excited state lifetime of 3.2 μs allows the light pulse to make a considerable number of passes through the amplifier to acquire high overall gain, allowing for the production of high pulse energies.

2.2 Design of the laser system

In section 2.1, the chirped pulse amplification technique (CPA) was described. The concept of CPA is to stretch the pulse in time, to amplify the pulse and then to compress it back as close as possible to the initial pulse duration. There are a few important parameters in the design of the amplification stages of a laser system, which have to be taken into consideration: nonlinear distortions associated with the high gain during the amplification (*gain shifting* and *gain narrowing*) and high-order dispersion compensation that allows compression of the pulses after amplification. These will now be discussed in turn.

2.2.1 Design of the amplifier

In our system the femtosecond pulses have to be amplified from an energy of $5nJ$ to $30mJ/pulse$. We have chosen to use two amplifiers. The first amplifier is a regenerative amplifier that brings the energy up to $1mJ/pulse$ at a $1kHz$ repetition rate and the second amplifier is a 5-pass amplifier that has an uncompressed output of $\geqslant 80mJ/pulse$ at a $50Hz$ repetition rate.

In this section, we present calculations performed for the regenerative amplifier in order to optimize the amplification process and to minimize the amplified pulse duration after compression (see also next section - dispersion compensation in the amplifier). Similar calculations were performed for the multi-pass amplifier (not presented here).

During amplification it is important that the spectrum of the femtosecond pulse is preserved. However, for large gain, both gain narrowing and gain shifting can occur. The gain during the amplification is wavelength dependent so that the middle part of the spectrum is more amplified than the tails (gain narrowing). Gain shifting occurs due to the fact that the amplified pulses are stretched in time. Colors on the front part of the chirped pulse (red) are amplified more than colors towards the end of the of the chirped pulse (blue) since the gain decreases when energy is extracted. Therefore the

spectrum of the amplified pulse shifts towards red wavelengths .

We analyzed our system based on the model of Le Blanc *et al.* [50] for short pulse amplification. This model assumes a homogeneously broadened gain medium, with a fluorescence lifetime much longer than the pulse duration pumped by a short laser pulse. The output fluence (energy/unit area) following an amplification step can be written as [51]:

$$J_{out} = J_{sat} \left[\ln\left(1 + G\left(\exp\left(J_{in}/J_{sat}\right) - 1\right)\right)\right](1 - L)\,, \tag{2.6}$$

where J_{sat} is the saturation fluence (defined in eq.2.5), J_{in} and J_{out} are respectively the input and output pulse fluence, L is a loss coefficient and G is the small signal gain.

The small signal gain G depends on the emission cross-section σ_e, the length of the medium l and the inversion $\Delta n = n_2 - n_1$ (where n_2 is the density of atoms in the excited level and n_1 is the density of atoms in the ground level):

$$G = \exp\left(\sigma_e \Delta n l\right) \tag{2.7}$$

For a medium with a low emission cross-section value, the parameter which keeps the gain high is the interaction length l. This is the reason why the pulse has to make several passes through the amplifier to achieve the maximum gain while the inversion is still present (i.e. during the lifetime of the excited level).

The small signal gain can alternatively be expressed as:

$$G = \exp\left(J_s/J_{sat}\right), \tag{2.8}$$

where J_s is the energy stored in the gain medium per unit area and is given by:

$$J_s = \frac{E_{stored}}{A} \times \frac{\lambda_a}{\lambda_e} * \beta \tag{2.9}$$

where E_{stored} is the pump energy (J), A is the pump area (cm^2), λ_a is the absorption wavelength (the pump wavelength), λ_e is the emission wavelength $(800nm)$ and β is an absorption coefficient that depends on the doping and on the length of the active medium.

One can differentiate the expression of J_{out} with respect to time to get the time evolution of the intensity:

$$I_{out}(t) = \frac{\exp(J_{in}(t)/J_{sat})(G(t)I_{in}(t) + J_{sat}\partial G(t)/\partial t) - J_{sat}\partial G(t)/\partial t}{1 + (\exp(J_{in}(t)/J_{sat}) - 1)G(t)}(1 - L) \tag{2.10}$$

where the time-dependent fluences are defined by:

$$J_{in}(t) = \int_{-\infty}^{t} I_{in}(t')dt' \qquad \text{and} \qquad J_{out}(t) = \int_{-\infty}^{t} I_{out}(t')dt' \tag{2.11}$$

with I_{in} and I_{out} respectively the input and the output intensities of the laser.

Due to depletion of the stored energy the small signal gain becomes time dependent:

$$G(t) = \exp(\frac{J_{s0} - (J_{out}(t) - J_{in}(t))}{J_{sat}}) \tag{2.12}$$

where J_{s0} is the initial stored energy per unit area.

In the case of strong linearly chirped pulses, the time and the instantaneous frequency are related by: $\omega = \omega_0 + Kt$, where K is the chirp coefficient (s^{-2}). In this case, any change in the temporal shape of the pulse directly influences its spectral profile and vice-versa. One can predict that the gain narrowing and the gain saturation will both have an effect on the pulse spectra.

Including the frequency-dependence in the amplification process, the equation that was numerically solved was given by:

$$I_{out}(t,\omega) = \frac{\exp(J_{in}(t)/J_{sat}(\omega))(G(\omega,t)I_{in}(t) + J_{sat}\partial G(\omega,t)/\partial t) - J_{sat}\partial G(\omega,t)/\partial t}{1 + (\exp(J_{in}(t)/J_{sat}(\omega)) - 1)G(\omega,t)}(1-L)$$

The input conditions used in the calculations were parameters describing the infrared seed beam and the pump geometry. For our laser system the seed has a central wavelength at $800nm$, a bandwidth that corresponds to a minimum pulse duration of $20fs$, a pulse energy of about $1nJ$ (after the stretcher) and an area of $\sim 1mm^2$ (on the crystal). The pump beam is described by a central wavelength at $527nm$, a pulse duration of $400ns$, a pulse energy of $12mJ$ and an area of $\sim 1mm^2$ on the crystal (i.e. stored energy $8.6mJ/mm^2$ for 10% cavity losses). The cavity losses L were varied between 10 and 20%.

Results of these calculations are shown in Fig.2.3 for two different focusing geometries of the pump and the seed lasers and for two values of the cavity losses. In Fig.2.3a the stored energy versus number of round-trips in the amplifier shows a constant value for the first few passes followed by a decay due to the energy extraction by the seed laser. The decay is slower for a larger pump geometry ($1mm^2$) and high losses (20%). In Fig.2.3b the energy of the amplified pulse is plotted as a function of the number of round-trips. The pulse noticeably starts to gain energy after a number of round-trips that corresponds to the starting point of the stored energy decay (a). One can conclude that for the input parameters presented above, for $8.5mJ/mm^2$ stored energy/unit area in the crystal, an output of $\sim 2mJ$ after 12 round-trips should be possible (upward triangles in Fig.2.3b). In the third and the fourth graph of this figure (2.3c and d), the spectral bandwidth at FWHM and the central wavelength as a function of number of round-trips are presented. These graphs show that for an initial pulse with a spectral bandwidth $\Delta\lambda = 46nm$ and a central wavelength of $800nm$, after 12 passes the bandwidth narrows down to $\sim 35nm$ due to gain narrowing and the central wavelength shifts to $814nm$ due to gain shifting (upward triangles in Fig.2.3c and d). In the future, we want to introduce an etalon in the regen cavity to increase the bandwidth. The etalon serves to attenuate the wavelength situated at the peak of the pulse spectrum and to allow the tail of the spectrum to be amplified [52].

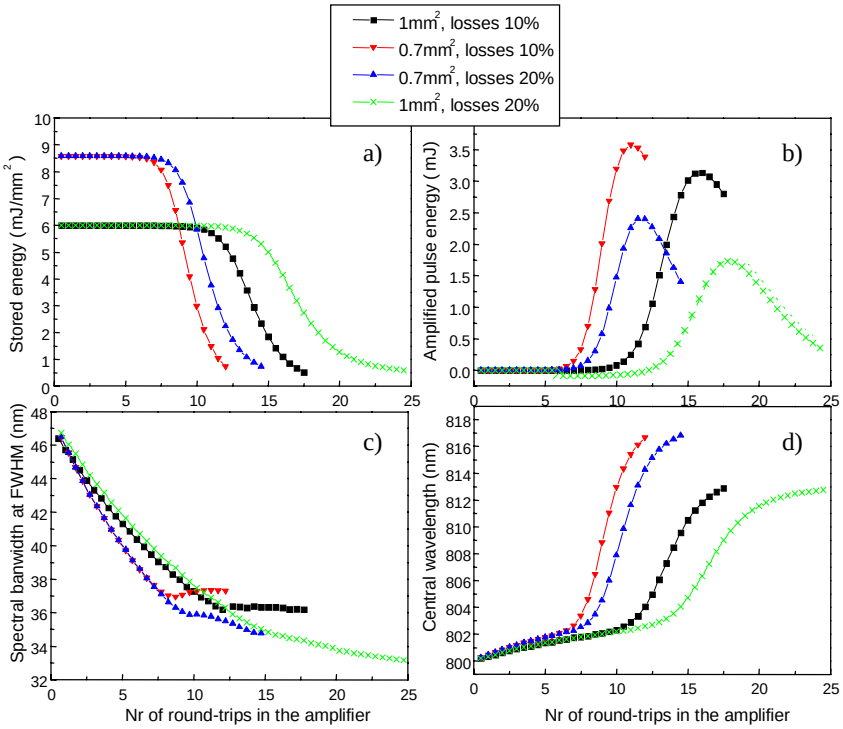

Figure 2.3: *Parameters of the regenerative amplifier as a function of the number of round-trips for different beam sizes and cavity losses: a) the stored energy per unit area; b) the energy of the amplified pulse; c) the spectral bandwidth; d) the central wavelength. The depletion of the energy stored in the crystal (a) correspond to an increase in the energy of the amplified pulse (b). For an initial pulse with a* $\sim 46nm$ *bandwidth and* $800nm$ *central wavelength, the amplified pulse has after 12 round-trips a reduced bandwidth of* $\sim 35nm$ *due to gain narrowing and a central wavelength of* $814nm$ *due to gain shifting.*

As mentioned in the introduction, when designing an amplifier one has to pay attention to the B-integral that must be kept below 3 to 5 to avoid nonlinear damage and distortion effects due to self phase modulation or self-focusing (see section 2.1.1 and 2.1.2). Therefore, there are constraints on the size of the beam. In the case of the regenerative amplifier, for $2mJ$ output pulse energy and a $1mm^2$ the beam size on a $6mm$ long Ti:sapphire rod traversed by a $30fs$ pulse (stretched to $200ps$), the value of the B-integral is 0.015 which allows for safe operation. For the multi-pass amplifier, we calculated the value of the B-integral for a $10mm$ long Ti:sapphire rod, for an output pulse energy of $80mJ$ and $4mm^2$ beam area, to be 0.25. The intensity reached at saturation in the multi-pass amplifier is $1 \times 10^{10} W/cm^2$.

For safe operation, one has to consider not only the intensity on the crystal but also on the optical components of the regenerative amplifier. To evaluate this we used

a program based on matrix optics calculations. The program calculates the waist of the beam on each component in the cavity (assuming that a gaussian beam propagates through the cavity). In this manner, the intensity on each optical component can be estimated and one can choose the optical components needed for safe operation.

2.2.2 Dispersion compensation in the amplifier

Higher-order dispersion compensation is very important for ultrashort pulses. The effect of uncompensated dispersion can not only broaden the pulse but can also degrade the pulse shape through the presence of a pedestal and pre- or post-pulses (shoulders), etc., which is undesirable for many high-intensity experiments.

In designing the amplifier we calculated the dispersion introduced in the system by examining the accumulated phase of the laser pulse along the amplification stages. The total phase $\phi(\omega)$ can be expanded in a Taylor series around the central frequency of the laser pulse:

$$\phi(\omega) = \phi(\omega_0) + \phi'(\omega_0)(\omega - \omega_0) + \frac{1}{2}\phi''(\omega_0)(\omega - \omega_0)^2 + \frac{1}{6}\phi'''(\omega_0)(\omega - \omega_0)^3 + ... \quad (2.13)$$

The time delay along the amplifying stages is the derivative of the phase with respect to the angular frequency:

$$T(\omega) = \phi'(\omega_0) + \phi''(\omega_0)(\omega - \omega_0) + \frac{1}{2}\phi'''(\omega)(\omega - \omega_0)^2 + \frac{1}{6}\phi''''(\omega)(\omega - \omega_0)^3 + ... \quad (2.14)$$

where $\phi'(\omega_0)$ is a constant, $\phi''(\omega_0)$ is the second order dispersion (also called group velocity dispersion - GVD) which describes the linear chirp in the pulse, $\phi'''(\omega_0)$ is the third-order dispersion (TOD) and $\phi''''(\omega_0)$ is the fourth-order dispersion (FOD).

Calculations were performed in order to determine the total dispersion in the amplifier (using a home-made Fortran program). The main components contributing to the dispersion are material dispersion $\phi_m(\omega_0)$ from the Ti:sapphire rod, the crystal in the Pockel Cell (see section 2.3.3) and a number of fused silica optical components (polarizer, etc.) and the dispersion $\phi_g(\omega_0)$ due to grating pairs used in the stretcher and compressor:

$$\phi(\omega) = \sum \phi_i(\omega) \quad (2.15)$$

$$\phi''(\omega_0) = \phi''_m(\omega_0) + \phi''_g(\omega_0) \quad (2.16)$$

$$\phi'''(\omega_0) = \phi'''_m(\omega_0) + \phi'''_g(\omega_0) \quad (2.17)$$

$$\phi''''(\omega_0) = \phi''''_m(\omega_0) + \phi''''_g(\omega_0) \quad (2.18)$$

The phase accumulated in a piece of material with length l_m and index of refraction $n_m(\omega)$ is given by:

$$\phi_m(\omega) = \frac{\omega \times l_m}{c} \times n_m(\omega) \quad (2.19)$$

where c is the light speed and ω is the frequency. Therefore the derivative of the phase will be:

$$\phi''_m(\omega) = \frac{\lambda^3 l_m}{2\pi c^2} \times \frac{d^2 n_m}{d\lambda^2} \tag{2.20}$$

$$\phi'''_m(\omega) = \frac{-\lambda^4 l_m}{4\pi^2 c^3} \times (3\frac{d^2 n_m}{d\lambda^2} + \lambda\frac{d^3 n_m}{d\lambda^3}) \tag{2.21}$$

$$\phi''''_m(\omega) = \frac{\lambda^5 l_m}{8\pi^3 c^4} \times (12\frac{d^2 n_m}{d\lambda^2} + 8\lambda\frac{d^3 n_m}{d\lambda^3} + \lambda^2\frac{d^4 n_m}{d\lambda^4}) \tag{2.22}$$

The dispersion introduced by a parallel pair of gratings is given by:

$$\phi_g(\omega) = \frac{\omega}{c} \times \frac{l_g}{\cos\beta(\omega)}(1 + \cos(\theta - \beta(\omega))) + \frac{2\pi l_g}{d}\tan\beta(\omega) \tag{2.23}$$

where l_g is the separation between the gratings , d is the groove density of the gratings and θ and β are the incident and the diffracted angle on the gratings (see Fig.2.9). Therefore the derivative of the phase will be:

$$\phi''_g(\omega) = \frac{\lambda^3 l_g}{\pi c^2 d^2} \times [1 - (\frac{\lambda}{d} - \sin\theta)^2]^{-3/2} \tag{2.24}$$

$$\phi'''_g(\omega) = -\phi''_g(\omega) \times (\frac{3\lambda}{2\pi c}) \times \frac{(1 + \frac{\lambda}{d}\sin\theta - \sin^2\theta)}{1 - (\frac{\lambda}{d} - \sin\theta)^2} \tag{2.25}$$

$$\phi''''_g(\omega) = -\phi'''_g(\omega) \times (\frac{3\lambda}{2\pi c}) \times \frac{(1 + \frac{\lambda}{d}\sin\theta - \sin^2\theta)}{1 - (\frac{\lambda}{d} - \sin\theta)^2} + \phi''_g(\omega) \times (\frac{3\lambda^2}{4\pi^2 c^2}) \times \tag{2.26}$$
$$\times\{\frac{1 + \frac{2\lambda}{d}\sin\theta - \sin^2\theta}{1 - (\frac{\lambda}{d} - \sin\theta)^2} + \frac{\frac{2\lambda}{d} \times (\frac{\lambda}{d} - \sin\theta) \times (1 + \frac{\lambda}{d}\sin\theta - \sin^2\theta)}{[1 - (\frac{\lambda}{d} - \sin\theta)^2]^2}\}$$

The formulas presented above hold for the setup used in our system for the compression of the pulse where the distance between the gratings is $l_g > 0$. For the stretcher these terms have the same functional expression but with opposite sign. This is because the distance between the stretcher gratings is negative $l_g < 0$ (see section 2.3.2). As a result the path-length introduced for each wavelength component in the stretcher is compensated in the compressor.

For completeness, we note that the dispersion introduced by a pair of prisms, as used in the oscillator, is given by:

$$\phi_p(\omega) = \frac{\omega}{c} \times P(\omega) \tag{2.27}$$

where $P = l_p \cos\gamma(\omega)$, with l_p the apex separation, $\gamma(\omega)$ the deflection angle of the beam with angular frequency ω, with respect to the line joining the apices. Therefore the derivative of the phase will be:

$$\phi''_p(\omega) = \frac{\lambda^3 l_p}{2\pi c^2} \times \frac{d^2 P}{d\lambda^2} \tag{2.28}$$

$$\phi'''_m(\omega) = \frac{-\lambda^4 l_p}{4\pi^2 c^3} \times (3\frac{d^2 P}{d\lambda^2} + \lambda\frac{d^3 P}{d\lambda^3}) \tag{2.29}$$

where

$$\frac{d^2P}{d\lambda^2} = 2\{(\sin\gamma)\frac{d^2n_p}{d\lambda^2} + [(2n_p - \frac{1}{n_p^3})\sin\gamma - 2\cos\gamma](\frac{dn_p}{d\lambda})^2\} \quad (2.30)$$

$$\frac{d^3P}{d\lambda^3} = 2\{(\sin\gamma)\frac{d^3n_p}{d\lambda^3} - 3[(2n_p - \frac{1}{n_p^3})\sin\gamma - 2\cos\gamma]\frac{d^2n_p}{d\lambda^2}\frac{dn_p}{d\lambda} + \\ +[(\frac{3}{n_p^4} - 2)\sin\gamma - 6(2n_p - \frac{1}{n_p^3})\cos\gamma](\frac{dn_p}{d\lambda})^3\} \quad (2.31)$$

with n_p the refractive index of the prisms.

In order to obtain the shortest pulse in the end of the laser system we have to minimize as many terms as possible in eq.2.14. The terms in this equation represent first, second, third, etc. order derivatives of the phase which, as shown above, are related to the amount of material used in the laser system and the settings of the stretcher and the compressor where grating pairs are used. The amount of material used in an amplifier is determined by the required optical components and, in general, can be minimized but is not easily adjustable. However, the separation between the gratings and the incident grating angle in the stretcher and compressor can be easily changed.

We have performed calculations for the dispersion compensation in the end of the laser system in the following way. The dispersion due to the material present in the laser system was calculated using eq.2.19-2.22. The dispersion introduced by the stretcher was calculated using eq.2.23-2.26. The incident grating angle in the stretcher was set based on maximum efficiency for $800nm$ central wavelength (Littrow angle of the grating). The distance between gratings in the stretcher was set so that the pulse is long enough to avoid optical damage during amplification (see section 2.2.1). The optimal incident grating angle and distance between the gratings in the compressor were calculated for each round-trip in the amplifier, so that the resulting dispersion introduced by the compressor compensates the dispersion introduced by the stretcher and due to materials passed by the laser pulse. We assumed in the calculations that a gaussian $20fs$ bandwidth limited pulse enters the stretcher.

By using gratings with the same groove density ($1200lines/mm$) in the stretcher and the compressor one can compensate both the second and the third-order dispersion. The residual fourth-order dispersion is plotted in Fig.2.4 (squares). One can observe that the fourth order dispersion increases with the number of round trips in the amplifier term increases. To minimize the fourth-order dispersion, one can choose a different groove density for the gratings in the compressor [53]. Considering the amount of dispersive material used in the our amplifier, one can calculate that for a combination of $1200lines/mm$ groove density for the grating in the stretcher and $1500lines/mm$ groove density for the gratings in the compressor, the fourth order dispersion term is zero for 17 round-trips in the regenerative amplifier (Fig.2.4 - upward triangles).

The effect of the fourth order dispersion compensation can be seen in the temporal profile of the output pulse (Fig.2.5). For an initial unamplified gaussian pulse with

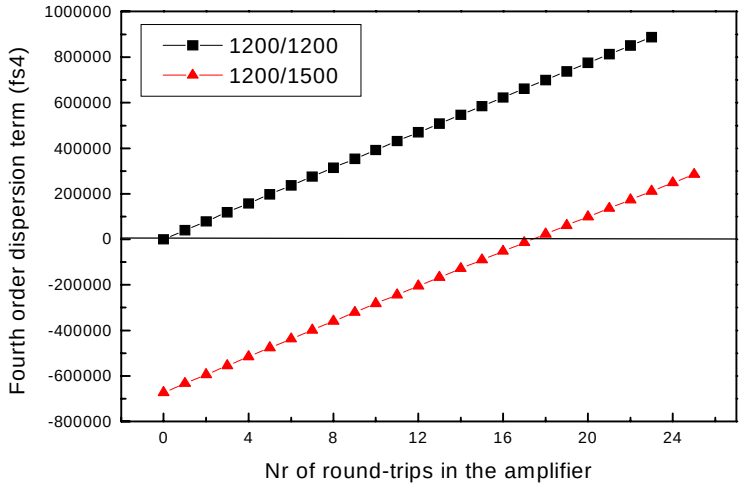

Figure 2.4: *Dispersion compensation in the amplifier for different gratings combination in the stretcher and in the compressor. The fourth-order dispersion term is minimized for a combination of* $1200 lines/mm$ *groove density in the stretcher and* $1500 lines/mm$ *groove density in the compressor.*

a spectral bandwidth corresponding to $20fs$ the duration of the amplified pulse is $45fs$ if the gratings in the stretcher and compressor have the same groove density ($1200 lines/mm$) (squares in Fig.2.5) and is $25fs$ if different groove densities are used (a $1200 lines/mm$ groove density for the stretcher gratings and a $1500 lines/mm$ groove density for the compressor gratings) (upward triangles in Fig.2.5). It is important to note that when using different groove density gratings in the stretcher and the compressor the pulse is not only shorter but has a pedestal on the front part of the pulse two orders of magnitude lower than in the case where identical gratings are used in the stretcher and the compressor (upward triangles in Fig.2.5). The amplitude of the pedestal is very important in many high-intensity experiments.

In conclusion, if we use a combination of $1200 lines/mm$ groove density for the gratings in the stretcher and $1500 lines/mm$ groove density for the gratings in the compressor, the second, third and fourth order dispersion can be compensated and it is the residual fifth order dispersion term that does not allow the pulse to reach its bandwidth limited value after the compressor. Therefore, we have a fifth order dispersion limited system. Based on the calculations presented in this section we concluded that amplification up to a Terawatt power level of ultrashort laser pulses ($\sim 25fs$) should be possible.

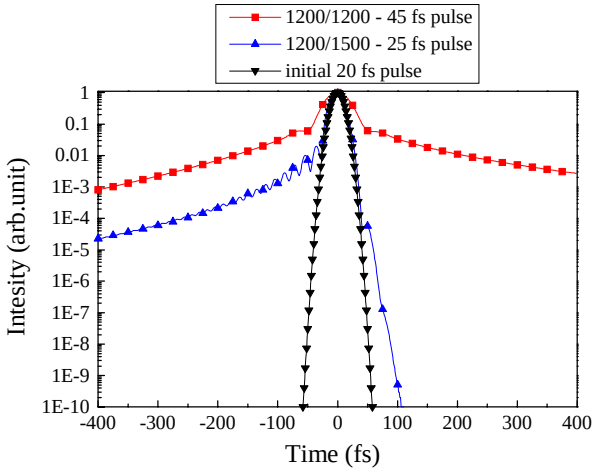

Figure 2.5: *Calculated temporal profile of the initial and amplified pulse. The FWHM of the amplified pulse is* $45fs$ *if the gratings in the stretcher and compressor have the same groove density (*$1200lines/mm$*) and is* $25fs$ *if different groove densities are used (*$1200lines/mm$ *for the stretcher gratings and* $1500lines/mm$ *for the compressor gratings).*

2.3 Practical implementation

Based on the considerations presented in the previous section a laser system was designed. An overview of the laser system as it is currently in operation can be seen in Fig.2.6. The laser system consists of an oscillator, a stretcher, two amplifiers and two compressors. The oscillator is the source of the femtosecond pulses. After they are stretched by a factor of 10^4, the pulses are amplified in the first amplification stage that consists of a regenerative amplifier pumped by a Nd:YLF laser ($527nm, 1kHz$). From the $1kHz$ output of the regenerative amplifier a $50Hz$ pulse train is selected in a Pulse Slicer (not shown). The pulses rejected by the Pulse Slicer are compressed in the first compressor, while the selected pulses are further amplified in a 5-pass amplifier pumped by a Nd:YAG laser ($532nm, 50Hz$). The output of the second amplification stage is compressed in the second compressor that is identical to the first one. In this section all the components will be described individually. A description of the alignment procedure used in the laboratory is included for each part of the laser system, which can be skipped by readers who are only interested in a description of the design of the laser.

2.3.1 The oscillator

The oscillator is the first component of the laser system and represents the source of femtosecond pulses. In our system we have a KLM (Kerr Lens Mode-locked)

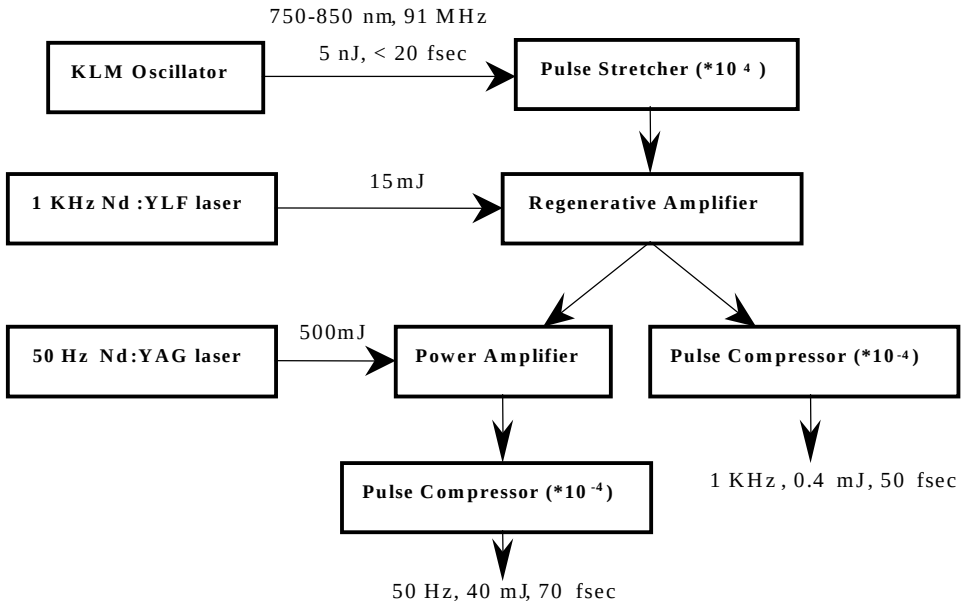

Figure 2.6: *Overview of the laser system.*

Ti:sapphire oscillator (*Kapteyn-Murnane Laboratories L.L.C,* Model TS) [34], which produces 5nJ pulses at a $91MHz$ repetition rate, with a central wavelength of $800nm$ and a pulse duration of about $20fs$ (N.B. More precisely, the output pulse is not bandwidth limited but the spectrum is broad enough to support a pulse shorter than $20fs$). An overview of the oscillator is shown in Fig.2.7. The convention of labelling optical components is as follows: L = lens, PM = pump mirror, M = flat mirror, A = aperture, CM = curved mirror, P = prism, S = slit. This convention will be used for the presentation of all the elements of the laser system described in this chapter. The convention for any new elements will be introduced when used for the first time.

There are several elements essential for a femtosecond laser: a broadband gain medium, a laser cavity, an output coupler, a dispersion compensating element, and a phase modulator or a loss process to obtain mode-locking. The Ti:sapphire rod provides gain and loss modulation (through the self lensing induced by the Kerr effect). The dispersion compensating element (a pair of prisms that compensates for material dispersion in the cavity) is necessary in order to reach femtosecond pulse durations.

The oscillator is pumped by the output of a $527nm$, $5W$, continuous wave frequency-doubled Nd:YVO_4 laser (Millennia V-1500, Spectra Physics Lasers, Inc.), which is focused by a $10cm$ focal length lens ($L1$). A $5mm$ long Ti:Sapphire crystal (absorption coefficient at $532nm$: $\alpha = 4$) is set at Brewster's angle near the pump focus. Mirrors $PM1$ and $PM2$ are used for adjusting the direction of the green on the crystal using aperture $A1$). The crystal is part of a folded cavity which contains $M5$ and $M6$ as end mirrors. $M6$ is a 12% output coupler that couples out pulses with a frequency of 91 MHz, dictated by the cavity length of $2 \times 1.65m$. The oscillator is operated in a

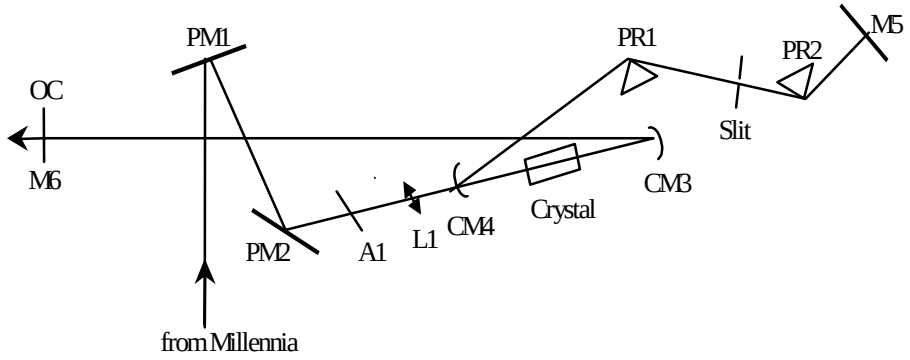

Figure 2.7: *Overview of the oscillator. OC=output coupler, L = lens, PM = pump mirror, M = flat mirror, A = aperture, CM = curved mirror, P = prism, S = slit.*

stable configuration, dictated by the concave mirrors $CM3$ and $CM4$. The radius of curvature of these mirrors is $-10cm$. From $CM4$ the beam passes through a pair of parallel prisms that are used to compensate the dispersion in the cavity. $M5$ reflects the pulse back through the prisms to compensate the spatial chirp (see section 2.3.2 where the principle of a pair of parallel gratings will be explained) and then it is coupled out by $M6$.

The slit situated between the two prisms is used for loss modulation and for tuning the central wavelength of the oscillator. After the first prism ($PR1$) the beam is dispersed and from the broad spectrum of the pulse the portion which is required is selected. The width and the position of the slit determine the maximum bandwidth of the spectrum and therefore the minimum pulse duration, and the central wavelength, which is tunable between $775nm$ and $825nm$.

A typical spectrum of the pulses generated by the oscillator in our system is presented in Fig.2.8. The $\sim 41nm$ FWHM wide spectrum supports a bandwidth limited pulse of $23fs$ if we assume a gaussian shape and $17fs$ if we assume a $sech^2$ shape (see eq.2.1). In section 2.1.3 we mentioned that Ti:sapphire laser can generate pulses with a bandwidth as wide as $75nm$. In practice, there is a compromise between stability and bandwidth which, in our case, reduced the bandwidth to $41nm$. In the current setup the output of the oscillator is not bandwidth-limited ($\sim 70fs$) due to dispersion in the cavity, but this is not important since in the next step of the laser system the pulse is stretched to $\sim 200ps$. Since the oscillator is a commercial unit developed by *Kapteyn & Murnane*, the alignment procedure (given in the manual of the laser) is not treated here.

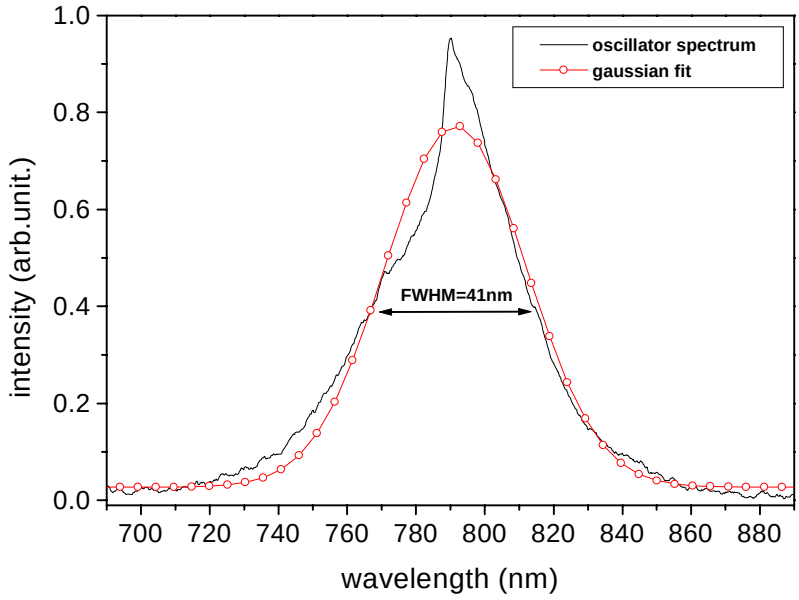

Figure 2.8: *The spectrum of the oscillator pulses. The shape of the spectrum is fitted by a gaussian fit with a FWHM of* $41nm$.

2.3.2 The stretcher

The second element of the system is the stretcher. The stretcher is an optical setup where the optical pathlength (and hence, the transition time) depends on the wavelength. For an easier understanding of the principle of the stretcher, the principle of a parallel pair of gratings (as used in the compressor) will be explained first (Fig.2.9).

In a parallel pair of gratings, the input beam is sent onto the first grating ($G1$) which disperses the laser beam according to the grating equation:

$$(\sin\theta + \sin\beta) \times d = m \times \lambda \tag{2.32}$$

where θ and β are respectively the incident angle and the diffraction angle with respect to the normal on the grating, d is the groove density of the grating and m is the order of diffraction.

From the eq.2.32 it follows that red wavelengths diffract at larger angles with respect to the normal than blue wavelengths. After the second grating, which is parallel to the first one ($G1 \parallel G2$), the different colors in the laser pulse again travel parallel. However, at this point the pathlength in the red part of the spectrum l_{red} is larger than the pathlength in the blue part of the spectrum l_{blue}. Therefore, in time, the blue part of the spectrum travels faster through the double grating setup (negative dispersion) and a time delay between wavelengths in the laser pulse is introduced (temporal chirp). The amount of delay introduced between the colors in the pulse depends on the angle θ between the input beam and the normal of the grating and the distance between

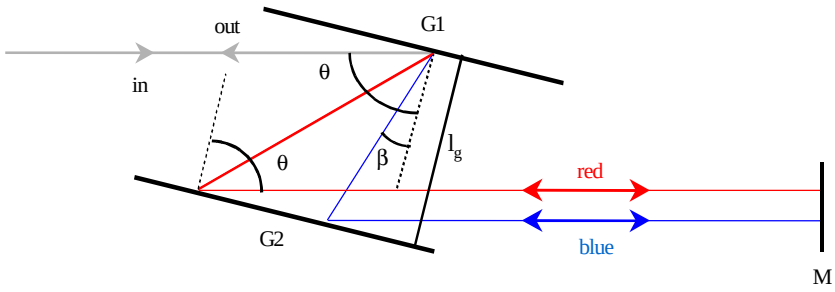

Figure 2.9: *The principle of a pair of parallel gratings. In this setup the optical pathlength depends on the wavelength ($l_{red} > l_{blue}$), therefore can be used to stretch or compress optical pulses. G = grating; M = mirror; θ = the diffraction angle; d = the distance between gratings;*

the two gratings l_g. These are the two parameters that can be adjusted to vary the dispersion and hence, the amount of chirp introduced in the pulse (see section 2.2.2).

After the two gratings the different wavelength components travel parallel with respect to each other. However, there exists a wavelength dependent offset of the central ray of the beam (spatial chirp). This spatial chirp is removed by double-passing the two grating assembly. Mirror M (Fig 2.9) sends the beam back on the same path through the setup such that after the second pass the colors again overlap spatially. In practice, mirror M is a retroreflector which not only reflects the beam back but also changes the height of the beam, giving the possibility to separate the input and the output beams.

The parallel pair of gratings setup presented above chirps the laser pulse such that $l_{red} > l_{blue}$. This setup is easy to adjust and therefore very suitable for use in the compressor (see section 2.3.5), where the output of the laser needs to be frequently optimized. In the stretcher a configuration has to be used where $l_{red} < l_{blue}$ in order to compensate the dispersion in the compressor.

To create positive dispersion using the same kind of setup as the parallel pair of gratings (i.e. to make the red part of the spectrum travel faster than the blue part $l_{red} < l_{blue}$), one would require a negative distance between the gratings. That cannot be realized directly but becomes possible by using a x(-1) telescope between the two gratings (Fig.2.10).

Depending on the position of the second grating ($G2$) with respect to the image of the first grating ($G1$) through the telescope, one can have a negative or a positive distance between that image and the second grating. Therefore positive or negative dispersion is introduced by setting $G2$ before or after the point which defines the image of $G1$. In practice, a mirror is used between the lenses which form the telescope, so that $G1$ is imaged onto itself and the stretcher contains only a single grating. In this way the stretcher is more compact and easier to align (the parallelism between the two gratings is automatically obtained).

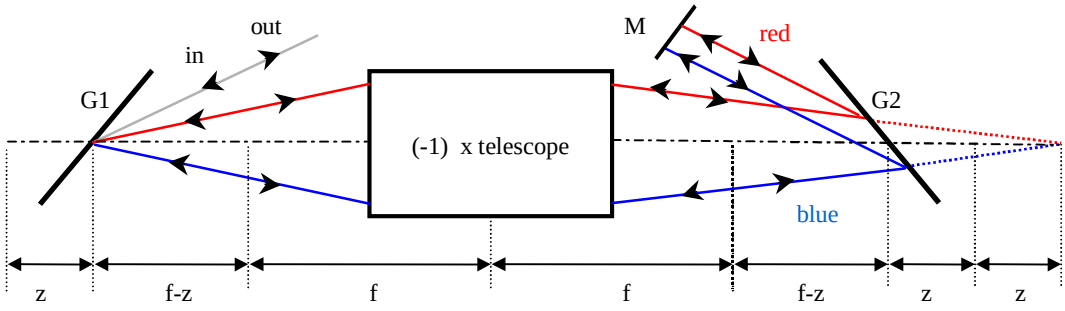

Figure 2.10: *The principle of the stretcher is based on a configuration where* $l_{red} < l_{blue}$ *in order to compensate the dispersion in the compressor.* G *= grating;* M *= mirror;*

In order to build the telescope in the stretcher for a broad bandwidth laser pulse, lenses cannot be used. For a pulse duration below $100fs$, such refractive elements introduce strong chromatic aberration. Therefore, in a geometric aberration-free system it is necessary to use reflective optics. In an ideal stretcher, the telescope has to satisfy three conditions: it has to have a magnification equal to -1, the image of the first grating has to be perfectly stigmatic on the axis and it has to have no on-axis coma, which means that the wavelength that is diffracted under an angle θ by the first grating has to intercept the second grating with exactly the same angle. An all-reflective triplet combination known as an *Offner*-type stretcher is used in our system [54]. This stretcher is shown in Fig.2.11. The confocal telescope is formed by a pair of concave and convex mirrors. This setup is completely symmetric, so that only symmetrical aberrations can appear (spherical aberrations and astigmatism). The presence of two spherical mirrors whose radius of curvature ratio is two and of opposite sign cancels these aberrations. This combination has no on-axis coma and exhibits no chromatic aberration, since all the optics are mirrors. In this optical combination, perfect stigmatism is ensured only when the grating is at the common center of curvature. When the grating moves away from the center of curvature, the image quality is affected and spectral phase distortions appear, leading to a degradation in the temporal pulse profile. Cheriaux *et al* [55] have shown that the spherical aberrations due to the fact that the grating is away from the center of curvature are weak enough not to affect the pulse shape. They also analyzed the influence of the quality of the mirrors on the compressed pulse shape and concluded that the size of the pedestal underneath the pulse strongly depends on the mirror quality. Therefore, in our setup mirrors with a flatness better than $\lambda/20$ are used.

The propagation of the laser beam in the stretcher was simulated using a Mathematica program and was used to calculate the required dimensions of the optical components needed in the stretcher: a $12cm \times 14cm$ grating, a $5cm \times 12.5cm$ convex mirror (effective used area $5cm \times 11.5cm$ - due to the holder), a $\phi = 25cm$ concave

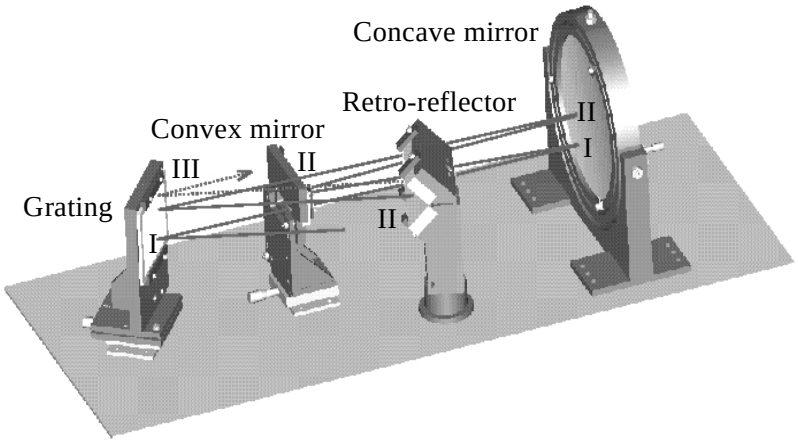

Figure 2.11: *Overview of the stretcher. The dispersed beam (I) propagates towards the concave mirror CC ($-1m$ radius of curvature) and is then focused onto the convex mirror CV ($50cm$ radius of curvature). After reflecting off the concave mirror a second time, the beam (II) is collimated and is diffracted again on the grating. This completes the first pass through the stretcher. The retroreflector RR sends the beam back (III) for the second pass through the stretcher to compensate for the spatial chirp and to change the height of the beam by $1cm$. Dimensions of the optical components in the stretcher: a $12cm \times 14cm$ grating, a $5cm \times 12.5cm$ convex mirror (effective used area $5cm \times 11.5cm$ - due to the holder), a $\phi = 25cm$ concave mirror and a retro-reflector that consists of two $5cm \times 15cm$ mirrors mounted at 90^0 with respect to each other and at 45^0 with respect to the vertical axis.*

mirror and a retro-reflector that consists of two $5cm \times 15cm$ mirrors mounted at $90^0$with respect to each other and at 45^0 with respect to the vertical axis. As shown in Fig.2.11, the dispersed beam (I) propagates towards the concave mirror CC ($-1m$ radius of curvature) and is then focused onto the convex mirror CV ($50cm$ radius of curvature). After reflecting off the concave mirror a second time, the beam (II) is collimated and is diffracted again on the grating. This completes the first pass through the stretcher. The retroreflector RR sends the beam back (III) for the second pass through the stretcher to compensate the spatial chirp and to change the height of the beam by $1cm$.

The program was also used to calculate the delay between various wavelength components. The delay depends on the incident angle θ, chosen to be 38^0 for the central wavelength (the Littrow angle of the grating is 13^0 for $800nm$ and the diffraction angle is 20^0), the groove density of the grating ($1200lines/mm$) and the position of the grating with respect to the center of the two mirrors. In our case, for a perpendicular distance of $39.4cm$ between the grating and its image in the telescope, the difference in distance between two rays corresponding to $785nm$ and $815nm$, on a single pass

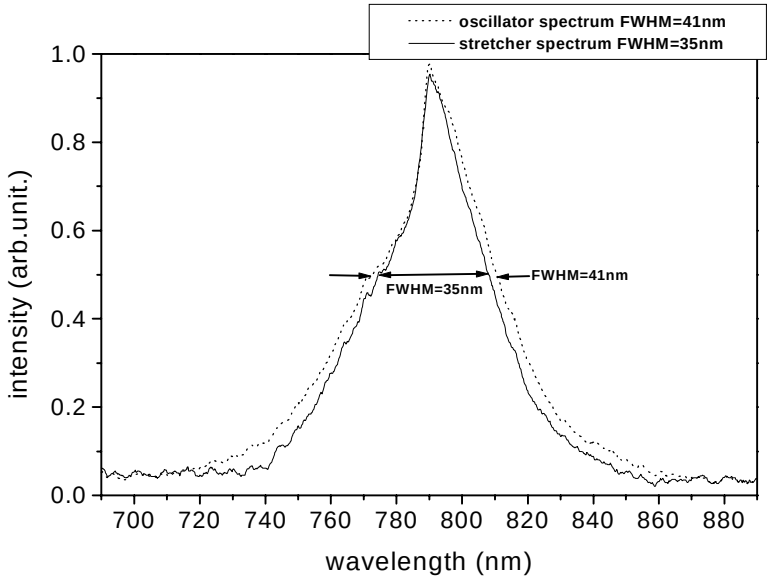

Figure 2.12: *Spectrum of the laser pulse before and after the stretcher. The spectrum is narrower than the input spectrum due to the wavelength-dependent reflectivity of the stretcher grating.*

through the stretcher, is $4.2cm$. By double-passing the stretcher (4 passes over the grating) a $30nm$ FWHM pulse is then stretched to a $280ps$ FWHM pulse.

In the actual operation of the system the bandwidth of the laser pulse before the stretcher is $\sim 41nm$ FWHM (see Fig.2.12). The spectrum of the output laser pulse of the stretcher is slightly narrower than the input due to wavelength-dependent reflectivity of the grating. Therefore, from this calculations one can conclude that the stretcher described above chirps the pulses to a value which is adequate for safe operation of the system (see the evaluation of the B-integral in section 2.2.1).

Alignment procedure for the stretcher

A detailed overview of the stretcher is shown in Fig.2.13. For clarity Fig.2.14 shows the spot of the beam on the grating, the convex mirror, the concave mirror and the retro-reflector as the beam propagates through the system.

The beam from the oscillator is collimated in a telescope which consists of mirror $CM9$ (a concave mirror with a radius of curvature of $-30cm$) and mirror $CM10$ (a concave mirror with a radius of curvature of $-50cm$). Two flat mirrors ($M11$ and $M12$) are used to send the input beam onto the grating ($1200lines/mm$) under an angle of 38^0 with respect to the normal (and 18^0 with respect to the diffracted beam for $800nm$). The diffracted beam propagates next as shown in Fig.2.11. The beam after the second pass (IV) is steered by the flat mirrors $M13$, $M14$ and $M15$ and the

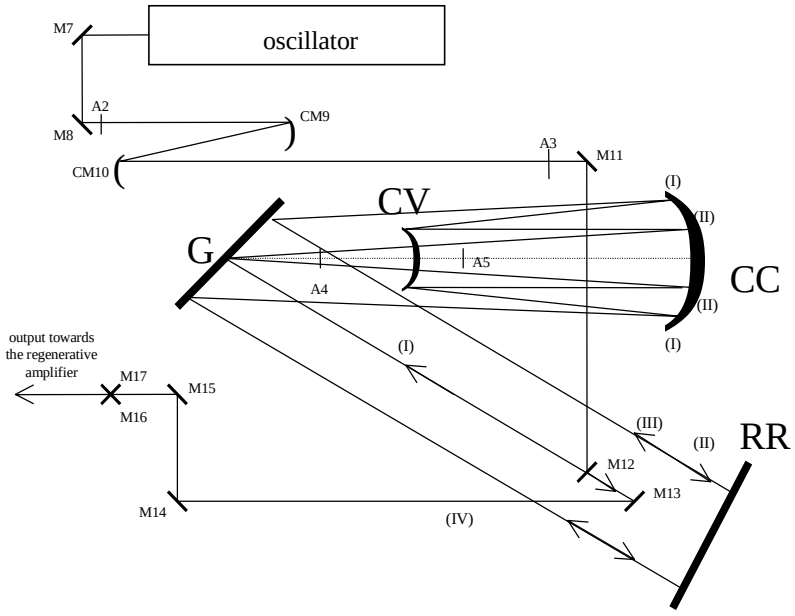

Figure 2.13: *Overview of the stretcher (see text for details). CC = concave mirror, CV = convex mirror, G = grating, RR = retroreflector, M = flat mirror, CM = curved mirror, A = aperture.*

periscope formed by the mirrors $M16$ and $M17$. These components are used to align the beam into the regenerative amplifier, which is the next step of the laser system.

When the stretcher is aligned, the appropriate pattern one should expect on the elements of the stretcher is shown in Fig.2.14. If the stretcher is only slightly misaligned, then the mirrors $M7$ and $M8$ (situated between the oscillator and the stretcher) can be used to send the beam through the apertures $A2$ and $A3$. If this adjustment is not enough a complete alignment has to be performed.

The procedure used for aligning the stretcher is called backward alignment and is as follows: A He-Ne laser is sent on the grating using mirrors $M15$, $M14$ and $M13$. The convex mirror CV is taken out. The grating G is replaced by a silver mirror, which reflects the beam on the axis of the stretcher, parallel to the optical table, under the correct angle (18^0 between the input and the reflected beam). When the axis of the stretcher defined, the apertures $A4$ and $A5$ are set for later alignment of the femtosecond beam. Next, the concave mirror CC sends the beam back focusing it at distance of $50cm$ and $4.2cm$ higher than the input. At this point, the mirror CV is installed in the focus of the mirror CC and adjusted so that the beam goes onto the mirror CC, which reflects the beam back, parallel to the optical table, at a height $8.4cm$ higher than the input on the silver mirror that replaces the grating. The first pass through the stretcher is aligned. The next pass is aligned using only the retro-reflector RR which elevates the beam by $1cm$. By adjusting the RR (horizontal and vertical adjustment) the output of the stretcher will appear on mirror $M12$. The next step is to use the

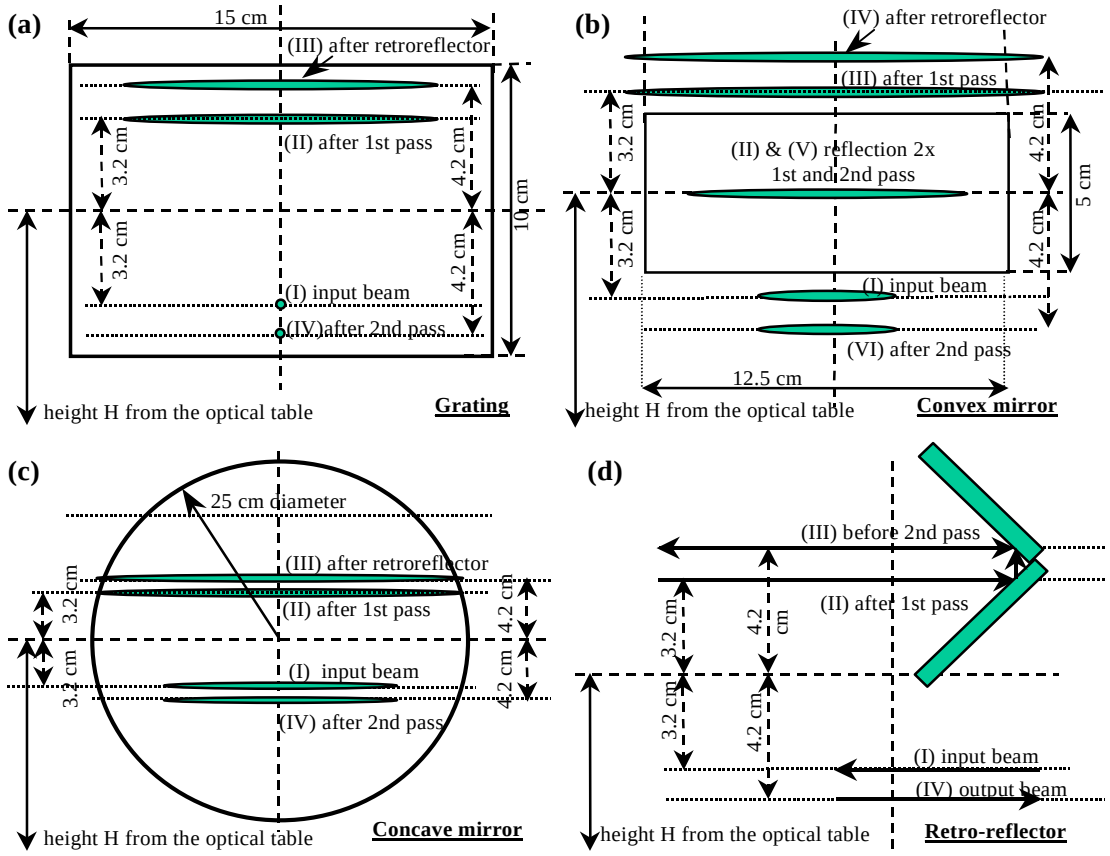

Figure 2.14: *Front view of several elements in the stretcher with the profile of the laser beam when the femtosecond laser propagates through the stretcher: a) the grating; b) the convex mirror; c) the concave mirror; d) the retro-reflector of the stretcher.*

mirrors $M12$ and $M11$ to send the He-Ne beam back into the oscillator and to define the input path of the femtosecond beam with apertures $A2$ and $A3$. At this point, all the components of the stretcher are aligned except the grating. The grating replaces the mirror used for the alignment and is adjusted such that the diffracted beam passes through the two apertures which define the axis of the stretcher $A4$ and $A5$. To ensure that the grating is perpendicular to the optical table and that the grating is not rotated (i.e. the grating grooves are perpendicular to the table), the different diffracted orders have to be adjusted to beat the same height with the input beam. The fs-pulse can now be sent into the stretcher and aligned through the first apertures $A2$ and $A3$ using $M7$ and $M8$. The angle of the grating is adjusted depending on the central wavelength of the fs-pulse.

When the pattern shown in Fig.2.14 is obtained on the elements of the stretcher the

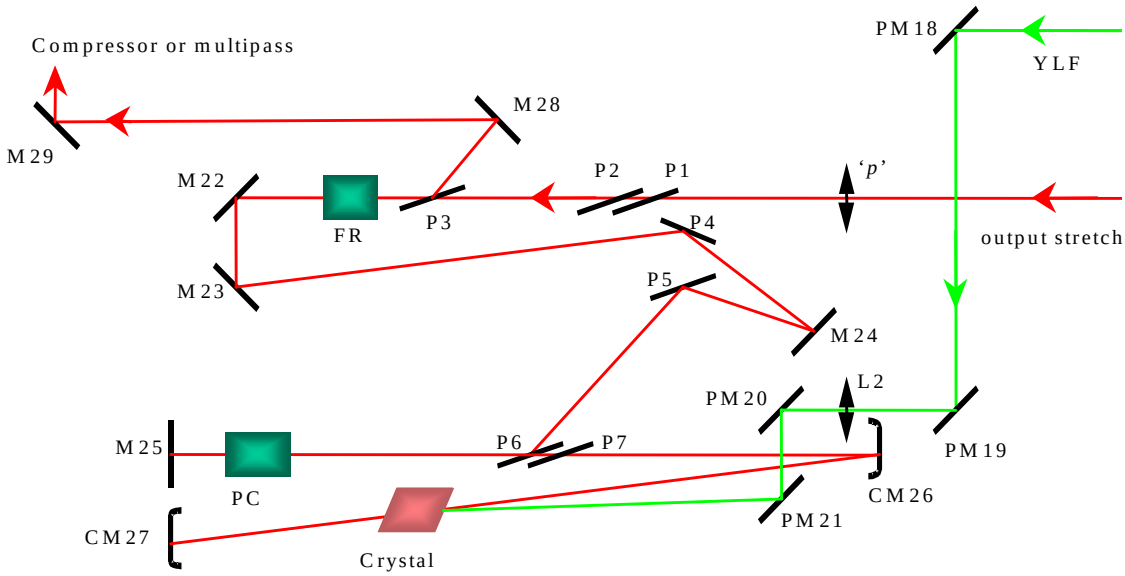

Figure 2.15: *Overview of the regenerative amplifier (see text for details). PM = pump mirror, M = flat mirror, CM = curved mirror, L = lens; P = polarizer; FR = Faraday Rotator; PC = Pockels Cell; p = the polarization of the laser beam.*

next step is to check the spatial chirp. The element responsible for spatial chirp in the stretched pulse is the convex mirror CV. If this mirror is not set exactly in the focus of the concave mirror CC then spatial chirp is introduced. To check the spatial chirp we use the following method. The fiber of a Optical Multichannel Analyzer (OMA) (see section 2.4) is set in the output of the stretcher in different positions across the spatial beam profile. The spectrum given by the OMA should be the same regardless of the position of the fiber. If the spectrum changes (shifts) as a function of the fiber position, then spatial chirp is present in the beam. To compensate for the spatial chirp the translation stage on which the mirror CV is set has to be fine adjusted until there is no spectral dependence on the fiber position.

2.3.3 The regenerative amplifier

As presented in Fig.2.6 the amplification consists of two stages. The first one is called the "regenerative amplifier" and is described below. A regenerative amplifier is a laser cavity containing a gain medium where the pulses propagate for a certain amount of time to be amplified and are coupled out when the amplification reaches saturation. The regenerative amplifier in the Amolf Terawatt laser system is shown in Fig.2.15.

The beam from the stretcher passes a combination of a polarizer ($P3$) and a Faraday

Rotator (FR), which has the property to change the polarization from *'p'* (parallel to the optical table as indicated by the double arrow in Fig.2.15) to *'s'* (perpendicular to the optical table) when the beam propagates from right to left but does not change the polarization when the beam propagates from left to right. Therefore an *'s'* polarized beam coming back from the regenerative amplifier cavity along the same direction will be reflected by polarizer $P1$ and then sent towards the compressor (or the next amplification stage) via mirrors $M28$ and $M29$. After passing the FR the input beam is reflected on two polarizers, $P4$ and $P5$, that serve to remove any *'p'* polarization which may have remained due to imperfections in the $FR - P3$ assembly. For the same reason we have implemented two polarizers in the input beam (P1 and P2). This assembly $P1 - P2$ reflects any amplified pulses that are not rejected completely by the $FR - P3$ assembly and that could go back into the oscillator distorting the 91MHz pulse train. Mirrors $M22$, $M23$ and $M24$ are used to steer the laser beam into the cavity. The cavity is folded and is formed by mirrors $M25$ (a flat mirror), $CM26$ (a concave mirror with a $-1m$ radius of curvature) and $CM27$ (a concave mirror with a $-25cm$ radius of curvature). The beam enters the cavity after a reflection on polarizer $P6$. This polarizer is a wedged polarizer (with a wedge angle of 2^0) so that multiple reflections are separated. The wedge is compensated by a second wedged polarizer $P7$, which is identical to the first one. Polarizer $P6$ together with a Pockels Cell (which is driven by a HV unit from Medox E.-O. Inc.) couples the pulses in and out the amplifier cavity (see below). The active medium of the cavity is a $6 \times 6 \times 6mm^3$ Ti:sapphire crystal (absorption coefficient at $532nm$: $\alpha = 2.5$). The crystal is pumped by a frequency-doubled $1kHz$ Nd:YLF (621-D laser, B.M.Industries) via mirrors $M18$, $M19$, $M20$ and $M21$. The pump beam is imaged on the crystal by a $50cm$ focal length lens ($L2$), to a spot of $\sim 1mm^2$ so that the pump is a bit larger than the infrared spot size that has to be amplified.

The pulse train coming from the stretcher has a 91 MHz repetition rate. A photodiode monitoring this pulse train sends a signal to the HV driver of the Pockels Cell (PC), which divides this rate by 91,000 and triggers the pump laser and the Pockels Cell. The Pockels Cell changes the polarization of the light by an amount depending on the voltage applied. Initially, when a pulse from the stretcher (seed pulse) comes on polarizer $P6$ with polarization *'s'*, a voltage is applied to the PC so that the PC rotates the polarization by $\lambda/4$. The flat mirror located behind the PC ($M25$) sends the pulse back through the PC where the polarization is rotated again by $\lambda/4$. Therefore, the polarization is changed from 's' to 'p' and when the pulse reaches $P6$ again, the pulse is transmitted through polarizers $P6$ and $P7$ and travels through the cavity. After one round trip the previous sequence takes place again so the polarization of the pulse is changed from 'p' to 's' and the pulse couples out on polarizer $P6$. If the PC voltage is switched *off* while the pulse is still in the cavity (before reaching the PC a third time), then the polarization is not affected passing through the PC and the pulse remains in the cavity. The switching of the PC has to be fast enough so as not to change the polarization of the pulse before the next pulse in the $91MHz$ train comes ($11ns$ later). Subsequent pulses will then be rejected on $P6$ without being amplified.

The pulse which is locked in the cavity is amplified in the Ti:sapphire crystal. When the amplification reaches its maximum the PC can be opened again and the amplified pulse is coupled out. This is done by once again applying a $\lambda/4$ voltage to the Pockels Cell which is turned *on* when the pulse being amplified is in the crystal containing arm of the cavity. On the next double-pass through the PC the polarization of the pulse is then changed again from 'p' to 's' and the amplified pulse is rejected from the cavity at $P6$.

The cavity length of the regen has to be similar to that of the oscillator, but not exactly identical, to avoid interferences between the pulses that couple in the cavity and the pulses that couple out the cavity. We chose to have the regen cavity length $\sim 5cm$ longer than the oscillator cavity length. The times at which the seed pulse enters or exits the cavity are given by the Pockels Cell driver as $Delay1$ and $Delay2$. The value of $Delay1$ is 270 round-trips and the value of $Delay2 - Delay1$ is 10 round-trips. One round-trip is about $11ns$, which means the PC opens after $\sim 3\mu s$ after the laser pump was triggered. This is the time necessary for the YLF laser to generate the pump pulse. The timing scheme for the PC, the pump laser and the amplification is shown in Fig 2.16.

The typical output of the regenerative amplifier is $\sim 1mJ$ for a pump power of $11mJ/pulse$ at a $1kHz$ repetition rate and for 10 round-trips through the cavity. After compression, the output of the laser system is $0.4mJ$ with a bandwidth of about $21nm$ (which can support bandwidth-limited pulses as short as $40fs$, assuming a gaussian shape). A typical spectrum of the pulse before and after amplification is shown in Fig.2.17. The pulse spectrum after the stretcher has a $35nm$ FWHM bandwidth, but the output bandwidth of the regen is only $21nm$ due to *gain narrowing* (see section 2.2.1). Therefore, the gain narrowing is more severe than anticipated in the calculations of section 2.2.1. The optical component responsible for this has not been identified yet. One can see that a little gain shifting is also present in the spectrum of the amplified pulse. The central wavelength of the amplified pulse is shifted towards red wavelengths.

The regenerative amplifier is able to generate light by itself. When the seed pulse (from the stretcher) is blocked, spontaneous emission appears and is amplified in the cavity. This Amplified Spontaneous Emission (ASE) is used to optimize and align the regenerative amplifier. The alignment procedure for the regenerative amplifier is presented below.

Alignment procedure for the regenerative amplifier

If the cavity of the regenerative amplifier is lasing for a pump power of about 6W (ASE present) when the seed beam is blocked, then the pump mirror $PM21$ can be adjusted to optimize the cavity. This is done by monitoring the power and the build-up time of the ASE. The powermeter is positioned after mirror $M28$ and has to indicate $\sim 1W$ for $11W$ pump power and about 12 round-trips in the cavity ($Delay2 - Delay1 + 1$). The build-up time of the ASE can be measured by setting a photodiode behind one of the cavity mirrors (e.g. $CM26$) and monitoring the photodiode signal on an oscilloscope.

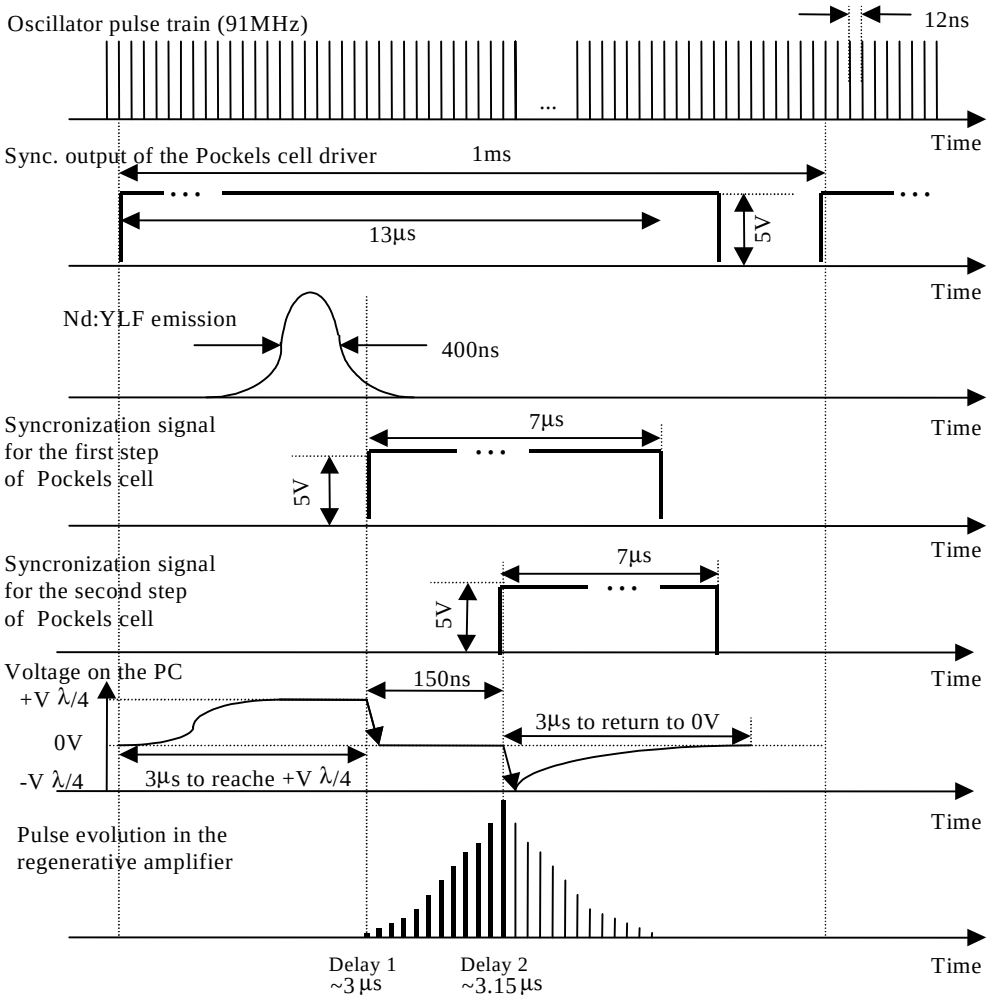

Figure 2.16: *The timing diagram of the regenerative amplifier.*

The shape of the ASE is an asymmetric function with a FWHM of about $70ns$ (see Fig.2.18a). The narrow peaks which appear are due to losses on polarizer $P6$ after each round-trip when the ASE propagates through the cavity. To optimize the build-up time means to optimize the cavity such that the spontaneous emission is amplified efficiently (in a time as short as possible), so the ASE starts as early as possible with respect to $Delay1$ and the rising edge is as sharp as possible (typical $50ns$). When graph a) in Fig.2.18 is obtained ($Delay1 = 270$ round-trips and $Delay2 - Delay1 + 1 = 28$ round-trips) the cavity is aligned. The seed can be unblocked and Fig.2.18b should be obtained for the same values of $Delay1$ and $Delay2$. To optimize the amplification of the seed in the regen cavity, mirror $M14$ has to be adjusted ($M14$ is situated in the stretcher - Fig.2.13). Comparing Fig.2.18b and 2.18a one should notice that the build-up time of the seed pulse is faster than the build-up time of the ASE. Therefore, once the seed is coupled in the cavity the ASE does not build up because the energy

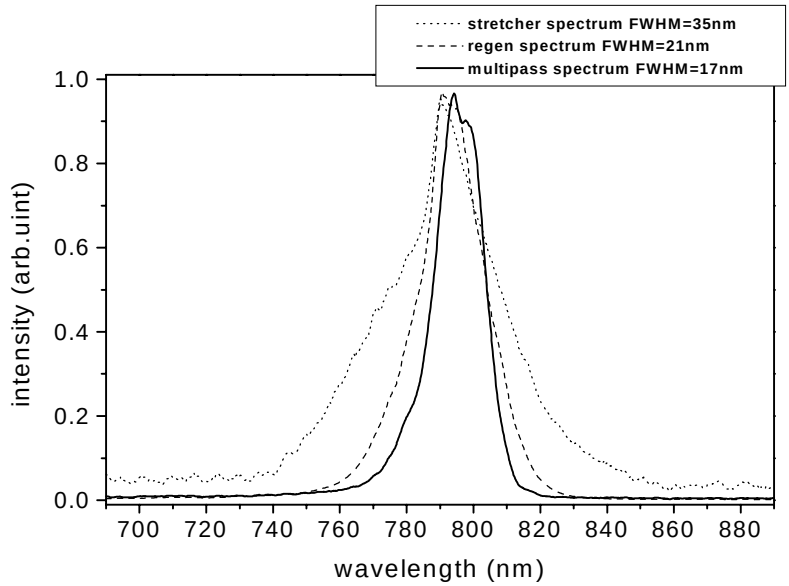

Figure 2.17: *The spectrum of the pulse before and after the amplification. Gain narrowing and gain shifting make the spectrum of the amplified pulse narrower and shift the spectrum towards red wavelengths.*

in the crystal is extracted by the seed pulse. When changing $Delay2 - Delay1 + 1$ from 28 round-trips to 10 round-trips the amplified pulse is coupled out of the cavity when the amplification is saturated by a $11W$ pump (see Fig.2.18c). For this value of $Delay2$ the total number of round-trips is 10 and the ASE does not have time to build-up (Fig.2.18d - the ASE obtained when the seed is blocked is 24 times weaker than the seed Fig.2.18c).

If the cavity of the regen is not lasing (no ASE present) and if the lasing cannot be obtained by turning the pump mirror ($PM21$) a little bit, then a complete alignment is necessary. The pump has to be turned off and the two arms of the cavity are aligned by sending the seed pulse. The seed pulse is reflected in and out on the polarizer $P6$ via the mirror $M25$. By checking the overlap between the input and the output on all the optics ($M22$, $M23$, $M24$, $P4$, $P5$, $P6$) and centering the beam on mirror $M28$, the first arm of the cavity that contains the PC is aligned. If a $\lambda/4$ plate is set behind the PC the pulse is not reflected by P6 anymore but is transmitted and makes a round-trip through the cavity, being rejected only after the second pass through the PC. In this way the second arm of the cavity can be adjusted. Mirror $CM26$ focuses the beam on the crystal and mirror $CM27$ sends the beam back all the way through the regen cavity. If the beams from the two arms of the cavity do not overlap on mirror $M28$ then the alignment of $CM26$ and $CM27$ has to be repeated. When the two arms overlap the pump laser is sent on the crystal at very low power (the value "zero" of the power unit) to check the superposition of the infrared and the green on the crystal. Once this

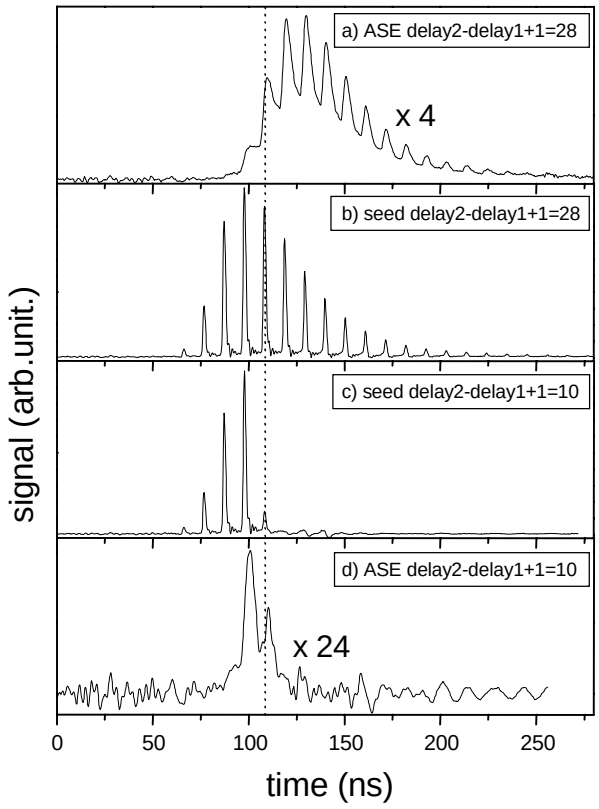

Figure 2.18: *The build-up time of the ASE (amplified spontaneous emission) and of the infrared seed pulse in the regenerative amplifier for two different values of Delay*2 *of the Pockels Cell:* $Delay2 - Delay1 + 1 = 28$ *round-trips and* $Delay2 - Delay1 + 1 = 10$ *round-trips. Delay1 is 270.1 round-trips and represents the origin of the graphs.*

is done, the seed is blocked, the $\lambda/4$ plate is taken out and the crystal is pumped with low power ($\leq 6W$) keeping Delay 2 of the PC on a high value ($\sim$ 300 round-trips) to enable the build up of ASE. To get the cavity lasing the pump mirror ($PM21$) has to be turned (scanning the surface of the crystal). When the cavity lases, it can be optimized by monitoring the power after mirror $M28$ and adjusting $M25$, $CM27$ and $PM21$ in an iterative way such that the build-up time of the ASE becomes as short as possible (as explained above).

The next step is to increase the power of the pump in $1W$ steps and to readjust the cavity every time reoptimizing the build-up time. At the maximum pump power ($11W$) the output of the cavity measured after the polarizer $P6$ is $1.5W$ for about 12 round-trips. The output of the regen (after mirror $M28$) in the unseeded operation is $1W$. If the ASE is well centered on all the optics following the cavity, $M22$ and $M23$ can be used to maximize the output through the FR and to align the leakage of the

ASE through the stretcher to ensure that the ASE has the same propagation axis as the seed from the femtosecond oscillator. The last step is the seeded operation. The seed is sent into the regen and the amplification is optimized with mirror $M22$ in the regen and mirror $M17$ in the stretcher as explained above (Fig.2.13) so that for $11W$ pump power and 10 cavity round-trips the seed pulse is amplified up to $1W$.

2.3.4 The multi-pass amplifier

For a number of experiments, energies exceeding $1mJ$ are required, so that a second power amplifier is necessary. This second amplification stage is designed as a five-pass amplifier. The scheme is shown in Fig.2.19. The output pulse of the regenerative amplifier is collimated with the telescope formed by the concave mirrors labeled $CM40$ and $CM41$ each having a $-1m$ radius of curvature. Before entering the multi-pass amplifier the laser pulse passes a Pulse Slicer (PS) consisting of a Pockels Cell (PC) and a polarizer ($P8$). The PS selects a pulse from the kHz train at a $50Hz$ repetition rate. This is necessary since the pump laser in the second amplification stage has a $50Hz$ repetition rate. The Pockels Cell in the Pulse Slicer changes the polarization of the pulses in the $1kHz$ train by 90^0 once every $20ms$ creating a $50Hz$ pulse train after reflection off polarizer $P8$. The rest of the pulses in the kHz train are transmitted through the same polarizer and form a second output of the laser system after they are compressed. Before entering the amplifier the beam passes a spatial filter, which is placed at the focus of a 1:1 telescope formed by mirrors $CM44$ and $CM46$ (radius of curvature $-50cm$). The 5 passes through the Ti:sapphire crystal ($8mm$ (width) $\times$ $8.5mm$ (height) $\times$ $10mm$ (length), with an absorption coefficient $\alpha = 3.5$) are directed by mirrors $M47$ to $M54$. After each pass a divergent lens ($L4$ and $L5$,$-4m$ focal length) is used to compensate for the thermal lensing in the crystal [56].

The pump beam is the frequency-doubled output of a Q-switched Nd-YAG laser (Spectra Physics, Quanta-Ray Pro 290-50, with a specified output of 500mJ/pulse at 50 Hz repetition rate). The pump laser is mounted on a table raised above the laser table and the pump beam is first lifted down by the periscope formed by mirrors $PM30$ and $PM31$. Window W reflects 1% of the pump beam and is used to monitor the pump power. The pump configuration consists of a lens L3 ($1m$ focal length) that images the 'flat-top' profile of the pump laser onto the Ti:sapphire crystal with a spot size of $\sim 4mm^2$. The pumping of the amplifier is done from two sides. The output of the YAG is split in two equal parts by beamsplitter BS and the two resulting pump beams are sent onto the crystal by mirrors $PM34$, $PM35$, $PM36$, $PM37$ and $PM38$. A $\lambda/2$ wave plate is set in each of the pump arms to control the penetration depth, the absorption and therefore the gain. The superposition of the pump beam and the IR is optimized by fine-tuning $M47 - M54$ for the IR and $PM34 - PM38$ for the pump.

Pumping from two sides has two major advantages: the total pump energy is divided over two pump beams and therefore the intensity of the pump beam on each of the two faces of the crystal is reduced. The second advantage is the more homogeneous longitudinal distribution of the pump intensity in the crystal.

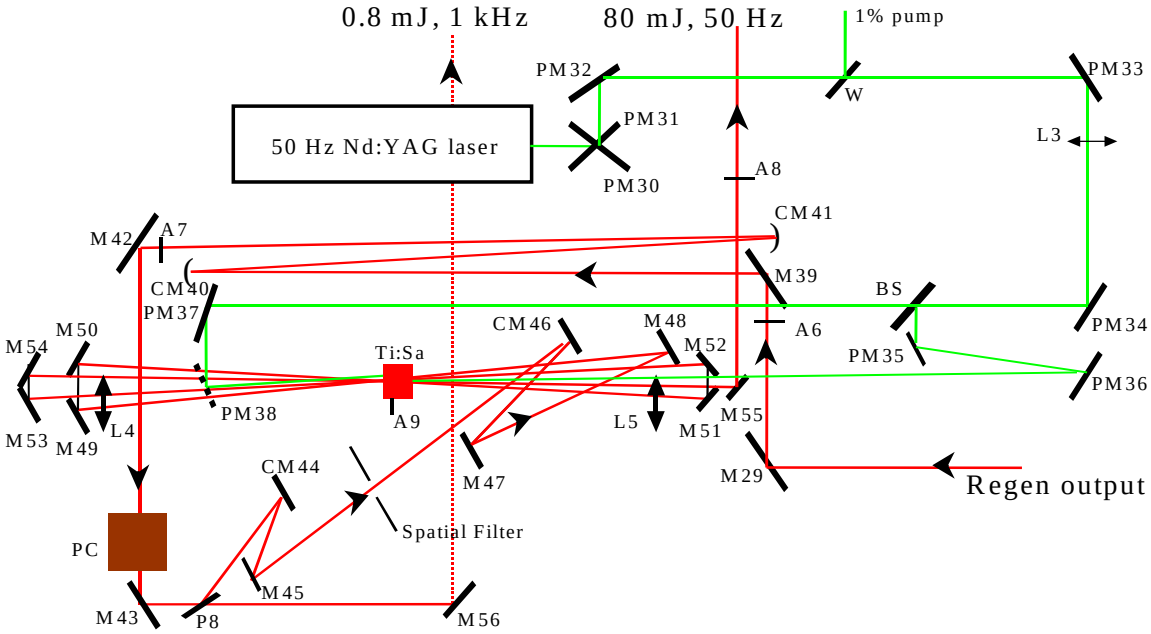

Figure 2.19: *Overview of the multi-pass amplifier. The $1KHz$ output of the regenerative amplifier is sent into a pulse slicer to form a $50Hz$ pulse train which is amplified in 5 passes to pulses with $80mJ$ energy. PM = pump mirror, M = flat mirror, CM = curved mirror, PC = Pockels Cell, L = lens, A = aperture, W = window.*

The spectrum of the output of the multi-pass amplifier was already shown in Fig.2.17. In this figure one can observe that the gain narrowing and the gain shifting is stronger for the multi-pass output compared to the output from the regenerative amplifier. The spectrum of the multi-pass amplifier output has a $17nm$ bandwidth. This corresponds to a bandwidth-limited pulse of $54fs$ assuming a gaussian shape. To measure the pulse duration we used an autocorrelator (see section 2.4). From the autocorrelation trace we obtained a FWHM of $70fs$. The difference between this value and the bandwidth-limited value comes from uncompensated dispersion. The compressor can be set to compensate the dispersion but for this other tools have to be used (see section 2.4).

The output energy of the multi-pass amplifier is $80mJ$. After compression this yields a pulse of $30mJ$ pulse energy and $70fs$ pulse duration with a $17nm$ bandwidth, at $50Hz$ repetition rate. The alignment procedure for the multi-pass amplifier is presented below.

Alignment procedure for the multi-pass amplifier

The output of the regenerative amplifier is aligned through apertures $A6$ and $A7$ (using the last mirror of the regenerative amplifier $M28$ and mirror $M29$) and goes through the multi-pass amplifier by way of mirrors $M39 - M55$. A check should be performed to see if the output of the multi-pass amplifier is centered on aperture $A8$ (Fig.2.19). Once the IR seed is aligned the pump beam can be checked. The powermeter should be positioned in the compressor after the telescope which is used to magnify the beam (see section 2.3.5). The oscillator of the YAG laser is turned on and the waveplate situated before the doubling crystal of the YAG is misaligned. The waveplate is turned for minimum output power of the laser. The YAG amplifier is turned on and the waveplate is slowly turned. When increasing the pump power the multi-pass IR output should increase. The pump can be adjusted using mirror $PM34$ to optimize the output IR power. The maximum output pulse energy is $80mJ$. In this geometry an output power of $100mJ$ is possible but we are currently limited by the damage threshold of the optical components.

If the output of the amplifier does not increase when the pump power is increased, then a full alignment has to be done. The pump beam is blocked. The translation stage on which the crystal is set is moved so that the IR passes through aperture $A9$ located on this translation stage. All the passes of the IR beam have to pass $A9$ without cutting the beam. If necessary the mirrors $M47$ till $M54$ can be used to correct the beampath of the IR through $A9$. The pump laser is set from Q-switched operation to the 'long pulse' regime (see the settings on the power supply of the YAG laser) and $PM34$, $PM36$ and $PM37$ are used to align the two arms of the pump through aperture $A9$. If the IR and the pump beams pass cleanly through $A9$, the crystal can replace aperture $A9$ and the Q-switched operation of the pump laser can be turned on by setting the power unit on 'ext' and slowly increasing the power using the waveplate of the YAG, as explained above. Now, the output of the multi-pass should increase with the pump power and can be optimized by fine adjusting $M29$ for the IR beam and $PM34$ for the pump. The maximum uncompressed output (supported by the optical components) is $80mJ/pulse$ ($4W$ at $50Hz$ repetition rate). In the compression stage $> 50\%$ energy is lost and this leads to a compressed pulse of $\sim 30mJ$. The compression procedure is presented in the next section.

2.3.5 The compressor

The last element of the laser system is the compressor. The compressor consists mainly of two gratings and a mirror and introduces a temporal delay between individual spectral components of the laser pulse in order to compensate the delay introduced in the stretcher and in the amplification stages (see 2.3.1).

As mentioned in the previous section our laser system has two outputs that are compressed individually in two identical compressors (see Fig.2.6). An overview of these compressors is given in Fig.2.20. The $50Hz$ amplified output is compressed in

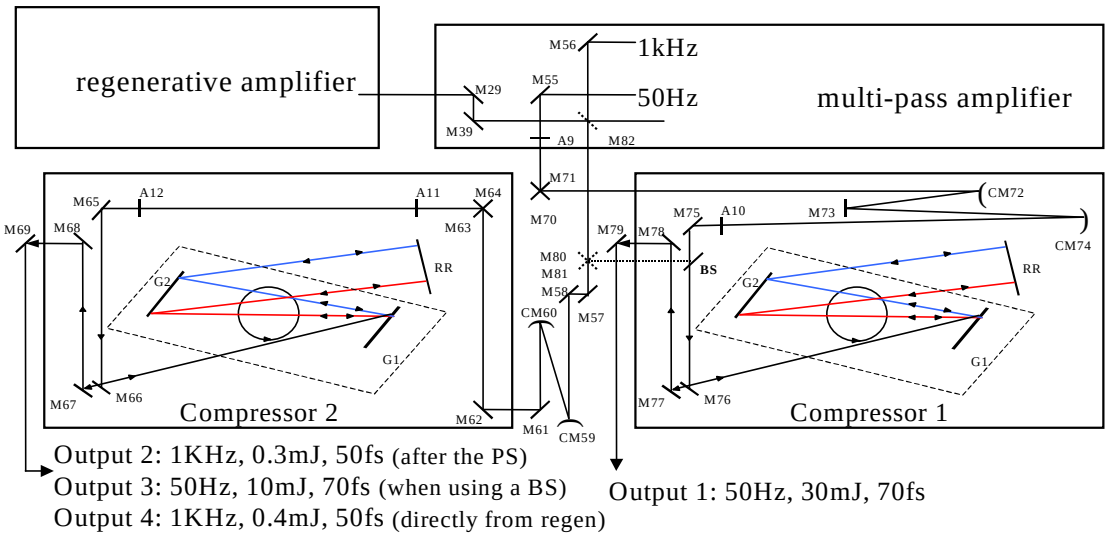

Figure 2.20: *Overview of the compressors. Different possibilities of coupling the beam into compressor are shown. Compressor 1 is set to give the output of a high energy pulse (Output 1). Compressor 2 is set, depending on experiment, to compress the 1kHz leakage pulses from the pulse slicer (PS) (Output 2), or to compress a part of the multi-pass output using a beam-splitter (BS) (Output 3), or to compress the output of the regenerative amplifier when the multi-pass amplifier is not in use (Output 4). M = flat mirror, CM = curved mirror, G = grating, RR = retroreflector, A = aperture.*

Compressor 1. This output is s-polarized (polarization perpendicular to the optical table) and is first sent through a periscope which changes the height and the polarization of the laser beam, since the grating efficiency is optimal for p-polarized light. The periscope is formed by mirrors $M70$ and $M71$. Before hitting the gratings the laser beam is magnified in order to keep the intensity low when the pulse is compressed. A magnification of 4 to a final diameter of $\sim 2cm$ is obtained using the telescope formed by mirrors $CM72$ (radius of curvature $25cm$) and $CM74$ (radius of curvature $-1m$). The telescope is folded using mirror $M73$. Mirrors $M75$ and $M76$ are used to send the beam onto the grating pair $G1 - G2$ (groove density $1500lines/mm$). The grating pair is set on a platform on a rotation stage which allows adjustment of the incidence angle of the beam with respect to the normal of the grating while keeping the two gratings parallel. The retroreflector (RR) compensates the spatial chirp by sending the beam back through the compressor for a second pass and changes the height of the beam (the reflected beam is $3cm$ higher). The incidence angle is 41.4^0 and the perpendicular distance between the gratings is $31.5cm$. These values are calculated taking into account the dispersion of the system - see section 2.2.2. Mirrors $M77$, $M78$ and $M79$ couple the compressed laser beam out of the compressor (*Output 1* in Fig.2.20).

Compressor 2 can be used for compression of three different outputs depending on the experiment. The first beam consists of the kHz pulse train rejected by the Pulse Slicer in the multi-pass amplifier (see section 2.3.4). Mirrors $M56$, $M57$ and $M58$ send the beam to a telescope that magnifies the beam diameter by a factor of 2 to a final diameter of $\sim 1cm$. The telescope consists of mirrors $CM59$ and $CM60$ (radius of curvature $25cm$ and $-50cm$). Mirrors $M61$ and $M62$ send the beam to a periscope formed by $M63$ and $M64$. This periscope is designed for the other two beams for which this compressor is used. In this case, the periscope changes the polarization of the beam from 'p' to 's'. In order to have 'p' polarized light entering the gratings, we use a $\lambda/2$ plate to rotate the polarization. Mirrors $M65$ and $M66$ transport the beam to *Compressor 2* which has the same elements as *Compressor 1.* Mirrors $M67$, $M68$ and $M69$ couple the beam out of the compressor (*Output 2* in Fig.2.20).

Another beam for which the *Compressor2* is used is obtained from a beamsplitter BS placed in *Compressor 1.* This setup is used in experiments where the pulse duration of two high power lasers has to be adjusted independently (see the pump-probe experiment Chapter 6 and 7). The beam is reflected by beamsplitter BS to the periscope formed by mirrors $M80$ and $M81$. This periscope changes the height of the beam and sends the beam on the path presented above. The periscope changes also the polarization so the $\lambda/2$ plate used earlier is no longer necessary. The compressed beam gives *Output 3* (see Fig.2.20).

There are situations when service and maintenance have to be made and the multi-pass amplifier can not be used. In this case the output of the regenerative amplifier is coupled directly into *Compressor 2* without passing the Pulse Slicer. To do this mirror $M82$ is inserted into the path of the beam after $M39$. Mirror $M82$ couples the beam into the *Compressor 2* on the path described above and the compressed beam gives *Output 4* (Fig.2.20).

Alignment procedure for the compressor

In the day-to-day operation of the laser system *Compressor 1* is aligned by adjusting $M55$ and $M71$ to center the beam on apertures $A9$ and $A10$, while *Compressor 2* is aligned by adjusting $M57$ and $M64$ to center the beam on apertures $A11$ and $A12$. The output of the compressors has to be parallel to the optical table and $3cm$ higher than the input. The compressor is set to give the required pulse duration by adjusting the distance between the gratings (the second grating is set on a translation stage) and/or adjusting the incidence angle (the two gratings are set on a rotation stage). If the output of the compressor is not on the same vertical axis $3cm$ above the input beam or if the spatial profile is not homogeneous (spatial chirp present), then a complete alignment has to be performed.

Since the two compressors are identical the complete alignment procedure will be given only for *Compressor 1.* In the alignment of the compressor the most difficult part is the parallelism of the two gratings. A backward alignment method can be used as follows: a monochromatic beam from a He-Ne laser or from the oscillator in CW-mode

is sent onto the first grating of the compressor, using $M79$, $M78$ and $M77$ to ensure that the beam propagates parallel to the optical table. For a monochromatic laser the diffracted beam after the grating is a collimated beam and therefore more easily aligned through the compressor. The input angle of the grating $G1$ can be adjusted for the monochromatic wavelength (horizontal adjustment) so that the beam hits the second grating. The vertical adjustment of grating $G1$ has to be done by checking whether different diffraction orders have the same height with respect to the table as the input beam, which means that the diffracted beams travel horizontally. By doing this we ensure that grating $G1$ and the grooves of grating $G1$ are perpendicular to the optical table. The beam diffracted by the second grating $G2$ has to be aligned parallel to the input beam. The vertical alignment of $G2$ and the check for the rotation of $G2$ has to be done in the same manner as for $G1$ by setting different diffraction orders at the same height with respect to the optical table as the input beam. The displacement between the input beam and the beam coming from $G2$ has to be equal all along the beams. In this way the two gratings are set parallel. The last element which has to be adjusted is the retro-reflector RR. The RR is aligned so that the retro-reflected beam moves parallel to the optical table (vertical adjustment of RR) and is $3cm$ lower than the input on the same vertical line (horizontal adjustment of RR). For fine adjustment of the parallelism of the gratings the fs-pulse from the stretcher is sent into the compressor on the same backward path. To check the alignment, the spectral homogeneity of the beam after the compressor is tested. This is done by scanning a mask along the spectrum on the convex mirror (CV) of the stretcher. In this procedure the spectrum on the compressor RR can be also used, however this is not as accurate since the spectrum in the compressor is not very well defined due to the big beam size ($\sim 1cm$ diameter in *compressor 1* and $\sim 0.5cm$ diameter in *compressor 2*). The output of the compressor should be spatially uniform (no spatial chirp) regardless of whether the spectrum is cut or not. If this is not the case then the horizontal of the second grating has to be fine adjusted and the horizontal shift of the output has to be compensated with the RR. The compensation of the spatial chirp can be also done by using the OMA (Optical Multichannel Analyzer) as presented in section 2.3.2 for the alignment of the stretcher. When all the elements of the compressor are aligned the beam is sent back into the multi-pass amplifier and apertures $A10$ and $A9$ are set to define the input beam of the compressor.

2.4 Performance of the laser system

As described in the previous sections, there are two amplification stages in our CPA laser system and therefore two outputs: the compressed output of the multi-pass amplifier and the compressed output directly after the regenerative amplifier. The performance of the $50Hz$ beamline is a $30mJ$ pulse energy and a $70fs$ pulse duration (supported by a $17nm$ bandwidth). The performance of the $1kHz$ beamline is a $0.4mJ$ pulse energy and a $50fs$ pulse duration (supported by a $21nm$ bandwidth). The central

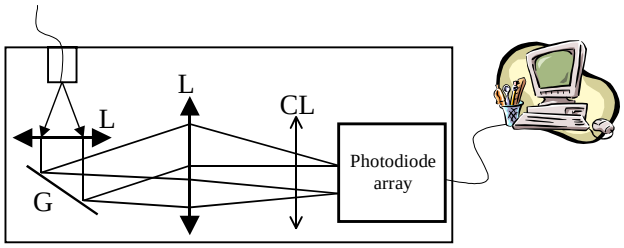

Figure 2.21: *Overview of the Optical Multichannel Analyzer (OMA). The beam is coupled into a fiber which represents a point source for a 8cm focal length lens that collimates the beam. The collimated beam is diffracted by a grating with a groove density of 600lines/mm. The diffracted beam is focused by another 8cm focal length lens onto a photodiode array which gives the pulse spectrum. L = lens, G = grating, CL = cylindrical lens.*

wavelength is tunable between $790nm$ and $820nm$.

The pulse spectra presented in Fig.2.8, Fig.2.12 and Fig.2.17 were measured with a home-built Optical Multichannel Analyzer (OMA). The beam is coupled into a fiber which represents a point source for a $8cm$ focal length lens that collimates the beam. The collimated beam is diffracted by a grating with a groove density of $600lines/mm$. The diffracted beam is focused by another $8cm$ focal length lens onto a photodiode array consisting of 2048pixels (see Fig.2.21). Before the photodiode array, a cylindrical lens is used to enlarge the vertical size of the focused spectrum and therefore to ensure that the whole spectrum lies on the photodiode array. The dynamic range of the analyzer is 4096 (12 bits). The photodiode array signal is read by a computer and the data can be written to a spreadsheet file.

The pulse duration was measured using a home-built single shot autocorrelator (SSA) which is depicted in Fig.2.22a. The basic idea of the method is to transform the temporal shape of the pulse into a spatial profile [17], which can be analyzed by a CCD camera. A beam splitter (50%) produces two replicas of the incident pulse that cross each other in a non-linear crystal (KDP). The image of the second harmonic (SH) formed on the crystal is recorded. If the two incident pulses are not collinear, the second harmonic is produced only when the two pulses are overlapped both spatially and temporally in the crystal. For a given angle between the two replicas of the pulse, the width of the second harmonic image is then determined by the pulse duration. If we assume a pulse with a gaussian shape, the pulse duration is obtained from the relation:

$$\tau = \frac{x \times \sin(\frac{\alpha}{2})}{\sqrt{2} \times c}, \tag{2.33}$$

where τ is the FWHM of the temporal profile of the fundamental laser pulse, x is the FWHM of the spatial profile of the SH, α is the angle between the two incident beams

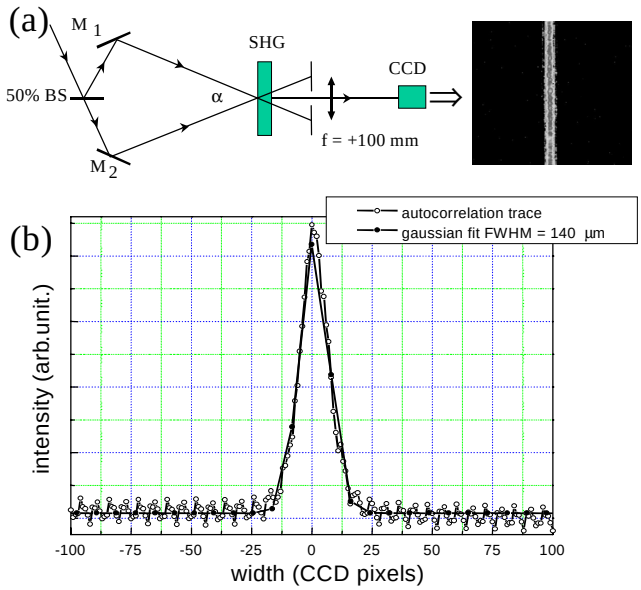

Figure 2.22: *Single-shot autocorrelator. a) The basic idea of the method is to transform the temporal shape of the pulse into a spatial profile, which can be analyzed by a CCD camera. b) The image is integrated along the vertical axis and the resulting trace has a width that corresponds to a* $70fs$ *FWHM pulse duration. This measurement was performed for the output of the multi-pass amplifier.*

and c is the speed of light. In Fig.2.22a a SSA trace obtained on the CCD camera is shown for the output of the multi-pass amplifier. This image is integrated along the vertical axis and the resulting trace is presented in Fig.2.22b. This corresponds to the determination of a $70fs$ FWHM pulse duration. The bandwidth of this pulse was $\sim 17nm$ at FWHM. As explained in section 2.3.1 the bandwidth limited value in this case is $55fs$ (assuming a gaussian shape) and $39fs$ (assuming a $sech^2$ shape). To reach the bandwidth-limited value the dispersion present in the pulse has to be compensated to all orders. To achieve this, other characterization tools have to be used in order to have more information about the chirp present in the pulse.

A second order interferometric autocorrelation has also been performed (Fig.2.23). Here, the output of the compressor is sent into a Michaelson interferometer. The two spatially overlapped beams from the interferometer are sent onto a doubling crystal and the frequency-doubled signal is detected by a CCD camera after the fundamental beam is filtered out. We performed an interferometric autocorrelation measurement for the regenerative amplifier output of the laser. We measured a $50fs$ pulse. The bandwidth of this pulse is $\sim 21nm$ at FWHM corresponding to a the bandwidth limited value of $44fs$ (assuming a gaussian shape) and $32fs$ (assuming a $sech^2$ shape). From these measurements one can extract information about the amount of chirp present in the IR pulse. However, since an interferometric autocorrelation does not provide a complete

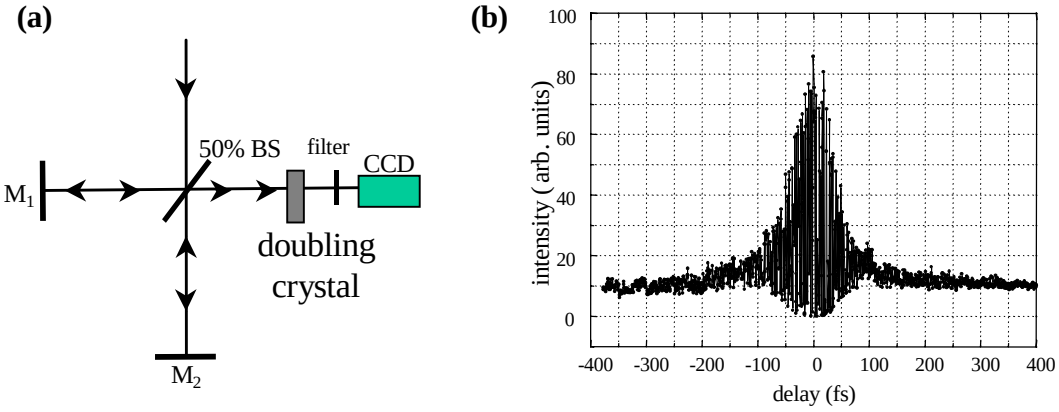

Figure 2.23: *Second order interferometric autocorrelator. a) The two spatially overlapped beams from the Michaelson interferometer are sent onto a doubling crystal and the frequency-doubled signal is detected by a CCD camera after the fundamental beam is filtered out. b) The signal detected by the CCD camera as a function of time gives the information about the pulse duration. In the case of the regenerative amplifier this was 50fs.*

characterization of a laser pulse (i.e. a determination of the phase at each frequency) and because more advanced characterization techniques are going to be implemented in the future, we have not performed any further analysis of the trace shown in Figure 2.22 [17].

Information about asymmetries in the pulse temporal shape (such as pre or post pulses) cannot be obtained from these measurements because of the symmetric nature of the autocorrelation function. Other techniques, such us third-order autocorrelator techniques [57] have to be used to completely characterize the intensity profile and the phase of the pulse.

A technique that gives complete information on the pulse duration and the amount of chirp present in the IR pulse is frequency-resolved optical gating (FROG) [58–61]. This technique makes use of both spectral and temporal information to reconstruct the properties of the IR pulse [17]. FROG is based on the use of so-called spectrograms:

$$S(\omega,\tau) = \left| \int \tilde{E}(t)\; g(t-\tau)\; e^{-i\omega t} dt \right|^2 \tag{2.34}$$

where $\tilde{E}(t)$ is the complex pulse envelope and $g(t)$ is a gate function. A FROG measurement corresponds to a measurement of the spectrum of the pulse within a time gate. Interestingly, this gate can be provided by the pulse itself, and one implementation of FROG is shown in Fig.2.24. Two replicas of a pulse are overlapped in a doubling crystal and the spectrum of the frequency-doubled light is measured as a function of delay between the pulses. By using iterative calculation algorithms the full time-dependence of the intensity and the phase of the pulses can be retrieved [17].

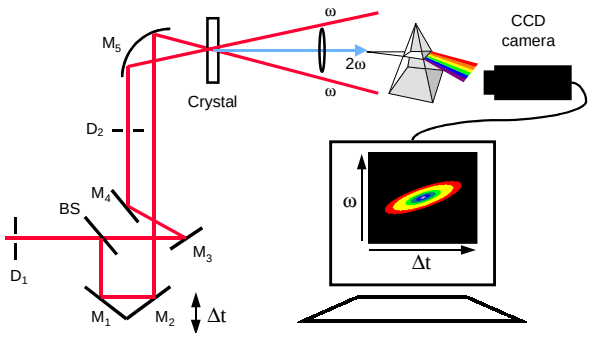

Figure 2.24: *Principle of a second order FROG setup. An intensity-autocorrelator setup is used to create a delay between two pulses. The pulses are focused onto a doubling crystal. The doubled light is diffracted by a prism or grating and the spectrum is measured as a function of delay τ by a CCD-camera or photodiode-array.*

A second-order FROG-system for the infrared output of the laser system is currently under construction. The results that will be obtained using the FROG technique will have to be compared with the predictions made by the calculations (see section 2.2.2). An alternative to the FROG technique is the so-called SPIDER technique (SPIDER = spectral phase interferometry for direct electric-field reconstruction). In this technique the interference between a pair of spectrally sheared replicas of an input pulse is measured. The interferogram which is subsequently recorded using a spectrometer yields the electric field of the input pulse [62].

In conclusion, we have built a Terawatt laser system that delivers at the moment pulses with a $30mJ$ pulse energy and a $70fs$ pulse duration (supported by a $17nm$ bandwidth). The central wavelength is tunable between $790nm$ and $820nm$. The improvements that have to be added to the system consist of adding an etalon in the regenerative amplifier cavity to enlarge the bandwidth and the development of better characterization tools to measure and compensate the chirp in order to obtain shorter bandwidth limited pulses. When these improvements are implemented, the laser should be able to generate $25fs$ amplified pulses.

Chapter 3

Experimental setup

The experimental setup used for the experiments that will be presented in the next chapters consists of a laser system, a vacuum system, detectors and a data acquisition system. In the previous chapter the laser system has been presented in detail. The other parts of the experimental setup are described in this chapter, which is divided as follows. The first section presents the vacuum system. A description of the detection assembly, which consists of a velocity-map imaging detector, is presented in the second section. In the last part the data acquisition system is described.

3.1 The vacuum system

The experimental apparatus that will be presented below is a new large machine, which, together with the femtosecond laser system presented in the previous chapter and the velocity map imaging detector that will be described in the next section, allows us to perform pump-probe XUV-IR experiments. In Chapter 4 and Chapter 6 part of this system is used, namely the experimental chamber. One of the first experiments where the setup is used as a whole is described in Chapter 7.

The vacuum system consists of four chambers: a high harmonic generation (HHG) chamber, an XUV-spectrometer chamber, an experimental chamber and a molecular/atomic beam source chamber (see Fig.3.1).

The high harmonic generation (HHG) chamber is the smallest chamber in the vacuum system ($\phi 30cm \times 30cm$) and is pumped by a cryo-pump (pumping speed $2000l/s$). The laser beam is focused onto a pulsed atomic beam of a rare gas (He, Ne, Ar, Kr, Xe) formed by a pulsed valve running at $50Hz$ (the repetition rate of the laser). The pulsed valve consists of a piezo crystal, a plunger and a nozzle [63]. Applying a voltage on the crystal (HVPZT P-286.23 High Voltage Piezoelectric Translator, Physik Instrumente) bends the crystal and releases the seal of the plunger onto the $1mm$ nozzle. The voltage applied on the crystal is provided by a HVPZT- Power- Amplifier supply (type E-500, Physik Instrumente) that is triggered by a pulse synchronized with the

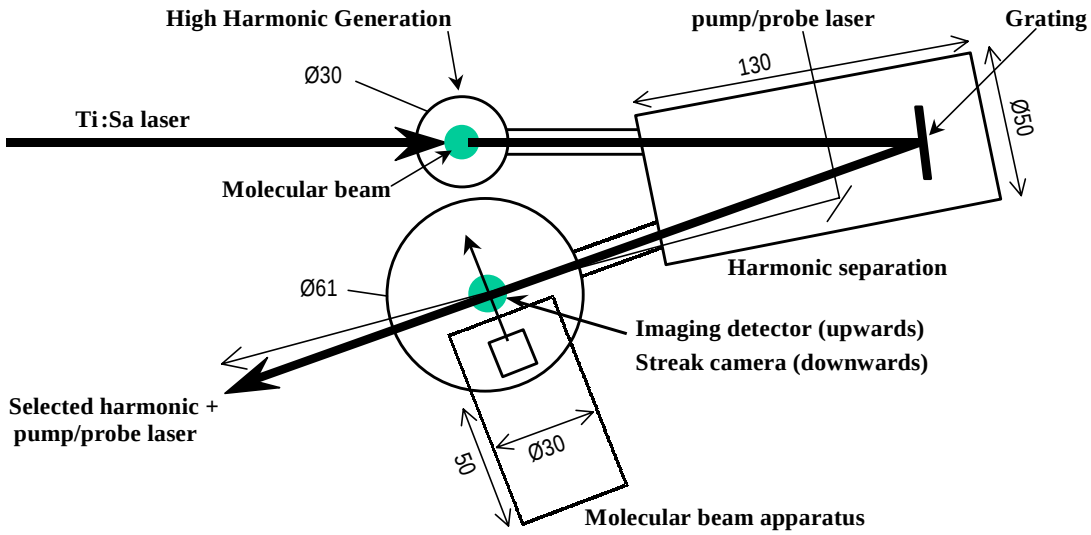

Figure 3.1: *Schematic overview of the vacuum system. Dimensions are given in cm.*

laser. The amplitude of the pulse can be adjusted using a home-built pulse shaper. Typically the valve is adjusted so that the voltage that has to be applied to the crystal to open the valve is approx. 200 Volt, and the typical value for operation is approx. 350 Volt (at $50Hz$). The typical opening time for the valve is $250\mu s$ and the time at which the valve has to be opened with respect to the laser depends on the gas (the atomic or molecular mass).

The laser beam generates high harmonics in the gas. The generation will be explained in Chapter 7. Because XUV-radiation is absorbed by air, the propagation of the light after the high harmonic generation needs to be in vacuum. Therefore, after the generation, both the fundamental and the high harmonic beams propagate through a tube, which can be closed by a valve, to the XUV-spectrometer chamber. This is a 130 cm long cylindrical chamber with a diameter of 50 cm, pumped by a turbo-molecular pump (EXT250, Edwards High Vacuum International, pumping speed $250l/s$). In this chamber a concave grating (Richardson) selects one of the harmonics and focuses this harmonic through another closeable tube into the experimental chamber. The grating has $600l/mm$ groove density, a 1.5^0 blaze angle and a $-2m$ radius of curvature. The radius of curvature of the grating was chosen so that the XUV radiation is focused on the molecular beam in the experimental chamber. This is done by imaging the high harmonic generation gas jet which is situated at the same distance with respect to the grating ($2m$) onto the experimental gas jet. The XUV spectrometer contains a breadboard that can be used as an in-vacuum optical table.

The experimental chamber is a cylindrical chamber (diam. 61 cm) where the molec-

ular beam crosses the laser beams in the horizontal plane and where the detectors are mounted (see Fig.3.2). In the upward direction along the vertical symmetry axis of the apparatus electrons or ions are detected by a velocity-map imaging detector [64]. The charges created by the laser in the interaction region are pulled upwards by the repeller and extractor through a 50cm field-free region towards the detector which consists of a dual micro-channel plate followed by a phosphor screen from which a CCD camera records the signal (see section 3.2.2). In the downward direction time-resolved detection of electrons will be done using an atomic streak camera [65]. The design of the imaging detector is described in the next section. For compensation of the earth's magnetic field, Helmholtz coils are mounted around the experimental chamber. The experimental chamber is pumped by a turbo-molecular pump (EXT250, Edwards High Vacuum International, pumping speed $250l/s$).

The molecular beam source chamber (diam. 30 cm, length 50 cm) is connected to the experimental chamber, which the beam enters through a $1.5mm$ skimmer. The molecular beam source chamber contains a pulsed valve similar to the one described for the HHG chamber. The experimental and the source chambers are differentially pumped and the molecular beam source chamber is pumped by an oil-diffusion pump (DIF320, Balzers, pumping speed $2400l/s$).

The experimental setup is very flexible and gives the possibility of setting up different kinds of experiments. One possibility is the setup presented in figure 3.1, for a pump-probe experiment (see Chapter 7) where a selected harmonic and another laser beam, used as pump or probe laser, propagates from the same direction. The breadboard in the XUV-spectrometer allows us to set up the path for the pump/probe laser beam. If the grating is used in "zero order", all the harmonics generated in the HHG chamber are reflected by the grating and enter the experimental chamber. The HHG generation chamber can also be placed on the other side of the experimental chamber, if the experimental conditions permit the use of all the harmonics without focussing them. In this way, the attosecond pulses which may be present in the harmonic train could be used directly in an experiment. In this setup, the number of XUV photons is considerable higher. In the setup presented in figure 3.1, the number of XUV photons generated in the HHG chamber decreases due to the grating efficiency ($\leq 10\%$). The experimental chambers can also be used independently. The HHG chamber can be used for generation, optimization and characterization of high harmonics. A detection system for high harmonics is available in the XUV-spectrometer. The experimental chamber can be used not only in combination with the XUV light but with any other laser if we use one of the other entrance ports of the chamber (this is how the experiments presented in Chapter 4 were performed). The molecular beam source chamber is also flexible enough to allow modifications for specific experiments. An example are the experiments performed by Nicole *et al.* [66] and Warntjes *et al.* [67] where a metastable source was used.

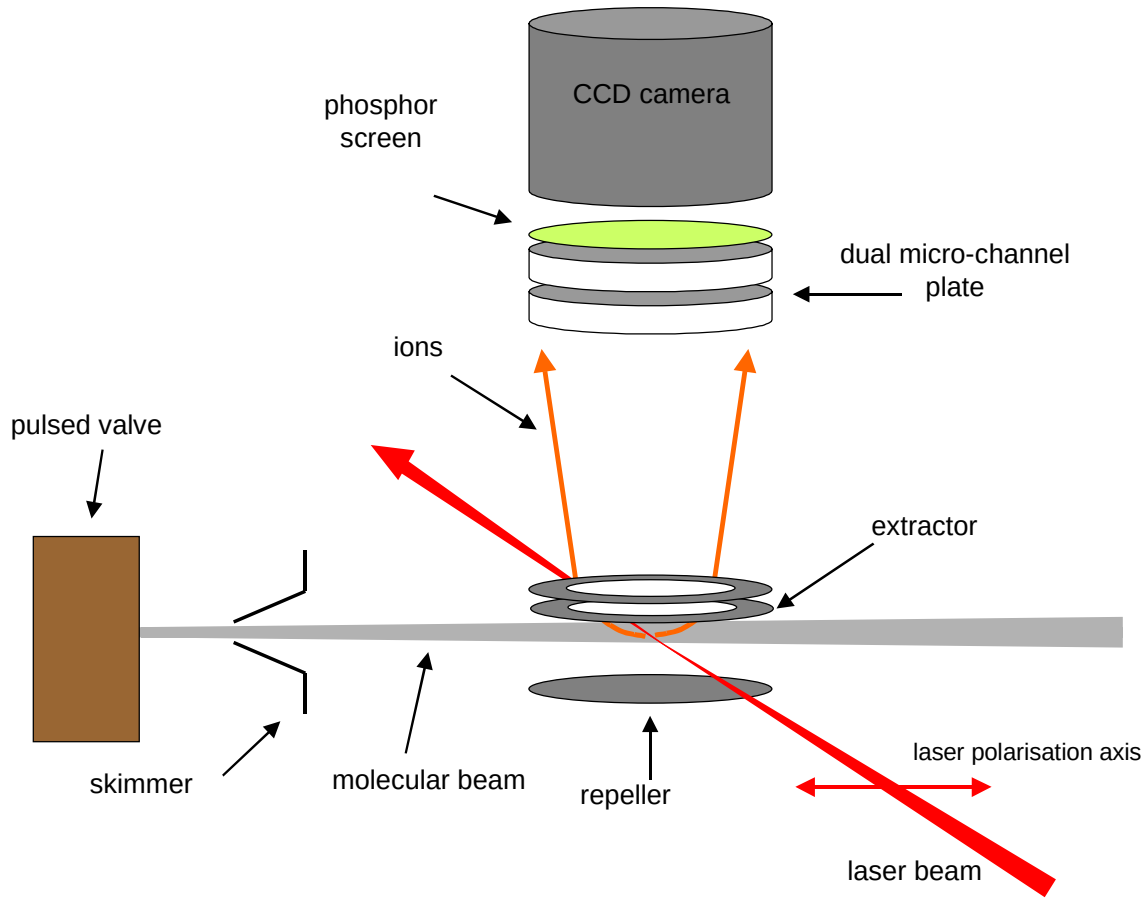

Figure 3.2: *Schematic of the experimental set-up used in the experiments presented in this thesis, showing the molecular and laser beam propagation directions and the ion imaging system.*

3.2 Detection system

A very common way to detect charged particles (electrons or ions) is using a drift-tube and a microchannel plate (MCP) detector to measure the time-of-flight (TOF). From the TOF-spectra, mass spectra and kinetic energy spectra can be obtained. The development of position sensitive detectors, in which the position of charged particles is measured, improved the TOF technique and gave additional information about the distribution of particles [68]. In 1988, the use of CCD cameras brought into play the "imaging" technique [69]. Since 1997, a new technique called " velocity-map imaging" has been successfully used for measuring the TOF and kinetic energy distribution of charged particles [64]. The principle is that an extraction electric field is used to accelerate ions or electrons in the direction of a position sensitive detector (dual MCP + fast phosphor screen) where their detected position provides a measurement of the

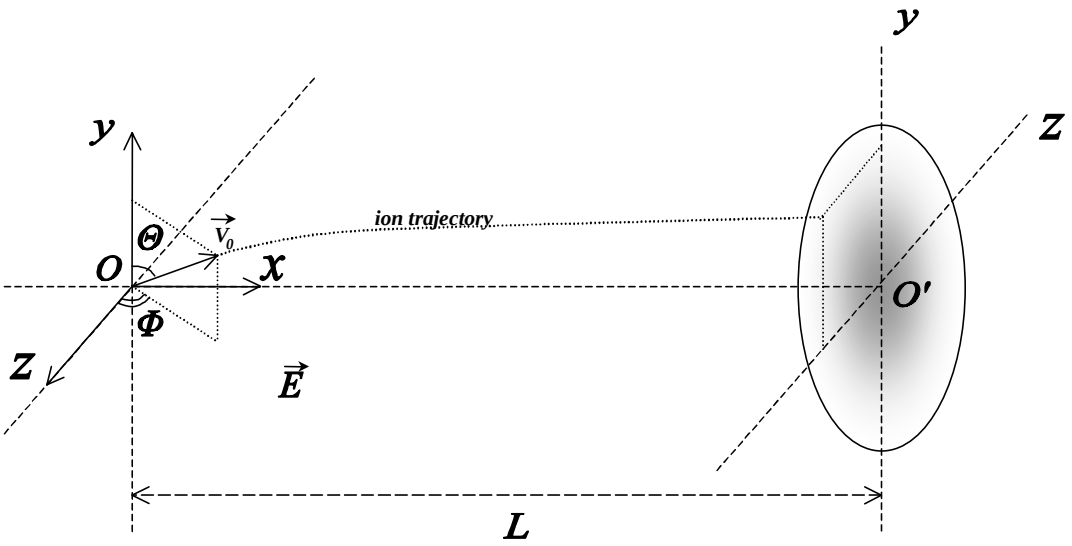

Figure 3.3: *Schematic of the imaging of a charged particle's velocity. An ion/electron created at O has an initial velocity v_0. The y- and z-component of this velocity are imaged on the plane at O′ by means of the electrostatic field $\vec{E}$. For projecting particles from a point source a homogeneous electric field is sufficient. In practice particles originating from different positions in a non-zero volume are projected on a position sensitive detector. Using velocity map imaging, particles having the same velocity vector are projected at the same spot on this detector.*

two perpendicular velocity components. A CCD-camera is used to capture the images. Using deconvolution algorithms the original 3D velocity-vector distribution can be obtained [75].

3.2.1 Velocity-map imaging

Introduction

Figure 3.3 shows a schematic of how the velocity of a charged particle can be imaged using a position sensitive detector. The electrostatic field accelerates the particle in the direction of the detector. The velocity component in the y–z-plane of the particle will not be changed, so that the position at which the particle hits the detector is directly related to this velocity component. The expanding sphere in the velocity domain is squeezed in one dimension (the x-dimension). The detector shows a ring with a certain radius R which is directly related to the expansion speed v_0 and the time of flight (TOF) t as $R = v_0 t$. This R corresponds to particles having a velocity perpendicular to the detection axis (the x-axis in our case).

For a particle with mass m and charge q created at an electrostatic potential V_c

with respect to the potential of the position sensitive detector and an initial velocity $\vec{v}_0$ directed perpendicular to the x-axis ($v_{0x} = 0$, $\sqrt{v_{0y}^2 + v_{0z}^2} = v_0$), the kinetic energy $T_E = qV_c$ has to be added to the initial kinetic energy $T = \frac{1}{2}mv_0^2$. In practice the electrostatic field is confined to a region where the particle is accelerated. Coming out of this region the particle flies through a field-free region towards the position sensitive detector with a speed $v_x = \sqrt{2T_E/m}$. If the acceleration region is small compared to the distance L from the detector (in other words: if the time the particle is in the acceleration region is much smaller than the total time needed to reach the detector) the time of flight can be approximated as:

$$t \approx L/v_x \approx L(\frac{m}{2qV_c})^{1/2} \tag{3.1}$$

Therefore, the radius $R = v_0 t$ behaves as:

$$R \approx L(\frac{T}{qV_c})^{1/2} \tag{3.2}$$

If the particles have velocity components along the x-axis, then all particles will not arrive at the detector at the same time. Particles flying in the $+x$-direction arrive first and particles flying in the opposite direction arrive last. Particles flying in the $-x$ direction are decelerated, reflected and again accelerated passing the start position with the same velocity component v_x but now in the $+x$-direction. The spread in the time of flight Δt is just two times the deceleration time. Thus $\Delta t = 2mv_0/qF$, where F is the local field strength at O. Divided by the average time of flight t this spread behaves as:

$$\frac{\Delta t}{t} \approx \frac{4}{LF}(\frac{V_c T}{q})^{1/2} \tag{3.3}$$

To distinguish between ions of different mass and charge, this relative spread in time of flight should be as small as possible. The difference in time of flight between two adjacent masses is obtained from eq.(3.1):

$$t_{m+1} - t_m = t_m(\sqrt{1 + 1/m} - 1) \approx \frac{t_m}{2m} \tag{3.4}$$

where m is in atomic units (amu) and the approximation can be made if $m \gg 1$. The maximum resolvable mass M, for which the time spread Δt equals the time between adjacent masses, $t_m/2m$ is then:

$$M \approx (2\frac{\Delta t}{t})^{-1} \text{ [amu]} = \frac{LF}{8}(\frac{q}{V_c T})^{1/2} \tag{3.5}$$

Practical implementation

With a set of electrodes, the repeller and the extractor, an electrostatic field can be applied to the region where the charged particles are created (position O in Fig. 3.4).

When imaging experiments were initially developed in the 1980's, the extractor and ground electrode apertures were covered with a grid in order to form a flat electric field. The important advance made by Eppink and Parker [64] was to use an open geometry (without grids), where the sensitivity of the detected position of a particle on the position of creation was greatly reduced. This technique is called velocity map imaging. With an open geometry the ratio $f \equiv V_E/V_R$ has to be a certain value that depends on the precise geometry of the setup, where V_E is the extractor voltage and V_R is the repeller voltage . V_E and V_R can be scaled up or down, keeping the same f, to change the electric field strength $\vec{F}$ at O.

For a flat field the following relations hold:

$$F = \frac{1-f}{d} V_R \tag{3.6}$$

$$V_c = [1 - \tfrac{a}{d}(1-f)]V_R \tag{3.7}$$

where d is the distance between repeller and extractor, and a is the distance between O and the repeller. Now, if $f = 0.8$, $d = 20mm$, $a = 5mm$, then F is on the order of $0.01 \times V_c$ (in V/mm) and eq.(3.3) can be rewritten as:

$$\frac{\Delta t}{t} \approx \frac{390}{L} (\frac{T}{qV_R})^{1/2} \tag{3.8}$$

The voltage V_R (in V) should be much larger than T (in eV) for $\Delta t/t$ to be small enough. E.g.: if $V_R = 4000$ V, $T = 1$ eV and $L = 500$mm, then $\Delta t/t \approx 0.025$, which means that $M \leq 40$ amu can be resolved.

In practice the ions are not created in a point-source. The molecular beam has a diameter of $1 - 2.5mm$ in the interaction region with the laser. The size of the focus of the laser beam is typically $\sim 200\mu m$. Therefore, the interaction volume is typically several mm^3. Eppink and Parker [64] removed the sensitivity of the image quality to the size of the interaction region by going away from the flat field geometry and using an open geometry where the field-lines in the extraction region are curved. They obtained much sharper images by omitting the grids. In this way the accelerator electrodes act as a lens, focussing ions from different origins with the same velocity to one spot at the detector, yielding a much better imaging resolution. By using holes instead of grids, the transmission is 100% and no deflections by any grid wires occur. Experiments showed that the time of flight t has the same behavior as in eq.(3.1), while the image is now magnified by a factor N. The voltage V_c can be replaced by the repeller voltage V_R to obtain the following proportionalities:

$$t \propto L(\frac{m}{qV_R})^{1/2} \tag{3.9}$$

$$R \propto NL(\frac{T}{qV_R})^{1/2} \tag{3.10}$$

Therefore, the image size (R) can be chosen by setting V_R. By setting V_E the velocity-map image can be focussed. After focussing, the image can be resized by scaling V_R,

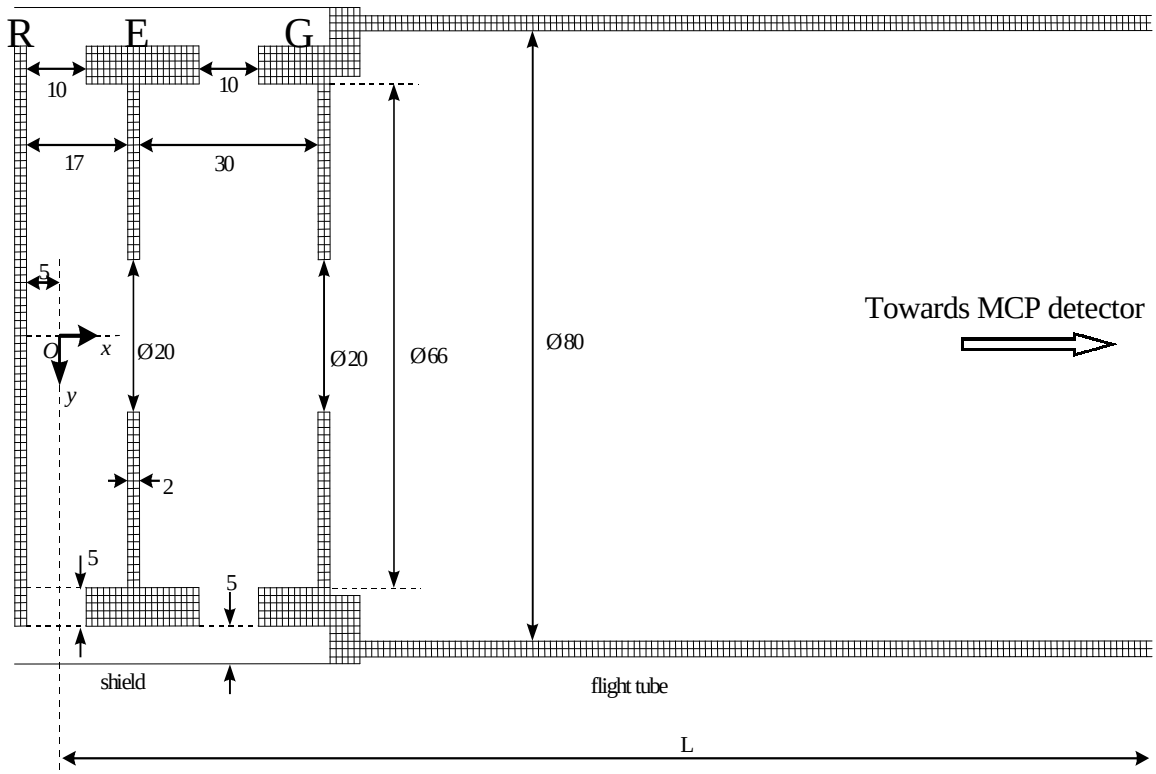

Figure 3.4: *Cross-section of the extraction region of the velocity map imaging detector where R is the repeller electrode, E is the extractor electrode, G is the ground electrode and L is the time of flight tube length.*

keeping the ratio $f \equiv V_E/V_R$ the same. The magnification factor N depends also on this ratio and lies between 1 and 1.4. N should be calibrated first by measuring ions or electrons with a known kinetic energy spectrum. The setting of f for velocity imaging is not necessarily the same one that fulfills the Wiley-McLaren condition [70]. The Wiley-McLaren condition is that ions having the same mass, created at different x-positions, arrive at the same time on the detector (mass-focus), whereas the imaging detector needs the condition that ions having initially the same velocity, created at different positions, arrive at the same position on the detector (velocity-focus). To combine both mass-spectroscopy and velocity map imaging both requirements should be met as much as possible.

Using the setup of Eppink and Parker [64] as a starting point, we have studied several geometries, using the simulation program SIMION 3D 6.0. Figure 3.4 shows a cross-section of the geometry of the optimized two-dimensional cylindrical symmetric model obtained from the calculations. The dimensions shown in the figure are optimized for velocity map imaging. This model differs from the final design in the following ways: the thickness of the experimental electrodes is $1mm$ instead of $2mm$; the distance between the electrodes and the shield (used as ground to isolate the elec-

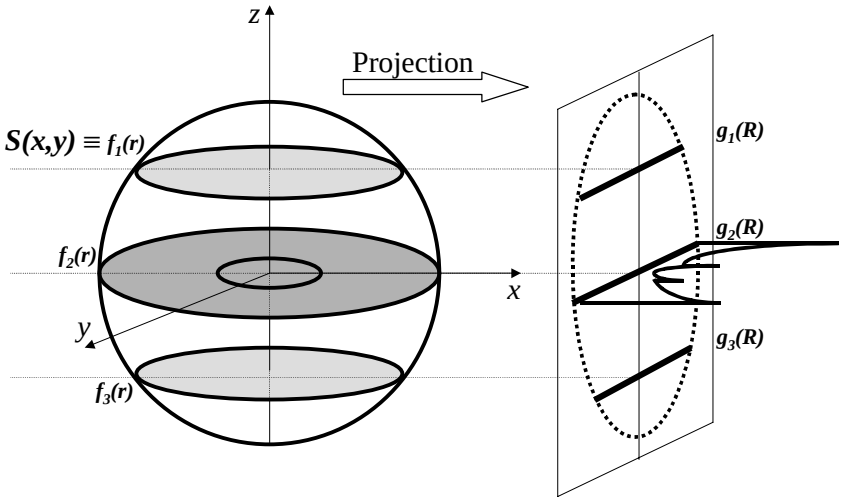

Figure 3.5: *Line by line Abel projection of a cylindrically symmetric 3D object.*

trodes from external fields) is $9mm$ instead of $5mm$ and there are 4 circular holes (diam. $15mm$) in the shield for the molecular and laser beam and a rectangular hole of 15 x 35 mm^2 for the electrode wire connections. The repeller electrode has a slit of $0.3 \times 10mm$ for future use of the extractor in the streak camera. It is important to note that a μ-metal shield is used around the TOF tube (not shown in Fig.3.4) to isolate the charged particles from the influence of magnetic fields from external sources (pumps, metastable source, etc.)

Data analysis

As explained earlier, the imaging detector creates an image on the phosphor-screen that represents a direct projection of the 3D velocity distribution of photoelectrons or ions onto a 2D plane. This is called an Abel transform. Provided it had an axis of cylindrical symmetry parallel to the plane onto which it was projected, the original distribution can be reconstructed from its projection by an inverse transform. As is apparent from Fig.3.5, each horizontal line in the image (perpendicular to the axis of symmetry z) is in itself an Abel-projection of a 2D distribution. Therefore, the inversion can be made line by line and reduced by one dimension (the dimension z along the axis of symmetry) to the 2D Abel-projection of the slice $S(x, y)$. The slice $S(x, y)$ can be represented by a 1D function $f(\sqrt{x^2 + y^2}) \equiv f(r)$. The inverse transform operating on the 1D projection $g(R)$ will yield this 1D function $f(r)$. This means that by performing an inverse transform on a complete image that is the 2D projection of a 3D distribution, another image is obtained that is a slice through the 3D distribution that contains its axis of symmetry, built up out of lines $f(r)$.

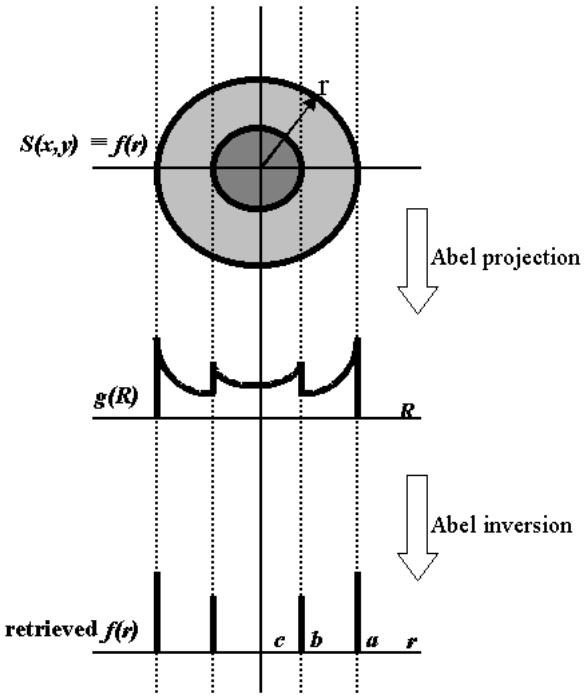

Figure 3.6: *Forward Abel transform represents the Abel projection g(R) of the slice of the 3D distribution S(x,y). From the projection g(R) the initial distribution is retrieved using the inverse Abel transform.*

The Abel projection (Fig.3.6) and its inversion are related by the formulas:

$$g(R) = \int_R^\infty \frac{f(r)r}{\sqrt{r^2 - R^2}} dr \tag{3.11}$$

$$f(r) = \frac{1}{\pi} \int_r^\infty \frac{dg(R)/dR}{\sqrt{R^2 - r^2}} dR \tag{3.12}$$

Numerically, performing an Abel inversion is difficult because of the singularity at the lower limit of integration, and because the derivative in the integrand tends to magnify noise. Several implementations can be found in reference [71]. Of all methods, the so-called onion peeling method is the most straightforward. It is based on the principle that a circularly symmetric 2D distribution $S(x, y)$ can be built up out of concentric rings, as illustrated in Fig.3.6. Each ring will contribute to the projection $g(R)$ in a well defined way. In the onion peeling method, the inversion of $g(R)$ is created from the outside in. At radius a the first nonzero intensity is encountered and in the inversion this contribution is assigned to a ring at radius a. Because of this contribution at radius a, there is an expected value for the intensity of $g(R)$ at radii

$b < a$. Any deviation from this expected value will be seen as originating from the projection of a ring at radius b. The expected value of g at pixel $c < b < a$ then takes into account the projection of both rings at a and b, and so on.

In practice this method turns out to be a time consuming process. A faster way of performing the inversion was suggested by Smith and Keefer [72] and involves reformulating the Able inversion in terms of standard (numerically fast) Fourier transforms. In this implementation, the Abel inversion is written as a Hankel (Fourier-Bessel) transform of the Fourier transform of the projected data. For the computation of the Hankel transform a fast algorithm was given by Candel [73]. However, this method tends to accumulate noise on the axis of the symmetry. A more extensive description of principles and inversion methods can be find in [74].

A new back-projection method has been developed in our group [75] and only a brief description will be presented below. A trial 3D velocity distribution is assumed, based on the radial and angular distribution observed in the 2D experimental image. From this assumed 3D velocity distribution a 2D projection is calculated, which is compared to the experimentally observed 2D projection. The differences between the calculated and the experimental 2D projections are evaluated and used to apply a correction to the 3D velocity distribution. This procedure is repeated until the differences between the calculated and the experimental 2D projections are acceptably small. Unlike the commonly used Abel inversion procedure (which tends to accumulate noise on the symmetry axis ($v_x = v_y = 0$) where the noise interferes with the accurate determination of angular distributions) our new inversion procedure projects the noise in the experimental image towards the centre of the 3D velocity distribution ($v = 0$), enabling us to obtain much cleaner angular distributions for non-zero kinetic energies. This method is therefore used in the experiments in the next chapters where the angular distribution is one of the experimental observables.

Calibration of the imaging detector

After applying the inversion procedure described above, one has to calibrate the detector in order to obtain the kinetic energy distribution from the radial distribution given by the inverted images. From eq.3.9, the time of flight t of a particle with mass m and charge q is proportional with $\sqrt{\frac{m}{q}}$. The velocity of a particle is then related to the radius of the image according to:

$$v_{rad} = R/t = CR\sqrt{\frac{q}{m}} \tag{3.13}$$

where R is the radius of the ring measured on the detector and C is a calibration factor. From eq.3.13 one can calculate the kinetic energy T of the particle as:

$$T = \frac{mv_{rad}^2}{2} = CqR^2 \tag{3.14}$$

The calibration factor can be calculated by using the electric field in the acceleration region of the detection system and the demagnification factor of the CCD camera lens when the image on the phosphor screen is imaged onto the CCD. Alternatively, a signal where the kinetic energy of the particles is well known can be used. In the experiments presented in the next chapters we used above threshold ionization (ATI) photoelectron spectra of Xe [76] for calibration.

3.2.2 The MCP-Phosphor assembly

The MCP-assembly used in our setup for the imaging of the ions or electrons consists of a dual microchannel plate detector (MCP) followed by a phosphor screen. For the imaging experiments, a large diameter MCP-detector is essential. In our setup, the maximum detectable radius R of the MCP-phosphor screen assembly is about 35 mm (Hamamatsu, type F2226-24PX). The assembly is designed in such a way that it is possible to measure the charge collection on the MCP in two ways (Fig.3.7). The MCP-assembly can be used in DC-mode (for time-of-flight measurements) and pulsed mode (for the velocity-map-imaging). When used in DC-mode, MCP-out is at $\sim 2kV$ and the phosphor-screen at $\sim 5kV$. The charge collection as a function of time can be measured as a signal V(t) using the simplified circuit shown in Fig.3.7a. The MCP and the phosphor screen are capacitively coupled and therefore the whole detector assembly can be gated in time with a gate width of $\sim 150ns$ (Fig.3.7b). The minimum value of the gate is given by the RC time of the electronic circuit (rising edge $\sim 40ns$). In pulsed mode the phosphor-screen is at $\sim 4kV$ and the MCP is at $\sim 1kV$, resulting in very low gain. To select a window in the time-of-flight spectrum, at a certain time the MCP-out is pulsed to $\sim 2kV$. Because of the capacitor the voltage difference between MCP-out and phosphor remains at $3kV$. The pulsed mode enables measurements for individual m/q ratios (where m = the mass of the fragment and q = the charge of the fragment). The signal on the phosphor screen is recorded by a CCD camera (Pulnix, TM-9701), transferred to a computer at $30Hz$ repetition rate and stored and analyzed by a LabVIEW data acquisition program.

3.2.3 An example: Photoionization of metastable Xe atoms

A typical example of images obtained in our experimental setup is shown in Fig.3.8a. The raw image shown in Fig.3.8a was obtained by collecting the photoelectrons resulting from photoionization of metastable Xe atoms with a $50fs$ laser pulse centered around $800nm$, from our Ti:Sapphire laser system. The metastable Xe atoms were formed in an electron impact source [77], leading to the production of predominantly Xe*(6s, J=2) (E = 8.315 eV) as well as smaller amounts of Xe*(6s', J=0) (E = 9.447 eV). The image in Fig.3.8a is the result of the acquisition of appr. 6000 laser shots and was recorded with a CCD camera (see section3.3). For each individual laser shot the image from the CCD camera was transferred to a computer, where the centroid was determined for the detected photoelectron spots, and where the data were binned

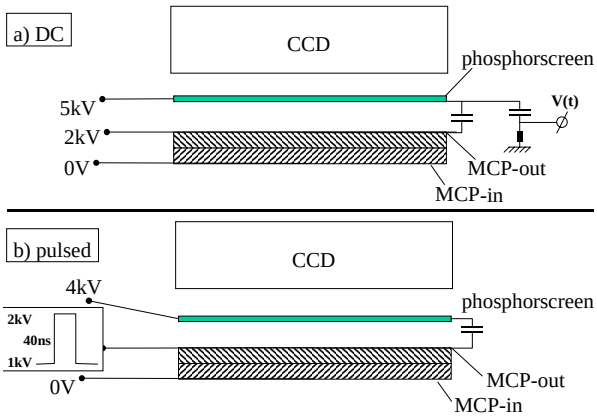

Figure 3.7: *Two ways of using the MCP/phosphor-assembly: a) DC-mode: MCP-out is at* $\sim$ *2kV and the phosphorscreen at* $\sim$ *5kV. The charge collection as a function of time can be measured as a DC-signal V(t) using the simplified circuit shown in the figure. b) Pulsed mode: The phosphorscreen is at 4kV and the MCP is at 1kV, resulting in very low gain. To select a window in the time-of-flight spectrum, at a certain time the MCP-out is pulsed to* $\sim$ *2kV for* $\sim$ *150ns. Because of the capacitor the voltage difference between MCP-out and phosphor remains at 3kV.*

accordingly. There were about 300 counts on the highest pixel in the image.

Several contributions can be recognized in the image, corresponding to two- and three-photon ionization of the Xe atoms. The most intense ring corresponds to three-photon ionization of Xe*(6s, J=2). This photoionization process takes place predominantly via an autoionizing resonance, leading to the production of an intense sharp peak in the photoelectron kinetic energy distribution. Two-photon ionization of Xe*(6s', J=0) leads to a double ring in the central portion of the image, namely a broad, weak ring surrounded by a more intense, narrow ring. Both signals are observed against the background of the strong signal from the afore-mentioned Xe*(6s, J=2) signal. The broad ring is due to direct excitation to the continuum, and its width is due to the bandwidth of the femtosecond laser, whereas the slightly more intense, narrow feature corresponds to the excitation of an autoionizing resonance in the wings of the femtosecond laser spectral profile. The appearance of a weak feature (the two-photon ionization of Xe*(6s', J=0)) inside a more intense feature (the three-photon ionization of Xe*(6s, J=2)) is awkward in conventional inversion methods, which have the tendency to project the noise horizontally towards the vertical symmetry axis. This is clearly observed in Fig.3.8b, which shows a cut through the 3D velocity and angular distribution of the image shown in Fig.3.8a, when the inversion is performed using the afore-mentioned Fourier-Hankel inversion algorithm [72, 73]. There is a strong centre-line noise component and the signal originating from Xe*(6s', J=0) is seen against a noisy background which is due to the presence of the Xe*(6s, J=2) signal.

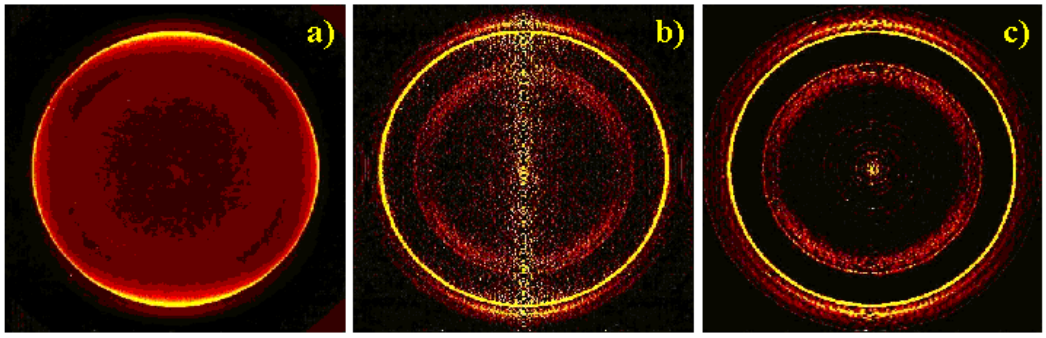

Figure 3.8: *a) Experimental image obtained for the photoionization of metastable Xe atoms by a $50fs$ Ti:Sa laser, showing contributions from two- and three photon ionization of both J=0 and J=2 states (see text), b) cut through the 3D velocity and angular distribution obtained by Fourier-Hankel Abel-inversion of the experimental image, showing characteristic centre-line noise, c) cut through the 3D velocity and angular distribution obtained by applying the iterative procedure developed in our group [75].*

By comparison we show the results obtained after 50 iterations according to the procedure developed in our group [75]. Fig.3.8c shows a cut through the 3D velocity and angular distribution that resulted from the iterative procedure. By comparison with Fig.3.8b there is a much less-pronounced inward noise-projection with no centre-line noise at all, resulting in a much clearer observation of the weak Xe*(6s', J=0)) contribution. The noise in the inversion is seen to accumulate near the centre of the image, where it does not interfere with the observation of any of the physically relevant signals.

3.3 Data acquisition system

The data acquisition system consists of an analog and digital I/O card (data-acquisition of DC-signals and trigger read-out) and a CCD-camera (acquisition of images).

Analog signals are acquired by a National Instruments data-acquisition card (LabPC-1200). This card has eight analog-input channels, two analog-output channels, three 8-bit digital-I/O ports and three clock/timer ports. LabView functions are supplied with the NI-DAQ for LabView (version 6.1.1) software package. The analog-I/O channels can be set to measure or supply voltages in the ranges -5 to $+5V$ or 0 to $10V$.

The CCD-camera is capable of taking 30 full-frame 8-bit images per second in non-interlaced mode or 60 half-frame images per second in interlaced mode. Non-interlaced mode means that all video-lines are read out subsequently and the image transmitted is a full frame capture of the object. Interlaced mode means that odd and even video-lines are read out alternately. The data acquisition can be done in two modes: an analog

mode and a counting mode. In analog mode the signal measured on each pixel of the CCD camera is stored without any further analysis. In counting mode the centre of each spot on the phosphor screen corresponding to an ion/electron is determined and stored. In this mode the signals have to be kept sufficiently low to ensure that there is no overlap between different counts on the phosphor-screen.

The CCD chip has 648×484 pixels. The pixel size is 11.6(H)×13.6(V) μm. The camera has two video outputs: an analog RS-170 format (TV) output and an 8-bit digital output. A National Instruments IMAQ PCI-1408 framegrabber is used to capture the images from the CCD camera. This PC-card is capable of capturing four analog video signals. It can be triggered by an external trigger signal. The framegrabber is supplied with driver software and programming tools for Labview and other programming languages.

Beside the camera the data acquisition program controls a delay stage (Newport, M-UTM 150CC.1) that was used in the pump-probe experiments, and the rotation of the grating in the XUV spectrometer.

Part 2
Single pulse experiments.

Chapter 4

Spatial alignment of diatomic molecules: experimental results

In this chapter we present measurements of the laser induced spatial alignment of two diatomic molecules, iodine (I_2) and bromine (Br_2). Dynamic alignment is inferred from the angular distribution of the ionic fragments from multi-electron dissociative ionization (MEDI). The angular distributions were determined for different pulse durations and energies of the short infrared laser pulses that induce the MEDI, and were measured using a velocity map ion imaging detector. The width of the angular distribution of the fragments with respect to the laser polarization axis depends only weakly on the laser pulse energy, and decreases rapidly for longer pulse lengths (a few picoseconds) at constant pulse energy. The interpretation of this result in terms of dynamic alignment is supported by an extended field ionization Coulomb explosion model that includes the rotation of the molecule induced by the laser field.

This chapter is organized as follows. In the first section the motivation for this experiment is presented in the context of experiments performed by other groups. The second section describes the experimental setup and discusses the advantages of using a velocity map imaging detector in studies of molecular alignment. The experimental results are presented in the third section, where the two subsections present a description of the angular distributions and the kinetic energy distributions of the ionic fragments. The model used to simulate the experimental results is only briefly described in section four, since it is the subject of the next chapter. In this section, a comparison between the theoretical and the experimental results is presented. Our conclusions are summarized in section five, where we compare our work to other experiments.

4.1 Introduction

In the last decade multi-electron dissociative ionization (MEDI) of molecules in intense laser fields has drawn considerable interest. A lot of attention has been given to the

angular distribution of the fragment ions, which is observed to be strongly peaked along the laser polarization axis. This anisotropy has alternatively been explained in terms of the dependence of the ionization rate on the angle between the molecular axis and the laser polarization axis (geometric alignment) [78] and in terms of a laser-induced reorientation of the molecules prior to or during the dissociative ionization (dynamic alignment) [79]. Improved understanding of the role of rotational pumping and the formation of pendular states in laser-induced dynamic alignment [80–84] and the role of electron localization in multi-electron dissociative ionization [85, 86] has led to the realization that the anisotropy is frequently caused by a combination of the geometric and dynamic alignment [12–15, 87].

Individual researchers have used different criteria to distinguish the role of geometric and dynamic alignment. Normand *et al.* [88] and Dietrich *et al.* [89] performed double-pulse experiments on CO and I_2, respectively, showing that fragment ion signals measured parallel to the laser polarization axis can be depleted by a preceding laser pulse with orthogonal polarization. This suggests that both lasers interact with all molecules in the focus and that the anisotropy is a manifestation of laser-induced alignment of the molecules. Posthumus *et al.* argued that the appearance of fragment ions at 90^0 with respect to the laser polarization at high enough laser intensities is a signature of the presence of dynamic alignment [12]. Based on this criterion they concluded that in MEDI of H_2 and N_2 with $50fs$ Ti:Sa laser pulses at intensities around $10^{14}W/cm^2$ dynamic alignment played a role, whereas in MEDI of I_2 with the same laser it did not and the anisotropy in the angular distribution was almost completely determined by geometric alignment. Ellert and Corkum used differences in the fragmentation patterns observed with linearly and circularly polarized laser pulses to conclude that Cl_2 is dynamically aligned by $80fs$ laser pulses around $625nm$, whereas I_2 is not [13]. Schmidt *et al.* inferred the occurrence of dynamic alignment in Cl_2 and N_2 from the dependence of the angular distributions on the molecular parent ion state, the laser wavelength, the laser intensity and the laser pulse duration ($130fs$ or $2ps$). In the case of I_2 they concluded that dynamic alignment was inefficient under the conditions accessed in the experiment [15]. Similarly, the dependence of the observed alignment on the laser intensity was also used by Banerjee *et al.* to distinguish dynamic from geometric alignment [90].

In this chapter, we present an experimental investigation of geometrical and dynamic laser induced alignment of I_2 and Br_2 molecules. We present experiments where we have used velocity map ion imaging [64] of the fragment ions from MEDI, to study changes in the fragment ion angular distributions when the pulse energy and the pulse duration are varied. The main conclusion from our work is that dynamic alignment of heavy-atom molecules like I_2 and Br_2 strongly depends on the laser pulse duration and is only weakly affected by the peak laser intensity in the focus. For pulse durations $\leq 100fs$ our experimental angular distributions are determined by geometric alignment, whereas for longer pulse durations dynamic alignment becomes dominant. Our results are supported by an extended field-ionization Coulomb-explosion model that includes the laser-induced rotation of the molecule (see Chapter 5 and ref. [91]). Our

results show that a measurement of the dependence of the angular distributions on the laser pulse duration clearly distinguishes between geometric and dynamic alignment.

4.2 Experimental setup

The experiment was performed using the home built Ti:Sapphire CPA (Chirped Pulse Amplification) laser system operating at 50 Hz that was presented in Chapter 2. This system provides pulses with an energy up to $40mJ/pulse$ and a minimum pulse duration of $80fs$ at an $800nm$ central wavelength. In the present experiment, the laser-molecule interaction was studied as a function of the laser pulse duration and pulse energy. The pulse duration was controlled by adjusting the distance between the compressor gratings. This puts a frequency chirp on the pulse, which in the absence of resonant intermediate states in the ionization processes, is not expected to influence the experiment. In agreement with this expectation, no dependence on the sign of the chirp was observed experimentally. The sign of the chirp introduced in the pulse was nevertheless kept the same for all the measurements reported here. The laser pulse duration was measured using a single-shot autocorrelator (see Chapter 2), which was calibrated using a commercial scanning autocorrelator (Femtochrome Research). The pulse duration was varied between $80fs$ and $6ps$. The pulse energy was controlled using a zero-order half-wave plate in combination with a polarizer, and was varied from $0.75mJ$ to $3mJ$, in the case of I_2, and from $0.9mJ$ to $3.9mJ$ in the case of Br_2. The maximum pulse energy used in the experiments was limited by the appearance of space charge effects in the observed images, which is recognized by appearance of streaks in the ion images. The infrared laser pulses were focused with an $f = 500mm$ plano convex lens ($f/D \simeq 100$) yielding a maximum peak intensity of about $2 \times 10^{15} W/cm^2$. The peak intensity was calibrated in each experiment using above threshold ionization (ATI) photoelectron spectra of Xe [76]. In these photoelectron spectra peaks due to 8-photon excitation to Xe(4f) and 9-photon excitation to Xe(5g) appear in addition to the non-resonant ionization signal at characteristic laser intensities. Thus, by comparing the photoelectron kinetic energy distributions obtained in our experiment to those reported at a range of intensities by Schyja *et al.* [76] the absolute intensity could be calibrated with an estimated accuracy of $10-20\%$. Furthermore, the ATI spectra were used to calibrate the absolute energy scale of the velocity map imaging spectrometer (see section 4.3).

The laser was focused onto a pulsed molecular beam formed by running neon (Ne) or argon (Ar) through a cell containing solid I_2 or liquid Br_2, and expanding the mixture through a pulsed valve with a $1mm$ nozzle (see Chapter 3 and [63]) placed $5cm$ in front of a $1.5mm$ diameter skimmer, which separates the source region from the experimental chamber (Fig.3.2). The I_2 sample was used at room temperature, whereas the Br_2 vapour pressure was controlled by placing the cell in a low temperature bath (-50^0C) consisting of a mixture of dry ice, water and acetone. The Ar/Ne backing pressure was adjusted to approximately 2 bar. The partial pressure of I_2 and Br_2 in

the interaction region was estimated to be about 10^{-6} millibar. In order to avoid space charge effects, care was taken to ensure that experiments were only conducted where the observed Ar+/Ne+ signal was less than one order of magnitude larger than the I+/Br+ signal. The absence of space charge effects was confirmed by repeating some of the measurements at reduced sample pressures (obtained by detuning the timing of the pulsed gas valve with respect to the firing of the laser).The gas inlet lines were replaced between the I_2 and the Br_2 experiments, to avoid contamination of the recorded signals due to the presence of IBr. The background pressure in the experimental chamber was $1x10^{-9}$millibar.

The laser and the molecular beam entered the vacuum chamber horizontally at 90^0 with respect to each other, and intersected at a point located between the repeller and extractor of a velocity map ion/photoelectron imaging detector [64], which was mounted perpendicular to the plane defined by the molecular and laser beams (Fig.3.2). The linear polarization of the laser was kept in the horizontal plane (i.e. along the molecular beam). The velocity map imaging has been described in Chapter 3. The detector consists of a dual microchannel plate detector (MCP) followed by a phosphor screen. The MCP and the phosphor screen are capacitively coupled and therefore the whole detector assembly can be gated in time with a gate width of $\sim 150ns$, enabling measurements for individual m/q ratios (m = mass of the fragment and q = charge of the fragment). The signal on the phosphor screen was recorded by a CCD camera (Pulnix), transferred to a computer at a $30Hz$ repetition rate and stored and analyzed by a LabVIEW data acquisition program. In the present experiment the data acquisition was done using the analog mode (see Chapter 3), to avoid the latter problem while varying the experimental conditions over a wide dynamic range.

A major advantage of velocity map imaging over the time-of-flight technique which has frequently been applied to studies of intense field dissociative ionization is the fact that the images created on the phosphor screen represent a direct projection of the 3D velocity distribution of a particular fragment ion onto a 2D plane. Therefore angular distributions can be measured directly without having to perform series of measurements where the laser polarization is rotated with respect to the detector axis. Velocity map imaging has a very high sensitivity, since the ions are projected onto the MCP detector with unit efficiency. Apart from the statistics of the experiment, the angular and kinetic energy resolution are only limited by the number of pixels of the CCD camera and are typically better than one degree and one percent, respectively. In the present experiment this improved detection capability has allowed us to observe sharp structures in the kinetic energy distribution and local minima in the angular distributions along the laser polarization axis, which had escaped observation in earlier experiments.

If the laser polarization is chosen in the plane of the MCP detector, then the 3D velocity distribution has an axis of symmetry in the detection plane. Therefore, the 2D projection contains enough information to reconstruct the 3D velocity distribution by means of an iterative projection procedure which has recently been developed in our group and which is described in more detail elsewhere (see Chapter 3 and [75]).

4.3 Experimental results

In the experiments presented in this chapter the influence of the laser pulse duration and pulse energy on the I^{n+} respectively Br^{m+} fragment angular and kinetic energy distributions resulting from the multi-electron dissociative ionization (MEDI) of I_2 and Br_2 were investigated, using a velocity map imaging detector. Typical experimental images are shown in Fig.4.1 (I_2) and Fig.4.2 (Br_2). The laser polarization axis corresponds to the vertical axis in these pictures. Individual rings correspond to fragment ions with kinetic energies resulting from specific ionization channels. The kinetic energy distribution is obtained from these images by using for calibration above threshold ionization (ATI) photoelectron spectra of Xe [76] as shown in Chapter 3. The left sides of Fig.4.1 and Fig.4.2 give the I^+, I^{2+}, Br^+ and Br^{2+} signals obtained with an $80fs$, $7.2 \times 10^{14} W/cm^2$ pulse for I^+ and I^{2+}, and with an $80fs$, $1.35 \times 10^{15} W/cm^2$ pulse for Br^+ and Br^{2+}. These $80fs$ results will from now on be referred to as the short pulse regime. The right sides of Fig.4.1 and Fig.4.2 give the I^+, I^{2+}, Br^+ and Br^{2+} signals for a $2.9ps$, $2.0 \times 10^{13} W/cm^2$ pulse for I^+ and I^{2+} and for a $2.5ps$, $4.3 \times 10^{13} W/cm^2$ pulse for Br^+ and Br^{2+}. These results will from now on be referred to as the long pulse regime. Comparing the images for the short and long pulse regime one can see a substantial narrowing of the angular distribution along the laser polarization axis in the long pulse situation. In the next subsection, this information is quantified by analyzing the angular distribution of these images for all the different charge channels systematically as a function of the laser pulse energy and the laser pulse duration.

4.3.1 Angular distribution

From the 2D distributions presented in Fig.4.1 and Fig.4.2, one can extract the angular distributions for I^+, I^{2+}, Br^+ and Br^{2+} fragments resulting from different ionization channels, for the long and short pulse regimes. An example of how the 3D velocity distribution is obtained from the 2D projected image and how the angular distribution is extracted from this 3D distribution is shown in Fig.4.3 and Fig.4.5 for I^+ fragments created using a short ($80fs$) and a long ($2.9ps$) pulse respectively, in both cases with $1mJ$ pulse energy (i.e. at intensities of $7.2 \times 10^{14} W/cm^2$ and $2.0 \times 10^{13} W/cm^2$, respectively). In Fig.4.3a the data presented in Fig.4.1a is reproduced, where the I^+ signal was obtained with an $80fs$ pulse duration. In Fig.4.3b a cut through the 3D velocity distribution is presented, which was obtained using the inversion procedure explained in Chapter 3. Unlike in the 2D projected image, fragments corresponding to different ionization channels are completely separated in the 3D cut. In the image presented in Fig.4.3a a slow modulation can be noticed, which is caused by the CCD camera. This modulation was removed by Fourier filtering prior to the inversion procedure. The sharp structure, which appears around the centre of the I^+- I image in Fig.4.3a and which is even more visible in the inverted image, will be discussed in the subsection 4.3.2 on fragment kinetic energy distributions.

The angular distributions obtained from the 3D velocity distribution are shown in

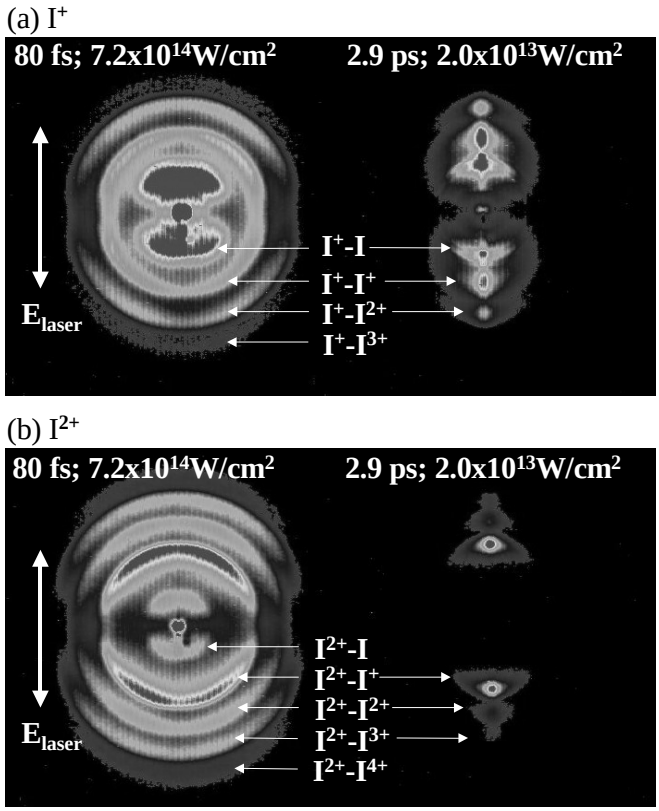

Figure 4.1: *Experimental images of I^+ (a) and I^{2+} (b) fragments resulting from the multi-electron dissociative ionization (MEDI) of I_2 for short and long laser pulses. The pulse durations and intensities are indicated in the figure. The laser polarization is along the vertical axis in the plane of the image.*

Fig.4.3c. The angular distributions are obtained by integrating contributions in the 3D velocity distribution corresponding to different ionization channels over the relevant velocity range and over the azimuthal angle ϕ. The angular distributions are given as a function of the angle θ between the laser polarization axis (the vertical axis in the images) and the atomic recoil direction, which coincides with the molecular axis. As indicated, $\theta = 0$ corresponds to the bottom of the cut shown in Fig.4.3b, and increases clockwise. Since in spherical coordinates the size of a volume element is equal to $\mathrm{dv}\sin\theta \mathrm{d}\phi \mathrm{d}\theta$ integration of the 3D velocity distribution P(v,θ,ϕ) over v and ϕ leads to a determination of P(cos θ). If the angular distribution is isotropic, then P(cos θ) is constant. To be able to compare the angular distributions of different channels they have been normalized individually. The angular distributions typically have minima at 90^0 and 270^0 (perpendicular to the laser polarization axis) and maxima at 0^0 and 180^0 (along the laser polarization). For very short pulses the distributions have a hole in the centre (at 0^0 and 180^0) which is less deep for higher charge channels (see

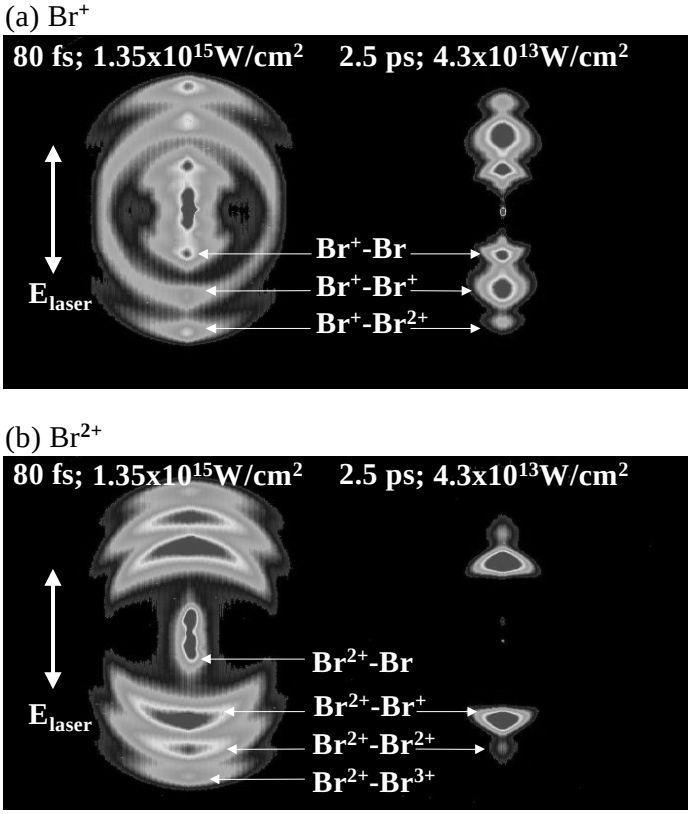

Figure 4.2: *Experimental images of Br^+ (a) and Br^{2+} (b) fragments resulting from the multi-electron dissociative ionization (MEDI) of Br_2 for short and long laser pulses. The pulse durations and intensities are indicated in the figure. The laser polarization is along the vertical axis.*

note in Fig.4.3c). We believe that the explanation for this hole, which has not been reported in earlier measurements using time-of-flight techniques [12, 15, 79], is likely to be that molecules that are aligned along the polarization axis can more easily reach higher charge states and therefore fewer ions are left in this direction for lower charge states in this direction. Some evidence for this is given by our modelling of the MEDI process [91]. The width of the angular distribution is narrower for higher charge states. This is because the higher charge ionization channels require the absorption of a higher number of photons [15,91]. The asymmetry between the lower part and the upper part of the images (at 0^0 and 180^0), and the appearance of a dark area near the centre of the image (which leads to some artefacts in the angular distribution of the I^+- I channel) is due to slight inhomogeneities of the detector as a result of extended use.

For the triply ionized iodine molecule I_2^{3+}, one of the dissociation channels is the formation of I^+- I^{2+}. The I^+ and I^{2+} fragments resulting from this channel can be detected independently and from momentum conservation one expects the angular

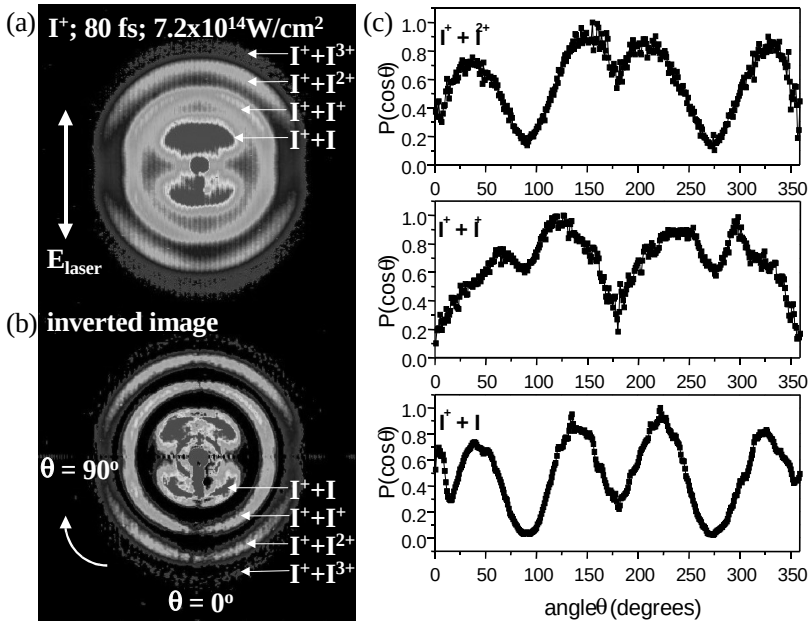

Figure 4.3: *Example of an experimental and an inverted image illustrating the inversion procedure used to extract the 3D velocity distribution from the measured 2D images: a) experimental image presented in Fig. 4.1a) for I^+ formed in the Coulomb explosion of I_2 using an $80fs$, $7.2 \times 10^{14} W/cm^2$ pulse; b) slice through the 3D velocity distribution obtained after the inversion procedure presented in section 4.2; c) angular distribution of the individual ionization channels. For the definition of θ see b).*

distributions of the two fragments to be the same. In Fig.4.4 the angular distributions of the I^+ and I^{2+} signal resulting from the I^+- I^{2+} channel are presented, for the measurements obtained with $80fs$, $7.2 \times 10^{14} W/cm^2$ laser pulses (see Fig.4.1a and b). The similarity of the two curves shows the accuracy of the experimental method.

In Fig.4.5 the angular distributions of the I^+ fragments are shown for the data presented in Fig.4.1a, obtained for $2.9ps$, $2.0 \times 10^{13} W/cm^2$ laser pulses. Again the angular distributions have a maximum along the laser polarization axis and a minimum perpendicular to it, and become narrower in higher charge channels. Comparing the width of the angular distributions in the short pulse regime (Fig.4.3c) and in the long pulse regime (Fig.4.5), one clearly sees that the fragment angular distributions are significantly narrower for longer pulses. For low charge states a pedestal is present in the angular distributions. From our simulations of the dissociative ionization process we believe the pedestal to be due to a volume effect [91]. Integrated over the focal volume, the angular distributions for individual charge states become wider as a function of the peak intensity. Molecules exposed to a relatively low intensity will contribute only to the low charge channels with a narrow angular distribution, while molecules

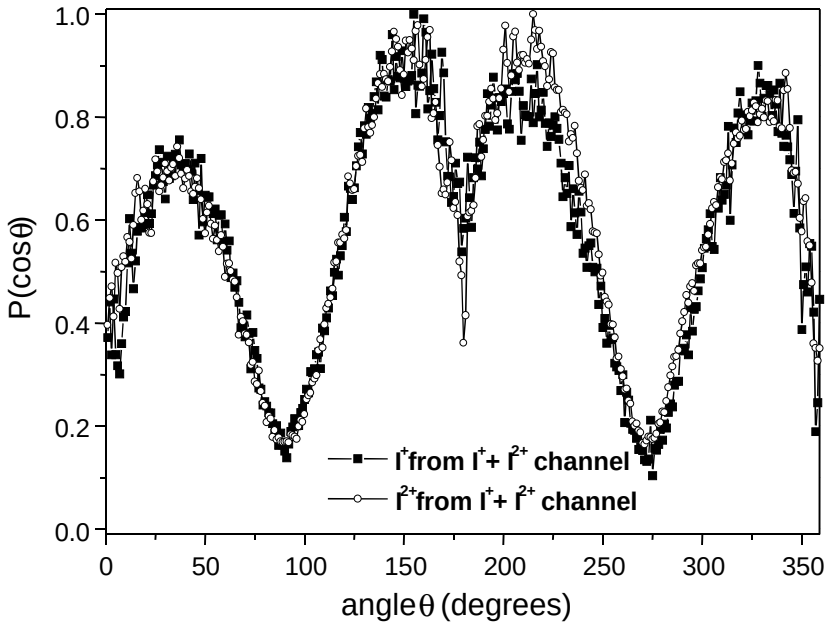

Figure 4.4: *Angular distributions of the I^+ (full squares) and I^{2+} (open circles) fragments resulting from I^+- I^{2+} channel formed in the Coulomb explosion of I_2 using an $80fs$, $7.2 \times 10^{14} W/cm^2$ pulse (see Fig. 4.1a) - b)).*

exposed to a higher intensity contribute with a wider angular distribution to the low charge fragment channels and with a narrow angular distribution to the higher charge channels. Therefore, the angular distribution is given by an average over narrow and wide angular distributions.

The angular distributions for long pulse durations are approximately gaussian, whereas for very short pulses they are somewhat non-gaussian, involving four-lobed distributions with a minimum near 0^0 and 180^0. Although a gaussian fit is a crude approximation to some of the angular distributions, we calculated the FWHM (full width at half maximum) for a gaussian fit for all angular distributions in order to quantitatively compare the distributions for different pulse durations and pulse energies. Taking into account that the measured 2D images are symmetric with respect to both the laser propagation axis and the laser polarization axis, every quadrant of the experimental image represents a complete measurement of the 3D velocity distribution. The FWHM is therefore calculated as the average of the values obtained from all four quadrants of the images, and error bars are calculated based on the differences encountered in the four quadrants.

In Fig.4.6 the FWHM of the angular distribution of the I^+ fragments resulting from the I^+- I^+ channel, is given as a function of the pulse energy and the pulse duration. In this 3D graph the pulse duration is given in fs and the pulse energy is given in mJ. Based on a calibration of the intensity using ATI in Xe, the intensity

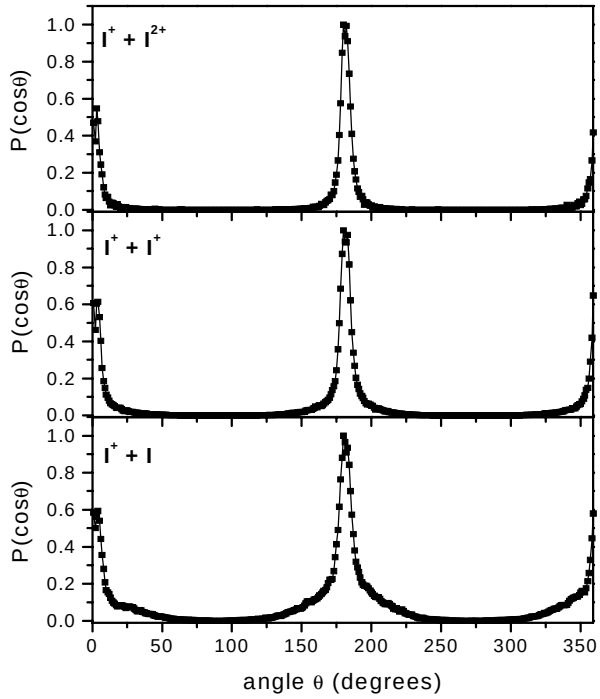

Figure 4.5: *Angular distributions obtained from Fig. 4.1a) after the inversion procedure, for I^+ fragments resulting from the Coulomb explosion of I_2 for a $2.9ps$, $2.0 \times 10^{13} W/cm^2$ pulse. Different curves correspond to different ionization channels (as indicated in the figure). We note that the pedestal which appears underneath the narrow peak influences the width of the gaussian fit used to calculate the FWHM for the angular distributions, which yields a FWHM of (a) 11.8 degrees, (b) 17.4 degrees and (c) 33.7 degrees.*

in the measurement can be calculated as $I = (2.65 \times 10^{16}) E(mJ)/\Delta t(fs) W/cm^2$. Fig.4.6 shows that for constant pulse duration, the FWHM of the angular distribution depends only weakly on the laser pulse energy, showing a small decrease with increasing intensity, except for very short pulses, where the FWHM increases again for the highest pulse energies. However, if the pulse duration is increased at a constant laser energy, the FWHM of the angular distribution decreases substantially. For example, the FWHM decreases from 64.4 +/- 2.0 degrees to 25.2 +/- 0.8 degrees when at a pulse energy of $3mJ$ the pulse duration is stretched from $500fs$ to $3ps$ (corresponding to a reduction in the intensity from $1.6 \times 10^{14} W/cm^2$ to $2.65 \times 10^{13} W/cm^2$). A detailed discussion of the results of Fig.4.6 will be presented in section 4.4, following a discussion of the extended Coulomb explosion model.

The measurements shown in Fig.4.6 were performed using Ar as seed gas. Space charge effects precluded the use of laser pulses with pulse durations $< 500fs$. Using

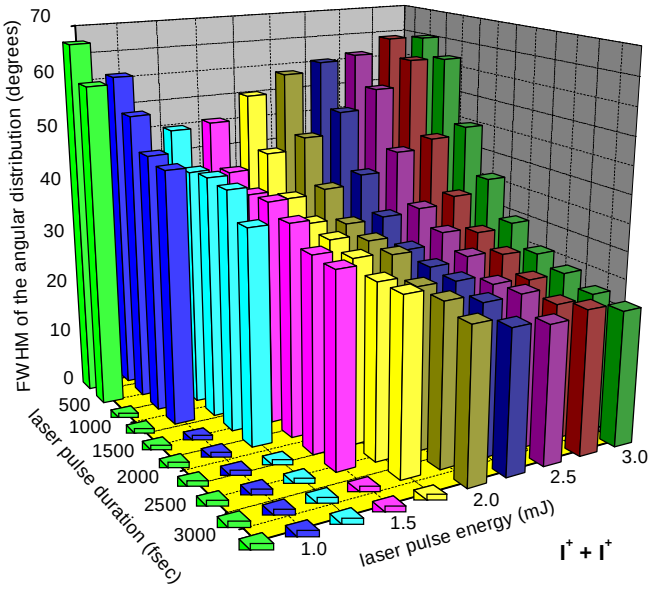

Figure 4.6: *The FWHM of the angular distribution versus the laser pulse duration and laser pulse energy for the I^+ signal resulting from the I^+- I^+ channel formed in the Coulomb explosion of I_2. The FWHM are calculated by a gaussian fit of the experimental angular distribution after the inversion, as shown in Fig.4.3. The pulse duration is given in fs and the pulse energy is given in mJ. Based on a calibration of the absolute intensity using ATI in Xe, the intensity in the measurement is equal to* $(2.65 \times 10^{16})\ E(mJ)/\Delta t(fs)\ W/cm^2$.

Ne as seed gas, the experiments could be extended to shorter pulse durations. This series of measurements further illustrates the role of the pulse duration (see Fig.4.7). In Fig.4.7a and b the FWHM of the angular distributions for individual I^+ and I^{2+} channels are presented as a function of the laser pulse duration, at a constant laser fluence of $58 J/cm^2$. All ionization channels exhibit similar behaviour. The width of the angular distribution is largest for short pulses, narrows and reaches a minimum for a longer pulse duration that depends on the channel (e.g. for I^+- I at $3.9ps$, for I^+- I^+ at $3.2ps$, for I^+- I^{2+} at $2.9ps$) and then starts increasing again as the pulse duration is increased further. For the I^+- I channel the maximum width of the angular distribution does not occur for the shortest pulse duration but for longer pulses ($500fs$) (Fig.4.7a). As before, the behaviour of different fragments resulting from the same channel is similar within the experimental error (e.g. I^+ and I^{2+} resulting from the I^+- I^{2+} channel).

The narrowing of the FWHM of the angular distributions for longer pulse durations observed for I_2 can similarly be seen in the case of Br_2. In Fig.4.7c and d the FWHM of the angular distributions for individual Br^+ and Br^{2+} channels are presented as a function of the laser pulse duration, at a constant laser fluence of $96 J/cm^2$. The

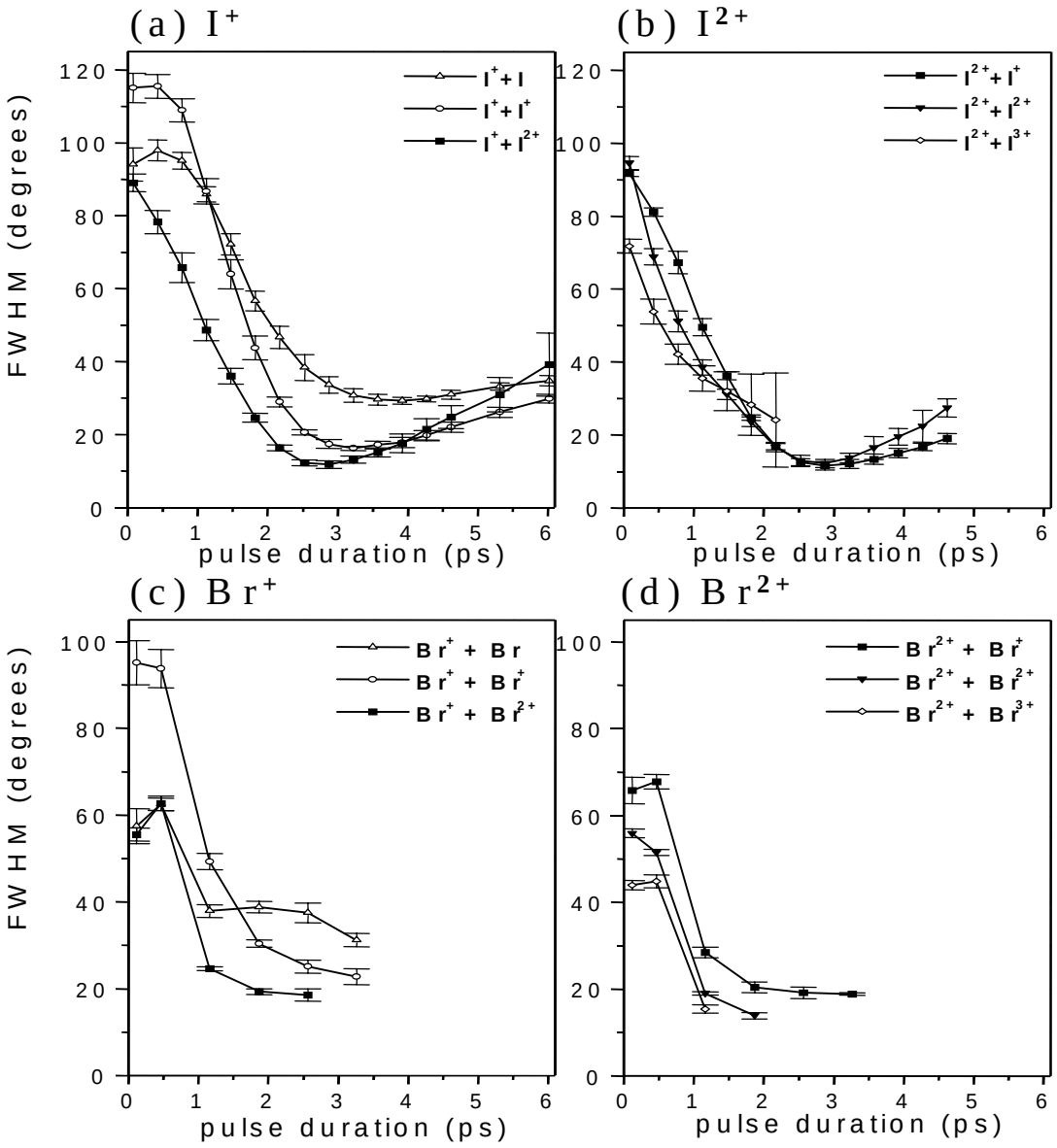

Figure 4.7: *The FWHM of the angular distribution versus laser pulse duration for I_2 (a) and Br_2 (b). The laser fluence was $58J/cm^2$ for I_2 and $96J/cm^2$ for Br_2. a) I^+ from I^+- I channel (open triangles), I^+- I^+ channel (open circles), I^+- I^{2+} channel (full squares); b) I^{2+} fragments I^{2+}- I^+ channel (full squares), I^{2+}- I^{2+} channel (full triangles), I^{2+}- I^{3+} channel (open diamonds); c) Br^+ fragments from Br^+- Br channel (open triangles), Br^+- Br^+ channel (open circles), Br^+- Br^{2+} channel (full squares); d) Br^{2+} fragments from Br^{2+}- Br^+ channel (full squares), Br^{2+}- Br^{2+} channel (full triangles), Br^{2+}- Br^{3+} channel (open diamonds).*

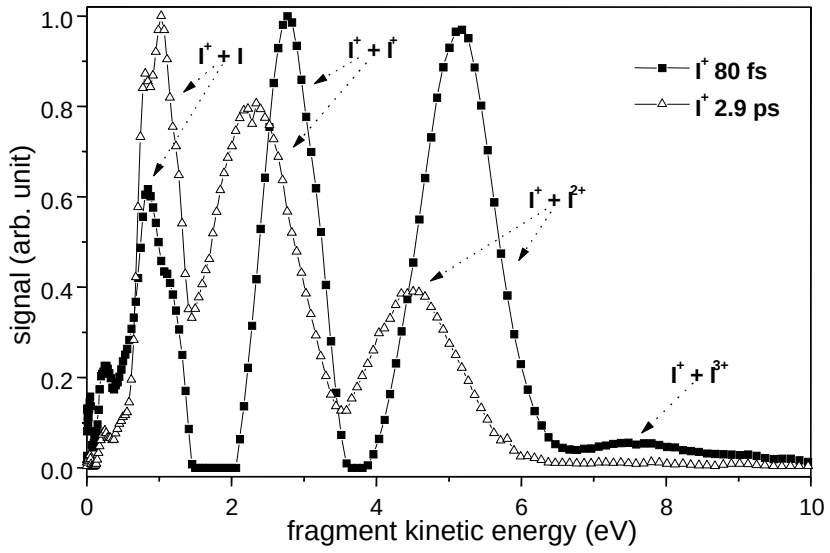

Figure 4.8: *Kinetic energy distribution of the I^+ fragments formed in the Coulomb explosion of I_2 for $80fs$ (squares) and $2.9ps$ (triangles) laser pulses at a laser fluence of $58J/cm^2$. The sharp structure that appears at low kinetic energy is explained in the text.*

evolution of the width of the angular distribution for Br_2 fragments is similar to that of I_2 fragments except for the fact that the pulse duration for which the FWHM reaches a minimum is smaller ($\sim 2ps$ for all the channels). As we will also see in the theoretical model to be discussed in section 4.4, a comparison of Fig.4.7a-b and Fig.4.7c-d shows that Br_2 molecules adapt to the laser field more rapidly than I_2 molecules.

4.3.2 Fragment kinetic energy distribution

The kinetic energy of the fragments in a Coulomb explosion depends on the charge of the fragments and the internuclear distance at which the fragments reach their final ionization state. Experimentally, the kinetic energy of the fragments can be obtained from the 3D velocity distributions following inversion of the measured images [75]. Fig.4.8 shows the energy distribution of I^+ fragments obtained using $1mJ$ pulses with a $80fs$ ($7.2 \times 10^{14}W/cm^2$) and a $2.9ps$ ($2.0 \times 10^{13}W/cm^2$) pulse duration, respectively. For the longer pulses the kinetic energy of the fragments is smaller. This will be explained in more detail in section 4.4.

Fig.4.9 shows the energy distributions of the I^+, I^{2+}, I^{3+} and I^{4+} fragments obtained using $80fs$, $7.2 \times 10^{14}W/cm^2$ laser pulse. The kinetic energies of different fragments from the same ionization channels are equal within the experimental errors (the vertical lines in Fig.4.9 connect the fragments of the same ionization channels). It is important

to note that channels with high charge asymmetry have been detected (e.g. I^{2+}- I^{5+}).

In some of the images we have observed sharp structures for the low charge channels I^+- I and Br^+- Br (see e.g. in the Fig.4.1a and Fig.4.2a). These contributions are clearly visible in the fragment kinetic energy distributions presented in Fig.4.8 for iodine fragments (below $1eV$) and similarly for bromine fragments (not shown here). The sharp structures may be due to resonances which appear in the ionization process and/or photodissociation of I_2/Br_2 followed by ionization of one of the atomic fragments. This is supported by the fact that the sharp structure is especially visible for longer laser pulses. Gordon and co-workers [92] recently reported velocity map imaging of dissociative ionization of I_2 at intermediate intensities ($10^{10} - 10^{12} W/cm^2$), using a narrowband tunable laser with a nanosecond pulse duration. They observed peaks in the fragment recoil kinetic energy distribution which were attributed to channels involving production of neutral and singly-charged iodine atoms in various spin-orbit states, as well as ion-pair states. It is likely that similar mechanisms are responsible for the sharp structures in our experiments.

4.4 The extended Coulomb explosion model. Comparison between experiment and theory.

When diatomic molecules are subjected to laser intensities $\geq 10^{13} W/cm^2$, multi-electron dissociative ionization (MEDI) occurs. Ions are predominantly ejected along the E-field of a linearly polarized laser and have kinetic energies that are typically about half of that expected from a Coulomb explosion at the equilibrium internuclear distance of the molecule. Both of these observations have been explained by the field-ionization Coulomb-explosion model [85]. This model allows the calculation of the minimum laser intensity required for over-the-barrier ionization, as a function of the internuclear distance. Geometric alignment arises in this model as a consequence of the reduction of the Stark shift experienced by the electron when the internuclear axis is at an angle with respect to the laser polarization axis [12]. The characteristic kinetic energies are associated with the enhancement of the ionization probabilities at a critical internuclear separation where the ionization threshold is lowest. Here the central barrier between the two atoms has risen to such an extent that it strongly inhibits adiabatic adjustment to the laser field, and localization of the outer electron on one of the two atoms occurs. To simulate the results of our experiment we have extended this model (similar to the work in reference [90]) by including the dynamic rotation of the molecule induced by the laser field [93]. Our model calculations are presented only briefly in this chapter since are subject of the next chapter [91].

The extended Coulomb explosion model makes explicit use of the fact that the ionization takes place in the tunnelling regime. Depending on the ionization potential, the laser intensity and the laser wavelength, ionization takes place in the tunnelling or the multiphoton regime. The transition between these regimes is described by the Keldysh parameter $\gamma = (IP/2E_{ponderomotive})^{1/2}$, where IP is the ionization potential and the

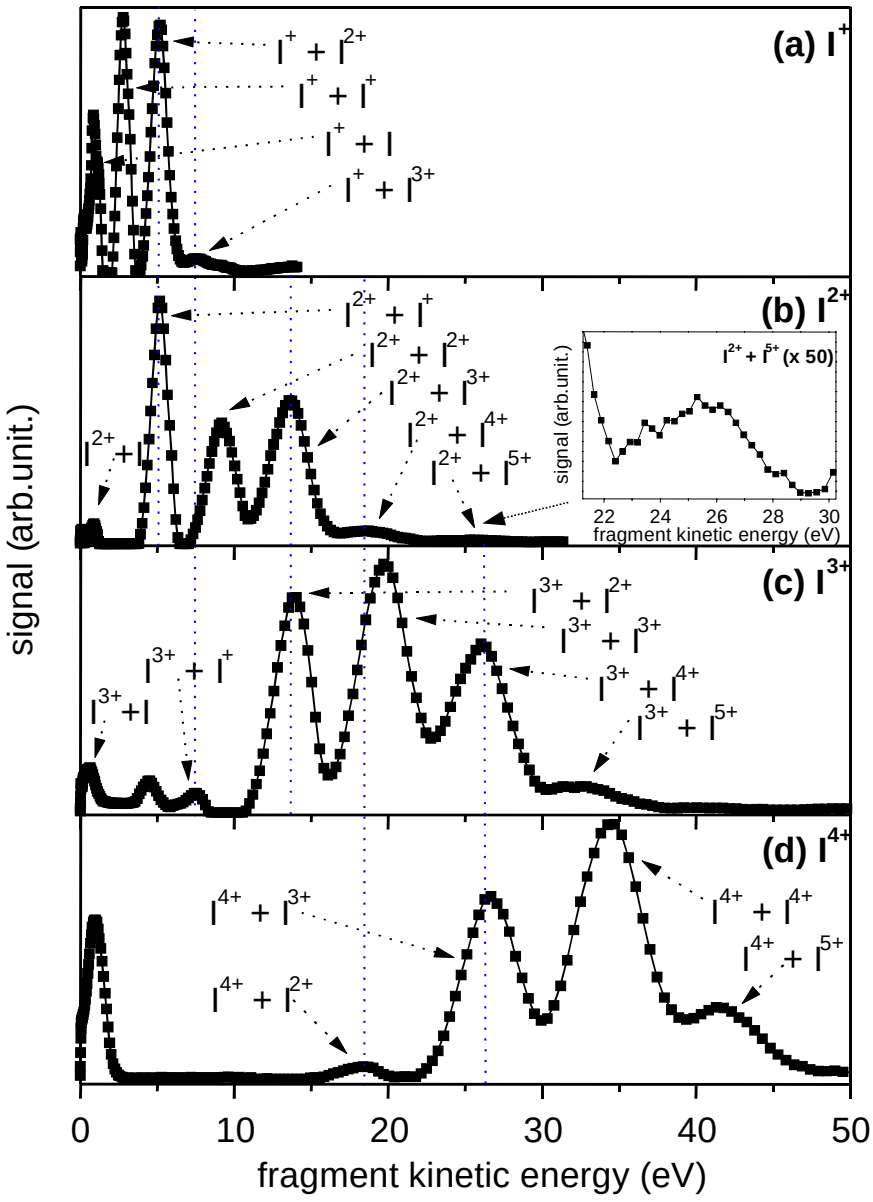

Figure 4.9: *Kinetic energy distribution of different charged fragments resulting from the Coulomb explosion of I_2 for an $80fs$, $7.2\times10^{14}W/cm^2$ pulse. The peaks in the kinetic energy distributions correspond to the ionization channels indicated in the figures of the (a) I^+, (b) I^{2+}, (c) I^{3+} and (d) I^{4+} fragments. The dotted lines connect fragments resulting from the same channel. The insert of figure b) shows a magnification of the I^{2+}- I^{5+} channel.*

ponderomotive energy $E_{ponderomotive} = e^2\varepsilon^2/4m\omega^2$, where ε is the electric field strength of the laser and ω the laser frequency. For $\gamma > 1$ (intensities below approximately $10^{14}W/cm^2$ using $800nm$ light) the ionization is a multiphoton process, whereas for $\gamma < 1$ it is a tunnelling process. In our experiment the initial ionization takes place at intensities near $10^{13}W/cm^2$ and is a multiphoton process, whereas the subsequent Coulomb explosion steps are progressively better described as tunnelling processes. Indeed, this is the way they are modelled in the extended Coulomb explosion model.

In MEDI the laser field not only ionizes and dissociates the molecule, but also induces a torque that depends on the anisotropic polarizability of the molecules, and causes a damped oscillation of the molecule around the polarization axis of the laser until ionization and dissociation takes place. This process depends on three factors: (i) the peak intensity, (ii) the temporal duration of the laser pulse, and (iii) the ratio between the anisotropic polarizability and the moment of inertia (α/I). The angular motion of the molecules in the laser field is given by [13, 90]:

$$\frac{d^2\theta}{dt^2} = -\frac{\alpha_{eff}}{4I(t)}\varepsilon(t)^2 \sin 2\theta - 2\frac{1}{R(t)}\frac{dR(t)}{dt}\frac{d\theta}{dt} \tag{4.1}$$

where θ is the angle between the laser polarization axis and the internuclear axis, α_{eff} is the anisotropic polarizability ($\alpha_{eff} = \alpha_{\parallel}$- $\alpha_{\perp}$), $I(t)$ is the time-dependent moment of inertia $\mu R(t)^2$, $\varepsilon(t)$ is laser electric field and $R(t)$ is the internuclear separation. The second term is a damping term that leads to a reduced acceleration as the molecule dissociates (due to conservation of the angular momentum). Note that apart from the parameters appearing in the equation for the angular motion, the mass of the molecule (included in the momentum of inertia) affects the speed at which the Coulomb explosion takes place and the ionization threshold affects how much the molecule rotates before it falls apart.

We have used this model to calculate the dependence of the fragment ion alignment from the Coulomb explosion as a function of the pulse duration and the pulse energy. Results of the model calculations are shown in Fig.4.10, which shows a comparison between the experimental (see Fig.4.7) and theoretical FWHM in various fragment ion channels, as a function of the laser pulse duration (at fixed laser fluence of $58J/cm^2$ in the case of I_2 and $96J/cm^2$ in the case of Br_2). The model predicts that the molecules become strongly aligned for pulses of a few picoseconds, although there is some alignment even at $500fs$. For a given pulse duration, the moment in time where the molecules ionize and subsequently dissociate, limits the amount of alignment that can be reached. Considering also that at a fixed pulse energy the peak intensity is inversely proportional to the pulse duration, this means that the alignment increases with increasing pulse duration. In the case of I_2, the width of the experimental and modelled angular distributions reaches a minimum value for a pulse duration around $3ps$. This minimum in the width of the angular distribution is a manifestation of the fact that the molecules undergo a damped oscillation around the laser polarization axis. For a $3ps$ pulse duration a large fraction of the molecules cross the laser polarization axis around the time that the laser intensity reaches the threshold intensity for

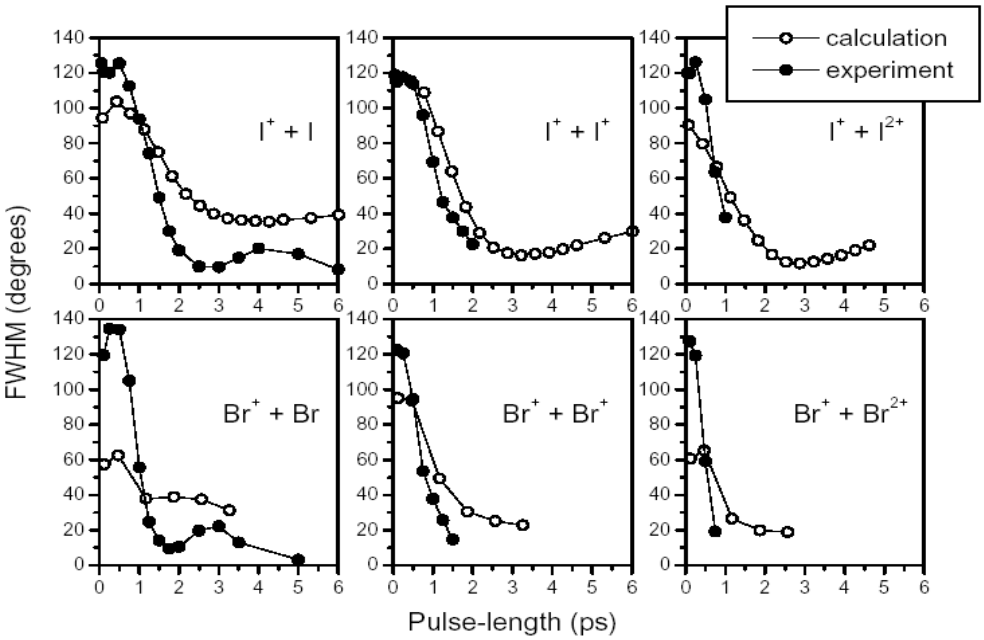

Figure 4.10: *Comparison between the FWHM of the angular distributions as a function of the laser pulse duration obtained experimentally (open circles) and calculated theoretically (full circles) using the model outlined in the text, for laser fluences of* $58J/cm^2$ *(*I_2*) and* $96J/cm^2$ *(*Br_2*). The different graphs represent individual ionization channels (as indicated in the figure) resulting from the Coulomb explosion of* I_2 *(a) and* Br_2 *(b) molecules.*

ionization. For pulses longer than this optimum value, we anticipate that the angular distribution has a further damped oscillatory structure, and the alignment dynamics approaches the adiabatic regime which was studied by Stapelfeldt and co-workers [84]. By averaging over all the I^+ ions from the I^+- I channel for I_2 seeded in argon Larsen *et al.* [84] found that $<<\cos^2\theta>>= 0.8$ for a $3.5ns$ second harmonic YAG laser pulse with a peak intensity of $1.4 \times 10^{12} W/cm^2$. This corresponds to a value for the FWHM of the angular distribution of 26.6 degrees. We cannot directly compare our results with the results obtained by Larsen *et al.* because the FWHM of the angular distribution depends, as could be seen above, not only on the pulse duration but also on the intensity and the wavelength of the laser and the seed gas (which influences the initial rotational temperature of the studied molecules).

The equation for the angular motion shows that the laser-induced angular acceleration depends on the ratio of the anisotropic polarizability to the moment of inertia of the molecule. I_2 has a higher polarizability than Br_2 ($\alpha_{iodine} = 45$ au, $\alpha_{bromine} = 28$ au), but the momentum of inertia of I_2 ($m = 63.5$ a.u.; $r_{equilibrium} = 5.04$ a.u.) is substantially larger than the moment of inertia of Br_2 ($m = 40.0$ a.u.; $r_{equilibrium} = 4.31$ a.u.)

so the I_2 molecules adapts more slowly to the laser field, as observed experimentally. Furthermore, the ionization potential of Br_2 is higher than the ionization potential of I_2 ($IP_{iodine} = 9.3eV$, $IP_{bromine} = 10.45eV$), which means that under identical laser conditions the ground state Br_2 molecules experience the alignment force for a longer time than their I_2 counterparts, leading to narrower angular distributions in the case of Br_2. The differences between MEDI of I_2 and Br_2 are further elaborated in the next chapter describing the model calculations performed [91].

As shown in Fig.4.6 the FWHM of the angular distribution initially decreases when the intensity is increased by increasing the pulse energy at a constant pulse duration, but then increases when the intensity is increased further, either by increasing the pulse energy at constant pulse duration (see results for $\leq 1.5ps$ pulse duration) or by decreasing the pulse duration (see results at all pulse energies). At the lowest energies where experiments were performed, aligned angular distributions are observed due to geometric alignment. Upon increasing the laser pulse energy, the FWHM of the angular distribution decreases due to dynamic alignment. If geometric alignment would be the only factor determining the angular distributions then a widening of the angular distributions with increasing laser intensity would be anticipated [12]. By contrast, at all pulse durations, a moderate decrease in the width of the angular distributions with increasing laser pulse energy is experimentally observed, due to an increase in the alignment forces with laser intensity. The increase in the FWHM of the angular distribution when the intensity of the laser pulse is increased further (observed for pulse durations $\leq 1ps$) is due to the fact that for laser intensities above the saturation intensity the molecules ionise earlier and earlier on the rising edge of the laser pulse, reducing the amount of dynamic alignment [15, 90]. In this short pulse, high intensity regime the angular distribution is dominated by geometric effects [12].

In experiments where the peak intensity is constant, we observe a strong decrease in the FWHM of the angular distribution with increasing pulse duration and energy. For example, in the experiments with $1mJ$, $1ps$ pulses and with $3mJ$, $3ps$ pulses (in both cases reaching a peak intensity of $2.65 \times 10^{13} W/cm^2$) the FWHM of the angular distribution in the I^+- I^+ channel was 54.3 +/- 0.9 degrees and 25.2 +/- 0.8 degrees, respectively. As in the previous discussion of measurements beyond the saturation intensity, the decrease is due to the fact that for a fixed peak intensity the molecules undergo a more extensive dynamic alignment before ionization takes place if the pulse duration is longer. If there were no dynamic alignment, then a widening of the angular distribution with pulse duration (at constant peak intensity) would be anticipated, due to the fact that for longer pulses the molecules can more efficiently reach the critical distance for Coulomb explosion, and hence Coulomb explosion from less-favorable alignment angles becomes possible. The fact that this is not observed experimentally is strong evidence for the presence of dynamic alignment.

The model also reproduces the experimentally observed shift in the kinetic energy release for long laser pulses (see Fig.4.8). This shift has been also observed in previous experiments [85]. For longer pulses, the intensity requirements for ionization are satisfied at later times and longer internuclear distances, where the Coulomb repul-

sion between the two ionic cores is weaker and the kinetic energy release smaller. In agreement with the work of Posthumus *et al.* [85] we observed a significant decrease in the fragment kinetic energy release for long pulses, suggesting that the Coulomb explosion takes place at a larger internuclear distance for longer pulses (e.g. for $3.9ps$ pulses we observe that the kinetic energy release decreases with 80% compared to the release from Coulomb repulsion at the equilibrium internuclear distance of the neutral molecule).

Based on the same argument, the peak width of the different ionization channels in the energy distribution can be explained. The width is caused by the variation of the intensity within the interaction volume. Molecules that experience a lower peak intensity dissociate at larger internuclear distance into fragments with a smaller kinetic energy release and this results in a spread of the kinetic energies which is larger for higher charge channels.

4.5 Conclusions

In recent years there has been considerable interest in the angular distributions of fragment ions resulting from multi-electron dissociative ionization (MEDI). A central issue has been the question whether observed fragment ion angular distributions are the result of the angular dependence of the ionization process (geometric alignment) or laser-induced reorientation of molecules prior to and during the MEDI process (dynamic alignment). In this chapter we have presented results on dynamic and geometric alignment of I_2 and Br_2 molecules, where we have studied fragment ion angular distributions as a function of the laser pulse energy and pulse duration. For heavy molecules, such as I_2 and Br_2, geometric alignment dominates for sub-picosecond pulses, where the laser pulse is too short for the molecule to rotate significantly, whereas dynamic alignment becomes important for pulse durations $\geq 1ps$, with an optimum for pulse durations of appr. $\sim 2-3ps$. The pulse duration for which the dynamic alignment starts to manifest itself depends on the characteristics of the studied molecule (momentum of inertia, polarizability, mass, ionization potential). The angular distributions are observed to be only weakly dependent on the peak intensity in the experiment. At low intensities and short pulses ($\leq 1ps$) an increase in the alignment is observed with increasing intensity, however this trend reverses for peak intensities exceeding the saturation intensity, when the ionization process takes place earlier in the laser pulse, reducing the role of the dynamic alignment.

The experiments presented in this chapter follow the work of several other researchers who have considered the possibility of geometric and dynamic alignment in I_2. Posthumus *et al.* studied MEDI of I_2 with $50fs$ pulses [12] and concluded on the basis of the intensity dependence of the angular distributions that dynamic alignment did not play a significant role in their experiments. Schmidt *et al.* reported measurements of iodine angular distributions for pulse durations of $130fs$ and concluded that angular distributions in the low (q=3) charge channels were determined by geometric

alignment, whereas higher (q>3) charge channels were strongly influenced by dynamic alignment [15]. In agreement with this, we find in our experiments that for $80fs$ pulses the angular distributions can be understood from geometric alignment, whereas for pulse durations of $500fs$ and above, dynamic alignment begins to play a significant role.

Our results clearly show the strength of using the velocity map imaging technique. Using velocity map imaging high quality measurements of the angular distribution can be performed very rapidly. For example, all the data points in Fig.4.6 were collected within a single day. This is probably the reason why we have been able to see two new features in MEDI of I_2, namely the observation of a minimum in the angular distribution near $\theta = 0$ degrees for short pulses and the observation of sharp features in the fragment kinetic energy distribution, which were not reported before.

The observation of dynamic alignment in MEDI using ultrashort ($\sim 1ps$) laser pulses suggests important opportunities for studies with aligned molecules. Under these experimental conditions the time evolution of the molecular rotational wavefunction is strongly non-adiabatic and the formation of an aligned molecule at the time of ionization in a MEDI process - as inferred from the experiments - suggests the formation of a rotational wavepacket at the end of the laser pulse [82, 94, 95] allowing for the preparation of samples of aligned molecules on subsequent revivals of the wavepacket. Indeed, building on the understanding gained from the experiments reported in this chapter, we have carried out a two-pulse pump-probe experiment in which we have been able to monitor the time-evolution of this rotational wavepacket, including the occurrence of revivals where the angular distribution of the molecule is suddenly narrowed or broadened during a short time interval (see Chapter 6 and [96]). Thus far studies with aligned/oriented molecules have been conducted using brute force orientation in strong external electric fields [97] and strong optical fields [84]. Exploiting the generation of a rotational wavepacket in short pulse excitation of molecules enables the formation of aligned or oriented samples of molecules under field-free conditions, making possible - among other things - studies of molecular frame photoelectron angular distributions.

Chapter 5

Spatial alignment of diatomic molecules: numerical modeling

The angular distributions of ionic fragments produced by multi-electron dissociative ionization of diatomic molecules are calculated using a field-ionization Coulomb explosion model that includes dynamic rotation of the molecule in the laser field. The majority of dynamic alignment occurs on the leading edge of the laser pulse at low intensities before the laser intensity reaches the dissociative ionization threshold. This makes the degree of alignment sensitive to the precise value of the dissociative ionization threshold. Measuring the total ion signal for different pulse-lengths enables angle-dependent dissociative ionization to be distinguished from dynamic alignment. Increased alignment with long pulses is an unambiguous sign that the molecules are forced into alignment with laser field.

5.1 Introduction

When small molecules irradiated by intense laser pulses fragment through multi-electron dissociative ionization (MEDI), the ions are preferentially ejected along the polarization axis [98]. There has been considerable debate about whether this means that the molecules are aligned prior to or during ionization and dissociation ('dynamic' alignment), or simply whether molecules that are already oriented along the polarization axis are preferentially ionized and dissociated ('geometric' alignment).

Several experiments have been carried out to identify which of these two alignment mechanisms is responsible for the observed anisotropy. Double-pulse experiments, where the molecules were irradiated with two laser pulses with crossed polarizations and a time delay between them, suggested that molecules could be aligned with intense picosecond or femtosecond pulses [88,89,99]. With circular polarization, molecules align to a plane rather than an axis (the field vector rotates too quickly for a molecule to follow). The differences between the fragmentation patterns obtained with linearly and

circularly polarized light can then be used to evaluate the degree of geometric alignment [13]. The ratio of the ion signals parallel and perpendicular to the polarization axis as a function of intensity has also been used to distinguish dynamic from geometric alignment [12, 14]. In these experiments, an increase in the signal perpendicular to the laser polarization and a broadening of the fragment angular distributions with increasing intensity were taken as the signatures of geometric alignment, as ions further from the polarization axis are ionized at higher intensities. In our group, we have identified our experimental observation of increased alignment of iodine and bromine molecules with increasing laser pulse-length as an indication of the occurrence of dynamic alignment [100].

The field-ionization Coulomb explosion model [7, 12, 85] has provided theoretical evidence for the importance of geometric alignment. This model, which considers a single outer electron bound by the double-well potential of a diatomic molecule in the laser electric field, predicts lower ionization thresholds for molecules oriented along the laser polarization axis. Once one electron has been removed from the molecule, the two ion cores begin to separate along a dissociative potential curve. Upon the loss of additional electrons, the ions move apart due to their mutual Coulomb repulsion. As the ions move apart, the central barrier between the two ions rises until the outer electron can become localized on one ion core. When this happens, the electron energy is Stark-shifted upwards. This results in a lower ionization threshold for molecules aligned close to the laser polarization axis at a critical internuclear separation, somewhat larger than the equilibrium internuclear separation. This model has been successful in explaining why the ion fragments produced by MEDI of diatomic molecules have lower energies than would be expected from Coulomb explosion at equilibrium separation [85].

Dynamic alignment can occur when the dipole moment induced by the electric field of an intense linearly polarized laser pulse aligns the internuclear axis of a molecule along the laser polarization axis [80]. Classical trajectory calculations of the dynamic alignment of molecules as they ionize and dissociate in intense laser fields have shown that, for light molecules, a substantial degree of alignment can occur even for laser pulses as short as $70 - 80 fs$ [89]. Solution of the time-dependent Schrödinger equation has demonstrated that HCN molecules can align on a sub-picosecond time scale when irradiated by laser pulses with intensities $\sim 10^{13} W cm^{-2}$ [93]. In contrast to techniques such as hexapole focusing [101] and orientation in a strong dc electric field [97] which are only applicable to polar molecules, this technique is potentially applicable to all molecules with a non-isotropic polarizability. It has recently been demonstrated that it is possible to align all three axes of a molecule along a given space-fixed coordinate frame using elliptically polarized laser fields [102]. The ability to create samples of aligned molecules has a number of important applications. From an aligned sample of molecules, it is possible to measure photoelectron angular distributions in the molecular frame. Enhanced high harmonic generation from aligned molecules has also been predicted [103]. For all these potential applications, it is important to establish under what conditions the strong anisotropies in MEDI fragment ion distributions are really due to dynamic alignment of molecules or just a result of the angle-dependent

dissociative ionization (geometric alignment).

In this chapter, we calculate angular distributions of the ions produced by multi-electron dissociative ionization of molecules. We use a field-ionization Coulomb explosion model [12, 85], extended to two dimensions, and include the effect of the dynamic rotation of the molecule in the laser field. We have investigated the dependence of the degree of alignment on laser intensity and pulse-length, as well as on molecular parameters such as mass, polarizability and dissociative ionization threshold intensity. The angular distributions are compared to those obtained with geometric alignment alone to demonstrate how geometric and dynamic alignment can be distinguished. The results of these numerical calculations are compared to experimental measurements presented in the previous chapter.

5.2 Description of the model

The model presented in this chapter is a classical calculation of the time evolution of the angular and internuclear coordinates of homonuclear diatomic molecules (I_2 and Br_2) irradiated by intense ($\sim 10^{13} - 10^{15} W cm^{-2}$) and short ($\sim 50 fs - 5 ps$), linearly polarized laser pulses. In this model, dynamic alignment of the molecules along the laser polarization axis is reflected in the time evolution of the angular coordinate due to the interaction of the laser-induced dipole with the laser field. The time evolution of the radial coordinate reflects the dissociation of the molecule during the multi-electron dissociative ionization process.

Schematically, the calculations (explained in more detail below) proceed as follows: Initially the molecule is considered to be at rest at the equilibrium internuclear bond distance, with a given initial angle between the internuclear axis and the laser polarization axis. As the laser turns on, the molecule begins to rotate due to the laser-induced dipole (dynamic alignment). When the laser intensity reaches a critical value, the molecule is ionized, and it is assumed that the molecule is excited to a dissociative curve. From here on the angular and the radial motion are coupled. Now, at each time-step in the calculation we assess whether the outer electron remains bound in the electrostatic potential of the laser electric field and both nuclei. As the shape of the potential energy surface depends on the angle between the internuclear axis and the laser polarization axis, it is responsible for the appearance of geometrical alignment in the calculation. If the electron energy is high enough to pass over the potential barriers, the electron leaves the molecule. The two nuclei then move apart due to their mutual Coulomb repulsion.

At the end of the laser pulse, the trajectory calculation gives the asymptotic recoil angle and the asymptotic charge state. We repeat the calculation for a number of initial angles between the internuclear axis and the laser polarization axis. By properly weighting these results, the calculations can be used to simulate the outcome of the experiments on the multi-electron dissociative ionization of I_2 and Br_2 presented in Chapter 4 (see Section 5.3). The remainder of this section is devoted to a more detailed

description of the ingredients mentioned above.

5.2.1 Angular motion (dynamic alignment)

Homonuclear diatomic molecules have no permanent dipole moment and so the angular rotation of the molecule is caused by the dipole moment induced by the laser field. This is also true for molecules that do possess a permanent dipole, as the interaction with a permanent dipole averages to zero over the laser period. The interaction potential with the induced dipole, averaged over the laser period, is given by [80]:

$$V(\theta) = -\frac{1}{4}\varepsilon_0^2(\alpha_\parallel \cos^2\theta + \alpha_\perp \sin^2\theta) \tag{5.1}$$

Here, $\alpha_\parallel$ and $\alpha_\perp$ are the polarizability components parallel and perpendicular to the internuclear axis, θ is the angle between the internuclear and laser polarization axes and ε_0 is the envelope of the electric field of the laser pulse. All the calculations presented in this chapter were performed with Gaussian laser pulses.

The equation of motion for the angular rotation of the molecule is then given by [13, 90]:

$$\frac{d^2\theta}{dt^2} = -\frac{\alpha_{eff}}{4I(t)}\varepsilon_0^2 \sin 2\theta - \frac{2}{R}\frac{dR}{dt}\frac{d\theta}{dt} \tag{5.2}$$

where $\alpha_{eff} = \alpha_\parallel - \alpha_\perp$ is the effective polarizability, R is the internuclear separation and $I(t)$ is the time-dependent moment of inertia. For iodine $\alpha_{eff} = 45.146au$ [104] and for bromine $\alpha_{eff} = 28.33au$ [105]. The second term in eq.5.2 is a damping term that leads to a reduced acceleration as the ions move apart. If the molecule does not ionize and dissociate, this term is zero and the molecule continues to rotate even after the laser field is switched off. In our calculations, we assume that α_{eff} is constant during rotation, ionization and dissociation. The effect of this approximation is discussed more fully in section 5.3.6.

The calculations presented in this chapter assume that the initial rotational velocity of the I_2 molecules is zero. We have examined the effect of non-zero initial rotational velocities on the observed angular distributions and find that no significant change in the angular distributions occurs for the rotational velocities expected in a molecular beam with a temperature of $\sim 10K$ (as used in the experiments described in Chapter 4).

The effect of the initial rotational temperature on degree of alignment has previously been studied experimentally by changing the carrier gas used in the expansion of I_2 into the vacuum chamber [83]. With nanosecond alignment pulses at an intensity of $\sim 10^{12} Wcm^{-2}$, it was found that the lower rotational temperature with Ar than with He as the carrier gas resulted in a more localized angular distribution. The initial rotational velocity plays a much less important role with the much faster alignment (due to the much shorter, more intense pulses) described here.

5.2.2 Dissociative ionization of the neutral molecule

The first step in MEDI is multiphoton ionization of the neutral molecule, followed by its dissociation. This occurs at a laser intensity in the region of $10^{13} Wcm^{-2}$ for I_2 and Br_2. The effect of the threshold intensity for dissociative ionization on the calculated degree of alignment is discussed in section 5.3.5.

The over-the-barrier (OTB) threshold for the appearance intensity of I_2^+ and Br_2^+ can be calculated from the shape of the potential energy surfaces of the singly charged molecules, as described in ref. [85]. For I_2, which has an ionization potential of $9.3eV$, this gives a value of $2.3 \times 10^{13} Wcm^{-2}$ at 0°. For Br_2, which has a higher ionization potential ($10.45eV$), the OTB threshold calculated in this way is $3.8 \times 10^{13} Wcm^{-2}$. However, these threshold intensities give a much stronger amount of alignment and a shorter optimum alignment time than we observed experimentally (see Chapter 4 and [100]). We found the best agreement with our experimental measurements were consistent with a threshold intensity at 0^0 of $7 \times 10^{12} Wcm^{-2}$ for I_2 and $1.1 \times 10^{13} Wcm^{-2}$ for Br_2. A multiphoton ionization threshold of $8 \times 10^{12} Wcm^{-2}$ for I_2 was measured in ref. [79] with $630nm$ radiation. The angular dependences of the threshold intensities were then obtained from the shape of the potentials (eq.5.4). Analytical fits to the numerically calculated threshold intensities give:

$$\begin{aligned} I_{threshold(I_2)} &= \frac{2.94 \times 10^{13}}{|\cos\theta|^{1.66} + 3.28} \\ I_{threshold(Br_2)} &= \frac{5.19 \times 10^{13}}{|\cos\theta|^{1.65} + 3.51} \end{aligned} \tag{5.3}$$

The calculations presented throughout this chapter use the threshold intensities for formation of I_2^+ and Br_2^+ obtained from these equations.

5.2.3 Field ionization and Coulomb explosion

Once the molecule has been singly ionized, it starts to dissociate. Following ref. [85], we assume that, for internuclear separations less than $10au$, the ions move apart as if due to the mutual Coulomb repulsion of two ions each with charge 1/2. Once the internuclear separation is greater than $10au$ the I and I^+ fragments are assumed to no longer repel each other. This division of the dynamics into two regions was found to reproduce the observed kinetic energy in this channel [85].

As the molecule flies apart and rotates in the time-dependent laser field, we check whether further ionization is possible. We assume the outer electron in the molecule moves freely in the potential well of the two ion cores. The two-dimensional double-well potential, V(x,y), of a diatomic molecule in a uniform electric field, ε_0, with the two ion cores located at $x = \pm R/2$ can be written as:

$$V(x,y) = -\frac{Q/2}{\sqrt{(x+R/2)^2 + y^2}} - \frac{Q/2}{\sqrt{(x-R/2)^2 + y^2}} - \varepsilon_0 x \cos\theta - \varepsilon_0 y \sin\theta \tag{5.4}$$

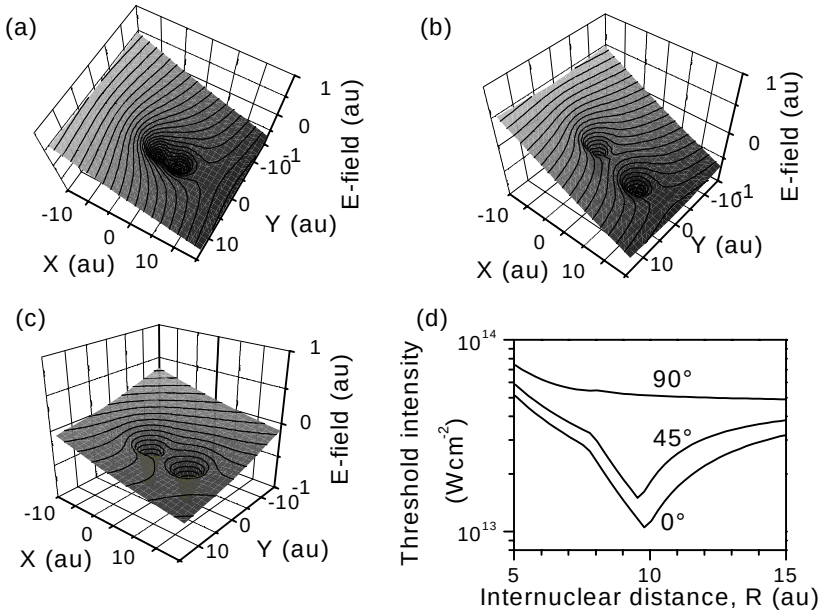

Figure 5.1: *(a) Potential energy landscape for an I_2^+ molecule oriented with the internuclear axis parallel to the laser polarization. The molecule is at the equilibrium internuclear separation of 5.04au and the laser intensity is $5.1 \times 10^{13} Wcm^{-2}$. (b) I_2^+ molecule parallel to the laser polarization. The internuclear separation is 10au and the laser intensity is again $5.1 \times 10^{13} Wcm^{-2}$. (c) I_2^+ molecule at 45^0 to the laser polarization. The internuclear separation is 9.54au and the laser intensity is $1.5 \times 10^{13} Wcm^{-2}$. (d) Threshold intensity for ionization from (I^+, I) to (I^+, I^+) as a function of internuclear separation for molecules oriented at 0^0, 45^0 and 90^0 to the laser polarization axis.*

Here, Q is the sum of the charges on the atomic cores. The shapes of the potential well for the I_2^+ molecule for three different values of θ, R, and ε are shown in Fig.5.1a, b and c. There are, in general, two saddle-points on the potential energy landscape defined by equation 5.4. If the electron has enough energy, it will leave the ion by travelling over one of these saddle-points. The positions of the saddle-points are found by looking for points where:

$$\frac{\partial V(x,y)}{\partial x} = \frac{\partial V(x,y)}{\partial y} = 0 \tag{5.5}$$

Following ref. [106], we approximate the electron energy, E, as the average of the ionization potentials, E_1 and E_2, of the two ions with charges Q_1, Q_2 where $Q = Q_1 + Q_2$, lowered by the Coulomb potential of the neighboring ion, $Q_{1,2}/R$:

$$E = \frac{(-E_1 - Q_2/R) + (-E_2 - Q_1/R)}{2} \tag{5.6}$$

As the ion cores move apart, the central barrier between the two ions becomes higher than the outer barrier on the 'downhill' side of the potential energy landscape. The electron can then become localized on the 'uphill' ion. If this happens, its energy is Stark-shifted upwards by an amount $\Delta E = \frac{1}{2}\varepsilon_0 R\cos\theta$. In Fig.5.1a, the iodine molecular ion is at the equilibrium internuclear separation of $5.04au$ and oriented along the polarization axis. In this case, there is no electron localization and no stark-shift as the central barrier is lower than the outer barrier. Fig.5.1b shows the potential wells for the molecule in the same orientation and same electric field strength, but with the ion cores $10au$ apart. At this larger internuclear separation, the central barrier has risen higher than the outer barrier. In Fig.5.1c, the molecule is 45^0 to the polarization axis and has an internuclear separation of $9.54au$. Because the electron is localized, the electron energy is Stark shifted upwards. This lowers the threshold ionization intensity to $1.5 \times 10^{13} Wcm^{-2}$, compared to $5.8 \times 10^{13} Wcm^{-2}$ for a molecule with the same orientation but at the equilibrium internuclear separation. The internuclear separation where the threshold intensity is lowest is referred to as the 'critical internuclear distance' [85] and is $\sim 10au$ in iodine. As the Stark shift is proportional to $\cos\theta$, it is zero when the molecule is perpendicular to the laser field, even though the electron can be localized on one ion.

Fig.5.1d shows the threshold intensity for ionization from (I^+, I) to (I^+, I^+) as a function of the internuclear distance for molecules oriented parallel to, at 45^0 to and perpendicular to the laser electric field. This same result is also shown in Fig.3 of ref. [12]. The threshold intensity for ionization is angle-dependent, being lowest for molecules oriented along the laser polarization axis. At small internuclear separations ($\lesssim 8au$), where the electron leaves the molecule by passing over the outer potential barrier, the outer barrier is furthest from the centre of the molecule when the molecule is parallel to the electric field, and so is lowered more by the electric field. At larger internuclear separations, the electron is localized and the angular dependence of the ionization rate arises primarily because the Stark shift of the electron energy is proportional to $\cos\theta$. This angular dependence of the threshold intensity for over-the-barrier ionization is geometric alignment.

Following further ionization, the molecule Coulomb explodes as the two ion cores repel each other. The equation of motion is given by:

$$\frac{d^2R}{dt^2} = (\frac{Q-1}{2})^2 \frac{1}{MR^2} \tag{5.7}$$

where M is the mass of the molecule and the net charge on the molecule is $Q-1$. Eq.5.7 assumes that the molecular charge is split equally between the two ions. In the equation of motion, we allow the molecules with asymmetric charge states to have non-integer charges on each ion for the purposes of calculating the radial motion due to Coulomb explosion.

The field-ionization Coulomb explosion model assumes that the only charge channels that can occur are ($I_2^{2n+} \Longrightarrow I^{n+}$, I^{n+}) or ($I_2^{(2n+1)+} \Longrightarrow I^{n+}$, $I^{(n+1)+}$). However, charge asymmetric dissociation channels ($I_2^{2n+} \Longrightarrow I^{(n+1)+}$, $I^{(n-1)+}$) have also been observed experimentally with significant branching ratios [100, 107].

5.2.4 Angular distributions and focal volume averaging

For each intensity and pulse-length, we calculated the trajectories of a set of molecules with initial angles with respect to the laser polarization axis varying from 0^0 to 90^0 in one degree steps. The angular distributions are calculated from the angle between each molecule and the polarization axis at the end of the laser pulse, once the angular velocity has returned to zero. The angular distribution is independent of the azimuthal angle, ϕ, around the laser polarization axis. The number of ions with initial angle θ to $\theta + d\theta$ is proportional to $sin\theta d\theta$. In spherical coordinates the size of a volume element is equal to $dvsin\theta d\phi d\theta$ where v is the ion velocity. Integration of the 3D velocity distribution P(v,θ,ϕ) over v and ϕ leads to a determination of P(cosθ). Throughout this chapter, we plot P(cosθ), which is constant for an isotropic angular distribution.

The final angular distributions were averaged over the intensity distribution in the focal volume, by taking the weighted sum of approximately 200 iso-intensity shells. To allow comparison with the experimental results reported in Chapter 4, we assume a loosely focused Gaussian beam intersecting a narrow molecular beam so that the laser intensity does not vary along the width of the molecular beam. If the entire chamber is filled with gas, it would then be more appropriate to use equations for the full focal volume distribution [12]. The angular distributions obtained in these two cases can be very different, due to the much larger low-intensity region sampled when the entire focal volume is considered.

As a measure of the width of the angular distribution, we use the full-width at half maximum of the angular distribution (FWHM) calculated assuming the distribution is a Gaussian centered at 0^0. The width of distribution is calculated using:

$$FWHM = 2\sqrt{\pi \ln 2}\frac{\int_0^{90} \theta F(\theta) d\theta}{\int_0^{90} F(\theta) d\theta} \tag{5.8}$$

It is difficult to use only one parameter to characterize an angular distribution, which may consist of multiple peaks. Equation 5.8 only gives meaningful results for angular distributions peaked at 0^0. We chose to use this formula to allow direct comparison with the experimental measurements presented in Chapter 4 [100].

5.3 Results

5.3.1 No dynamic alignment

In order to be able to evaluate the degree of dynamic alignment occurring, we first need to understand the angular distributions that arise in the case of geometric alignment alone.

If there is no dynamic alignment and we assume an angle-dependent ionization rate only, the angular distribution of the total ion signal depends on intensity but not

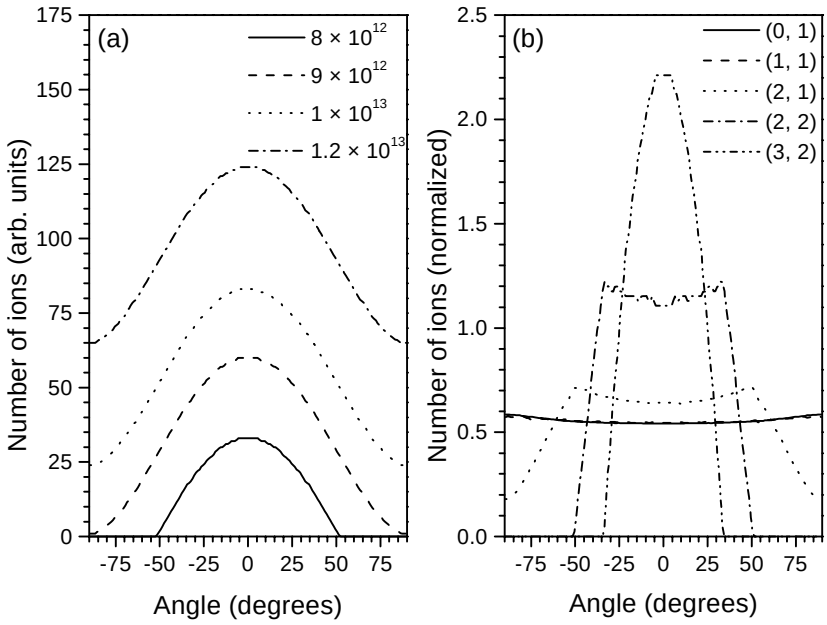

Figure 5.2: *(a) The angular distribution of all dissociated ions for a range of intensities with a* $100fs$ *laser pulse. Geometric alignment alone is considered. (b) Angular distributions of ions in each charge channel from* $I + I^+$ *(0, 1) to* $I^{3+} + I^{2+}$ *(3, 2), with geometric alignment alone. The laser pulse is* $100fs$ *long and the peak laser intensity is* $1.25 \times 10^{14} Wcm^{-2}$*. The number of ions in each channel has been normalized.*

pulse duration. This is because whether a molecule ionizes or not depends only on whether the intensity is high enough at its original orientation. Above the intensity at which all the molecules ionize, the angular distribution just has an increasing uniform background (Fig.5.2a). The width of the angular distribution (calculated using eq.5.8) increases from $\sim 84^0$ at an intensity of $9 \times 10^{12} Wcm^{-2}$ (the lowest intensity where molecules at 90^0 to the polarization axis can be ionized) to $\sim 130^0$ above $10^{14} Wcm^{-2}$.

The width of the angular distributions for each charge channel decreases with the charge of the channel (Fig.5.2b). In Fig.5.2b the number of ions in each channel has been normalized (the relative number of ions in channel 1 to 5 is 68:19:9:2:1). The most highly charged ions are peaked along the laser polarization axis, where the threshold intensity for these charge states is lower. The lowest charge channels have distributions that are lower along the laser polarization axis, where the ions have been ionized to higher charge states. (Due to the large numbers of ions in the (0, 1) and (1,1) channels produced in the low-intensity regions of the focus in Fig.5.2b, the angular distributions of these channels are only very slightly depleted at the centre). The intermediate charge states have angular distributions peaked at intermediate angles as those molecules at large angles are in lower charge states, and those at small angles have been ionized

to higher charge states. Experimental measurements (see Chapter 4) have also shown that, with $80fs$ pulses, the angular distribution for low charge channels has a minimum along the polarization axis, indicating depletion due to ionization to higher charge channels, but the highest charge states are peaked along the polarization axis.

Although the angular distribution summed over all ions is independent of pulse-length if geometric alignment alone occurs, the angular distributions and branching ratios of individual channels can change with pulse-length (as do the kinetic energies of the ions [85]). The highest charge states are observed at intermediate pulse durations of a few hundred femtoseconds. For these pulse durations, the molecule reaches the critical internuclear distance ($\sim 10au$ for iodine) near the peak of the laser pulse so enhanced ionization occurs.

5.3.2 Ion trajectories with dynamic alignment

When the dynamic rotation of the molecules by the laser field is included in the calculation, the length of the laser pulse has a major influence on the degree of alignment. Calculated trajectories for ions with a range of initial angles irradiated by a $500fs$ or $5ps$ pulse with the same energy are shown in Fig.5.3. With the $500fs$ pulse (Fig.5.3a), the molecules are rotated slightly towards the polarization axis by the laser field early in the laser pulse. However, the molecules ionize and start to dissociate $\sim 500fs$ before the peak of the laser pulse and, at this point, the angular velocity drops rapidly to zero due to conservation of angular momentum (eq.5.2). When the molecules are irradiated by the lower intensity $5ps$ pulse, dissociation does not occur until $\simeq 1.8ps$. By this time, most molecules have had time to cross the laser polarization axis and the final angles are distributed close to this axis.

The angular distributions obtained with short pulses ($\lesssim 100fs$) are similar to those obtained from geometric alignment alone (compare Fig.5.4a with Fig.5.2b). As the pulse-length increases, the distributions narrow, first to sharp peaks with a shoulder (Fig.5.4b) and then the size of the shoulder decreases (Fig.5.4c). Two contradictory factors affect the relative widths of the charge channels. Firstly, the highest charge-state produced tends to be closely aligned due to geometric effects because the highly charged ions are produced close to the polarization axis. (See, for example, the (2, 2) channel in Fig.5.4b.) Secondly, low charge states tend to have narrow angular distributions when dynamic alignment dominates because (as it is explained in the following section) ions from the low intensity regions of the focus align more. In Figs.5.4a,b and c the number of ions in each channel has been normalized (the relative number of ions is : (a) 57:16:8:2:1 channel 1 to 5, (b) 42:41:35:1 channel 1 to 4, (c) 15:2:1 channel 1 to 3).

Experimentally, we observed that the angular distributions change from short to long pulses in qualitatively the same way as described here. With the shortest pulses used ($80fs$), the angular distributions were broad (FWHM of 90°to 120°) and the maximum was away from 0°due to depletion of ions to higher charge states (Fig.4.1). With $\sim 3ps$ laser pulses, the angular distribution was sharply peaked along the laser polarisation axis with FWHM of 10°to 40°, and no ions were present perpendicular to

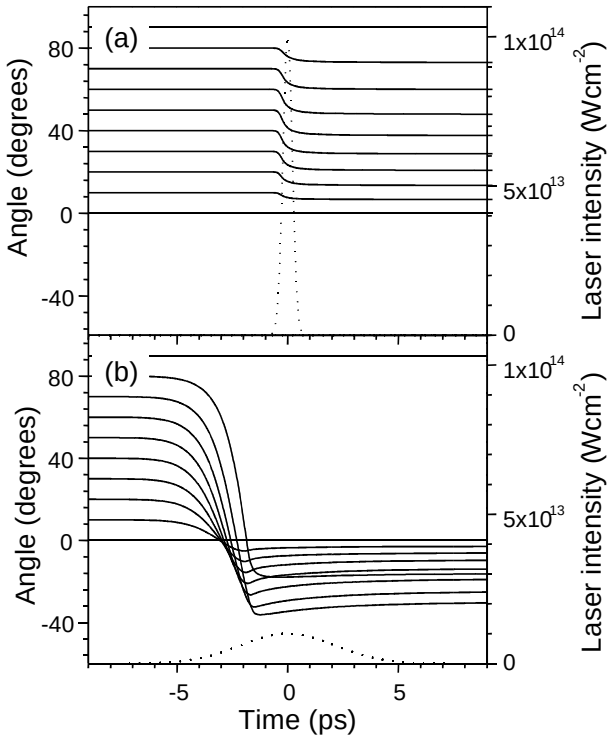

Figure 5.3: *Calculated trajectories for ions with a range of initial angles for, (a), a* $500fs$ *pulse with a peak intensity of* $1 \times 10^{14} Wcm^{-2}$ *and, (b), a* $5ps$ *pulse with peak intensity* $1 \times 10^{13} Wcm^{-2}$*. The dotted curves show the intensity of the laser pulse.*

the laser polarisation (Fig.4.5).

5.3.3 Intensity scaling

The behavior of the width of the angular distribution with increasing intensity is complicated by several competing effects. For a given angle, the initial amount of rotation increases with increasing intensity because the angular acceleration is proportional to the square of the electric field ($\frac{d^2\theta}{dt^2} = E^2$). However, molecules that experience higher laser intensities dissociate earlier on in the pulse. With the Gaussian laser pulses used in these calculations molecules that experience higher intensities can end up less aligned. Fig.5.5 shows the final angles of molecules with initial angles of 20^0, 40^0, 60^0 and 80^0 as a function of laser intensity. The molecules irradiated with the lowest intensity laser pulses undergo the most rotation.

When geometric alignment alone is considered, the width of the angular distribution for all ions increases with laser intensity. The intensity dependence is the same for all

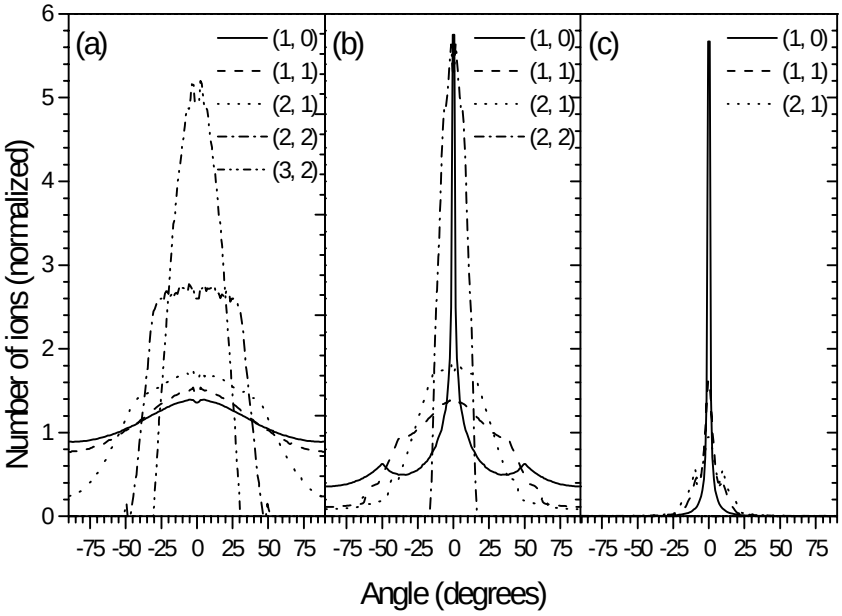

Figure 5.4: *Angular distributions of ions in each charge channel with both geometric and dynamic alignment. In (a) the laser pulse is* $100fs$ *long, in (b) it is* $1ps$ *and in (c)* $3ps$*. In each case, the peak laser intensity is* $1.25 \times 10^{14} Wcm^{-2}$*. The number of ions in each channel has been normalized.*

pulse-durations as whether or not a molecule reaches the first ionization stage depends only on the angle it makes with the laser polarization axis and the peak intensity it experiences. When dynamic alignment is included in the model, the intensity dependence is different for different pulse durations, as shown in Fig.5.6. For short ($\sim 100fs$) pulses, the intensity dependence is close to that for geometric alignment alone, showing that selective dissociative ionization dominates over dynamic alignment. For longer pulses ($\sim 5ps$), dynamic alignment dominates and the angular distribution is much narrower and varies less with laser intensity. In this case, the majority of alignment occurs before the molecule starts to dissociate. As the laser intensity is increased, the dissociative ionization threshold moves earlier and earlier in the laser pulse so that the net amount of alignment does not necessarily increase.

We have observed these trends experimentally as shown in Fig.4.6 (Chapter4). We observe that for intensities above $\sim 6 \times 10^{13} Wcm^{-2}$ the width of the angular distribution increases with intensity because, through the mechanism outlined above, the dynamic alignment decreases and the alignment is dominated by geometric effects. This effect was also seen by Posthumus and co-workers, who observed an increase in FWHM with increasing intensity for iodine molecules irradiated with $50fs$ laser pulses at intensities between 10^{13} and $10^{15} Wcm^{-2}$ [12], consistent with geometric alignment. For longer pulses, we observed progressively narrower angular distributions and the an-

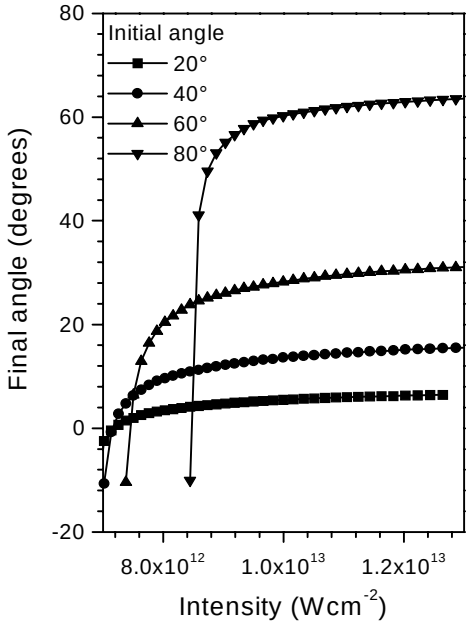

Figure 5.5: *Final angles reached by molecules with initial angles of 20^0 (squares), 40^0 (circles), 60^0 (up triangles) and 80^0 (down triangles) as a function of laser intensity. For each data point plotted, the laser pulse was $1500fs$ long and the charge channel reached was (0, 1).*

gular distributions vary less with laser intensity, in qualitative agreement with Fig.5.6. At a fixed intensity, the width of the angular distribution decreases with increasing pulse duration, indicating that dynamic alignment occurs. For example, with a fixed intensity of $2.65 \times 10^{13} Wcm^{-2}$, the FWHM of the angular distribution of the $I^+ - I^+$ channel decreases from 54.3 ± 0.9^0 with $3ps$ pulses to 25.2 ± 0.8^0 with $1ps$ pulses.

Experimentally, we observed a decrease in FWHM with intensity for intensities below $\sim 3 \times 10^{13} Wcm^{-2}$ (Chapter4), which is not reproduced by the calculations. This is because, under these conditions, we are below the threshold intensity for over-the-barrier field ionization and are no longer in the regime treated by this model. At these lower intensities, dynamic alignment dominates and the increase in alignment with intensity reflects the increased alignment forces when the intensity is increased. In nanosecond-pump femtosecond-probe experiments (e.g. ref [83]), the degree of alignment increases with the intensity of the nanosecond laser pulse, so long as it remains below the ionization threshold.

5.3.4 Variation with pulse duration

Fig.5.7 shows the FWHM of the angular distribution with pulse-length at constant pulse energy (or fluence) for the total ion signal (Fig.5.7a) and for each individual

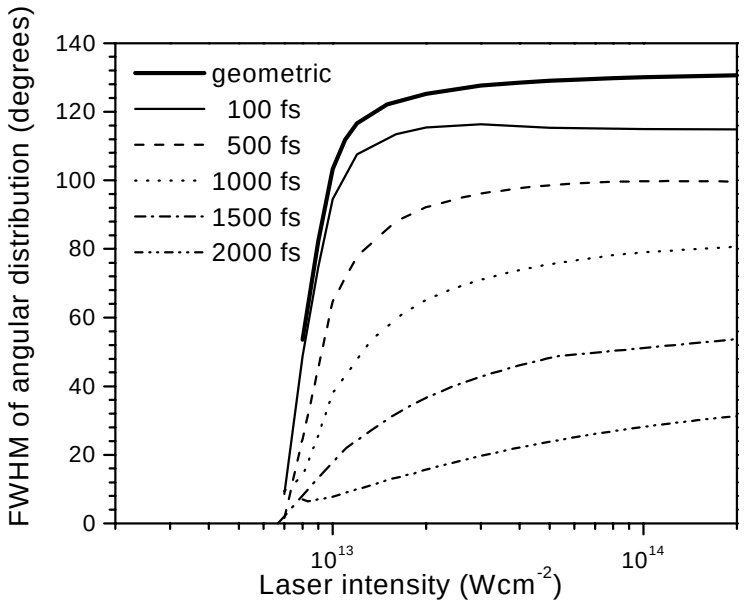

Figure 5.6: *The FWHM of the angular distribution of all ions plotted as a function of the laser intensity for geometric alignment alone (thick solid line) and including dynamic alignment for* $100fs$, $500fs$, $1ps$, $1.5ps$ *and* $2ps$ *pulses.*

dissociative ionization channel (Fig.5.7b). When dynamic alignment is included, the angular distributions narrow with increasing pulse-length, reaching a minimum width of $\sim 10^0$ at a pulse-length of $3ps$ before broadening and then narrowing again. The broadening of the angular distributions beyond an optimum pulse-length has been also observed experimentally (see Chapter 4, Fig.4.7a and b). The initial narrowing of the angular distributions as the pulse-length increases is due to the ionization threshold being reached closer to the peak of the laser pulse. As the pulse-length increases beyond the optimum, the molecules rotate too much and overshoot the internuclear axis (as in Fig.5.3b) before being ionized. This results in a broadening of the angular distribution. If the pulse-length is increased still further, the angular distribution will narrow again as the molecules oscillate and return to the internuclear axis before ionization. The optimum pulse-length is longer for higher energy pulses because the ionization point occurs earlier in the laser pulse. This means that longer pulses are required to give the molecule time to rotate to the laser polarization axis before the intensity rises past the ionization threshold.

Fig.5.7b shows that the highest charge channel produced at a given pulse length tends to be the most strongly aligned. This is because more aligned molecules reach higher charge states due to the lowered ionization thresholds for molecules oriented close to the laser polarization axis.

With geometric alignment alone, the width of the angular distribution for all ions is

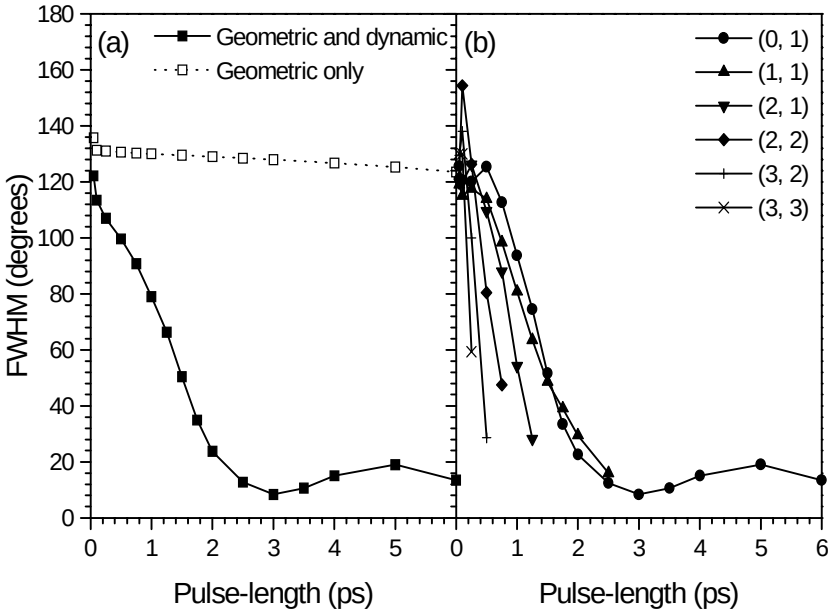

Figure 5.7: *FWHM with pulse duration at fixed fluence of* $100 Jcm^{-2}$. *(a) For all ions at fluences of* $100 Jcm^{-2}$ *with both geometric and dynamic alignment (solid lines, filled squares) and with geometric alignment alone (dotted lines, open squares). (b) For each charge channel from (0, 1) to (3, 3).*

independent of pulse-length at constant intensity. At a constant fluence of $100 Jcm^{-2}$, the width of the distribution decreases from $\sim 135^0$ to $\sim 130^0$ as the pulse length is increased from $50 fs$ to $6ps$, due to the drop in intensity. If the angular distributions of the individual charge channels are analyzed, we find that the highest charge channels narrow as the pulse-length increases (as the intensity drops, these high charge states can only be produced close to the internuclear axis). In this case, the low charge channels will be depleted about the polarization axis (as described in section 5.3.1).

The results of our numerical calculations are compared with those measured experimentally in Fig.4.10 (Chapter4). The experimental results show good agreement with the calculations and confirm that dynamic alignment narrows the angular distributions for pulses longer than $\sim 500 fs$. In particular, we experimentally observe a decrease in FWHM with increasing pulse duration for pulse lengths below $3ps$, followed by a broadening of the angular distribution as the pulse-length increases. We also observe that higher charge channels are more tightly aligned at a given pulse duration, in agreement with our calculations.

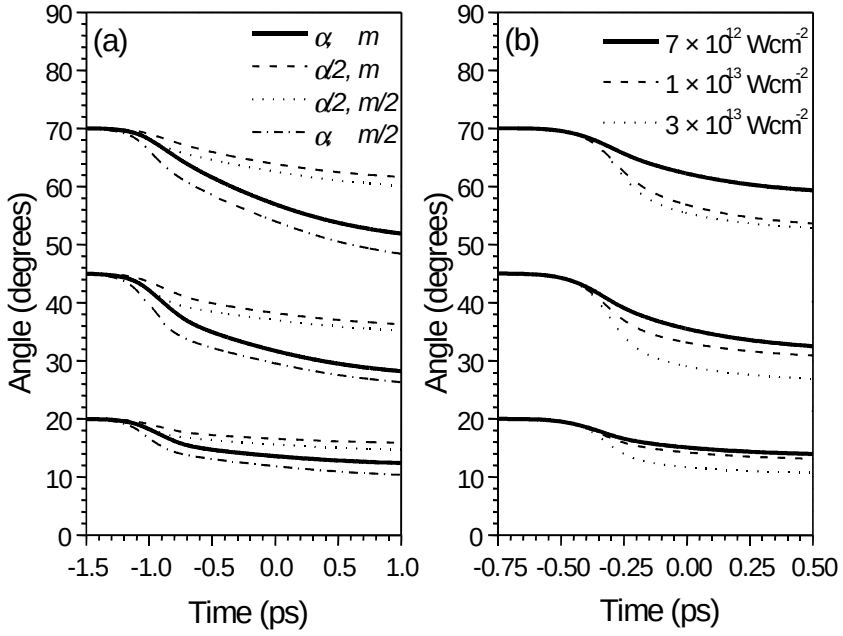

Figure 5.8: *Trajectories for ions with 3 different initial angles (20^0, 45^0 and 70^0) for $500fs$ laser pulses with a peak intensity of $2 \times 10^{14} Wcm^{-2}$. (a) Mass or polarizability changed. Thick solid lines: iodine ions ($\alpha = \alpha_{iodine} = 45.146au$, $m = m_{iodine} = 126.9$). Dashed lines: $\alpha = \alpha_{iodine}/2$. Dash-dotted lines: $m = m_{iodine}/2$. Dotted lines: $\alpha = \alpha_{iodine}/2$, $m = m_{iodine}/2$. (b) Trajectories with 3 different threshold intensities: 7×10^{12}, 1×10^{13} and $3 \times 10^{13} Wcm^{-2}$.*

5.3.5 Effect of changing molecular parameters

In order to understand how the molecular parameters affect the rate at which a molecule aligns, we have examined the effect of changing the polarizability, mass and dissociative ionization threshold (Fig.5.8a). Decreasing α_{eff} simply reduces the angular acceleration, with the obvious result that the ions are less aligned. Decreasing both the mass and α_{eff} but keeping their ratio the same means that the first term in eq.5.2 remains the same as it depends on $\alpha_{eff}/mass$. Therefore, before dissociation, the molecules with the same $\alpha_{eff}/mass$ ratio follow the same path. However, once the molecule is ionized, the one with the lower mass will dissociate more rapidly leading to a more abrupt end to its rotation and less alignment. A molecule with low mass but high α_{eff} experiences the strongest alignment as the rotation of the undissociated ion is more rapid, even though the deceleration due to the Coulomb explosion is also faster.

The intensity at which a molecule ionizes and begins to dissociate is an important factor in determining the amount of alignment. The effect of reducing the threshold intensity at which the ions begin to dissociate is to reduce the amount of alignment (Fig.5.8b). Rotation slows once the molecule begins to dissociate, and so a molecule

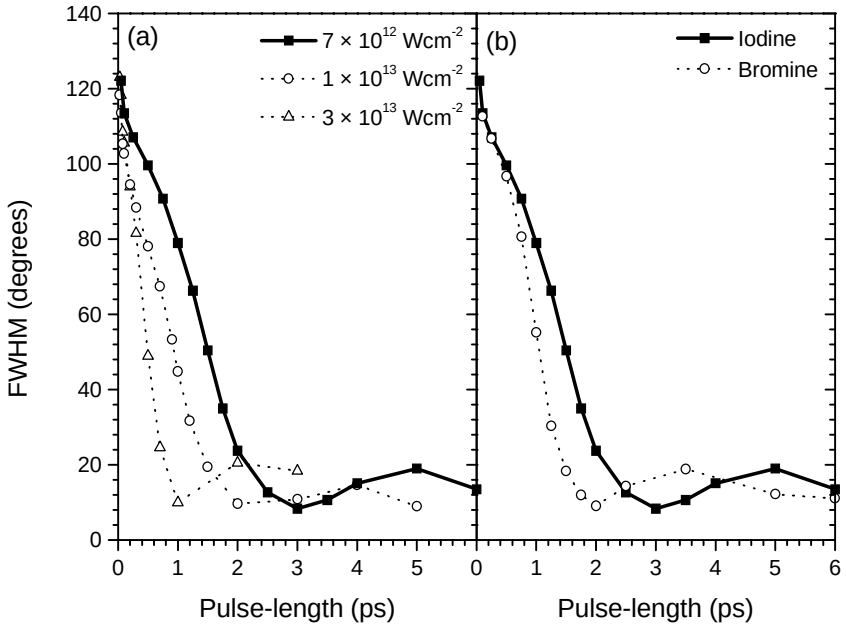

Figure 5.9: *(a) FWHM with pulse duration for 3 different threshold intensities:* 7×10^{12}, 1×10^{13} *and* $3 \times 10^{13} Wcm^{-2}$*.(b) FWHM of distribution as a function of pulse-length for iodine (solid line, filled squares) and bromine (dotted line, open circles). The threshold intensity here is* $7 \times 10^{12} Wcm^{-2}$ *for iodine and* $1.1 \times 10^{13} Wcm^{-2}$ *for bromine. In both (a) and (b) the product of the pulse-length and intensity is kept constant at* $100 Jcm^{-2}$.

that dissociates earlier in the laser pulse will have experienced less rotation. We find that the optimum pulse-length for alignment is longer for a lower threshold (Fig.5.9a). For example, for pulses with a constant flux of $100 Jcm^{-2}$, the optimum pulse-length is $1ps$ for a threshold intensity of $3 \times 10^{13} Wcm^{-2}$. If the threshold intensity is dropped to $1 \times 10^{13} Wcm^{-2}$, the optimum pulse-length increases to $2ps$ and with a threshold of $7 \times 10^{12} Wcm^{-2}$, the optimum pulse-length is $3ps$.

	Iodine	**Bromine**
α, au	45.146 [104]	28.33 [105]
Mass, m	126.9	79.904
Internuclear separation, au	5.04	4.31
Molecular IP, eV	9.31	10.54
Threshold intensity at 0°, Wcm^{-2}(eq.5.3)	6.9 × 1012	1.15 × 1013
Threshold intensity at 90°, Wcm^{-2} (eq.5.3)	9.0 × 1012	1.48 × 1013

Table 1. *Comparison of molecular parameters for* I_2 *and* Br_2.

From these arguments, molecules that align most strongly will have (a) a high α/mr^2 ratio and in order to maximize the amount of alignment of the neutral molecule (b) a high ionization potential (as most alignment occurs before the molecule ionizes and begins to dissociate).

Table 1 compares the properties of I_2 and Br_2. The bromine molecule has a higher ionization potential and α/mr^2, but a lower mass. We have compared the degree of alignment observed in Br_2 to that in I_2 and find that bromine aligns much faster, with the optimum pulse-length being $2ps$ for Br_2 compared to $3ps$ for I_2 (Fig.5.9b). This is in agreement with the experimental measurements shown in Fig.4.10 (Chapter 4).This suggests that the higher α/mr^2 and ionization potential are more important than the mass. While the mass affects the degree of alignment after dissociation, the other two factors affect how the un-dissociated molecule aligns.

5.3.6 Change in polarizability on dissociation

We assume in our model that the value of the effective polarizability remains constant throughout the interaction. It is obvious that this is an approximation for several reasons. First, the values of $\alpha_{\parallel}$ [108] and α_{eff} [105] increase with elongation of the molecule. For example, for Bromine $\alpha_{eff} = 28.33$ at the equilibrium distance of $4.31au$ and 30.90 at just $4.40au$ [105]. This is an increase of nearly 10% for a 2% increase in bond length. Second, α_{eff} decreases with increasing charge and can even become negative in some states [13]. Third, α_{eff} differs from the zero-field value even in the ground state in intense fields [109] and, finally, the electron localization that occurs at the critical internuclear distance must reduce the polarizability [13].

To estimate the degree of the error introduced by this approximation, we have performed some calculations where α_{eff} is set to zero immediately upon ionization (Fig.5.10). The effect of this is to bring the angular velocity more rapidly back to zero when the molecule starts to dissociate. We find that, averaged over the focal volume distribution, the effect of this is to increase the width of the angular distribution by $\sim 20^0$ for short ($< 1ps$) pulses and $\sim 5^0$ for long ($> 2ps$) pulses. This means that, in this model, at short pulse-length a significant fraction of the rotation takes place while the molecule is dissociating. However, for longer pulses more rotation occurs before dissociation, so the fraction of rotation that occurs during dissociation is smaller.

5.4 Discussion. Geometric versus dynamic alignment

Several experiments [12, 14] have used the intensity scaling of the angular distribution to attempt to distinguish between dynamic and geometric alignment. For geometric alignment (angle-dependent ionization), the FWHM and the number of ions perpendicular to the laser polarization will increase with intensity as molecules progressively closer to 90^0 to the laser polarization become able to dissociate. The signature of

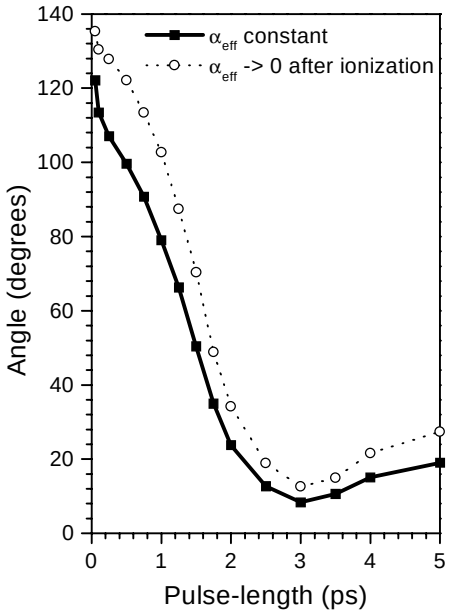

Figure 5.10: *FWHM of angular distribution as a function of pulse-length for all dissociated ions. The molecule is iodine and the fluence is* $100 Jcm^{-2}$. *Solid line with filled squares:* α_{eff} *constant throughout. Dotted line with circles:* α_{eff} *set to zero immediately upon dissociation.*

dynamic alignment (rotation of the molecules) was predicted [12, 14] to be a decrease in the FWHM of the distribution with increasing intensity, as the acceleration of the molecules is proportional to the square of the electric field. A lack of fragments perpendicular to the laser polarization at all intensities was also predicted.

We find, however, that dynamic alignment can also result in an angular distribution that broadens as the intensity increases, because the majority of alignment takes place on the leading edge of the pulse before the molecule dissociates. As the intensity increases, the energy in the leading edge of the pulse below the dissociation threshold actually decreases for a Gaussian pulse. Our calculations suggest that to distinguish between geometric and dynamic alignment it is necessary to vary the pulse-length. The cleanest test is to measure the angular distribution of all ions as a function of pulse-length, keeping the intensity constant. If geometric alignment alone takes place the angular distribution summed over all fragment charge states will be independent of pulse-length, within the over-the-barrier ionization model. However, if dynamic alignment takes place the angular distribution will narrow as the pulse-length increases.

5.5 Conclusions

We have calculated the angular distributions of the ions produced by multi-electron dissociative ionization of iodine and bromine molecules, using a two-dimensional field-ionization Coulomb explosion model including dynamic rotation of the molecule in the laser field. We have investigated the dependence of the degree of alignment on laser intensity and pulse-length, as well as on molecular parameters such as mass, polarizability and dissociative ionization threshold intensity.

We find that the majority of dynamic alignment occurs on leading edge of the laser pulse at low intensities before the laser intensity reaches the dissociative ionization threshold. This makes the degree of alignment sensitive to the value of the dissociative ionization threshold, with the optimum pulse-length for alignment being longer for a lower ionization threshold.

With short pulses ($< 100fs$), the anisotropy of the fragment ions is primarily due to selective dissociative ionization of molecules aligned close to the polarization axis (geometric alignment). For pulses longer than $\sim 1ps$, the observed angular distributions are dominated by dynamic rotation of the molecules. Angular distributions as narrow as 10^0 FWHM can be achieved with long pulses.

Depletion close to the polarization axis of the angular distributions of the lowest charge channels produced is an indication that geometric alignment dominates. Increased alignment of all charge channels as the pulse-length increases is an unambiguous sign that the molecules are forced into alignment with laser field.

Building on the understanding gained from the calculations presented in this chapter and the experimental results shown in the previous chapter, we have performed a two-pulse pump-probe experiment in which we have been able to monitor the dynamics of the alignment process during and after the pump laser pulse excitation as a function of a number of parameters (pump pulse duration and energy, molecular beam temperature, etc.). In the time-evolution of the molecular macroscopic ensemble the occurrence of revivals were observed, where the angular distribution of the molecule is suddenly narrowed or broadened during a short time interval. These results are presented in the next chapter.

Part 3

Pump-probe experiments.

Chapter 6

Time resolved alignment of diatomic molecules: IR-IR pump-probe experiments

In this chapter we report the experimental observation of revival structures in the alignment of a ground state rotational wavepacket following non-resonant excitation of I_2 molecules by an intense picosecond laser pulse. In the experiment, angular distributions were probed using Coulomb explosion of the molecules by an intense femtosecond infrared laser pulse. Revivals appear at characteristic time delays following the excitation by the pump laser pulse, and show a significant narrowing of the angular distribution with respect to the pump laser polarization axis during a few picoseconds. The interaction of the pump laser with the molecule also leads to a steady-state alignment of the molecule, due to rotational pumping.

This chapter is divided in four sections. The first section gives an overview of experimental and theoretical investigations related to the work presented in this chapter. Theoretical considerations are presented in the second section. The experimental setup is described in the third section. In the next section results and discussions are presented.

6.1 Introduction

In the last few years there has been an increasing awareness that intense femtosecond lasers provide unique inroads towards controlling the properties of matter on a microscopic level. A new field of 'molecular optics' is emerging, where intense lasers are used to control and/or manipulate the internal and external degrees of freedom of molecules [110]. Intense femtosecond lasers have been used to deflect beams of molecules [111], to control molecular dynamics [112] and to dissociate molecules in an 'optical centrifuge' [113]. Considerable attention has been devoted to the ability of intense laser fields to align molecules (dynamic alignment). The role of dynamic

alignment in multi-electron dissociative ionization (MEDI) has been considered [12] and the formation of pendular states in the presence of a strong laser field has been firmly established [80,84,114]. Recently Stapelfeldt *et.al.* demonstrated the possibility to align a molecule in three dimensions using a judicious choice of experimental conditions [102]. There have been a number of theoretical contributions in the literature concerning the possibility of aligning molecules under field-free conditions, by waiting an appropriate amount of time following the excitation of a molecule by a short laser pulse. Seideman [95] and Friedrich and co-workers [82] performed calculations illustrating that the interaction of a molecule with an intense laser pulse can lead to the formation of a ground state rotational wavepacket, whose subsequent time evolution involves the formation of aligned molecular states at well-defined time delays with respect to the pump laser pulse, given by the rotational structure of the molecule.

This chapter presents what is, to our knowledge, the first experimental observation of this behavior. Building on results which we have obtained for MEDI of I_2 (see Chapters 4 and 5) [91,100], we present experiments where a picosecond infrared pump laser is used to form a rotational wavepacket in the ground electronic state of I_2, and where the angular distribution of the molecules with respect to the polarization axis of the pump laser is monitored as a function of time using a femtosecond infrared probe laser pulse, which induces a Coulomb explosion of the molecules. The recoil velocity of the charged fragments in the Coulomb explosion is determined using a velocity map ion imaging detector [64,115] (see Chapter 3). We observe revival structures in the angular distributions which are reminiscent of the revival structures observed in a number of other rotational coherence spectroscopies [116, 117]. However, whereas in these other experiments the signal consists of time-dependent photon emission/scattering and/or time-dependent molecular ionization, the measured signal in the present experiment is the time-dependent angular distribution of the molecules. Moreover, previous rotational coherence experiments were performed under conditions where the interaction of the laser(s) with the molecule can be described by perturbation theory, whereas the present experiment relies on a strongly non-perturbative interaction of the pump laser with the molecule. As a result, unlike the afore-mentioned experiments (where the rotational coherence signal is derived from a small subset of molecules in the molecular beam), our experiment leads to the formation of a macroscopic sample of aligned molecules. The formation of a macroscopic sample of aligned molecules has important implications for the utility of the current technique. Aligned molecules prepared in this fashion can be used in a range of important applications, such as studies of photoelectron angular distributions, where the measurements are no longer limited to a determination of the β-parameter (involving averaging over all possible molecular alignments in the laboratory frame), but where the angular distributions can be studied directly in the molecular frame [118].

6.2 Theoretical considerations

As mentioned above, the experiments described in this chapter are based on earlier results presented in Chapter 4 and 5. The conclusions of these measurements and calculations were that the angular distribution of fragments resulting from the Coulomb explosion of I_2 and Br_2 by an intense femtosecond laser strongly depends on the laser pulse duration. For short pulses ($< 1psec$) the fragments have a wide angular distribution given mostly by geometric alignment (= alignment due to the dependence of the ionization rate on the angle between the molecular axis and the laser polarization axis), while for longer pulses the process that dominates is dynamic alignment (= alignment due to the laser-induced reorientation of molecules prior to and/or during the dissociative ionization). Therefore, for heavy molecules like I_2 and Br_2, short laser pulses do not align molecules, while long laser pulses pull the molecules along the laser polarization axis. To have a better understanding of how the alignment process takes place and to study the dynamic alignment without the simultaneous occurrence of the geometric alignment, we have set up a pump-probe experiment. Here, the pump laser consisted of a long infrared pulse which is used to align molecules along its polarization axis and for which the intensity is attenuated in order not to ionize the molecules. The probe laser consisted of a short infrared pulse which, as shown above, does not align molecules and is used to probe the effect of the pump laser at different time delays with respect to the excitation induced by the pump laser. Results of this pump-probe experiment are presented in section 6.4.

The alignment induced by a long infrared pulse is due to the laser-induced dipole moment which pulls the molecules along the polarization axis. This rotational motion induced by the laser can be explained in terms of rotational redistribution of the population in the sample of molecules. The way in which the rotational distribution influences the angular distribution of a molecule is explained below.

The angular distribution P($\cos\theta$) can be calculated by integrating the square modulus of the wavefunction of a molecule Ψ over the two Euler angles χ and ϕ ([119]):

$$P(\cos\theta, t) = \int_0^{2\pi}\int_0^{2\pi} \Psi^*(t)\Psi(t) d\chi d\phi \tag{6.1}$$

For several rotational eigenstates with rotational quantum number J and projection on the laser polarization axis M, the angular distributions are presented in Fig.6.1. For $J = 0$ the angular distribution is isotropic. For $J > 1$ and $M = 0$, J is perpendicular to the polarization axis which means that the molecule rotates in a plane that contains the polarization axis. For $J > 1$ and $M = J$, J lies along the polarization axis, so the molecule rotates in a plane perpendicular to the polarization axis. Therefore, for $J = 1$ the angular distribution is aligned along ($M = 0$) or perpendicular ($M = \pm 1$) to the laser polarization axis, while for larger J the angular distribution peaks along the laser polarization axis if $J >> M$. For a statistical M-distribution the average angular distribution for a given J consists of a summation of distributions like the ones presented in Fig.6.1 and therefore no net alignment is observed. Therefore also, when

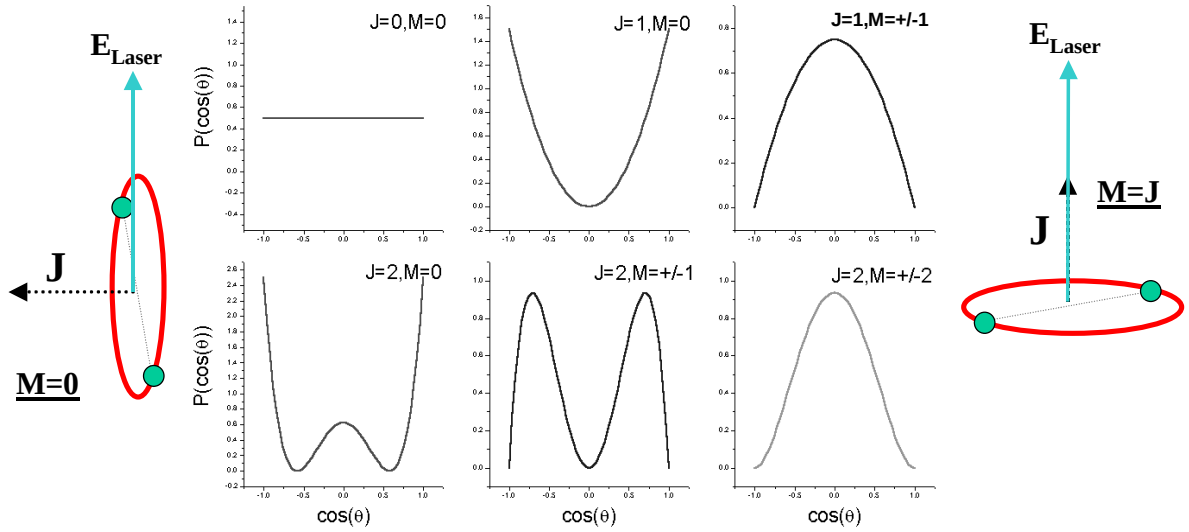

Figure 6.1: *The angular distribution for different rotational quantum number J and different value of the projection M on the laser polarization axis.*

averaging over the rotational temperature (all J), no alignment is observed.

When the sample of molecules interacts with an intense laser pulse a wavepacket is formed. This wavepacket consists of a coherent superposition of rotational states and is formed via Raman transitions by upward and downward transitions between the ground state and an electronically excited state (Fig.6.2). Since the excited state is far off-resonant, no population accumulates in the excited state.

The experiment simultaneously measures the alignment starting from all rotational levels ($J_{initial}$, $M_{initial}$) which are initially populated in the molecular beam. Since $\Delta M = 0$ for an excitation with linearly polarized light, the M-distribution is conserved in this excitation process. Since $M \leqslant J$, there is a maximum number of levels with $J < J_{initial}$ that can couple to the initial state, whereas for $J > J_{initial}$ no such restrictions exist. As a result, the pump laser interaction will form wavepackets where the expectation value of J is typically larger than M. In other words, the rotational angular momentum tends to align in a plane perpendicular to the laser polarization axis. Since the rotational angular momentum is perpendicular to the internuclear axis in a diatomic molecule, the rotation of the molecule tends to include the laser polarization axis, which shows up as preferential alignment along the laser polarization axis compared to an isotropic distribution.

The individual states that form the wavepacket evolve independently of each other. They dephase with respect to each other as a function of time and at later times rephase again. The rephasing at a later time is called a revival and corresponds to a situation where the angular distribution is again preferentially parallel to the laser polarization

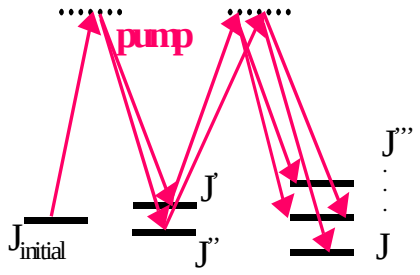

Figure 6.2: *The formation of a coherent superposition of states by Raman excitation (rotational wavepacket). The projection of the rotational quantum number, M, is conserved while the rotational quantum number J is shifted, leading to a distribution with J>>M.*

axis or perpendicular to it. Around a revival time, the phase factors of all component wavefunctions in the wavepacket have advanced by the same amount modulo 2π, and therefore the wavefunction near the end of the pump laser interaction is restored. From the level structure of a rotational ladder - $E = BJ(J+1)$ - it follows that the phase difference between two component wavefunctions in the wavepacket which differ by N rotational quanta is equal to:

$$\Delta\phi(J+N,J) = 2\pi cBt[(J+N)(J+N+1) - J(J+1)] = 2\pi cBt[2NJ + N + N^2] \tag{6.2}$$

where B is the rotational constant of the molecule and c is the speed of light.

Since the expression in brackets is even for all combinations (N,J) it follows that a full revival of the wavepacket takes places whenever:

$$2\pi cBT_{rev} = \pi \tag{6.3}$$

leading to the well-known result $T_{rev} = 1/2Bc$. As an example the revival time for the I_2 molecule is 450 picoseconds ($B = 0.037cm - 1$).

Halfway towards the revival, at $T_{rev}/2 = 1/4Bc$ the phase difference between two component wavefunctions in the wavepacket is given by:

$$\Delta\phi(J+N,J) = (\pi/2)[2NJ + N + N^2] \tag{6.4}$$

For N=2, 6, 10,..., this phase function is an odd multiple of π, whereas for N=4, 8, 12, it is an even multiple of π. If N=2 is the dominant contribution the wavepacket at the half revival $T_{rev}/2 = 1/4Bc$ is 180^0 out of phase with the wavepacket at the full revival $T_{rev} = 1/2Bc$. In addition to the full and half revivals, one may expect revival structures to be observed at multiples of $T_{rev}/4$ and $T_{rev}/6$. The time evolution of the wavepacket and the observation of revival structures are investigated in the present experiment and results and discussions are presented in section 6.4.

In the literature ([114]) there have been a number of papers on the formation of so-called pendular states when a molecules is exposed to an intense laser field. In the presence of a strong field the appropriate eigenfunctions are eigenfuctions of the combined molecule and laser field Hamiltonian. These eigenfunctions can have strongly anisotropic angular distributions. The implication of this formalism in the alignment of molecules will be explained in section 6.4.

6.3 Experimental setup

In the experiment, the output from the $50Hz$ Ti:Sa femtosecond laser amplifier described in Chapter 2 was split and compressed in two dual grating compressors (see Fig.6.3). One beam, containing 30 % of the energy, was compressed to a $100fsec$ pulse, and was used to probe the alignment via MEDI. The second beam, containing 70% of the pulse energy, was compressed to pulse durations of $1-10psec$, and was used as pump laser to align the molecules. After variable attenuation and a variable delay of the pump laser beam using a motorized delay stage, both beams were recombined on a beamsplitter (R=30%/T=70% for p-polarization, R=50%/T=50% for s-polarization, R=reflection, T=transmission), and were focussed collinearly into the molecular beam apparatus described in Chapter 3, using a $20cm$ focal length lens. A telescope was used to reduce the spotsize of the pump laser beam on the lens, to ensure that the probe laser focus was smaller than the pump laser focus. A molecular beam was formed by passing Ne gas over an I_2 sample and expanding the mixture through a $1mm$ pulsed nozzle, located $5cm$ in front of a $1.5mm$ skimmer separating the source and experimental chambers (see Chapter 4, Fig.3.2). The lasers and the molecular beams were crossed at the center of the velocity map imaging detector (see Chapter 3), which was mounted orthogonal to the plane defined by the lasers and the molecular beam, and which was used to project charged fragments onto a gated dual microchannel plate (MCP) assembly, enabling detection of individual charge states, followed by a phosphor-screen. A CCD camera was used to record the 2D distributions on the phosphor-screen. Recorded images were transferred to a lab computer, where a peak-finding routine determined the centroids of the observed spots on the phosphor-screen, and where the images were accumulated. Detection of both I^+ and I^{2+} fragments was used to monitor the time-dependent alignment.

6.4 Results and Discussion

In a pump-probe experiment one can choose to have the polarization axis of the two laser beams parallel or perpendicular to each other. As an extension of the results of Chapter 4, we first present results for a pump-probe experiment where the polarizations of the probe and the pump beams are parallel to each other in the plane of the detector (Fig.6.4). The probe is a short femtosecond infrared laser pulse ($100fsec$ pulse duration and $0.9mJ$ pulse energy) which gives an anisotropic angular distribution due

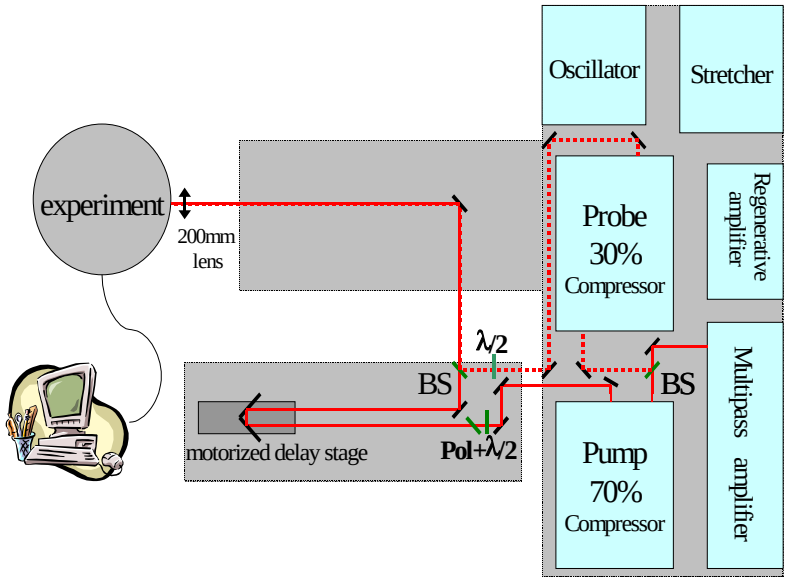

Figure 6.3: *The experimental setup used for the IR-IR pump-probe experiment.*

to geometric alignment. The pump is a long chirped infrared laser pulse ($4.2p$ sec pulse duration and $2.2mJ$ pulse energy) which is used to align the molecules along its polarization axis and has an intensity low enough that it does not ionize the I_2 molecules. Fig.6.4a shows the I^{2+}signal obtained when the probe precedes the pump. Here the observed angular distribution of the I^{2+} fragments is due to geometric alignment of the molecules induced by the probe laser. In Fig.6.4b the pump and the probe lasers are overlapped in time. There is clear evidence that the angular distribution becomes now narrower due to dynamic alignment induced by the pump laser. In Fig.6.4c and d the I^{2+}signal is obtained when the probe comes $\sim 219p$ sec and $\sim 225p$ sec after the pump laser. These times correspond to a half revival in the evolution of the wavepacket formed by the pump laser, which was described earlier. Clearly, even at long times after the pump laser interaction rapid changes in the angular distribution still occur in the angular distribution. More details about the time dependence of the angular distribution are presented below.

In Fig.6.5 the polarization of the pump laser pulse is along the molecular beam axis (in the plane of the MCP detector), whereas the probe laser pulse is along the detector axis (perpendicular to the MCP detector). An advantage of this choice of polarizations is that the signal resulting from the probe laser alone has no angular dependence on the detector, whereas changes in the angular distribution as a result of the interaction with the pump laser can readily be observed. Fig.6.5a shows the I^{2+}signal obtained when the probe precedes the pump by $17p$ sec (pump pulse energy of $3.8mJ/pulse$ and pump pulse duration of $2.8p$ sec). Here the angular distribution on the detector is isotropic. In Fig.6.5b the pump and the probe lasers are overlapped in time. At this time delay

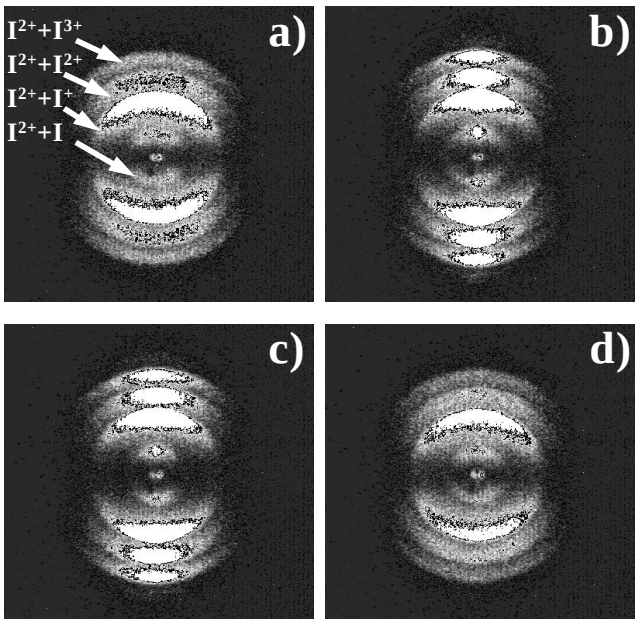

Figure 6.4: *Raw I^{2+} images, recorded with a 4.2 psec 2.2mJoule pump laser (polarized parallel to the plane of the imaging detector along the vertical axis of the image) and a 100 fsec 0.9mJ probe laser (polarized parallel to the imaging detector); a) with the probe before the pump laser, b) with the pump and probe lasers overlapped in time, c) with the pump laser preceding the probe laser by 219 psec, d) with the pump laser preceding the probe laser by 225 psec.*

the distribution peaks along the pump laser polarization (parallel to the detector) due to the alignment induced by the pump laser. In Fig.6.5c and d images recorded at long pump-probe time delays of 212 and 220$p$sec, respectively, are shown. At these long pump probe time delays rapid changes in the angular distribution of the I^{2+}signal occur due to a revival of the rotational wavepacket formed by the pump laser.

When using the perpendicular configuration one can easily optimize the spatial and temporal overlap between the pump and the probe laser. In Fig.6.6 the I^{2+} time-of-flight signal is shown. When the probe laser polarization is perpendicular to the detector the I^{2+}signal consists of two peaks: forward and backward contributions from ions flying towards and away from the detector after the MEDI (circles). When the pump and the probe lasers are spatially overlapped and the probe comes after the pump laser (any time delay $\Delta t \geqslant 0$), molecules are aligned along the polarization direction of the pump laser (parallel to the detector) and therefore the fragment ions will have a contribution in the time-of-flight in the middle, between the afore-mentioned forward and backward peaks (squares). By optimizing the amplitude of the middle peak at the expense of the outer peaks one can adjust the spatial overlap of the two lasers. By changing the time delay one can identify the temporal overlap of the pump

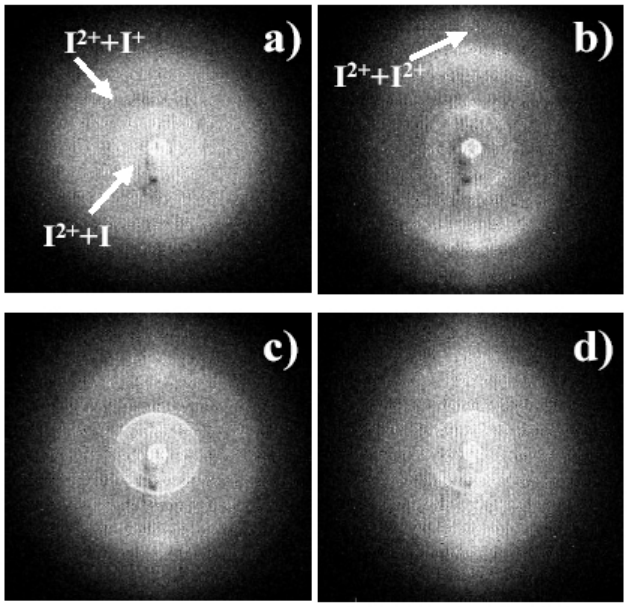

Figure 6.5: *Raw I^{2+} images, recorded with a 3.8mJ 2.8 psec pump laser (polarized parallel to the plane of the imaging detector along the vertical axis of the image) and a 100 fsec 1.2mJ probe laser (polarized perpendicular to the imaging detector); a) with the probe laser preceding the pump laser by 17 psec, b) with the pump and probe laser overlapped in time, c) with the pump laser preceding the probe laser by 212 psec, and d) with the pump laser preceding the probe laser by 220 psec. N.B. the small dark area visible in these images is due to the presence of a segment on the imaging detector where the detection efficiency has degraded due to extensive use.*

and the probe lasers, which is reached when the distribution changes from a single peak to the double peak distribution. It is important to note that throughout this procedure the pump intensity is low enough that it does not create fragment ions by itself (up triangles). The integrated signal decreases when the pump and the probe lasers are overlapped due to the fact that the efficiency for ionization decreases when the molecules are aligned parallel to the pump polarization axis and therefore perpendicular to the probe polarization axis.

Series of measurements were performed where images were recorded as a function of the time delay between the pump and probe lasers. Results of these measurements, obtained in the parallel configuration under similar conditions as the images presented in Fig.6.4 (for a pump pulse energy of $2.2mJ/pulse$ and a pump pulse duration of $4.2psec$), are shown in Fig.6.7a. In this figure the time-evolution of the angular distribution near the time-overlap of the pump and the probe laser is shown by plotting the time dependent angular distribution P(cosθ,t) corresponding to the I^{2+}- I^{2+} channel,

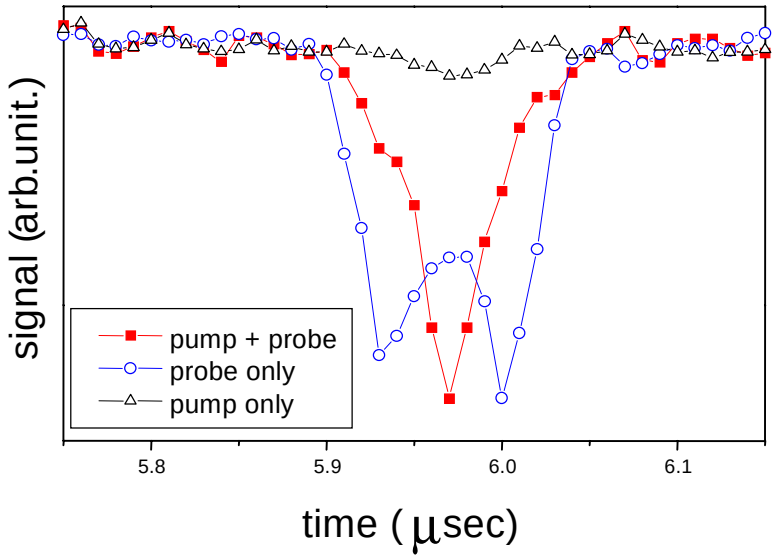

Figure 6.6: *Time-of-flight measurement of I^{2+} fragments. The shape of the peaks is used to optimize the spatial and temporal overlap between the pump and the probe lasers. The probe only signal contains two peaks corresponding to the backward and forward ejection of fragments with respect to the detector (circles). The pump laser alone gives almost no signal (up triangle). The pump + probe signal has only one contribution corresponding to molecules aligned by the pump laser in the plane of the detector (squares).*

which was obtained after using the inversion procedure presented in Chapter 3 [75]. One can observe that the angular distribution becomes narrower when the pump and the probe are overlapped and that a moderate alignment remains after the pump excitation.

To quantify the time-evolution of the angular distribution an effective angular width α of an ionization channel can be calculated, defined by the equation:

$$\int_0^{\alpha/2} P(\cos\theta, t)d\theta = \int_{\alpha/2}^{\pi/2} P(\cos\theta, t)d\theta \tag{6.5}$$

where θ is the angle with respect to the vertical axis of the image. This integral can be evaluated for the signal between a minimum and maximum radius in the image where the contribution from a particular charge combination I^{n+}- I^{m+} appears. If the angular distribution is given by a Gaussian then the angular width α is equal to 0.69 times the full-width-at-half-maximum (FWHM) of this Gaussian. For an isotropic angular distribution the angular width α is 90^0.

Based on the angular distributions shown in Fig.6.7a, the angular width α defined above can be calculated for this serie of measurements. The results are presented in

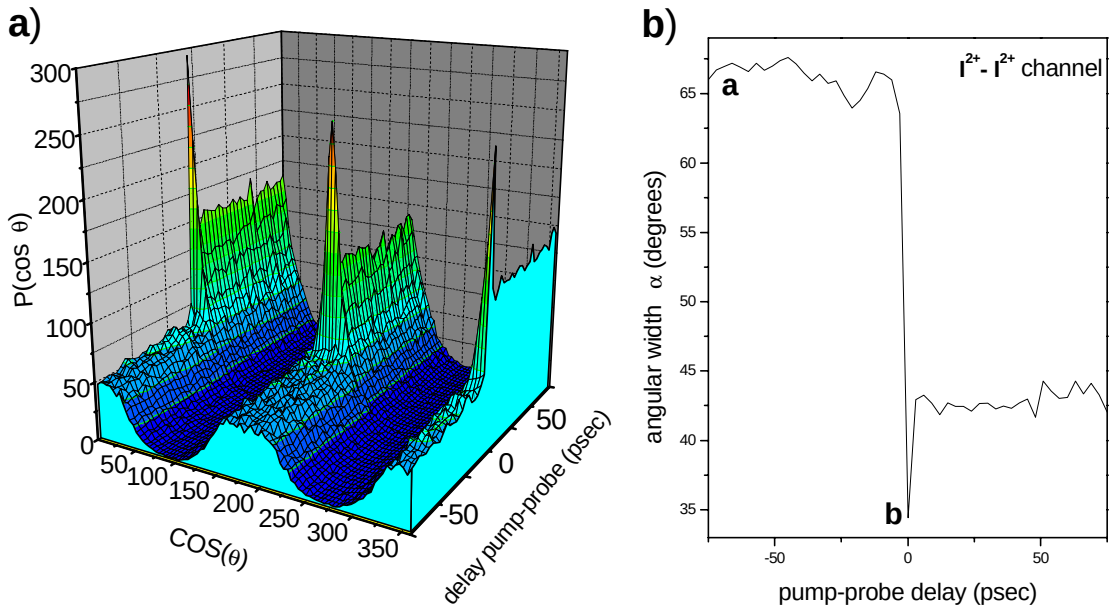

Figure 6.7: *The time-evolution of the angular distribution of the I^{2+}-I^{2+} channel is shown by plotting (a) the angular distribution or (b) the angular width α as a function of the time delay between the pump (2.2 mJ pulse energy and 4.2 psec pulse duration) and the probe (1 mJ pulse energy and 100 fsec pulse duration). The polarization of the two lasers is parallel to each other and parallel to the detector. Labels a and b given in the right graph refer to measurements shown in Fig 6.4.*

Fig.6.7b where the labels (a) and (b) refer to the measurements shown in Fig.6.4. For time delays where the probe precedes the pump the angular distribution is wide and therefore the value of α is large (67^0), while for the time overlap between the pump and the probe the angular distribution gets narrower and α is reduced by as much as 32^0. After the pump excitation, a moderate alignment is visible which is characterized by an angular width of 42^0.

Following this initial illustration of time-dependent alignment, more extensive measurements were performed in the perpendicular geometry. Results of these measurements, obtained under conditions where the pump pulse duration was $2.8psec$ and the pump laser had a pulse energy of $3.8mJ/pulse$, are shown in Fig.6.8, where the labels (a)-(d) refer to the measurements shown in Fig.6.5. In this figure the time-evolution of the angular distribution is shown by plotting the effective angular width α as a function of the pump-probe delay. Is has to be noted that in this analysis no inversion was applied to the experimental images since in this polarization geometry there is no symmetry axis in the 3D fragment velocity distribution.

The time-evolution of the angular distribution of the I^{2+} fragment, as presented in

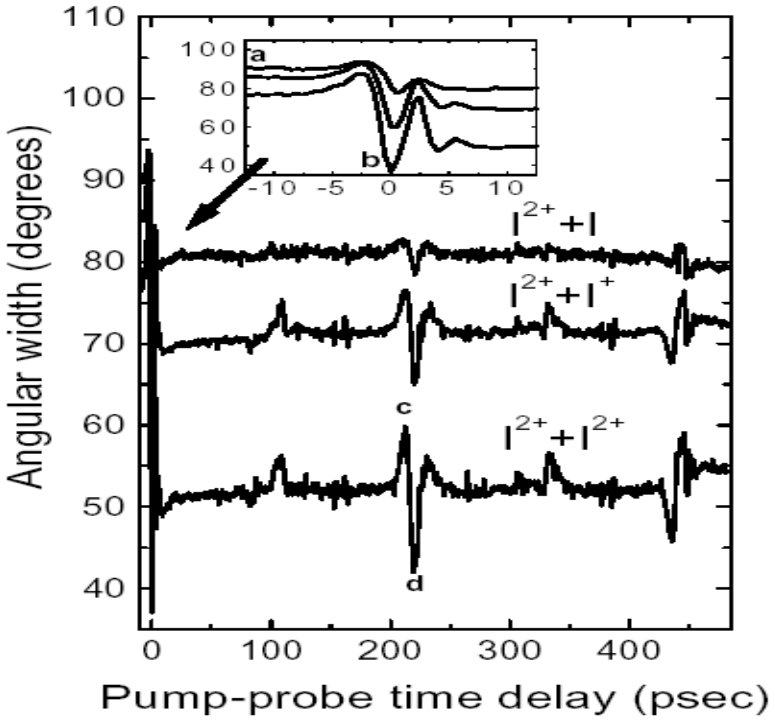

Figure 6.8: *Pump-probe time delay scan, showing the angular width α of the I^{2+}- I, the I^{2+}- I^{+} and the I^{2+}- I^{2+} channels, recorded using a 3.8mJ 2.8 psec pump pulse polarized parallel to the plane of the imaging detector and a 1.2mJ 100 fsec probe pulse polarized perpendicular to the plane of the imaging detector. The measurements show alignment of the molecule during the pump laser pulse (see inset), residual alignment at the end of the pump laser pulse and the occurrence of rotational revivals. The labels (a)-(d) refer to the measurements shown in Fig. 6.5.*

Fig.6.8, contains four distinct regions as a function of the time delay between the pump and the probe lasers:

a) $\Delta t < 0$, when the probe laser precedes the pump laser. In this region no alignment is present. The fact that α slightly deviates from 90^o is due to the presence of a small segment on the imaging detector where the detection efficiency has somewhat degraded due to extensive use of the detector as well as the presence of a weak pump-only background signal.

b) $\Delta t = 0$, when the pump and probe lasers overlap in time. Here an onset of the alignment is observed. In the $I^{2+} + I^{2+}$ channel the width of the angular distribution decreases by as much as 50^o. The alignment reaches a maximum towards the end of the pulse, when the number of states that have become part of the wavepacket reaches its maximum. After the pump laser pulse the alignment decreases again.

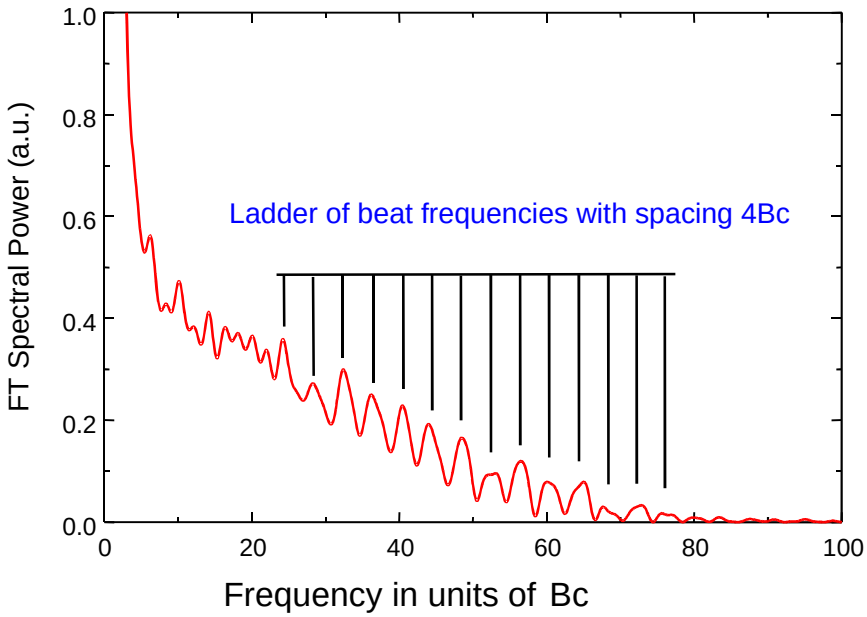

Figure 6.9: *Fourier transform power spectrum of the time-dependence angular width of the I^{2+}- I^{+} channel shown in Fig. 6.8. To facilitate assignment of peaks, the horizontal axis is given in terms of units of Bc.*

c) $\Delta t > 0$, when the probe comes after the pump laser. The angular width remains below the un-pumped value since the pump laser interaction has shifted the rotational population to higher-J. This will be referred to as residual alignment.

d) $\Delta t = mT_{rev}/4$, where m is an integer and T_{rev} is the revival time. As mentioned in section 6.2, from the rotational level structure it follows that a full revival of the wavepacket is expected at a revival time $T_{rev} = 1/2Bc$, which is $450psec$ for the I_2 molecule ($B = 0.037cm{-}1$). At these well-defined time delays with respect to the time-overlap of the pump and probe lasers, revivals are observed in the angular distributions, where the angular width α suddenly decreases or increases during several picoseconds. The observation of these revivals indicates that the pump laser excitation has led to the formation of a rotational wavepacket that keeps evolving in time after the pump laser interaction has ceased. A strong revival is observed around this time delay, $450psec$. In addition significant partial revivals are observed at delay times T/4, T/2 and 3T/4. At the revival times a rephasing of the rotational wavepacket occurs such that the molecule is once more strongly aligned along or perpendicular to the polarization axis of the pump laser.

In Fig.6.9, a Fourier transform power spectrum is shown for the angular width time dependence of the I^{2+}-I^{+} channel given in Fig.6.8. This power spectrum reveals that the time dependence in Fig.6.8 is dominated by beats between levels which differ in their rotational quantum number by $N = 2$. As a result the wavepacket at the half revival $T_{rev}/2 = 1/4Bc$ is 180^0 out of phase with the wavepacket at the full revival

$T_{rev} = 1/2Bc$ and therefore the half revival structure is a nearly exact mirror image of the full revival. Fig.6.9 shows that rotational states up to $J = 15$ are involved in creating the time-dependent signal. This reflects both the initial rotational temperature of the beam and the rotational heating of the molecules due to the laser interaction.

A remarkable feature of the measurements shown in Fig.6.8 is the fact that the alignment manifests more strongly in the highest charge channel I^{2+}- I^{2+}. This is surprising, since molecules aligned along the pump laser polarization axis are aligned orthogonally to the probe laser polarization axis, and therefore difficult to ionize. The fact that the highest charge states show the highest degree of alignment is probably due to a volume effect: at the common focus of the pump and probe lasers the alignment forces are strongest, and the probe laser intensity is highest, enabling the formation of higher charge states.

The observation of maximum alignment towards the end of the pump laser pulse, the observation of a residual alignment after the pump pulse for $\Delta t > 0$ and revival structures at specific times after the pump laser ends, distinguishes the alignment reported here from the alignment observed in earlier experiments with pump laser pulses of $0.1 - 10nsec$ duration [84]. For long pump laser pulses the eigenstates of the system evolve adiabatically from the field-free molecular eigenstates to field-dressed pendular states [114]. This results in an alignment which peaks at the peak of the laser pulse, and which is turned off at the end of the laser pulse. By contrast, the short pulse excitation reported here leads to a non-adiabatic propagation in terms of the dressed states, i.e. during and after the laser interaction the wavefunction is neither a field-free molecular eigenstate nor a dressed eigenstate. As a result, at the end of the laser pulse, the molecule does not return to the field-free eigenstate which it occupied at the start of the experiment, but is in a coherent superposition state involving several of the field-free molecular eigenstates. This coherent superposition state displays an anisotropic angular distribution both during and after the pump laser interaction.

We have investigated the occurrence of alignment during the pump laser pulse, the residual alignment after the interaction with the pump laser pulse and the occurrence of revivals in the angular distribution as a function of a number of experimental parameters, such as the pump-probe polarization geometry, the charge state of the molecule, the pump laser pulse energy and pulse duration and the expansion conditions of the molecular beam (i.e. the initial temperature of the molecular beam). These dependences are presented below.

6.4.1 Polarization and charge dependence

As mentioned earlier the polarization of the two laser beams can be chosen in two geometries. In the perpendicular configuration (probe laser polarization perpendicular to the pump laser polarization and perpendicular to the detector) the angular distribution given by the probe laser is isotropic and therefore any deviation from isotropy is due to the pump laser, while in the parallel configuration (probe laser polarization parallel to the pump laser polarization and parallel to the detector) the probe laser

gives an offset in the initial value of the angular width due to geometric alignment. In fig.6.10 and 6.11 a comparison between the parallel and perpendicular configuration is presented, where the pump pulse energy and pulse duration was $2mJ/pulse$ and $1.4psec$, while the probe pulse energy and pulse duration was $0.9mJ/pulse$ and $100fsec$. While the observed time-evolution is qualitatively similar in the parallel and perpendicular geometry, the time-dependent alignment (both near $\Delta t = 0$ and around the revival) is observed more clearly in the perpendicular geometry in both the I^+ and I^{2+} measurements. It is again noticeable in Fig.6.10 and 6.11 that larger changes in the angular width occur for the highest charge states. As explain earlier this effect is probably due to a volume effect.

We thus conclude that studying the pump-probe experiments in the perpendicular configuration and monitoring higher charge state, is advantageous. This is why in all further measurements of the angular width presented below, the polarization of the probe laser was perpendicular to the pump polarization axis and perpendicular to the plane of the detector, and high charge states were chosen for monitoring the pump-probe time dependence.

6.4.2 Pump pulse energy dependence

The alignment depends strongly on the pump laser pulse energy. An example of this dependence is shown in Fig.6.12, where we compare the angular width α which is observed near the time-overlap of the pump and probe beams and around the full revival time for three medium to high pulse energies, in experiments carried out with a $1.4psec$ pump laser pulse, with detection of I^{2+}.

For $\Delta t = 0$, when the pump and the probe lasers are overlapped, the alignment increases with the pump pulse energy with some changes in the time dependent alignment between the different channels (I^{2+}- I vs. I^{2+}- I^+). The structure that appears in the angular width as a function of time does not follow the temporal shape of the pump pulse. Some counter-intuitive alignment appears ($\alpha > 90^0$) within the pump pulse interaction and this is not the same for all the charge states. For the lowest pulse energy ($1mJ$, squares in Fig.6.12) the time-dependent angular width presents small oscillations (which are however reproducible) for the I^{2+}- I channel (a) and the alignment becomes more visible for I^{2+}- I^+ channel (b). For $2mJ$ pulse energy (circles in Fig.6.12) the alignment in the I^{2+}- I channel becomes stronger and comparable to the alignment present in the I^{2+}- I^+ channel. For higher intensity ($3.5mJ$, upward triangles in Fig.6.12) the I^{2+}- I^+ channel presents a stronger alignment than the I^{2+}- I channel. For the high charge channels there is an offset in the initial angular width due to pump only background signal.

The experimental observations presented above are correlated with the number of Raman transitions that can take place in the molecule during the laser pump pulse for different pulse energies and therefore for different intensities. For low intensity the number of transitions is low and results in a wavepacket that contains a low number of states and therefore a weak alignment is observed. For higher energy, the number of

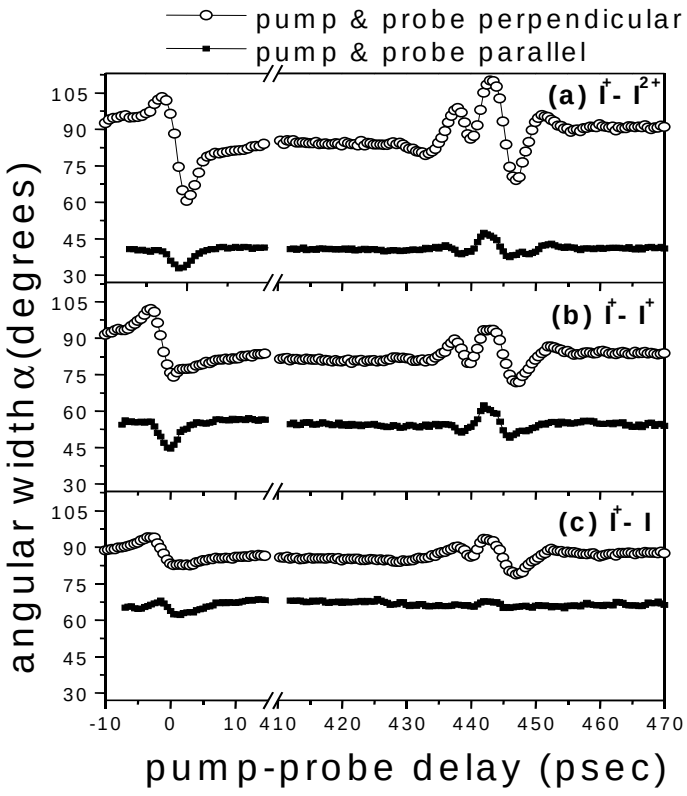

Figure 6.10: *The time evolution of the I^+ fragment angular distributions as a function of the time delay between the pump (1.4psec and 2mJ) and the probe (100fsec and 0.9mJ) around $\Delta t = 0$ and around the revival time. The pump polarization is in the plane of the detector, while the probe polarization either is perpendicular to the detector (circles) or parallel to the detector (squares). The graph shows the time evolution of different channels: (a) I^+- I^{2+}; (b) I^+- I^+; (c) I^+- I.*

Raman transition increases and therefore the alignment gets stronger. The number of states involved in the rotational wavepacket formed by the pump beam has, therefore, direct influence on the peak amplitude observed in the time-dependent angular width distributions.

For $\Delta t > 0$, when the pump laser excitation ends, an offset in the angular width can be observed. This residual alignment increases with pump energy as can be seen in Fig.6.12. This behavior can also be explained by the shift of the rotational population in the molecular beam. For increasing pump energies, the number of rotational levels involved in the wavepacket increases and leads to a non-statistical population of rotational levels such that the value of J is significantly larger than M for higher pump energy.

At a given delay between the pump and the probe lasers a full revival is measured

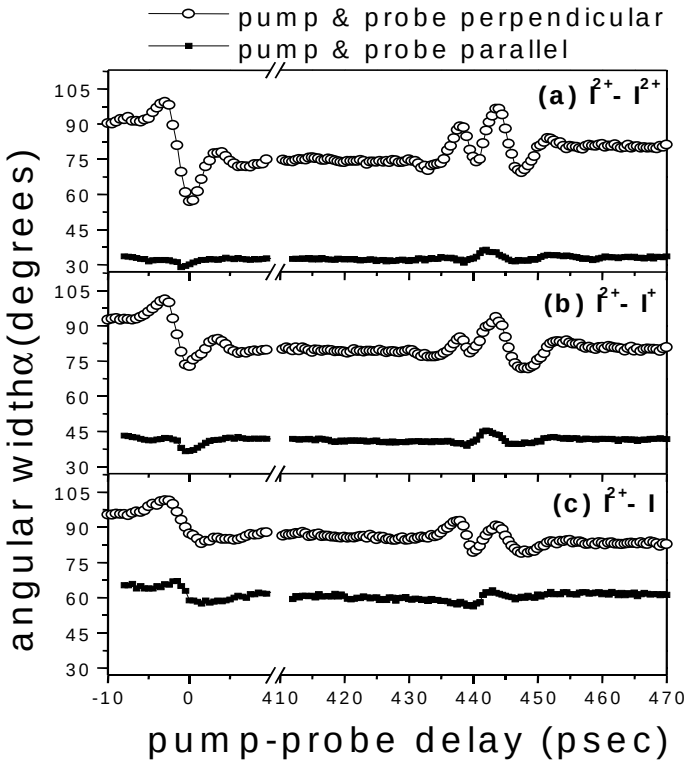

Figure 6.11: *The time evolution of the I^{2+} fragment angular distributions as a function of the time delay between the pump (1.4psec and 2mJ) and the probe (100fsec and 0.9mJ) around $\Delta t = 0$ and around the revival time. The pump polarization is in the plane of the detector, while the probe polarization either is perpendicular to the detector (circles) or parallel to the detector (squares). The graph shows the time evolution of different channels: (a) I^{2+}- I^{2+}; (b) I^{2+}- I^{+}; (c) I^{2+}- I.*

(Fig.6.12c and d). The alignment on the revivals also depends strongly on the pump energy. The alignment initially increases with pump energy, but then the angular width starts to have a more complicated structure and rapid oscillations are observed. The amplitude of the revival is larger for the I^{2+}- I^{+} channel (d). The observation of oscillatory structure in the revivals (indicative of the participation of a large number of states in the wavepacket) while angular widths remains above 60^0 suggests that the alignment is limited by the initial rotational population in the molecular beam (see also section 6.4.4).

6.4.3 Pump pulse duration dependence

The effect of the pump laser on the alignment can be monitored not only by varying the pulse energy for constant pulse duration as shown in Fig.6.12, but also by varying

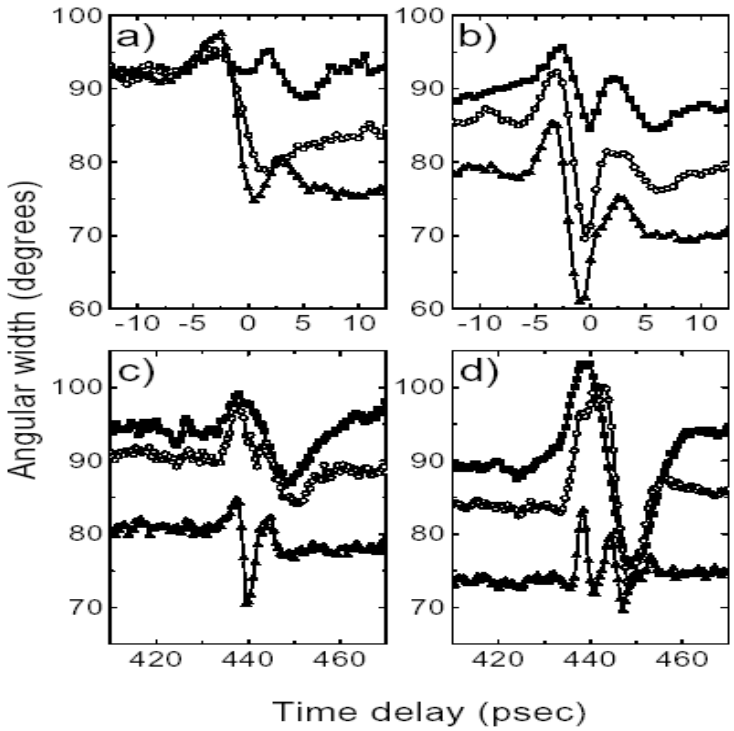

Figure 6.12: *Intensity dependence of the alignment obtained with 1.4 psec pump laser pulses around the time-overlap of the pump and probe lasers and at the full revival. a) I^{2+}- I around $\Delta t = 0$; b) I^{2+}- I^{+} around $\Delta t = 0$; c) I^{2+}- I around the full revival; d) I^{2+}- I^{+} around the full revival. The pump pulse energies used were 1 mJ/pulse (squares), 2 mJ/pulse (circles) and 3.5 mJ/pulse (triangles).*

the pulse duration. In order to obtain a good signal-to-noise ratio in the measurements we have chosen to vary the pulse duration while adjusting the pump pulse energy to be just below the onset of the dissociative ionization of I_2 (so that the pump laser alone gives almost no signal). In Fig.6.13 measurements of the angular distribution of I^{2+} fragments from the I^{2+}- I^{+} channel are presented as a function of the pump-probe delay around the $\Delta t = 0$ and around the half revival, for three different pump pulse durations. One can observe how the alignment during the pump laser pulse, the residual alignment and the alignment at the half revival are maximum for a pump pulse duration of $2.8p$ sec and decrease for longer or shorter pulses.

Based on the time-dependent evolution of the angular width presented in Fig.6.13, one can plot the decrease of the angular width near $\Delta t = 0$, near a revival and between $\Delta t = 0$ and the revival, as a function of the pump pulse duration. In Fig.6.14a the maximum alignment reached during the pump laser pulse is plotted. For very short pulse durations ($\lessapprox 1psec$) limited population transfer occurs during the laser pulse. The initial field-free rotational distribution is projected onto a number of pendular states, without however significantly changing any of its angular properties. For very

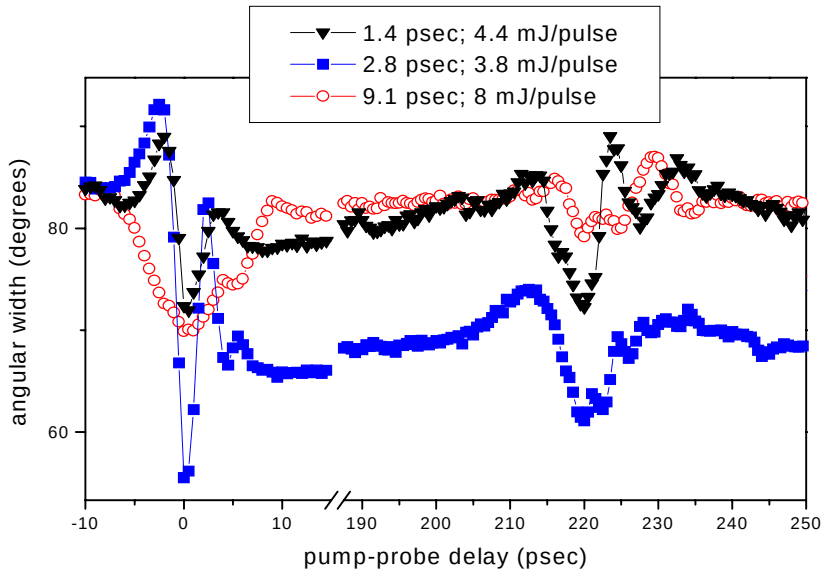

Figure 6.13: *The time evolution of the angular width of the I^{2+} fragment from I^{2+}-I^{+} channel as a function of the pump pulse duration around $\Delta t = 0$ and around half revival. 1.4 psec and 4.4 mJ/pulse (down triangles), 2.8 psec and 3.8mJ/pulse (squares), 9.1 psec and 8mJ/pulse (circles).*

long pulse durations ($> 10psec$) the time-evolution becomes predominantly adiabatic and each initial rotational state is connected to one pendular state which is occupied during the laser pulse. The alignment at the peak of the laser pulse is determined by the peak intensity in the experiment (which is considerably lower in the $9psec$ experiment compared to the $1.4psec$ and $2.8psec$ situations). For medium pulse duration a combination of diabatic and adiabatic behaviour occurs. Changes in the alignment occur because the laser field is time-dependent, leading to a change in the alignment properties of individual pendular states and because the wavefunction evolves and the decomposition of the wavefunction in terms of the pendular states is non-stationary. For medium pulse durations (see the $2.8p$ sec measurement) the time evolution of the angular width has an oscillatory structure which is likely due to the fact that the pump laser forces the molecules into alignment so strongly that the molecules start to oscillate along the laser polarization axis. These effects are similar to the oscillations observed in the angular distribution in the one-laser experiments presented in Chapter 4 and 5. An optimum in the alignment is experimentally observed for pulse durations of $2.8p$ sec. This coincides with the pulse durations range where theoretical calculations predict the largest population transfer as a result of the laser interaction, for pulses reaching constant peak intensity ([119]). The pulse duration which leads to optimum alignment around $\Delta t = 0$ depends on the peak intensity encountered in the pulse. A decrease in the optimal pulse duration with increasing peak laser intensity is expected, where the maximum alignment actually appears some time after the peak

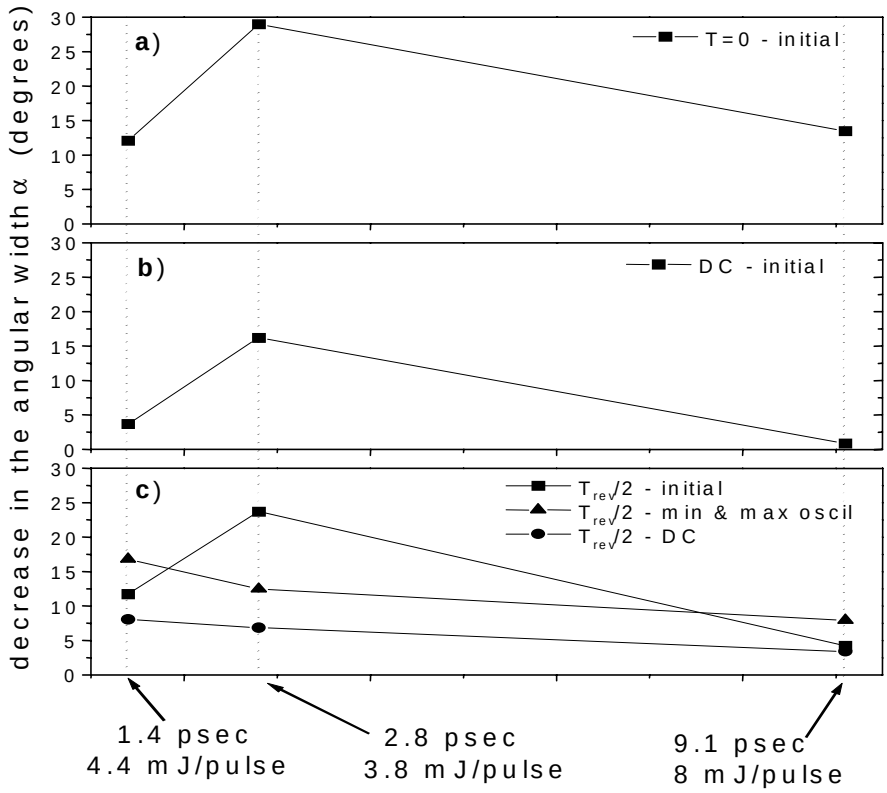

Figure 6.14: *The decrease in the angular width α of the I^{2+} fragments from the I^{2+}-I^{+} channel for: (a) the maximum alignment at $\Delta t = 0$, (b) the amplitude of the half revival and (c) the residual alignment as a function of the pump pulse duration. This results are based on the measurements shown in Fig. 6.13.*

of the pump laser pulse. In the adiabatic long pulse regime, the maximum alignment occurs exactly at the peak of the laser intensity. However, for short pulses, the alignment occurs at a point towards the end of the laser pulse, when the maximum number of states have become part of the coherent superposition. Model calculations which have been performed in our group [119], indicate that for short pulses the degree of alignment during the pulse is determined by the energy rather than the intensity of the laser pulse. Hence the observed increase in alignment when going from 1.4*psec* to 2.8*psec* likely means that the overlap between the pump and the probe lasers was slightly better in the latter experiment.

As explained in the previous section, the average alignment for $\Delta t > 0$ is nonzero, due to the fact that the rotational pumping leads to a non-statistical population of the available rotational levels such that the expectation value of J is significantly larger than M. Fig.6.14b shows the decrease of the angular width α corresponding to the residual alignment with respect to the initial angular width as a function of the pump pulse duration . When going from 1.4*psec* to 2.8*psec* pulses the residual alignment increases,

but then it decreases again for a pulse duration of $9psec$, where the effective angular width approaches 90^0. For short pulse durations the increase in the residual alignment versus pulse duration reflects the fact that at a constant peak intensity a longer pulse length allows for a more significant population transfer out of the initially populated rotational state. However, for pulse durations of $5psec$ and higher, the propagation of the wavepacket becomes progressively more adiabatic, and a situation is approached where the molecule returns to its original rotational state when the pump pulse is over. Therefore, though the $9psec$ measurement showed appreciable alignment near $\Delta t = 0$, there is no residual alignment after the pump pulse.

The decrease of the angular width α that occurs at the half revival time is shown in Fig.6.14c. The amplitude of the alignment at the half revival time can be calculated in three ways: with respect to the initial angular width (squares), with respect to the residual alignment (circles) and measuring the difference between the maximum and the minimum in the oscillations that appears at the revival time (upward triangles). It is observed that the revival amplitudes correlate to the evolution of the residual alignment shown in 6.14b) when measuring the decrease of the angular width with respect to the initial value (6.14c) squares). The explanation is also based on similar arguments. For medium pulse durations a combination of diabatic and adiabatic behavior leads to the formation of a wavepacket that containing the largest number of states. The evolution of this wavepacket gives therefore the maximum alignment on the revival for medium pulse length. If one plots the decrease of the angular width on the revival with respect to the residual alignment (6.14c) circles), the result is that this difference decreases with increasing pump pulse duration. For short pulses ($1.4psec$) the value is large because the residual alignment is not as strong as in the case of medium pulses ($2.8psec$), while for long pulses ($9.1psec$) the amplitude of the revival itself is lower due to the fact that the system is approaching the adiabatic regime where no wavepacket is formed, and therefore no revivals are visible. The slope of the function becomes larger when plotting the amplitude of the full revival as the difference between the maximum and minimum oscillation that appears at the revival time (6.14c) up triangles). For an increasing pump pulse duration (and therefore an increasing number of states that are involved in the wavepacket induced by the pump laser) the oscillations between alignment along the laser polarization and the counter-intuitive alignment, when the molecule is perpendicular on the laser polarization, become more rapid and cancelation processes occur. Therefore the amplitude difference is not maximum for medium pulse duration when the maximum alignment occurs but for short pulse duration when the revival is less structured. For longer pulses the difference between the oscillations decreases due to approaching the adiabatic regime.

To summarize, our studies on the pulse duration dependence of the time-dependent alignment show, in agreement with our model calculations [119], that the alignment near $\Delta t = 0$ tends to peak for intermediate pulse durations, whereas the observation of revival structures favors the use of slightly shorter laser pulses. For long laser pulses the alignment at a revival is considerably weaker than the alignment at the peak of the laser pulse.

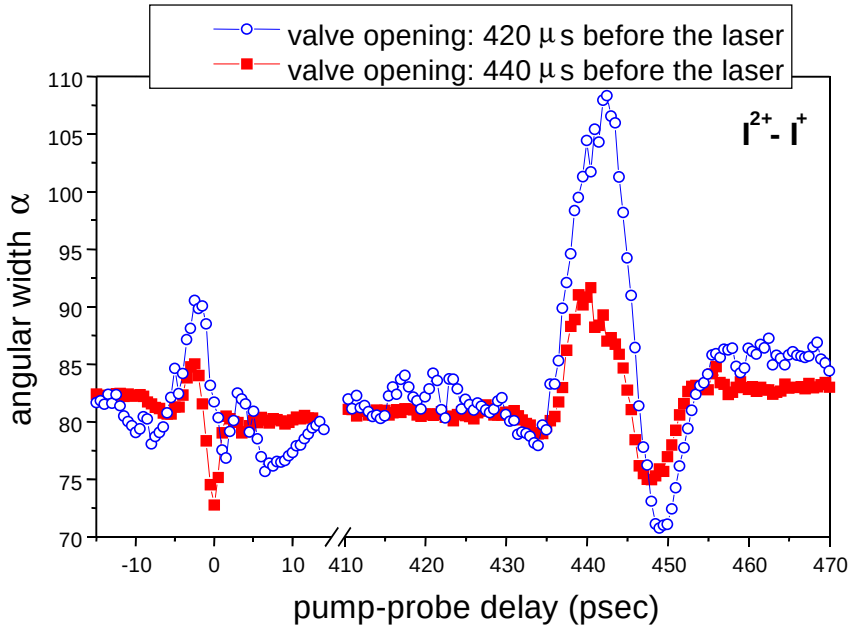

Figure 6.15: *The time evolution of the angular width of the I^{2+} fragments from the I^{2+}- I^{+} channel as a function of the opening time of the valve: 420 µsec before the laser (circles), 440 µsec before the laser (squares). The time-dependent angular width α is shown both around $\Delta t = 0$ and around the full revival. The pump pulse energy and pulse duration were $\sim 3mJ/pulse$ and 1.4psec, and the probe pulse energy and pulse duration were $\sim 1mJ/pulse$ and $100fsec$. The backing pressure was 1.2bar.*

6.4.4 Temperature dependence

As already suggested in section 6.4.2, another important parameter in the creation and evolution of the rotational wavepacket is the initial temperature of the molecular beam. Therefore we have investigated the occurrence of alignment during the pump laser pulse, the residual alignment after the interaction with the pump laser pulse and the occurrence of revivals in the angular distribution as a function the expansion conditions of the molecular beam.

The molecular beam is formed as a pulsed expansion of gas through a nozzle (see Chapter 3). The temperature of the molecular beam is therefore not constant in time. On the rising edge of the gas pulse a colder rotational temperature is expected than on the falling edge or at the onset [120]. The temperature of the molecules in the laser focus can thus be controlled by changing the time delay between the laser pulse and the moment when the pulsed valve opens in order to release the molecules. The time evolution of the angular width as a function of the opening time of the valve is shown in Fig.6.15, where the pump pulse energy and pulse duration were $3mJ/pulse$ and $1.4psec$, while the probe pulse energy and pulse duration were $1mJ/pulse$ and $100fsec$.

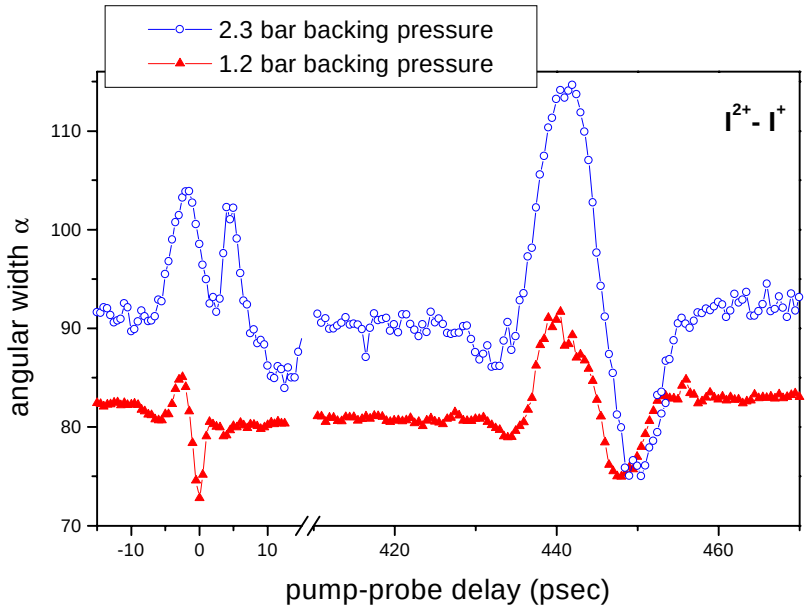

Figure 6.16: *The time evolution of the angular width for I^{2+} fragments from the I^{2+}- I^{+} channel for backing pressures of 2.3 bar (circles) and 1.2 bar (up triangles). The time-dependent angular width is shown both around $\Delta t = 0$ and around the full revival. The valve was oppened $440\mu s$ before the lasers. The pump pulse energy and pulse duration were $\sim 2mJ/pulse$ and $1.4psec$, and the probe pulse energy and pulse duration were $\sim 0.5mJ/pulse$ and $100fsec$.*

As expected, for lower initial temperature (corresponding to the earlier opening time of the valve) the alignment for $\Delta t = 0$ and the alignment on the full revival are stronger, as shown in Fig.6.15 for the I^{2+} fragments from the I^{2+}- I^{+} channel.

The fact that the alignment is stronger for lower initial temperature of the molecular beam is due to the fact that the experiment simultaneously measures the alignment starting from all rotational levels which were initially populated in the molecular beam. The alignment will be averaged out for a larger number of initial rotational states.

To control the temperature one can also change the backing pressure which is related to the number of collisions among molecules and therefore the collisional rotational relaxation. An example is shown in Fig.6.16. For higher backing pressure and therefore lower rotational temperature, the time evolution of the angular width is more structured for $\Delta t = 0$ and the revivals are stronger despite the offset due to a pump laser only contribution in the measurements for the lower backing pressure (triangles).

The model calculations on the interaction of an intense ultrashort laser pulse with a diatomic molecule, which reproduce all qualitative aspects of the experiments presented here, suggest that in the current experiment the initial rotational temperature of the I_2 molecules (estimated to be approximately $10K$ both based on REMPI measurements

on N_2 which were carried out under similar conditions and on the Fourier transform power spectrum presented in Fig.6.9) eventually limits the minimum width in the angular distribution that can be observed [119]. Narrower angular distributions are likely to be possible for lighter molecules, where the number of rotational states that are initially populated is more limited.

6.5 Conclusions

In this chapter experiments on ultrashort laser induced alignment of I_2 molecules have been presented. These experiments demonstrate that it is possible to prepare a wavepacket of ground state rotational levels, which leads to a moderate steady-state alignment after the pump laser interaction, as well as the formation of an aligned sample of molecules at well-defined revival times following the preparation of the wavepacket. These aligned molecules are formed under field-free conditions, which distinguishes this form of alignment from the adiabatic alignment of molecules using long laser pulses, as successfully applied by several other groups [84, 114]. In the near future we will attempt to use these aligned molecules to study molecular-frame photoelectron angular distributions.

Chapter 7

Outlook: XUV-IR pump-probe experiments

In this last chapter experiments related to the generation and the use of high harmonics are presented. After an introduction on high harmonic generation, preliminary results obtained in our laboratory concerning the generation of harmonics are presented. The third section shows ways of measuring the duration of the harmonic radiation in our experimental setup. Next, the use of XUV radiation in the laboratory to study photoionization and photodissociation processes is discussed and an outlook for future experiments will be given.

7.1 Introduction

When an atom is subjected to the intense electro-magnetic field of a laser, multiphoton processes can occur. One of these highly non-linear processes is High Harmonics Generation (HHG). This name refers to the conversion of the fundamental wavelength of the driving laser to odd harmonic wavelengths. This process can be explained as follows. Due to the Heisenberg uncertainty relation $\delta E \delta t \geqslant \hbar$, there is a finite probability for a bound electron to non-resonantly absorb a photon and return almost immediately to its original state, emitting the photon again. So the atom can be in a virtual state for a short time. In an intense laser field the atom may absorb another photon while still in the virtual state. This can happen again and again, and can be extended to a large number of photons. If the atom eventually returns to the ground state, it can emit a photon with an energy corresponding to the number of photons that were absorbed. Only odd harmonics can be observed in gases because of the dipole selection rule and the symmetry of the potential.

Third harmonic generation in rare gas media was observed for the first time by New and Ward in 1967 [121]. Fifth- and higher-order harmonic generation were observed a few years later by Reintjes *et al.* [122], Metchkov *et al.* [123] and Groseva *et*

al. [124]. Since then, these phenomena have been extensively studied with the aim of increasing the conversion efficiencies and reaching shorter wavelengths [125]. Conversion efficiencies can be maximized by choosing the frequency of the driving laser close to an atomic resonance [126–129], by adding a buffer gas in order to optimize the phase matching [130, 131] or by using an appropriate interaction geometry [132–134].

Progress in short-pulse intense laser technology led to the discovery of the generation of high harmonics in the non-perturbative regime. This radiation has unique properties: high photon energy and short pulse duration. The HHG technique is relatively easy to implement in the laboratory. Therefore, HHG rapidly became a very attractive source of short duration soft X-ray radiation. The harmonic intensities present a characteristic distribution. After a rapid decrease for the first orders, there is a long plateau, which ends with a sharp cutoff. The length of the plateau increases with the laser power, up to intensities at which the medium becomes ionized [135, 136]. Beyond this intensity (called the saturation intensity), the signal increases much less rapidly than before, the distribution becomes smoother and the maximum observable harmonic order remains constant. There are two reasons why multiphoton ionization limits HHG. The main medium responsible for harmonic generation gets depleted when the medium becomes ionized and harmonics are produced in the periphery of the interaction volume or at the beginning of the laser pulse. Ions can also generate harmonics, but their response is less efficient at these intensities. The second effect that is responsible for the limitation of the harmonic conversion efficiency is the breaking of the phase matching owing to the presence of free electrons in the medium. These free electrons have a nonnegligible effect on the refractive index (at the fundamental frequency or at a harmonic frequency). Consequently, they induce a large positive phase mismatch between the generated beam and its driving polarization, which reduces the conversion efficiency.

In general, the power efficiency for plateau harmonics at the highest laser intensity (before reaching the ionization intensity) is between 10^{-5} (for Xe) and 10^{-8} (for Ar). From this the order of magnitude for the number of photons produced can be estimated to be about 10^{10} photons/pulse for harmonics generated in Xe and about 10^{7} photons/pulse for Ar. Therefore the advantage of using Xe or in general heavier gases, is that the conversion efficiency is higher than in Ar (lighter atoms). On the other hand, due to the fact that Ar has a higher ionization potential, it can be used for generation of higher order harmonics and therefore shorter wavelength radiation.

The use of short and intense pulses also led to the observation of other exciting phenomena such as multi-photon ionization [137–139], above-threshold ionization [140,141] and resonant multiphoton ionization through ac-Stark shifted excited states [142, 143]. The insights gained in these studies are important for understanding the mechanism of high harmonic generation. The same theoretical techniques employed for describing multiphoton ionization in strong radiation fields can be applied to calculating the photoemission spectrum of an atom. Time-dependent methods involving the numerical solution of the Schrödinger equation [144–147] and Floquet calculations [148,149] have been successfully employed. Classical methods [150, 151], one-dimensional approximations [152] and many other model calculations [153–157] also provide some insight into

the physics involved. The calculated single-atom photoemission spectra are generally in good qualitative agreement with the experimental data. Phase-matching conditions are known to play an important role in the overall response of the medium and to be very sensitive to various parameters such as the atomic density, the focusing geometry, the laser frequency and the process order. On the basis of weak-field calculations [158] one would expect phase matching to severely degrade with the order. In contrast, the comparison between experimental data and single-atom calculations seems to indicate that propagation effects affect all the harmonics in the same way. This implies a new treatment of the single-atom response and of the collective response of the medium. Perturbative calculations were carried out which could find accurately the nonlinear susceptibilities for the low order harmonics [159]. However, from previous work it is known that behaviour in the intensity regime needed for HHG is non-perturbative. The same workers have also predicted a critical intensity above which the perturbation theory breaks down for each harmonic order. These calculations have been verified using numerical integration of the Schrödinger equation by Krause *et al.* [160], who in addition found that high order harmonics did not scale perturbatively with intensity but that they scaled much slower and contained many resonant structures. This behaviour has been shown to be responsible for the favorable phase matching which can be achieved in strong fields [19, 161, 162].

Krause *et al.* [163] discovered an empirical law governing the extent of the plateau. They found from their numerical calculations that the highest harmonic (the cut-off) had an energy approximately given by:

$$E_c \approx I_p + 3.17U_p \tag{7.1}$$

where I_p is the ionization potential of the target atoms and U_p the ponderomotive energy ($U_p = E^2/4\omega^2$ for a laser field of amplitude E and frequency ω). Therefore longer plateaux could be produced by increasing U_p (using long wavelength or higher intensities) or increasing I_p (using ions). This empirical law has been experimentally verified [164,165] although in some experiments the cut-off was measured to be I_p+kU_p, where k was between 1 and 2 [165,166]. This discrepancy has been ascribed to the short wavelength and tight focusing limit used in these experiments which made propagation effects very influential and lowered the harmonic cut-off.

To explain this cut-off law a simple semiclassical argument is used [167–169] based on earlier 'simple-man' approaches to above-threshold ionization [170]. This has since become known as the 'recollision model' of harmonic generation. As the atom is perturbed it ionizes and can be seen as a source of electrons (with essentially classical properties) that are 'born', with zero initial velocity, in the laser field. The electron trajectories depend sensitively on the phase of the electric field at the time of their birth; some may ionize and others will return to recollide with the nucleus. The maximum energy with which an electron born at zero velocity can return to the core is $3.17U_p$. Assuming all this kinetic energy may be added to the ionization potential when a photon is radiated in a recombination process, we find a qualitative explanation for the cut-off rule.

Extending the cut-off towards shorter wavelengths stimulated a large number of papers. A variety of wavelength and pulse durations have been used to generate harmonics. Harmonics orders well exceeding one hundred have been observed by L'Huillier and Balcou [172] from He and Ne using $1ps$, $1054nm$ laser pulses. They obtained a conversion efficiency of about 10^{-6}. Macklin *et al.* [164] observed harmonics up to the $109th$ order in Ne using $125fs$, $806nm$ laser pulses. In heavier noble gases, which have smaller ionization potentials, the number of harmonics which can be generated is less, although they have higher conversion efficiencies [171]. L'Huillier and Balcou [172] observed up to the $55th$ and $27th$ harmonics from Ar and Xe, respectively, with $1ps$, $1054nm$ laser pulses. Zhou et al. [173] observed harmonics up to the $131st$ order in Ne, the $61st$ order in Ar, the $41st$ order in Kr and the $29th$ order in Xe, by using $25fs$, $805nm$ laser pulses. They also observed that the harmonic spectra are asymmetric with respect to the sign of the chirp and that the harmonics may be tuned by adjusting the chirp. By improving the experimental conditions the same group could observe harmonics up to the $155th$ order in Ne and the $221st$ order in He. In He, unresolved harmonic emission was observed up to the $297th$ order [174]. These wavelengths are well within the "water window" region of the x-ray transmission. In this spectral range, between 532eV (oxygen K-edge) and 284 eV (carbon K-edge), the absorption coefficient of oxygen is significantly smaller than that of carbon and nitrogen. This results in good contrast of organic molecules (consisting mainly of carbon and nitrogen) against water. Therefore it may be very important for applications such as imaging through aqueous solutions.

It was found theoretically that high-harmonics generated in one- or two-electron molecular ions can extend well beyond the $I_p + 3U_p$ atomic maximum cut-off low [175]. A second plateau was found with cut-off at energy $I_p + 6U_p$ for one-electron systems and $I_p + 12U_p$ for two-electron systems. This effect is due to the electron repulsion as a result of an increased separation and delocalization of electrons in extended systems. The existence of a second plateau in the high-harmonic spectra was also found in theoretical studies, in the presence of a static magnetic field perpendicular to the laser field polarization direction [176]. The high-harmonics in the second plateau reach a maximum enhancement when the cyclotron frequency of the electron is about equal to one half of the laser frequency. A 'synchrotron radiation'-like mechanism was found to be responsible for the production of the second plateau.

Increasing the conversion efficiencies of generating high harmonics has been an important topic in the last few years. The recently developed technique of guided-wave frequency conversion [177] was used to upshift light from 800nm to the range from 17 to 32nm with increase in the coherent x-ray output by factors of 10^2 to 10^3 compared with the earlier work. Optimization of the pulse shape can also lead to an increase of the coherent emission of high-harmonics [178].

It is not the purpose of this chapter to cover the entire field of harmonic generation in gases (including the generation of high harmonics with intense femtosecond lasers) that has been extremely well documented in review articles [5, 19, 179] and textbooks [180–183]. Therefore, after this introduction, we shall concentrate on the

use of the XUV radiation in our laboratory to study photoionization and photodissociation processes. In the XUV Physics group at Amolf, one of the main goals is to use the unique properties of the high harmonics (high photon energy and short pulse duration) in time-domain physics and chemistry experiments. For this we shall first present results of the high harmonic generation obtained in our laboratory, then ways of measuring the duration of the harmonics in the conditions of our experimental setup will be presented and in the last part of this chapter preliminary results on the photoionization/dissociation of H_2 and an outlook for future experiments will be given.

7.2 Experimental setup

A schematic diagram of our experimental setup is shown in Fig.6.3 in Chapter 3. The light source used for HHG is a 70fs Ti:sapphire laser emitting at $800nm$ and operating at a $50Hz$ repetition rate that was extensively described in Chapter 2. A $2m$ focal length lens focuses the laser beam onto the gas jet situated in the HHG chamber. The size of the beam on the lens is approximately $2cm$ and the pulse energy $30mJ$, so that the intensity in the focus can reach intensities around $10^{15}W/cm^2$. The lens and the gas jet were set on translation stages in order to adjust the harmonic conversion efficiency as a function of the position of the gas jet relative to the laser focus. The gas sample was injected in the interaction chamber by a piezoelectric valve (see Chapter 3) with a $1mm$ nozzle. The gas jet has the shape of a cone, but because the laser passes very close to the nozzle, the gas jet width can be estimated to be about $1mm$ and the average pressure at the focus of the laser beam is the same order of magnitude as the backing pressure which was about 2 bar. The interaction chamber was evacuated by a cryopump to a background pressure of 10^{-8} Torr. During the operation, the background pressure reached values around 10^{-4} Torr. The spectrum of the harmonic generation was analyzed by using a normal incidence spherical grating with $600grooves/mm$ and radius of curvature of $2m$. An MCP/Phosphorscreeen assembly was mounted at the focus of the harmonic beam coming from the grating. The signal from the phosphor screen was collected by a CCD camera and the signal was integrated within a $\sim 50\mu m$ wide slit. This setup ensured a spectral resolution of few tens of millielectronVolt. Measurements of the relative harmonic photon yield were performed by integrating the harmonic signal (approx. 300 laser shots) as a function of the position of the grating. The output signal was recorded on a personal computer which also controlled the grating movement. It is important to note that in order to calculate the absolute number of photons obtained in the high harmonic generation process one has to take into account all the efficiencies involved in the detection, namely, the diffraction efficiency of the grating as a function of wavelength (there is a cut-off in the diffraction efficiency beyond $\simeq 30nm$) and the detection efficiency of the MCP detector. Both devices (grating and detector) have to be calibrated and the spectra has to be convoluted with the efficiency curve resulted from these calibrations. These measurements are still in progress.

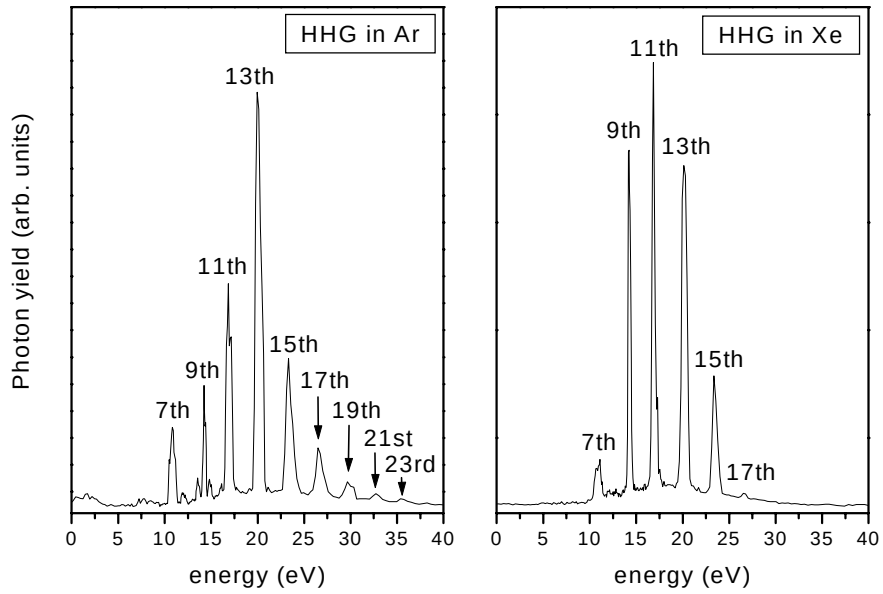

Figure 7.1: *Harmonic spectra obtained with 70fs, 800nm laser pulses. The non-linear medium is a 1mm Ar (left) and Xe (right) gas jet at about 2 bar. The laser intensity is* $\sim 10^{15} W/cm^2$. *The small peaks that appear in the HHG spectrum generated in Ar (left) at* $11.89eV$, $13.55eV$ *and* $14.82eV$ *result from the second order diffraction of the 15th, 17th and 19th harmonic.*

Typical high harmonics spectra measured in the conditions presented above are shown in Fig.7.1. As mentioned in the previous section, when using Ar as non-linear medium harmonics with shorter wavelength can be generated then if we use Xe. In our experimental conditions we could detect harmonics up to the 17th order ($26.35eV$) using Xe and up to the 23rd order ($35.65eV$) using Ar.

The transverse variation of the laser intensity can result in oscillations in the atomic polarization, leading, in turn, to strong distortion of the harmonic beams [184]. Using the setup presented above we could monitor also the spatial shape of the harmonic beam. In this way we could adjust the focussing geometry and the pressure and timing of the gas jet in order to increase the conversion efficiency while keeping a homogeneous spatial profile for the harmonic beam. Because of the relatively low ionization potentials of the noble gases used (Ar and Xe), and the relatively high local pressure used in the experiment, the effect of free electrons on the propagation of the pump and harmonic beam across the generating medium cannot be neglected. Therefore, further optimization could increase the harmonic yield generated in our laboratory.

7.3 Measurements of the harmonic pulse duration

Although high harmonics have been present in many laboratories for more than 10 years, and although their generation is understood experimentally and theoretically, some features of the generation process have remained inaccessible to direct experimental measurements. In particular, questions relating to the time profile of the harmonic emission are not easily resolved. Measurements of the harmonic pulse duration show that it is much shorter than that of the driving laser [185–187] and lasts for only a few femtoseconds. Moreover, recent experimental measurements show that the natural phase with which groups of neighboring harmonics are generated is sufficient to support the generation of attosecond pulses [23].

For temporal characterization of harmonic pulses a few methods are available. One of them is autocorrelation, where the measured quantity is the convolution of the pulse with itself (see Chapter 2). In an autocorrelation one records the result of a nonlinear process (e.g. second-harmonic generation in a nonlinear crystal, two-photon ionization, or refractive index variation in Kerr medium [188]) in which two copies of the pulse contribute simultaneously, as a function of delay between them. This method does not give complete information about the temporal shape of the pulse, and furthermore a serious drawback is that the efficiency of the nonlinear process depends on the square of the pulse intensity, so that only for very low harmonics an autocorrelation is feasible.

An alternative method is the cross-correlation technique. By replacing one of the XUV beams by a "probe" beam of longer wavelength (visible or infrared), where virtually unlimited intensities are available, it is the single-photon XUV process that becomes the limiting factor. The disadvantage of this method comes from the fact that the probe pulses that are available tend to be longer than the XUV pulse, and this imposes a serious limitation on the temporal durations that can be measured. If the probe pulse contributes in a higher order to the process, its effective duration shrinks accordingly and shorter pulses can be measured [189, 190]. Cross-correlation techniques can also be used by means of Auger decay processes [191], changes in the bound-free absorption of the XUV radiation [192], ionization induced defocusing [193] and ponderomotive streaking of the ionization potential [21].

In our experimental setup the harmonic radiation is frequently used in experiments after it is diffracted by the spherical grating situated in the spectrometer chamber. After the grating the harmonic pulse is expected to have a longer duration than the infrared pulse. Therefore in our experimental conditions a cross-correlation measurement XUV-IR is an appropriate technique. We implemented the cross-correlation technique by measuring the amplitude of side-bands in the photoelectron spectra, which are obtained when high harmonics are sent into the interaction region together with the fundamental radiation in order to ionize atoms. The side-bands are produced when atoms absorb one harmonic photon and absorb or emit one or more fundamental photons. At low IR intensities each harmonic has only a single side-band on each side. These side-band peaks appear at energies corresponding to even multiples of the IR photon energy, and are thus located between the peaks caused by the harmonics them-

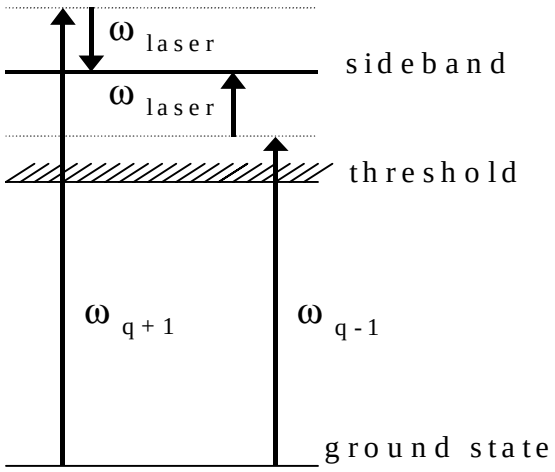

Figure 7.2: *The quantum paths contributing to the photoelectrons generated by two-color two-photon ionization.* ω_{laser} *is the IR frequency and* $\omega_q = q\omega_{laser}$*. A side-band peak is present in between the signal from the harmonic* $q+1$ *and* $q-1$*.*

selves. Only the two nearest harmonics contribute to each side-band peak (Fig.7.2). The appearance of side-bands requires spatial and temporal overlap of the harmonics and the fundamental radiation.

The experimental setup used for this cross-correlation measurement is shown in Fig.6.3 (Chapter 3). The output from the $50Hz$ Ti:Sa femtosecond laser amplifier was split and compressed in two dual grating compressors. 70% of the laser output ($\sim 22mJ$) was used for harmonic generation. This beam had $\sim 2cm$ diameter and was focused with an $1m$ lens on the gas jet. Xe gas was used as nonlinear medium for the harmonic generation. The fundamental pulse duration, divergence and focusing geometry were adjusted to obtain the highest conversion efficiency for $13th$ harmonic (see section 7.2 and Fig.7.1). The spherical grating situated in the monochromator selected the 13th harmonic and focussed it in the experimental chamber. By using the grating to steer the harmonic radiation in the experimental chamber we ensured that no fundamental radiation used for the harmonic generation reached the interaction region. The other 30% of the laser output ($\sim 6mJ$) was used as probe beam. This IR beam was focused nearly colinearly with the harmonic beam by a $2m$ lens through the monochromator onto the interaction region situated in the experimental chamber. The size of the IR beam on the lens was $\sim 5mm$. The path of the probe IR beam is shown in Fig.3.1. Before entering the monochromator the IR beam passed a translational stage that was used to change the delay between the XUV and the IR beams. The signal that was monitored in the cross-correlation measurement was the side-band produced in the photoelectron spectrum of Ar by the 13th harmonic and the IR radiation. It is important to note that the IR beam does not generate electrons by itself.

In any pump-probe XUV-IR experiment one has to find the overlap in time and in

space between the two laser beams. An accurate way to do this is to find an ion/electron signal which depends on both lasers and which therefore requires spatial and temporal overlap. If the two laser beams have pulse durations on the order of $100fs$, finding the spatial and temporal overlap becomes a two dimensional problem where a spatial alignment error on the order of $\sim 100\mu m$ could destroy the possibility of finding the "zero" in time. An easier way would be therefore if the two problems could be solved independently and this solution based on the dissociative ionization of H_2 is presented below.

Two-color dissociative ionization of H_2 involving one XUV and one or more IR photons is possible according to:

$$H_2 + XUV \rightarrow H_2^+ \; and \;\; H_2^+ + IR \rightarrow H^+ + H \tag{7.2}$$

If one chooses as XUV radiation the $11th$ harmonic of the $800nm$ fundamental radiation, then the H_2 molecule can be ionized (the ionization potential for H_2 molecule is $15.425eV$) but not dissociated (eq.7.2). Therefore after the interaction with the XUV radiation the molecule is in one of the vibrational states of the ionic ground state. If after this step the resulting H_2^+ molecular ion is irradiated with $800nm$ radiation, then dissociation of the ion can take place and H^+ fragments are detected. Hence, there is an obligatory order in time between the two laser beams in order to obtain H^+ fragment. If the IR radiation hits the H_2 molecules before the XUV radiation no H^+ signal is detected, while when the XUV radiation comes on the sample before the IR radiation H^+ fragments are formed. Hence the method presented above does not only allow one to find the zero time delay between the two pulses but can be also a way of estimating the pulse duration of the XUV pulse.

The photoelectron spectrum obtained in Ar when the IR pulse comes $\sim 2.5ps$ before the XUV pulse is shown in Fig.7.3 (squares). In this figure contributions from the 13th harmonic and a very weak contribution from the 15th harmonic can be observed. The ratio between the two peaks in the kinetic energy distribution is about 1:90. The kinetic energy distribution was obtained by integrating the radial distribution of the experimental data (images are not shown here) after applying the inversion procedure presented in Chapter 3. The detector was calibrated by using an ATI photoelectron spectrum obtained with the IR pulse from Xe atoms. In the electron spectrum obtained when the XUV and the IR beams are temporally overlapped one can observe the appearance of a side-band between the harmonic 13th and 15th (Fig.7.3 (circles)). A few other features of the kinetic energy distribution can also be observed. The amplitude of the peak that appears in the electron spectrum due to the 13th harmonic alone ($\sim 4eV$) decreases by $\sim 5\%$ when the XUV and the IR pulses are overlapped (circles) compared to the situation when they come $\sim 2.5ps$ apart (squares). This shows that the channel due to the 13th harmonic is depleted when the IR beam overlaps with the XUV beam. At the same time an increase of about $\sim 45\%$ in the signal at the energy of the 15th harmonic ($\sim 7.1eV$) is observed when the two beams are overlapped. This can be explained by the fact that if the IR radiation is strong enough, sideband peaks corresponding to absorption of two IR photons appear in the electron spectrum.

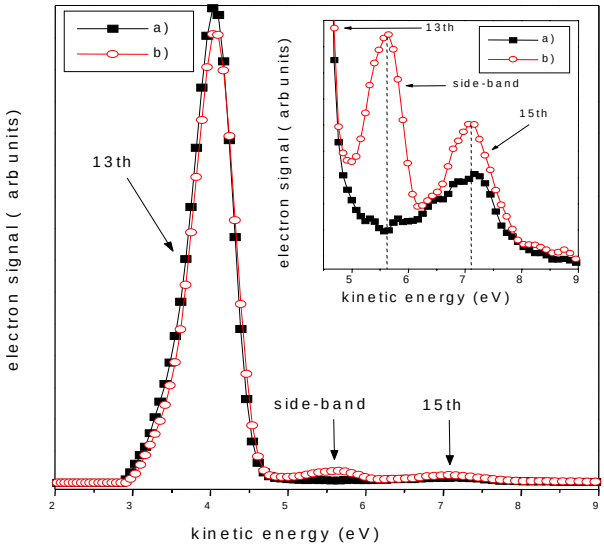

Figure 7.3: *Photoelectron spectra obtained by ionizing Ar using XUV and IR radiation when a) the IR pulse comes* $\sim 2.5ps$ *before the XUV and b) the IR and the XUV radiation are ovelaped. The insert shows a magnification of the kinetic energy distribution of the portion where the side-band appears in the photoelectron spectra.*

Because the energy difference between the 13th harmonic and its second side-band is exactly 2 x the IR photon energy, the latter will be overlapped with the next or previous harmonic (15th or 11th). Because of the very strong signal resulting from the 13th harmonic the side-bands with smaller kinetic energy (where IR photons are emitted) could not be observed. Because the IR pulse duration is $< 100fs$ and the expected XUV pulse duration is $\sim 500fs$, the temporal overlap is obtained only for the duration of the IR pulse and therefore the XUV photons are not all participating in the formation of the side-bands. This is the reason why, although we can observe the second side-band, the first side-band represents only 2.5% of the signal obtained from the 13th harmonic when the IR pulse is not overlapped with the XUV pulse.

By monitoring the amplitude of the first side-band (Fig.7.3 - insert, circles) as a function of the time delay between the 13th harmonic and the IR pulse we could measure the pulse duration of the 13th harmonic (Fig.7.4a). We obtained a broad non-gaussian distribution (squares) that could be fitted by two gaussians with a FWHM of about $750fs$ and $375fs$ separated by $\sim 540fs$. Below we will present calculations that we have performed in order to understand this result.

Similar measurements were also performed for lower harmonics (11th - see Fig.7.4b). For these measurements the influence of the neighboring harmonics was larger. Therefore these measurements have to be repeated in conditions where (by using a pinhole for example) only one harmonic is selected and focused in the interaction region to

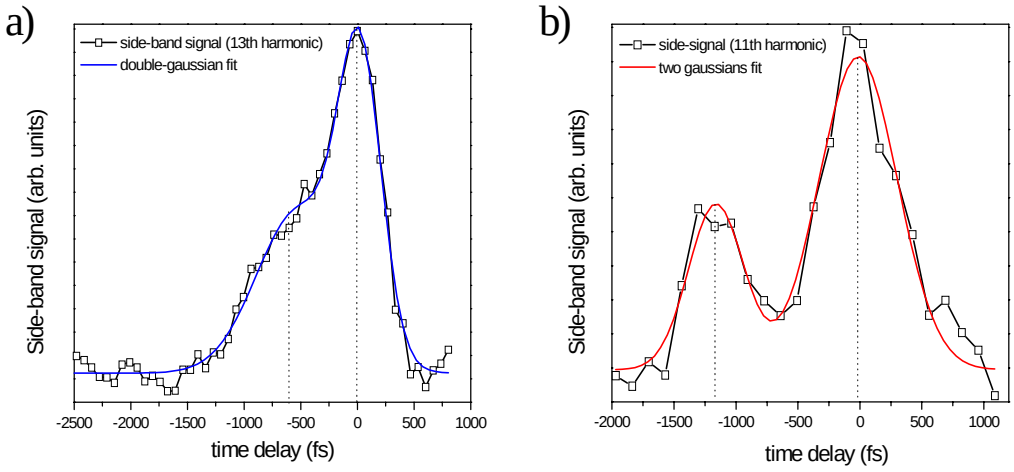

Figure 7.4: *The side-band signal in the electron spectrum obtained from the ionization of Ar with a) the 13th harmonic or b) 11th harmonic and IR pulse, as a function of the delay between the XUV and the IR radiation. The experimental data (squares) could be fitted with two gaussians (solid line). a) In the 13the harmonic measurement the first (small) gaussian has a FWHM of about* $750fs$ *and the second (tall) gaussian has a FWHM of about* $375fs$ *and they are separated by* $\sim 540fs$*. b) In the 11the harmonic measurement the first (small) gaussian has a FWHM of about* $450fs$ *and the second (tall) gaussian has a FWHM of about* $650fs$ *and they are separated by* $\sim 1140fs$*.*

ensure a clean XUV-IR dependence of the side-band signal. In principle, shorter pulse durations for higher-order harmonics are expected.

Raytracing was performed to calculate the expected value for the harmonic pulse duration measured in a cross-correlation in conditions of our experimental setup where the harmonics are used after reflection on the grating. The parameters on which the pulse duration depends strongly are shown in Fig.7.5. The first parameter is the divergence of the incident harmonic on the grating ($\Delta\beta$). Rays that hit the grating in different places have different path length from the generation point source to the point where the experiment takes place ($[ABD] \neq [ACE]$). The difference in the path length results in a difference in the time needed by the different rays to reach the intersection with the IR beam. The second parameter is the bandwidth of the harmonic ($\Delta\lambda$). After the curved grating, different wavelength are focused in different places in the interaction region. Therefore, one would expect the bandwidth of the harmonic to influence the pulse duration measurement as long as all the wavelengths overlap with the IR beam. Hence, the size of the IR radiation (w) represents another important parameter that one has to take into consideration.

Calculations of the propagation of the laser beams, where all the above mentioned parameters were varied, are presented in Fig.7.6 and Fig7.7. In these calculations the

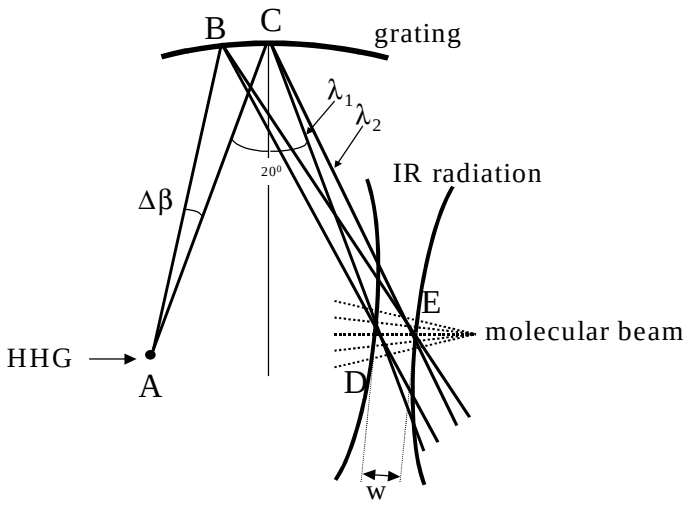

Figure 7.5: *The harmonic pulse duration after the grating is determined by the parameters shown in the figure: the divergency of the incident harmonic on the grating ($\Delta\beta$), the bandwidth of the harmonic ($\Delta\lambda$) and the size of the IR beam (w).*

molecular beam was considered to have a rectangular shape with $2mm$ width across the interaction region. Fig.7.6 shows that for a collimated, monochromatic harmonic beam and a very narrow IR beam ($w = 0.1mm$) the stretch of the harmonic due to the grating is very small (dotted line). The measured harmonic pulse duration in this situation is $< 20fs$. If we consider that the collimated harmonic beam has a bandwidth of $\Delta\lambda = 0.5nm$, then the pulse duration is increased to $60fs$ (full circles). For the same harmonic properties but a wider IR beam ($w = 0.5mm$), the FWHM of the harmonic pulse duration increases to $260fs$ (open circles). If a harmonic beam with the same properties as the one presented above is considered to have a divergence $\Delta\beta = 0.001rad$ (this value is the expected for the conditions of our experimental setup), then the width of temporal profile increases to $335fs$ (triangles). Based on the calculations presented in Fig.7.6 one can conclude that the measured harmonic pulse duration depends on its bandwidth ($\Delta\lambda$), where the range of wavelengths that contributed is limited by the width of the IR beam (w). Hence for narrow IR beam the resolution of the cross-correlation measurement can still be $< 100fs$.

Fig.7.7 shows the same kind of dependencies as Fig.7.6 but in the conditions where the divergence of the harmonic beam is varied. The dotted line is the same as the one shown in Fig.7.6 and is presented only for comparison with the other curves. For a monochromatic harmonic beam with a divergence of $\Delta\beta = 0.001rad$ and an IR spot size of $w = 0.1mm$, the FWHM of the harmonic pulse duration increases to $175fs$ (full circles). If in the same conditions, a larger IR spot size ($w = 0.5mm$) is used to probe the measurement (open circles) an increase to $195fs$ is obtained. As before, if

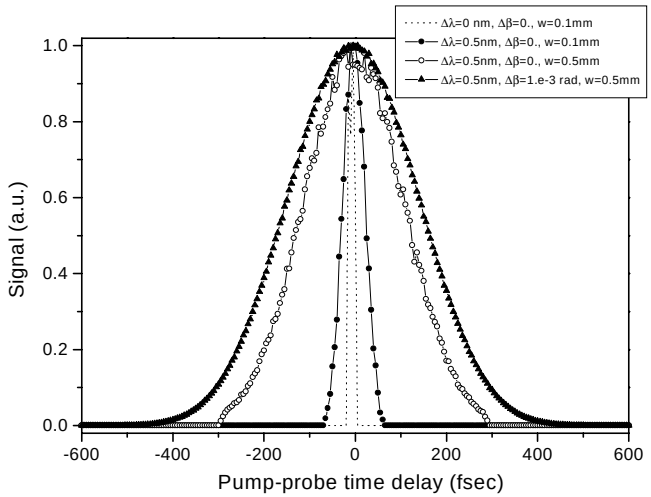

Figure 7.6: *The harmonic pulse duration as a function of the bandwidth of the harmonic ($\Delta\lambda$), the divergence of the incident harmonic on the grating ($\Delta\beta$), and the size of the IR beam (w). From the comparison of the four curves results that the size of the IR beam is a very important parameter in a cross-correlation measurement.*

the harmonic beam has a bandwidth $\Delta\lambda = 0.5nm$ and a divergence $\Delta\beta = 0.001rad$ and the IR size spot is $w = 0.5mm$, the FWHM of the harmonic temporal profile is increased to $335fs$ (triangles). Based on the calculations presented in Fig.7.7 one can therefore conclude that the measured harmonic pulse duration in a cross-correlation measurement strongly depends on the harmonic divergence ($\Delta\beta$), without a strong dependence on the width of the IR beam (w). This is due to the fact that all divergent rays of the same wavelength are focused to the same spot in the detection region.

From these calculations we can therefore conclude that the influence of the grating on the harmonic pulse duration is related, as expected, to the divergence of the harmonic beam incident on the grating and to the bandwidth of the harmonic beam. The first parameter seems to influence the harmonic pulse duration in the experimental interaction region the most. Moreover, the size of the IR beam that is used as a probe in measuring the harmonic pulse duration is also a very important parameter. Using the conclusions of these calculations we have tried to analyze the distribution obtained from the cross-correlation measurement (Fig.7.4). Based on the focal geometry of the harmonic generation and the probe IR laser and assuming a scaling of harmonic bandwidth with the square root of the harmonic order, we would expect a harmonic divergence of $0.001rad$, a bandwidth of $0.5nm$ and a width for the IR beam of $500\mu m$. For negligible pulse duration of the XUV and the IR and according to Fig.7.6 and Fig7.7, we anticipate a $335fs$ FWHM cross-correlation measurement for the harmonic pulse duration under these conditions. In the cross-correlation measurement we have obtained a non-gaussian distribution with a FWHM of about $1ps$ (Fig.7.4a). The dif-

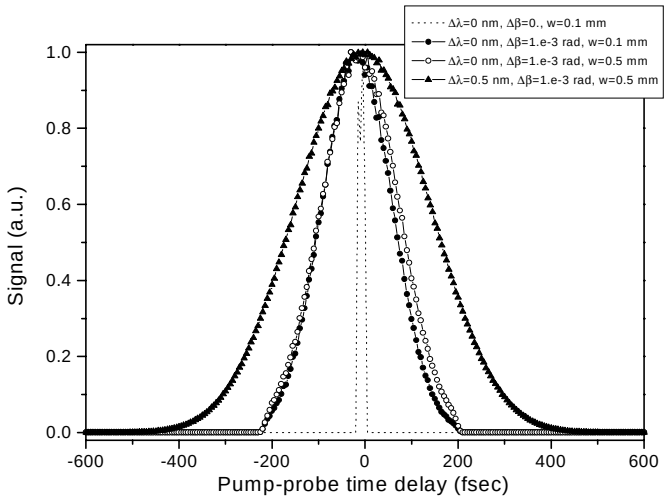

Figure 7.7: *The harmonic pulse duration as a function of the bandwidth of the harmonic ($\Delta\lambda$), the divergence of the incident harmonic on the grating ($\Delta\beta$), and the size of the IR beam (w). From the comparison of the four curves results that the divergence of the harmonic beam is a very important parameter in a cross-correlation measurement.*

ference is either due to the pulse duration of the XUV and/or the IR beam or it is due to the differences in the parameters mentioned above. Since the IR and XUV pulse duration are not expected to exceed 100fs the difference between the calculated and the measured value may come from the fact that in our experiment the divergence of the harmonic beam was larger than the value considered in the calculations. This can be in part, due to the fact that the spatial profile of the driving field is not a perfect gaussian and therefore the focus spot size of the fundamental is not equal with the diffracted-limited value. This would induce a higher divergence in the harmonic beam than the one calculated based on the diffraction-limited value. Nevertheless, this is not expected to generate a large difference. Another reason why the divergence may be much larger than the one considered in the calculations is related with the harmonic generation process itself. It has been predicted theoretically [184,194] and observed experimentally [195] that if the driving laser focuses before the gas jet used for harmonic generation, the optimum phase-matching condition is realized mainly *on axis*, thus resulting in a smooth spatial profile of the harmonic beam. On the other hand, when the diving field focuses after the gas jet, this results in an optimization of harmonic efficiency *off axis,* which gives rise to complex ring structures, wide beam divergences and poor spatial coherence. In the conditions of the experiment presented in [195], the divergence of the harmonic beam could be varied by one order of magnitude by changing the focussing geometry. We can therefore conclude that the divergence of the harmonic beam in our experiment could have been much larger than the value used in the calculation and therefore a larger pulse duration could be measured in the

cross-correlation. The *off axis* generation of the harmonic beam could also explain the shape of the distributions presented in Fig.7.4. If we assume that the spatial profile of the harmonic beam in the detection region has a donut-like distribution, then the cross-correlation measurement results in a two-peaks distribution where the time separation is correlated with the spatial separation. The fact that in the measurement of the 13th harmonic (Fig.7.4a) the two gaussian are closer to each other, than in the measurement performed with the 11th harmonic (Fig.7.4b), suggests, as expected, that the harmonic divergence is larger for lower order harmonics.

Another parameter which can introduce a difference between the theory and experiment is the bandwidth of the harmonic. Although the $13th$ harmonic that has been used for the cross-correlation measurement is well in the plateau of the harmonic generation, we have calculated the harmonic bandwidth as if it was in the perturbative regime. This means that the actual bandwidth may be larger than the $0.5nm$ considered in the calculations and therefore a larger pulse duration could be measured. As mentioned before, another important parameter is the size of the IR beam that is used to probe the cross-correlation measurement. The value considered in the calculation was $500\mu m$, but due to the non-gaussian spatial distribution, it is possible that the actual spot size of the IR beam in the detection region was larger in the experiment, leading therefore to lower resolution. In conclusion, we think that a convolution of all these parameters led to an increased measured pulse duration above the expected value.

In the future a more detailed series of harmonic pulse duration measurements is planned where cross-correlation measurements will be combined with simultaneous measurements of the harmonic spectrum and beam divergence.

7.4 Outlook

The work presented in this thesis shows that in the XUV Physics group at Amolf, we have developed a laser system which is able to generate short-intense infrared laser pulses (Chapter 2) which can be used directly in experiments (Chapter 4 and 6) or can be used for generation of short wavelength radiation (Chapter 7). Therefore we have at this moment all the tools that are necessary for XUV-IR pump-probe experiments that are very important for time-resolved studies of molecular dynamics.

The cross-correlation measurement was just an example how one can use our system to set up such a pump-probe experiment. Other interesting experiments are yet to come. One of these experiments is based on the results obtained in the experiment presented in Chapter 6. Here we have used a long IR laser pulse ($\sim 1ps$) to align molecules along the polarization axis via Raman transitions and we have used a short IR pulse ($\sim 70fs$) to probe the alignment at different time delays following the excitation. In this pump-probe experiment we have discussed the influence of the probe laser on the final angular distributions based on the results obtained from the experiment presented in Chapter 4, where only one laser was use to induce and to probe the alignment. Hence,

the use of an XUV pulse as a 'clean' probe of the alignment induced by the IR pulse would be a more convenient way the follow the evolution of the molecular alignment in time.

Another application for the pump-probe XUV-IR setup is the study of the photodissociation of H_2^+. The mechanism to produce H^+ through $XUV + IR$ dissociative ionization of H_2 shown in eq.7.2 is not only useful for finding the zero time delay between the XUV radiation and the IR radiation as was presented in the previous section, but is also interesting from the point of view of the physics which is involved in this photodissociative ionization process [197, 198].

Experimental and theoretical studies have revealed a number of interesting features in strong-field photodissociation, which can only be understood in terms of complex multiphoton interactions, involving stimulated emission as well as absorption. The availability of XUV radiation allows us to study strong field IR dissociation completely separately from the (strong field) ionization process. Using the XUV radiation as a preparation tool to create hydrogen molecular ion in a well known vibrational state, could be an easier way of studying in more details the dissociation process. Examples of processes that can occur during the dissociation are: above-threshold dissociation (ATD) [199], bond-softening [200] and bond hardening or population trapping [201].

Molecular photodissociation/ photoionization processes can be studied in our laboratory also in combination with an atomic streak camera [65]. As presented in Chapter 3, in the experimental chamber, in the upward direction along the vertical symmetry axis of the apparatus ions are detected by a velocity-map imaging detector [64]. In the downward direction an atomic streak camera [65] will be installed. The combination of the two detection systems will allow time-resolved detection of electrons and ions produced in the same photodissociation/ionization process and therefore much better physical insight into these processes can be obtained.

In conclusion, in our group we have set up all the tools that are necessary for time-resolved studies of the dynamics that are involved in molecular photodissociation/ photoionization processes, where the XUV radiation can be used as a pump or as a probe laser pulse in XUV-IR pump-probe experiments.

Summary

The title of this thesis is "Alignment of diatomic molecules by intense laser fields". In the interaction with intense laser fields, molecules can not only be excited, ionized (lose electrons) or dissociated (break in fragments), but can also be forced to align along the direction of the laser polarization axis. In the following pages, a simple description and explanation of this process is presented.

First of all, to study these processes an intense laser is needed. This is why, in the first part of my Ph.D., I was part of the team that built what we call now "the Amolf Terawatt laser system" (Chapter 2). Alignment is a rapid process that takes place on a (sub)picosecond (10^{-12} sec $= p$sec) time scale. Therefore, the pulse duration of the laser pulse that follows the dynamics of this process has to be on the same order of magnitude or shorter to ensure time resolution.

In the majority of experiments, a relatively high intensity is required. Therefore, the short laser pulses have to be amplified. The amplification of short pulses is done using a technique called "Chirped Pulse Amplification" that will be explained below (Fig.2.1).

The intensity of a laser pulse is defined as:

$$Intensity = \frac{Energy}{Beam\ size \times Pulse\ duration}$$

To keep the pulse intensity low during the amplification (when the pulse energy increases), the size of the laser beam or the pulse duration has to be increased. The first option has a practical limitation related to the size of the optical components when we talk about amplification by a factor of 10^6. Therefore, in order to amplify the laser pulse without reaching the damage threshold of the optical components, the pulse duration has to be increased. This is done by stretching the pulse. Stretching the short pulse makes its frequency spectrum vary linearly in time, just like the frequency spectrum of the chirp of a bird. This is why the pulse at the output of the stretcher is called a "chirped pulse".

In the "Chirped Pulse Amplification" technique, the short pulse is first stretched, then amplified and, at the end of the laser system, compressed back to its original duration (Fig.2.1). In our system, the laser pulse after the compressor has a duration of $50f$ sec, an energy of $30mJ$ at a $50Hz$ repetition rate and a central wavelength around

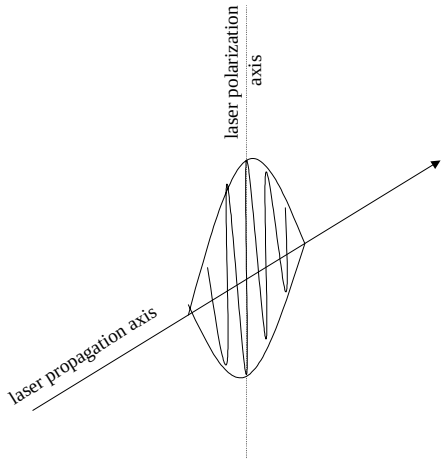

Figure 1: *A laser is electromagnetic radiation that has a direction of propagation ("laser beam") and a direction of oscillation ("polarization axis" - in the simplest case of linearly polarized light).*

$800nm$ (near-infrared). This performance brings the output power of the system to the Terawatt regime ($10^{12}W$) .

Now that we have a powerful laser, it is time to come back to the studies mentioned in the beginning: laser-induced alignment of molecules. To understand this effect, one has first to understand a little about the interaction between matter and lasers. The laser is electromagnetic radiation that has a direction of propagation ("laser beam") and a direction of oscillation ("polarization axis" - in the simplest case of linearly polarized light) (see Fig.1). Molecules can absorb light (photons) and as a result, they can be excited and emit radiation or can ionize or dissociate. About a decade ago, it was observed that the fragments resulting from the interaction of molecules with an intense laser were emitted mainly in the direction of the laser polarization axis. The question was: Does the laser break only the molecules that are aligned along the polarization axis, resulting in fragments along this axis? Or does the laser rotate the molecules towards the polarization axis before it breaks them? (Fig.2).

When a molecule is situated in an electric field, the molecule becomes polarized: the negative charges (electrons) move towards the positive part of the electric field and the positive charges (nuclei) towards the negative part of the laser pulse. In this way, one end of the molecule becomes a little bit positive and the other end becomes a little bit negative and the molecule is forced to rotate towards the polarization axis of the laser field. The laser field oscillates, which means that the direction of the field is reversed every half cycle. However, as shown in Fig.3, the direction of the force on the molecule is always in the same direction - towards the laser polarization axis.

To study the alignment of molecules, we have chosen to use a detection system

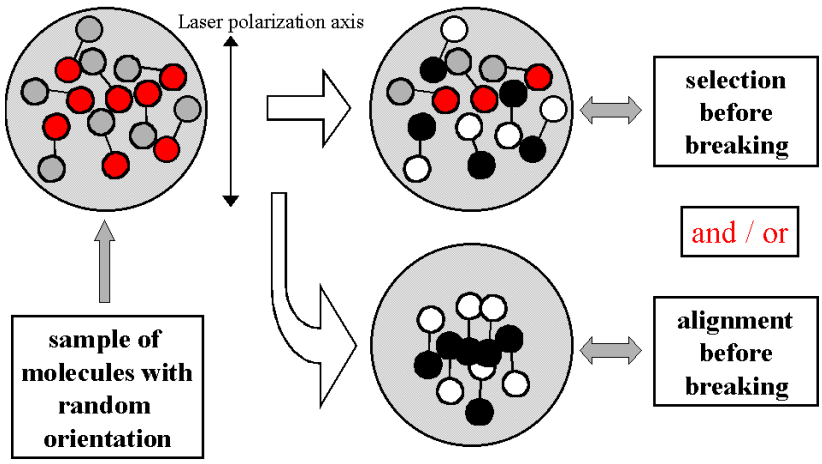

Figure 2: *Does the laser break only the molecules that are aligned along the polarization axis, resulting in fragments along this axis? Or does the laser rotate the molecules towards the polarization axis before it breaks them?*

that give us a direct measurement of the velocity of molecules with respect to the laser polarization axis before the fragmentation takes place.

Typical images showing molecular fragments resulting from the interaction of the laser with diatomic molecules (bromine/ iodine) are shown in Fig.4 (one of these images is also shown on the cover of the thesis). The laser polarization is along the vertical axis of these images. Fig.4a was obtained when the laser pulse was too short ($80f$ sec) and too intense to permit any rotation of the molecule before fragmentation. This conclusion is drawn from the fact that the angular distribution of the fragments is relatively wide with respect to the laser polarization axis. The fact that the distribution peaks along the polarization axis is due to the fact that, in the fragmentation process, the laser selects the molecules whose molecular axis makes a small angle with the polarization axis. In Fig.4b, where the fragmentation was done using a $2.5p$ sec laser pulse, the distribution is much narrower along the polarization axis due to the fact that molecules are aligned along the polarization axis before the fragmentation process takes place.

Using the results of this experiment, which are presented in detail in Chapter 4 and 5 of this thesis, one can answer the question asked above: The fact that the fragments are flying along the polarization axis after the laser breaks the molecule is due to a combination of two factors. First, the laser can more easily break the molecules that are aligned along the polarization axis and therefore the probability of breaking a molecule is not the same for any initial angle of the molecule with respect to the laser

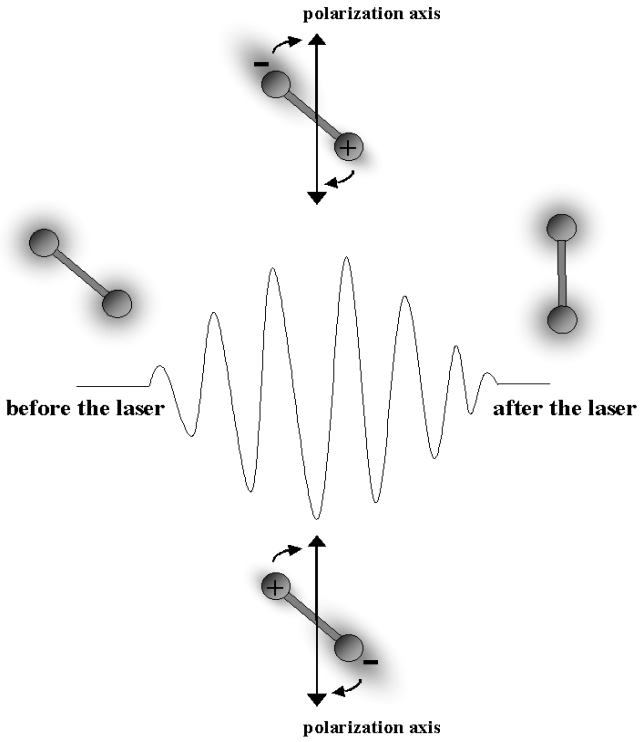

Figure 3: *A molecule is polarized by an electric field: the negative charges (electrons) move towards the positive part of the electric field and the positive charges (nuclei) towards the negative part of the laser pulse. In this way, one end of the molecule becomes a little bit positive and the other end becomes a little bit negative and the molecule is forced to rotate towards the polarization axis of the laser field.*

polarization axis. Secondly, the laser can also force the molecules to align along its polarization axis. If the laser pulse is very short ($\leqslant 100f$ sec), molecules have no time to rotate and therefore the distribution is wide and mostly given by the selectivity in the fragmentation process (Fig.4a), while if the laser pulse is long ($\geqslant 1p$ sec) the distribution is narrow, dominated by the alignment process (Fig.4b).

In the alignment process, the molecules are aligned along the polarization axis towards the end of the laser pulse. When the laser pulse is finished, molecules start to rotate freely and the alignment is lost. Due to the fact that at the end of the laser pulse the molecules are aligned, they all become aligned again along the polarization axis at later times, but this time in field-free conditions (the laser field is no longer present).

To study the dynamics of the alignment process, one can use one laser to induce the alignment (this laser pulse must be weak enough not to break the molecules) and a second laser to probe the alignment by breaking the molecules and detecting the

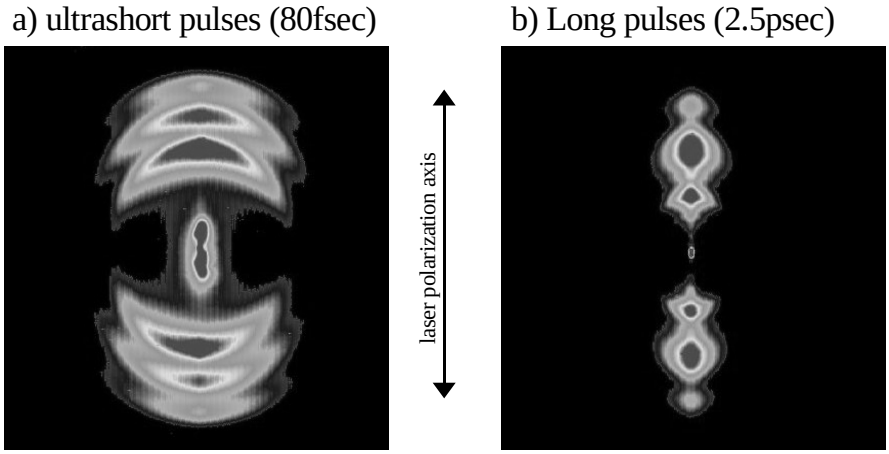

Figure 4: *a) For ultrashort pulses the angular distribution is wide and is mostly given by the selectivity of the laser in the fragmentation process. b) For long pulses the angular distribution is narrow due to the alignment of the molecules induced by the laser before the fragmentation process.*

distribution of the fragments at different time delays with respect to the action of the first laser. One example of this kind of measurement is shown in Fig.6.8 where the width of the angular distribution with respect to the polarization axis of the first laser is plotted as a function of the delay between the first and the second laser. One can observe from this graph that, indeed, the molecules have in the beginning a wide distribution (a) that gets narrower during the laser pulse (b). After the laser pulse is finished the distribution gets wider but still narrower than the initial distribution and at a very well defined time (depending on the properties of the molecules) it gets narrower again (c) showing the alignment in field-free conditions.

The possibility of creating a sample of aligned molecules in field-free conditions (when the laser action is finished) was predicted theoretically a few years ago, but we are the first laboratory to demonstrate this effect, which is presented in detail in Chapter 6. The importance of these studies is that aligned molecules represent a system with less degrees of freedom and therefore the study of chemical reactions or other molecular processes can be simplified (one can study the angular dependence of these processes relative to the direction of the molecule).

Samenvatting

De titel van dit proefschrift is "Het uitlijnen van twee-atomige moleculen met behulp van intense laser velden". Tijdens de interactie met intense laser velden, worden moleculen niet alleen geexciteerd (toename van electronische, vibrationele of rotationele energie), geioniseerd (het verliezen van electronen) of gedissocieerd (in fragmenten gebroken), maar kunnen moleculen ook gedwongen worden om zich te richten naar de polarisatie as van de laser. In de volgende pagina's wordt een simpele verklaring gegeven van dit proces, dat het hoofdthema vormt van dit proefschrift.

Om het uitlijnen van moleculen te bestuderen is een intense laser nodig. Daarom maakte ik in het eerste gedeelte van mijn promotie deel uit van het team dat de "De Amolf Terawatt Laser" heeft gebouwd (hoofdstuk 2). Uitlijnen van moleculen is een snel proces dat plaatsvindt op een (sub)picoseconde ($10^{-12} sec$) tijdschaal. Daarom moet de pulsduur van de laser die de dynamika van dit proces volgt van dezelfde grootte orde of korter zijn. Voor de meerderheid van de experimenten is een relatief hoge intensiteit nodig. Daarom moet de korte laser puls versterkt worden. De versterking van korte pulsen wordt gedaan door gebruik te maken van een techniek die "Chirped Pulse Amplification" heet, en die hieronder uitgelegd zal worden (Fig.2.1).

De intensiteit van een laser puls is gedefinierd als:

$$Intensiteit = \frac{Energie}{Bundeloppervlak \times Pulsduur}$$

Om de laser puls te versterken zonder de optische componenten te beschadigen, moet de puls intensiteit gedurende de versterking (wanneer de puls energie toeneemt) laag gehouden worden. Hiertoe kan het oppervlak van de laser bundel of de pulsduur vergroot worden. De eerste optie kent practische bezwaren die te maken hebben met de grootte van de optische componenten die nodig zijn als we praten over een versterking van een factor 10^6. Daarom wordt ervoor gekozen de duur van de puls langer te maken. Het uitrekken van een korte puls is mogelijk door het frequentie spectrum lineair in de tijd te variëren, vergelijkbaar met het frequentie spectrum bij het tjilpen van een vogel. Daarom wordt deze puls een "gechirpte puls "genoemd.

In de "Chirped Pulse Amplification" techniek, wordt een korte puls eerst langer gemaakt, dan versterkt en aan het einde van het laser systeem gecomprimeerd naar zijn oorspronkelijke pulsduur (Fig.2.1). In ons systeem zijn de parameters van de laser puls: een pulsduur van $50 fsec$, een energie van $30 mJ$, een $50 Hz$ repetitie frequentie

en een centrale golflengte van $\pm$ 800nm (nabij infrarood). Deze opstelling brengt het eind vermogen naar het Terawatt regime ($10^{12}W$).

Nu we een krachtige laser hebben, is het tijd om terug te komen op het uitlijnen van moleculen. Om dit effect te begrijpen moeten we eerst iets begrijpen van de interactie tussen lasers en materie. De laser is een bron van electromagnetische straling die een voortplantingrichting heeft (de "laser bundel") en een oscillatierichting (de "polarisatie as" - in het eenvoudigste geval van lineair gepolariseerd licht) (zie Fig.1). Moleculen kunnen licht absorberen (fotonen) en als gevolg daarvan kunnen zij aangeslagen worden en straling uitzenden, en zij kunnen ioniseren of uit elkaar vallen. Ongeveer tien jaar geleden was waargenomen dat geioniseerde fragmenten gevormd in de interactie van moleculen met een intense laser hoofdzakelijk werden uitgezonden in de richting van de laser polarisatie as. De vraag was: Breekt de laser alleen moleculen die zijn uitgelijnd langs de polarisatie as en resulteert dit in fragmenten langs die as? Of trekt de laser de moleculen naar de polarisatie as toe, voordat de laser ze breekt? (Fig.2).

Wanneer een molecuul zich in een laser veld bevindt, wordt het molecuul gepolariseerd: de negative ladingen (de electronen) bewegen zich enigszins naar de positieve kant van het laser veld en de positieve ladingen (de atoomkernen) bewegen zich naar de negatieve kant van de laser puls. Op deze manier wordt het ene uiteinde van het molecuul een beetje positief en het andere uiteinde een beetje negatief en tevens wordt de as van het molecuul gedwongen te draaien langs de laser polarisatie as. Het laser veld oscilleert, wat betekent dat de richting van het veld elke halve periode omdraait. Echter, zoals in Fig.3 kan worden gezien, de richting van de krachten op de moleculen is altijd in dezelfde richting - naar de laser polarisatie as.

Om de uitlijning van moleculen te bestuderen, hebben wij gekozen voor een detectie systeem dat ons direct een meting geeft van de stand van de moleculen ten opzichte van de polarisatie as voordat de fragmentatie plaatsvindt. Typische plaatjes, die moleculaire fragmenten laten zien die resulteren van de interactie van de laser met twee-atomige moleculen (bromine / iodine) zijn te zien in Fig.4 (één van deze plaatjes is ook te zien op de omslag van het proefschrift). De laser polarisatie is langs de verticale as van deze plaatjes. Fig.4a werd verkregen onder omstandigheden waar de laser puls te kort (80fsec) en te intens was om het molecuul te laten roteren voordat de fragmentatie plaatsvond. Deze conclusie werd getrokken uit het feit dat de hoekverdeling van de fragmenten ten opzichte van de polarisatie as relatief breed is. Het feit dat de verdeling piekt langs de polarisatie as komt omdat de laser met name moleculen selecteert van wie de moleculaire as een kleine hoek maakt met de polarisatie as. In Fig.4b, waar de fragmentatie werd gedaan met een 2.5psec laser puls, is de hoekwerdeling langs de polarizatie as veel smaller omdat de moleculen eerst werden uitgelijnd langs de polarisatie as voordat het fragmentatie proces plaatsvond.

Op basis van deze resultaten, die in detail worden gepresenteerd in hoofdstukken 4 en 5 van dit proefschrift, kunnen wij de eerder gestelde vraag nu beantwoorden: Het feit dat de fragmenten langs de polarizatie as wegvliegen komt door een combinatie van twee factoren. Ten eerste kan de laser gemakkelijker moleculen breken die zijn uitgelijnd langs de polarisatie as en is daarom de waarschijnlijkheid van ionisatie en splitsing van

een molecuul niet hetzelfde voor elke starthoek van het molecuul ten opzichte van de laser polarisatie as. Ten tweede kan de laser het molecuul ook dwingen om zich naar de polarisatie as te richten. Als de laser puls erg kort is ($\leq 100 fsec$), hebben moleculen geen tijd om te draaien en daarom is de verdeling breed en voornamelijk bepaald door de selectiviteit in het fragmentatie proces (Fig.4a). Als de laser puls lang is ($\geq 1 psec$), is de verdeling smaller als gevolg van het uitlijnproces (Fig.4b).

In het uitlijnproces, zijn de moleculen aan het einde van de laser puls uitgelijnd langs de polarisatie as. Wanneer de laser puls voorbij is, beginnen de moleculen vrij te draaien en verdwijnt de uitlijning. Als gevolg van het feit dat aan het einde van de laser puls de moleculen uitgelijnd zijn, worden ze later - als ze allemaal een geheel aantal keren gedraaid hebben - opnieuw langs de polarisatie as uitgelijnd, maar deze keer onder veld-vrije omstandigheden (zonder dat er een laser puls aanwezig is).

Om de dynamika van het uitlijnproces in detail te bestuderen, hebben we een eerste laser (zwak genoeg om de moleculen niet te breken) gebruikt om het uitlijnproces teweeg te brengen en een tweede - tijdvertraagde - laser om het uitlijnproces te volgen. Dit laatste gebeurde door de moleculen te breken en de distributie van de fragmenten te detecteren op verschillende tijdstippen na de interactie met de eerste laser. Een voorbeeld van dit soort metingen is te zien in Fig.6.8, waar de breedte van de hoekverdeling ten opzichte van de polarisatie as van de eerste laser wordt gegeven als functie van het tijdsverschil tussen de eerste en de tweede laser. We kunnen zien dat de moleculen in het begin een brede hoekverdeling hebben (a) die smaller wordt tijdens de laser puls (b). Nadat de laser puls voorbij is, wordt de verdeling weer breder al blijft hij nog steeds smaller dan de oorspronkelijke verdeling, en op latere tijdstippen (afhankelijk van de eigenschappen van het molecuul) wordt de verdeling weer smaller (c) als het uitlijnen in veldvrije condities optreedt.

De mogelijkheid om een sample van uitgelijnde moleculen onder veldvrije omstandigheden te maken was theoretisch enkele jaren geleden voorspeld, maar we zijn het eerste laboratorium dat dit effect (dat in hoofdstuk 6 gedetailleerd beschreven wordt) heeft waargenomen. Het belang van deze studie is dat uitgelijnde moleculen een systeem met minder vrijheidsgraden vormen, waardoor de bestudering van chemische reacties of andere procesen gesimplificerd kan worden. Op basis van de resultaten van dit proefschrift kunnen we deze processen nu in afhankelijkheid van de richting van het molecuul bestuderen.

Bibliography

[1] A.H. Zewail, *Femtochemistry. Ultrafast Dynamics of the Chemical Bond*, vol. 2, Ed. World Scientific (1994).

[2] H.C. Kapteyn and M.M. Murnane, Opt. Soc. Am.: Optics and Photonics News **3**, 20 (1994).

[3] P. Agostini and G. Petite, Contemp. Phys. **29** (1), 57 (1988).

[4] K. Burnett, V.C. Reed and P.L. Knight, J. Phys. B: At. Mol. Opt. Phys. **26**, 561 (1993).

[5] M. Protopapas, C.H. Keitel and P.L. Knight, Rep. Prog. Phys. **60**, 389 (1997).

[6] B. Sheehy and L.F. DiMauro, Annu. Rev. Phys. Chem. **47**, 463 (1996).

[7] K. Codling, L.J. Frasinski and P.A. Hatherly, J. Phys. B: At. Mol. Opt. Phys. **22**, L321 (1989).

[8] M.M. Murnane, H.C. Kapteyn, M.D. Rosen and R.W. Falcone, Science **251**, 531 (1991).

[9] R.A. London, M.D. Rosen and J.E. Trebes, Appl. Opt. **28** (15), 3397 (1989).

[10] K. Codling and L.J. Frasinski, Contemp. Phys. **35** (4), 243 (1994).

[11] X. Fang, K.W.D. Ledingham, P. Graham, D.J. Smith, T. McCanny, R.P. Singhal, A.J. Langley and P.F. Taday, Rapid Commun. Mass Spectrom. **13**, 1390 (1999).

[12] See J.H. Posthumus, J. Plumridge, M.K. Thomas, K. Codling, L.J. Frasinski, A.J. Langley and P.F. Taday, J. Phys. B: At. Mol. Opt. Phys. **31**, L553 (1998), and references therein.

[13] Ch. Ellert and P.B. Corkum, Phys. Rev. A **59** (5), R3170 (1999).

[14] S. Banerjee, G. Ravindra Kumar and D. Mathur, Phys. Rev. A **60** (5), R3369 (1999).

[15] M. Schmidt, S. Dobosz, P. Meynadier, P. D'Oliviera, D. Normand, E. Charron and A. Suzor-Weiner, Phys. Rev. A **60** (6), 4706 (1999).

[16] a) S.Z. Bum, S.C. Hoi, C. Keunchang, H.L. Sung, H. Sungu, Y. Jongwan, Y.H. Ahn, J.K. Sohn, D.S. Kim, K.K. Wee, S.C. Doo, Phys. Rev. Lett. **85** (13), 2705 (2000). b) D.M. Villeneuve, S. Aseyev, M.Yu. Ivanov, P. Dietrich, P.B. Corkum, Proceedings of the International Conference on Lasers '99. STS Press, McLean, VA, USA; 2000; xiii+710 pp. p.260 (2000). c) T. Seideman, Journal of Chemical Physics **111** (10), 4397 (1999).

[17] J.-C. Diels and W. Rudolph, *Ultrashort Laser Pulse Phenomena*, Ed. Optics and Photonics (Academic Press 1996).

[18] G. Mourou, Apl. Phys. B **65**, 205 (1997).

[19] A. L'Huillier, L.A. Lompre, G. Mainfray, C. Manus, *Atoms in Intense Laser Fields*, Ed. M. Gavrila p.139 (Academic Press, New York, 1992).

[20] T. Sekikawa, T. Ohmo, T. Yamazaki, Y. Nabekawa and S. Watanabe, Phys. Rev. Lett. **83** (13), 2564 (1999).

[21] E.S. Toma, H.G. Muller, P.M. Paul, P. Beger, M.Cheret, P. Agostini, C. Le Blanc, G. Mullot and G. Cheriaux, Phys. Rev. A **62**, 061801 (R) (2000).

[22] M. Drescher, M. Hentschel, R. Kienberger, G. Tempea, Ch. Spielmann, M. Hentschel, G.A. Reider and F. Krausz, Science **291**, 1923 (2001).

[23] P.M. Paul, E.S. Toma, P. Breger, G. Mullot, F. Auge, Ph. Balcou, H.G. Muller and P. Agostini, Science **292**, 1689 (2001).

[24] a) H.M. Hertz, M. Berglund, G.A. Johansson, M. Peuker, T. Wilhein and H. Brismar, AIP-Conference Proceedings **507**, 721 (2000). b) Y. Yamamoto, H. Friedman, H. Yoshimura, Y. Kinjo, S. Shioda, K. Debari, K. Shinohara, J. Rajyaguru and M. Richardson, AIP Conference Proceedings **507**, 174 (2000). c) E. Uggerhoj, J.V. Abraham Peskir , AIP Conference Proceedings 507, 484 (2000).

[25] T.H. Maiman, Nature **187**, 493 (1960).

[26] J. Ringling, O. Kittelmann, F. Noack, U. Stamm, J. Kleinschmidt, F. Voss, Optics Letters **19** (20), 1639 (1994).

[27] R. Beck, W. Englisch, K. Gurs, *Table of Laser Lines In Gases and Vapors*, Springer Ser. Opt. Sci., Vol. **2**, 3rd ed. (Springer, Berlin, Heidelberg 1980).

[28] O.G. Peterson, S.A. Tuccio, B.B. Snavely, Appl. Phys. Lett. **17** (6), 245 (1970).

[29] H. Kressel, *Semiconductor Devices*, Topics Appl. Phys., Vol. **39**, 2^{nd} ed. (Springer, Berlin, Heidelberg 1982).

[30] A.J. DeMaria, D.A. Stetser, H. Heynau, Appl. Phys. Lett. **8** (7), 174 (1966).

[31] W. Krause, F. Volker and H. Weber, Proceedings of an ESA Workshop on SPLAT. Space Laser Applications and Technology (ESA-SP-202), ESA, Paris, France, P161 (1984).

[32] R.L. Fork, B.I. Greene, C.V. Shank, Appl. Phys. Lett. **38** (9), 671 (1981).

[33] D.E. Spence, P.N. Kean, W. Sibbett, Opt. Lett. **16** (1), 42 (1991).

[34] C.-P. Huang, H.C. Kapteyn, J.W. McIntosh and M.M. Murnane, Opt. Lett. **17** (2), 139 (1992).

[35] C.-P. Huang, M.T. Asaki, S. Backus, M.M. Murnane, H.C. Kapteyn, Opt. Lett. **17** (18), 1289 (1992).

[36] M.T. Asaki, C.-P. Huang, D. Garvey, J. Zhou, H.C. Kapteyn, M.M. Murnane, Opt. Lett. **18** (12), 977 (1993).

[37] Ch. Spielmann, P.F. Curley, T. Brabec, F. Krausz, IEEE Journal of Quantum Electronics **30** (4), 1100 (1994).

[38] A. Stingl, Ch. Spielmann, F. Krausz, R. Szipocs, Opt. Lett. **19** (3), 204 (1994).

[39] A. Stingl, M. Lenzner, Ch. Spielmann, F. Krausz, Opt. Lett. **20** (6), 602 (1995).

[40] a) V.P. Kalosha and J. Herrmann, Opt. Soc. Am. **318**, 114 (2000). b) L. Chai, Q. Wang, W. Zhang, Q. Xing, Chinese Journal of Lasers **A 27**(5), 407 (2000).

[41] P. Maine, D. Strickland, P. Bado, M. Pessot, G. Mourou, IEEE J. of Quantum Electronics **24** (2), 398 (1988).

[42] J.D. Kmetec, J.J. Macklin, J.E. Young, Opt. Lett. **16** (13), 1001 (1991).

[43] A. Sullivan, H. Hamster, H.C. Kapteyn, S. Gordon, W. White, H. Nathel, R.J. Blair, R.W. Falcone, Opt. Lett. **16** (18), 1406 (1991).

[44] C.P.J. Barty, C.L. Gordon III, B.E. Lemoff, Opt. Lett. **19** (18), 1442 (1994).

[45] J. Zhou, C.-P. Huang, M.M. Murnane, H.C. Kapteyn, Opt. Lett. **20** (1), 64 (1995).

[46] S. Backus, J. Peatross, C.P. Huang, M.M. Murnane, H.C. Kapteyn, Opt. Lett. **20** (19), 2000 (1995).

[47] M. Lenzner, Ch. Spielmann, E. Winter, F. Krausz, A.J. Schmidt, Opt. Lett. **20** (12), 1397 (1995).

[48] C.P.J. Barty, T. Guo, C. Le Blanc, F. Raksi, C. Rose-Petruck, J. Squier, K.R. Wilson, V.V. Yakovlev, K. Yamakawa, Opt. Lett. **21** (9), 668 (1996).

[49] K.F. Wall and A. Sanchez, Lincoln Laboratory Journal **3**, 447 (1990).

[50] C. Le Blanc, P. Curley, F. Salin, Optics Comunications **131**, 391 (1996).

[51] L.M. Frantz, J.S. Nodvik, Journal of Applied Physics **34** (8), 2346 (1963).

[52] a) M.W. McGeoch, Optics Communications **7** (2), 116 (1973). b) A.K. Hankla, A.B. Bullock, W.E. White, J.A. Squier, C.P.J. Barty, Opt. Lett. **22** (22), 1713 (1997).

[53] J. Squier, C.P.J. Barty, F. Salin, C. Le Blanc, S. Kane, Appl. Opt. **37** (9), 1638 (1998).

[54] R. Kingslake, Proceedings of the Society of Photo Optical Instrumentation Engineers **237**, 448 (1980).

[55] G. Cheriaux, P. Rousseau, F. Salin, J.P. Chambaret, B. Walker, L.F. Dimauro, Opt. Lett. **21** (6), 414 (1996).

[56] F. Salin, C. Le Blanc, J. Squier, C. Barty, Opt. Lett. **23** (9), 718 (1998).

[57] C. Le Blanc, PhD thesis, Ecole Polytechnique (1993).

[58] R. Trebino, D.J. Kane, J. Opt. Soc. Am. A **10** (5), 1101 (1993).

[59] D.J. Kane, R. Trebino, Opt. Lett. **18** (10), 823 (1993).

[60] K.W. DeLong, R. Trebino, J. Opt. Soc. Am. A **11** (9), 2429 (1994).

[61] K.W. De Long, R. Trebino, D.J. Kane, J. Opt. Soc. Am. B **11** (9), 1595 (1994).

[62] C. Iaconis and I.A. Walmsley, IEEE Journal of Quantum Electronics **35**, 501 (1999).

[63] D. Proch and T. Trickl, Rev. Sci. Instrum. **60** (4), 713 (1989).

[64] A.T.J.B. Eppink and D.H. Parker, Rev. Sci. Instrum. **68** (9), 3477 (1997).

[65] G.M. Lankhuijzen and L.D. Noordam, Opt. Commun. **129**, 361 (1996).

[66] C. Nicole, I. Sluimer, F. Rosca-Pruna, M. Warntjes, M. Vrakking, C. Bordas, F. Texier and F. Robicheaux, Phys. Rev. Lett. **85** (19)**,** 4024 (2000).

[67] J.B.M. Warntjes, C. Nicole, F. Rosca-Pruna, I. Sluimer, M.J.J. Vrakking and L.D. Noordam, Phys. Rev. A **63**, 053403 (2001).

[68] D.P. de Bruijn and J. Los, Rev. Sci. Instrum. **53** (7), 1020 (1982).

[69] D.W. Chandler and P.L. Houston, Journal of Chemical Physics **87** (2), 1445 (1987).

[70] W.C. Wiley and I.H. McLaren, Rev. Sci. Instrum. **26** (12), 1150 (1955).

[71] C.J. Dasch, Appl. Opt. **31** (8), 1146 (1992).

[72] L. Montgomery Smith, D.R. Keefer and S.I. Sudharsanan, J. Quant. Spectrosc. Radiat. Transfer **39** (5), 367 (1988).

[73] S.M. Candel, Comp. Phys. Comm **23**, 343 (1981).

[74] C. Bordas, F. Paulig, H. Helm and D.L. Huestis, Rev. Sci. Instrum. **67** (6), 2257 (1996).

[75] M.J.J. Vrakking, Rev. Sci. Instrum. (in press 2001).

[76] V. Schyja, T. Lang and H. Helm, Phys. Rev. A **57** (5), 3692 (1998).

[77] A. Kohlhase and S. Kita, Rev. Sci. Instrum. **57** (12), 2925 (1986).

[78] L.J. Frasinski, K. Codling and P. Hatherly, Phys. Rev. Lett. **58** (23), 2424 (1987).

[79] D.T. Strickland, Y. Beaudoin, P. Dietrich and P.B. Corkum, Phys. Rev. Lett. **68** (18), 2755 (1992).

[80] a) B. Friedrich and D. Herschbach, Phys. Rev. Lett. **74** (23), 4623 (1995).
b) B. Friedrich and D. Herschbach, Chem. Phys. Lett. **262**, 41 (1996).

[81] T. Seideman, J. Chem. Phys. **103** (18), 7887 (1995).

[82] a) J. Ortigoso, M. Rodriguez, M. Gupta and B. Friedrich, J. Chem. Phys. **110** (8), 3870 (1999).
b) C. Long, J. Marango and B. Friedrich, Phys. Rev. Lett. **86** (5), 775 (2001).

[83] H. Sakai, C.P. Safvan, J.J. Larsen, K.M. Hilligsoe, K. Hald and H. Stapelfeldt, J. Chem. Phys. **110** (21), 10235 (1999).

[84] J.J. Larsen, H. Sakai, C.P. Safvan, I. Wendt-Larsen and H. Stapelfeldt, J. Chem. Phys. **111** (17), 7774 (1999).

[85] a) J.H. Posthumus, A.J, Giles, M.R. Thompson, W. Shaikh, A.J. Langley, L.J. Frasinski and K. Codling, J. Phys. B **29**, L525 (1996). b) J.H. Posthumus, A.J. Giles, M.R. Thompson and K. Codling, J. Phys. B **29**, 5811 (1996).

[86] a) T. Seideman, M.Yu. Ivanov and P.B. Corkum, Phys. Rev. Lett. **75** (15), 2819 (1995). b) M. Ivanov, T. Seideman, P. Corkum, F. Ilkov and P. Dietrich, Phys. Rev. A **54** (2), 1541 (1996).

[87] L.J. Frasinski, J. Plumridge, J.H. Posthumus, K. Codling, P.F. Taday, E.J. Divall and A.J. Langley, Phys. Rev. Lett. **86** (12), 2541 (2001).

[88] D. Normand, L.A. Lompré and C. Cornaggia, J. Phys. B: At. Mol. Opt. Phys. **25**, L497 (1992).

[89] P. Dietrich, D.T. Strickland, M. Laberge and P.B. Corkum, Phys. Rev. A **47** (3), 2305 (1993).

[90] S. Banerjee, D. Mathur, and G. Ravindra Kumar, Phys. Rev. A. **63**, 045401 (2001).

[91] E. Springate, F. Rosca-Pruna, H.L. Offerhaus, M. Krishnamurthy and M.J.J. Vrakking, J. Phys. B: At. Mol. Opt. Phys. (accepted for publication 2001).

[92] S. Unny, Y. Du, L. Zhu, R.J. Gordon, A. Sugita, M. Kawasaki, Y. Matsumi and T. Seideman, Phys. Rev. Lett. **86** (11), 2245 (2001).

[93] C.M. Dion, A. Keller, O. Atabek and A.D. Bandrauk, Phys. Rev. A **59** (2), 1382 (1999).

[94] E. Charron, A. Giusti-Suzor and F.H. Mies, Phys. Rev. A **49** (2), R641 (1994).

[95] T. Seideman, Phys. Rev. Lett. **83** (24), 4971 (1999).

[96] F. Rosca-Pruna and M.J.J. Vrakking, Phys. Rev. Lett. **87** (15), 159302 (2001).

[97] H.J. Loesch and A. Remscheid, J. Chem. Phys. **93** (7), 4779 (1990).

[98] C. Cornaggia, J. Lavancier, D. Normand, J. Morellec, P. Agostini, J.P. Chambaret and A. Antonetti, Phys. Rev. A **44** (7), 4499 (1991).

[99] J.H. Posthumus, J. Plumridge, L.J. Frasinski, K. Codling, A.J. Langley and P.F. Taday, J. Phys. B: At. Mol. Opt. Phys. **31**, L985 (1998).

[100] F. Rosca-Pruna, E. Springate, H.L. Offerhaus, M. Krishnamurthy, N. Farid, C. Nicole and M.J.J. Vrakking, J. Phys. B: At. Mol. Opt. Phys. (accepted for publication 2001).

[101] K.H. Kramer and R.B. Bernstein, J. Chem. Phys. **42** (2), 767 (1965).

[102] J.J. Larsen, K. Hald, N. Bjerre, and H. Stapelfeldt, Phys. Rev. Lett. **85** (12), 2470 (2000).

[103] D.G. Lappas and J.P. Marangos, J. Phys. B: At. Mol. Opt. Phys. **33**, 4679 (2000).

[104] D.W. Callahan, A. Yokozeki and J.S. Muenter, J. Chem. Phys. **72** (9), 4791 (1980).

[105] E.F. Archibong and A.J. Thakkar, Chem. Phys. Lett. **201**, 485 (1993).

[106] J.H. Posthumus, L.J. Frasinski, A.J. Giles and K. Codling, J. Phys. B: At. Mol. Opt. Phys. **28**, L349 (1995).

[107] G.N. Gibson, M. Li, C. Guo and J.P. Nibarger, Phys. Rev. A **58** (6), 4723 (1998).

[108] W. Kolos and L. Wolniewicz, J. Chem. Phys. **46** (4), 1426 (1967).

[109] G. Ravindra Kumar, P. Gross, C.P. Safvan, F.A. Rajgara and D. Mathur, J. Phys. B: At. Mol. Opt. Phys. **29**, L95 (1996).

[110] P.B. Corkum, Ch. Ellert, M. Mehendale, P. Dietrich, S. Hankin, S. Aseyev, D. Rayner and D. Villeneuve, Faraday Discuss. **113**, 47 (1999).

[111] H. Stapelfeldt, H. Sakai, E. Constant and P. B. Corkum, Phys. Rev. Lett. **79** (15), 2787 (1997).

[112] C.J. Bardeen, V.V. Yakovlev, K.R. Wilson, S.D. Carpenter, P.M. Weber and W.S. Warren, Chem. Phys. Lett. **280**, 151 (1997).

[113] D.M. Villeneuve, S.A. Aseyev, P. Dietrich, M. Spanner, M.Yu. Ivanov and P.B. Corkum, Phys. Rev. Lett. **85** (3), 542 (2000).

[114] W. Kim and P.M. Felker, J. Chem. Phys. **104** (3), 1147 (1996).

[115] A.J.R. Heck and D.W. Chandler, Annu. Rev. Phys. Chem. **46**, 335 (1995)

[116] J.S. Baskin, P.M. Felker and A.H. Zewail, J. Chem. Phys. **84** (8), 4708 (1986).

[117] a) E. Hertz, O. Faucher, B. Lavorel, F. Dalla Via, and R. Chaux , Phys. Rev. A **61**, 033816 (2000). b) E.J. Brown, Q. Zhang and M. Dantus, J. Chem. Phys. **110** (12), 5772 (1999).

[118] S.C. Althorpe and T. Seideman, J. Chem. Phys. **110** (1), 147 (1999).

[119] F. Rosca-Pruna and M.J.J. Vrakking, J. Chem. Phys. (submitted for publication 2001).

[120] B. Friedrich and D. Herschbach, J. Phys. Chem. **99**, 15686 (1995).

[121] G.H.C. New and J.F. Ward, Phys. Rev. Lett. **19** (10), 556 (1967).

[122] a) J. Reintjes, R.C. Eckardt, C.Y. She, N.E. Karangelen, R.C. Elton and R.A. Andrews, Phys. Rev. Lett. **37** (23), 1540 (1976). b) J. Reintjes, C.Y. She, R.C. Eckardt, N.E. Karangelen, R.A. Andrews and R.C. Elton, Appl. Phys. Lett. **30** (9), 480 (1977). c) J. Reintjes, C.Y. She and R.C. Eckardt, IEEE J. Quant. Electron **QE-14** (8), 581 (1978).

[123] D.I. Metchkov, V.M. Mitev, L.I. Pavlov and K.V. Stamenov, Opt. Comm. **21** (3), 391 (1977).

[124] M.G. Groseva, D.I. Metchkov, V.M. Mitev, L.I. Pavlov and K.V. Stamenov, Opt. Comm. **23** (1), 77 (1977).

[125] S.E. Harris, Phys. Rev. Lett. **31** (6), 341 (1973).

[126] J.F. Young, G.C. Bjorklund, A.H. Kung, R.B. Miles and S.E. Harris, Phys. Rev. Lett. **27** (23), 1551 (1971).

[127] K.M. Leung, J.F. Ward and B.J. Orr, Phys. Rev. A **9** (6), 2440 (1974).

[128] A.T. Georges, P. Lambropoulos and J.H. Marburger, Phys. Rev. A **15** (1), 300 (1977).

[129] E.S. Toma, Ph. Antoine, A. de Bohan and H.G. Muller, J. Phys. B: At. Mol. Opt. Phys. **32**, 5843 (1999).

[130] R.B. Miles and S.E. Harris, IEEE J. Quant. Electron. **QE-9** (4), 470 (1973).

[131] B. Sheehy, J.D.D. Martin, L.F. DiMauro, P. Agostini, K.J. Schafer, M.B. Gaarde and K.C. Kulander, Phys. Rev. Lett. **83** (25), 5270 (1999).

[132] J.F. Ward and G.H.C. New, Phys Rev. **185** (1), 57 (1969).

[133] G.C. Bjorklund, IEEE J. Quant. Electron. **QE-11** (6), 287 (1975).

[134] A.H. Kung, Opt. Lett. **8** (1), 24 (1983).

[135] A. L'Huillier, L.A. Lompre, G. Mainfray and C. Manus, J. Phys. B **16**, 1363 (1983).

[136] X.F. Li, A. L'Huillier, M. Ferray, L.A. Lompre and G. Mainfray, Phys. Rev. A **39** (11), 5751 (1989).

[137] I.S. Aleksakhin, I.P. Zapesochnyi and V.V. Suran, JETP Lett. **26** (1), 11 (1977).

[138] A. L'Huillier, L.A. Lompre, G. Mainfray and C. Manus, Phys. Rev Lett. **48** (26), 1814 (1982).

[139] T.S. Luk, H. Pummer, K. Boyer, M. Shahidi, H. Egger and C.K. Rhodes, Phys. Rev. Lett. **51** (2), 110 (1983).

[140] P. Agostini, F. Fabre, G. Mainfray, G. Petite and N.K. Rahman, Phys. Rev. Lett. **42** (17), 1127 (1979).

[141] P. Kruit, J. Kimman, H.G. Muller and M.J. van der Wiel, Phys Rev. A **28** (1), 248 (1983).

[142] R.R. Freeman, P.H. Bucksbaum, H. Milchberg, S. Darak, D. Schumacher and M.E. Geusic, Phys. Rev. Lett. **59** (10), 1092 (1987).

[143] P. Agostini, P. Breger, A. L'Huillier, H.G. Muller, G. Petite, A. Antonetti and A. Migus, Phys. Rev. Lett. **63** (20), 2208 (1989).

[144] a) K.C. Kulander and B.W. Shore, Phy. Rev. Lett. **62** (5), 524 (1989). b) K.C. Kulander and B.W. Shore, J. Opt. Soc. Am. **B7** (4), 502 (1990).

[145] J.H. Eberly, Q. Su, J. Javanainen, K.C. Kulander, B.W. Shore and L. Roso-Franco, J. Mod. Opt. **36** (7), 829 (1989).

[146] P.L. DeVries, J. Opt. Soc. Am **B7** (4), 517 (1990).

[147] K.J. LaGattuta, Phys. Rev. A **41** (9), 5110 (1990).

[148] R.M. Potvliege and R. Shakeshaft, Phys. Rev. A **40** (6), 3061 (1989).

[149] M. Dörr, R.M. Potvliege and R. Shakeshaft, J. Opt. Soc. Am. **B7** (4), 433 (1990).

[150] G. Bandarage, A. Maquet and J. Cooper, Phys. Rev. A **41** (3), 1744 (1990).

[151] S.I. Chu, K. Wang and E. Layton, J. Opt. Soc. Am. **B7** (4), 425 (1990).

[152] a) J.H. Eberly, Q. Su and J. Javanainen, Phys. Rev. Lett. **62** (8), 881 (1989). b) J.H. Eberly, Q. Su and J. Javanainen, J. Opt. Soc. Am. **B6** (7), 1289 (1989).

[153] B.W. Shore and P.L. Knight, J. Phys. B **20**, 413 (1987).

[154] L.C. Biedenharm, G.A. Rinker and J.C. Solem, J. Opt. Soc. Am. **B6** (2), 221 (1989).

[155] B. Sundaram and P.W. Milonni, Phys. Rev. A **41** (11), 6571 (1990).

[156] W. Becker, S. Long and J.K. McIver, Phys Rev. A **41** (7), 4112 (1990).

[157] R.A. Sacks and A. Szöke, J. Opt. Soc. Am. **B8** (9), 1987 (1991).

[158] A. L'Huillier, X.F. Li, and L.A. Lompre, J. Opt. Soc. Am. **B7** (4), 527 (1990).

[159] a) L. Pan, K.T. Taylor and C.W. Clark, Phys. Rev. Lett. **61** (23), 2673 (1988). b) L. Pan, K.T. Taylor and C.W. Clark, Phys. Rev. A **39** (9), 4894 (1989).

[160] J.L. Krause, K.J. Schafer and K.C. Kulander, Phys. Rev. A **45** (7), 4998 (1992).

[161] A. L'Huillier, K.J. Schafer and K.C. Kulander, Phys. Rev. Lett. **66** (17), 2200 (1991).

[162] A. L'Huillier, Ph. Balcou, S. Candel, K.J. Schafer and K.C. Kulander, Phys. Rev. A **46** (5), 2778 (1992).

[163] J.L. Krause, K.J. Schafer and K.C. Kulander, Phys. Rev. Lett. **68** (24), 3535 (1992).

[164] J.J. Macklin, J.D. Kmetec and C.L. Gordon III, Phys. Rev. Lett. **70** (6), 766 (1993).

[165] A. L'Huillier, M. Lewenstein, P. Salieres, Ph. Balcou, M.Yu. Ivanov, J. Larsson and C.G. Wahlström, Phys. Rev. A **48** (5), R3433 (1993).

[166] K. Kondo, N. Sarukura, K. Sajiki and S. Watanabe, Phys. Rev. A **47** (4), R2482 (1993).

[167] P.B. Corkum, Phys. Rev. Lett **71** (13), 1994 (1993).

[168] K.C. Kulander and K.J. Schafer, *Proc. Int. Conf. Multi Photon ProcessesVI,* ed D.K. Evans (World Scientific, Singapore, 1993).

[169] K.J. Schafer, B. Yang, L.F. DiMauro and K.C. Kulander, Phys. Rev. Lett. **70** (11), 1599 (1993).

[170] H.B. van Linden van den Heuvell and H.G. Muller, *Multiphoton Processes,* ed S.J. Smith and P.L. Knight p.25 (Cambridge University Press, Cambridge, 1988).

[171] K.C. Kulander and T.N. Rescigno, Comp. Phys. Comm. **63**, 523 (1991).

[172] A. L'Huillier and P. Balcou, Phys. Rev. Lett. **70** (6), 774 (1993).

[173] J. Zhou, J. Peatross, M.M. Murnane, H.C. Kapteyn and I.P. Christov, Phys. Rev. Lett. **76** (5), 752 (1996).

[174] Z. Chang, A. Rundquist, H. Wang, M.M. Murnane and H.C. Kapteyn, Phys. Rev. Lett. **79** (16), 2967 (1997).

[175] A. Bandrauk and H. Yu, Phys. Rev. A **59** (1), 539 (1999).

[176] X.M. Tong and S.I. Chu, J. Phys. B: At. Mol. Opt. Phys. **32**, 5593 (1999).

[177] A. Rundquist, C.G. Durfee III, Z. Chang, C. Herne, S. Backus, M.M. Murnane and H.C. Kapteyn, Science **280**, 1412 (1998).

[178] R. Bartles, S. Backus, E. Zeek, L. Misoguti, G. Vdovin, I.P. Christov, M.M. Murnane and H.C. Kapteyn, Nature **406**, 164 (2000).

[179] V.G. Arkhipkin and A.K. Popov, Sov. Phys. Usp. **30**, 952 (1987).

[180] D.C. Hanna, M.A. Yuratich and D. Cotter, *Nonlinear Optics of Free Atoms and Molecules*, Springer-Verlag, Berlin (1979).

[181] J. Reintjes, *Nonlinear Optical Parametric Processes in Liquids and Gases*, Academic Press, Orlando (1984).

[182] Y.R. Shen, *The Principles of Nonlinear Optics*, Wiley, New York (1984).

[183] N.B. Delone and V.P. Krainov, *Fundamentals of Nonlinear Optics of Atomic Gases*, Wiley, New York (1988).

[184] P. Salieres, A. L'Huillier and M. Lewenstein, Phys. Rev. Lett. **74** (19), 3776 (1995).

[185] M.J. McCaughrean, H. Chen, J. Bally, E. Erickson, R. Thompson, M. Rieke, G. Schneider, S. Stolovy and E. Young, Astrophys. J. **492**, L157 (1998).

[186] D. Johnstone, D. Hollenbach and J. Bally, Astrophys. J. **499**, 758 (1998).

[187] J. Bally, C.R. O'Dell and M.J. McCaughrean, Astron. J. **119**, 2919 (2000).

[188] A. Brun, P. Georges, G. Le Saux and F. Salin, J. Phys. D **24**, 1225 (1991).

[189] A. Bouhal, R. Evans, G. Grillon, A. Mysyrowicz, P. Breger, P. Agostini, R.C. Constantinescu, H.G. Muller, D. von der Linde, J. Opt. Soc. Am. **B14** (4), 950 (1997).

[190] A. Bouhal, P. Salières, P. Breger, P. Agostini, G. Hamoniaux, A. Mysyrowicz, A. Antonetti, R. Constantinescu and H.G. Muller, Phys. Rev. A **58** (1), 389 (1998).

[191] J.M. Schins, P. Breger, P. Agostini, R.C. Constantinescu, H.G. Muller, G. Grillon, A. Antonetti and A. Mysyrowicz, Phys. Rev. Lett. **73** (16), 2180 (1994).

[192] M.H. Sher, U. Mohideen, H.W.K. Tom, O.R. Wood, G.D. Aumiller, R.R. Freeman and T.J. McIlrath, Opt. Lett. **18** (8), 646 (1993).

[193] S.P. Le Blanc, Z. Qi and R. Sauerbrey, Opt. Lett. **20** (3), 312 (1995).

[194] M. Lewenstein, P. Salieres and A. L'Huillier, Phys. Rev. A **52** (6), 4747 (1995).

[195] C. de Lisio, C. Altucci, C. Beneduce, R. Bruzzese, F. De Filippo, S. Solimeno, M. Bellini, A. Tozzi, G. Tondello and E. Pace, Opt. Comm. **146**, 316 (1998).

[196] M.Gavrila, *Atoms in Intense Laser Fields*, Adv. At. Mol. Opt. Phys. Suppl.1 (1992).

[197] A. Giusti-Suzor, F.H. Miles, L.F. DiMauro, E. Charron and B. Yang, J. Phys. B: At. Mol. Opt. Phys. **28**, 309 (1995).

[198] K. Codling and L.J. Frasinski, J. Phys. B: At. Mol. Opt. Phys. **26**, 783 (1993).

[199] A. Giusti-Suzor, X. He, O. Atabek and F.H. Miles, Phys. Rev. Lett. **64** (5), 515 (1990).

[200] P.H. Bucksbaum, A. Zavriyev, H.G. Muller and D.W. Schumacher, Phys. Rev. Lett. **64** (16), 1883 (1990).

[201] A. Giusti-Suzor and F.H. Miles, Phys. Rev. Lett. **68** (26), 3869 (1992).

Acknowledgment

The work presented in this thesis would not have been possible without all of those who helped me in finding the right path, from my first day in Amolf, when I performed my undergraduate project, throughout my entire Ph.D. period.

First of all, I would like to thank my co-promotor Marc Vrakking. I consider myself to have been very lucky to have worked under his supervision. When I started, I did not have very much 'practical' experience, but he patiently taught me a lot of experimental skills, so that at the end of these four years I can be proud of building a very powerful laser and performing very beautiful experiments. Moreover, I greatly appreciate Marc's vision and the way he always has new ideas for interesting projects.

My great appreciation goes also to my promotor Harm Muller for taking the time to listen to and answer all my clever and less clever questions. All his remarks were based on top scientific reasoning and proved to be a real challenge for me.

I would like to thank my mentor, Prof.Voicu Grecu, for his support and very useful comments and advice. I am most grateful for his encouragement not to miss the opportunity of coming to Amolf for doing top research.

Being one of the first members of the "XUV Physics" group that started in Amolf in the beginning of 1997, I have had the privilege to meet all the members or, by now, ex-members that have joined the group so far. Some of them shared the office with me at different periods of time, creating a challenging but at the same time a nice and relaxing work environment. I thank Celine Nicole for showing me that it is possible to follow the thread of a problem until the smallest detail, ending up with fixing small electronic or electro-mechanic bugs. I thank Emma Springate for the nice time we spent together in trying to understand how molecules align in the laser field and for patiently bringing down the number of grammar mistakes I made, by correcting my English in our day-by-day discussions and especially in this thesis. I thank Herman Offerhaus for showing me how I can plan my work and be more efficient. Although we have been working together only for few months so far, I would like to thank Sergey Aseyev for trying to inspire me with his enthusiasm for physics. It has been a pleasure as well to work on various projects with Arnoud Witt, Ingrid Sluimer, M. Krishnamurthy, Nadia Farid and Arjan Houtepen.

The building of the laser and the XUV experimental setup is finalised and we have already published the first Physical Review Letters, but none of these could have been possible without the daily help of Anton Buyserd, Rob Kemper and Hinco Schoenmaker. I thank Anton Buyserd for patiently teaching me from his experience.

I thank Rob Kemper for his moral support during the experiments and for being concerned for our health.

The assistance provided by E&I department helped me to successfully tackle the computer related jobs. Dennis Driessen and Richard Schaafsma were aware of the fact that I did not know very much about computers. Thanks to them my computer kept running well. Hans Alberda, Else Homan, Marco Konijnenburg and Sjoerd Wouda helped me in my attempt to learn C and Labview for the data-acquisition system. Hans ter Horst, Idsard Attema and Duncan Verheijde assisted us with building the triggering/synchronization system and made safety boxes to stop us destroying the detectors and oscilloscopes.

The other departments of Amolf have been involved in the development of our set-ups as well. The drawing room together with the workshop always knew that we need that particular piece of equipment 'yesterday'. The 'magazijn' and the financial department helped us with processing materials before payment and other long paperwork procedures.

From the period of my undergraduate studies and throughout my Ph.D. I have interacted with students from the group of Harm Muller, Bart Noordam, Wim van der Zande and Huib Bakker. Philippe Antoine, Raluca Constantinescu, Diederik Maas, Marcel Lankhuijzen, Lavina Snoek, Simon Clement, Bart Buijsse, Eloy Wouters and Antonio Paiva helped me to find my first way through the lab. Later on, I enjoyed working with Anouk Wetzels, Andreas Gürtler, Kees Wesdorp and Marcel Warntjes. I would like to thank Han Kwang Nienhuys, Frederik van den Broek, Michel Kropman and Arjan Lock for sharing 800nm optics with us. Igor Shvarchuck *et al.* was a funny, friendly group, nice to meet especially when the things were not going so well.

Amolf did not help me only from the scientific point of view but also with all the official matters and with finding comfortable and convenient accommodation. For this I would like to thank Wouter Harmsen, Esther Coster, Daniëlle de Vries, Roudy van der Wijk and Ed Kruller. Special thanks to Helen and Ed Kruller for their great friendship, support and help throughout these years.

"The Romanian clan", Elena Toma, Georgiana Languri, Laura Dinu, Catalin Dinu and Catalin Tanase, are acknowledged for reducing my homesickness (especially after a long time away from Romania) and for being very reliable messengers. I thank Henk Sodenkamp for being always interested in the economical, political and social situation of Romania. I would also like to thank my family and friends from Romania for their support and for encouraging me at critical moments. I thank Nicu for his love and his patience in whole of this period and for helping me with the 'home computer' problems.

Mulţumesc tuturor celor de acasă pentru sprijinul acordat şi pentru încurajările primite în toată această perioadă. Mama, tata şi draga mea bunică, în tot ceea ce am facut pană acum am încercat să folosesc cele învăţate de la voi şi sper ca voi sa fiţi mândri de tot ceea ce am realizat.

Florentina Roşca-Prună - Amsterdam, October 2001